Waveform simulation and source characterization of acoustic emissions in concrete tensile fracture processes

A lattice modelling approach

Yubao ZHOU

Waveform simulation and source characterization of acoustic emissions in concrete tensile fracture processes: a lattice modelling approach

Dissertation

for the purpose of obtaining the degree of doctor

at Delft University of Technology

by the authority of the Rector Magnificus, Prof.dr.ir. T.H.J.J. van der Hagen,

chair of the Board for Doctorates

to be defended publicly on

Monday 12 January 2026 at 10:00 o'clock

by

Yubao ZHOU

Master of Engineering in Hydraulic Engineering,

Tongji University, China.

This dissertation has been approved by the promotors.

Promotor: Prof.dr.ir. M.A.N. Hendriks
Promotor: Dr.ir. Y. Yang

Composition of the doctoral committee:

Rector Magnificus,	chairperson
Prof.dr.ir. M.A.N. Hendriks,	Delft University of Technology Norwegian University of Science and Technology, Norway, promotor
Dr.ir. Y. Yang,	Delft University of Technology, promotor

Independent members:

Prof.dr.ir. H.E.J.G. Schlangen,	Delft University of Technology
Prof.dr. A.V. Metrikine,	Delft University of Technology
Prof.dr. T. Shiotani,	Kyoto University, Japan
Prof.dr. D. Aggelis,	Vrije Universiteit Brussel, Belgium
Prof.dr.-Ing. C.U. Große,	Technical University of Munich, Germany

Keywords: Acoustic emission, Lattice model, Concrete fracture, Source mechanisms, Elastic waves.

Cover design: Yubao Zhou

To my parents and my wife Xinling

谨以此书献给我的父亲母亲和亲爱的小岳

Summary

To prevent catastrophic structural failures, it is essential to monitor the condition of aging concrete structures and provide early warnings that enable timely maintenance and repair. Structural health monitoring (SHM) of concrete structures has attracted considerable attention in the research community. Among various SHM techniques, acoustic emission (AE) has emerged as a particularly effective method for early fracture detection, owing to its real-time monitoring capabilities and sensitivity to early crack formation.

However, a comprehensive review of the mechanisms and models related to AE phenomena in concrete fracture (Chapter 2) reveals ongoing challenges in applying AE reliably. A key difficulty lies in accurately correlating localized fracture events with AE signals recorded after wave propagation through complex structural media. Both experimental inversion and forward modelling approaches have been explored to address this issue. Nevertheless, experimental techniques face inherent limitations due to complex wave propagation effects and sensor responses. Furthermore, existing modelling methods are not yet capable of explicitly simulating AE signals generated by concrete fracture.

This dissertation aims to investigate the source mechanisms underlying AE phenomena induced by concrete fracture and to establish a quantitative relationship between localized fracture events and the resulting AE signals. The overarching goal is to enhance the reliability of AE-based techniques for early warning applications in concrete structures. Particular attention is given to AE signals generated by tensile cracking, which is the dominant source of AE activity, especially in the early stages of fracture when timely warnings are most critical. The research is organized into three main topics:

First, a general modelling framework is developed for AE simulation based on lattice modelling, which is well-established for simulating concrete fracture. Chapter 3 extends traditional lattice models to simulate elastic wave propagation by introducing a proportional-integral-derivative (PID) control algorithm to suppress spurious noise and a Rayleigh damping-based approach to model signal attenuation. Chapter 4 further incorporates sensor response modelling into this framework, resulting in a comprehensive system for simulating AE signal generation due to tensile cracking.

Second, the dissertation investigates the fundamental mechanisms by which tensile cracking generates AE signals. Chapter 5 explores these mechanisms analytically using a simplified one-degree-of-freedom (1-DoF) system. Chapter 6 applies the proposed lattice model to a more realistic two-dimensional scenario, analysing the relationship between AE signals and both local and global mechanical behaviour during tensile cracking.

Third, the research quantifies AE sources generated by concrete tensile cracking using the developed modelling framework. Chapter 7 establishes quantitative relationships between AE source parameters and tensile cracking behaviour, including a correlation between AE peak frequency and fracture volume, offering a physically grounded AE indicator. Chapter 8 provides a physical interpretation of trends in AE parameters observed during crack propagation, supporting more rational, physics-based interpretations of AE signals.

In summary, this dissertation advances the understanding of AE source mechanisms and contributes to more reliable AE-based early warning systems for concrete fracture through the following key achievements:

- Development of a comprehensive lattice modelling framework capable of simulating full AE waveforms, with potential applicability to other AE source types in quasi-brittle materials (Chapters 3 and 4)
- Elucidation of the physical mechanisms driving AE from tensile cracking in concrete, providing a robust foundation for reliable AE applications (Chapters 5 and 6).
- Introduction of a physically grounded AE indicator for quantifying tensile cracking, enabling fracture volume estimation from measured AE peak frequency and offering guidance on sensor layout and selection (Chapter 7).
- Provision of physical interpretations for the evolution of AE parameters during tensile crack propagation, facilitating more rational, physics-based analysis of AE data in experimental fracture mechanics (Chapter 8).

Samenvatting

Om catastrofale falen van constructies te voorkomen, is het essentieel om de conditie van verouderende betonconstructies te monitoren en om vroegtijdige waarschuwingen te geven die tijdig onderhoud en herstel mogelijk maken. Constructieve gezondheidsmonitoring (SHM) van betonconstructies heeft aanzienlijke aandacht gekregen binnen de onderzoeksgemeenschap. Onder de diverse SHM-technieken is akoestische emissie (AE) naar voren gekomen als een bijzonder effectieve methode voor het vroegtijdig detecteren van scheurvorming, dankzij de mogelijkheden voor real-time monitoring en de gevoeligheid voor vroege scheurinitiatie.

Een uitgebreide analyse van de onderliggende mechanismen en modellen (Hoofdstuk 2) met betrekking tot AE-fenomenen bij betonbreuk laat echter zien dat het nog steeds een uitdaging is om AE betrouwbaar toe te passen. Een belangrijke moeilijkheid is het nauwkeurig correleren van gelokaliseerde breukgebeurtenissen met AE-signalen die worden geregistreerd nadat de golven zich door het complexe structurele medium hebben voortgeplant. Zowel experimentele inversie- als forward-modelleringsbenaderingen zijn onderzocht om deze uitdaging aan te pakken. Desondanks ondervinden experimentele technieken inherente beperkingen als gevolg van complexe golfvoortplantingseffecten en sensorrespons. Bovendien zijn bestaande modelleringsmethoden momenteel nog niet in staat om AE-signalen die door betonbreuk worden gegenereerd expliciet te simuleren.

Dit proefschrift heeft tot doel de brontheorieën te onderzoeken die ten grondslag liggen aan AE-fenomenen die worden opgewekt door betonbreuk, en om een kwantitatieve relatie vast te stellen tussen gelokaliseerde breukgebeurtenissen en de resulterende AE-signalen. Het overkoepelende doel is het verbeteren van de betrouwbaarheid van AE-gebaseerde technieken voor toepassingen op het gebied van vroegtijdige waarschuwing bij betonconstructies. Bijzondere aandacht gaat uit naar AE-signalen die worden gegenereerd door trek-scheurvorming, de dominante bron van AE-activiteit, met name in de vroege fasen van breuk, waarin tijdige waarschuwingen het meest cruciaal zijn. Het onderzoek is georganiseerd rond drie hoofdthema's:

Ten eerste wordt een algemeen modelleringskader ontwikkeld voor AE-simulatie op basis van vakwerkmodellering, een methode die breed wordt toegepast voor het simuleren van betonbreuk. Hoofdstuk 3 breidt traditionele vakwerkmodellen uit om elastische golfvoortplanting te simuleren door een proportionele, integrerende en differentiërende (PID) regelalgoritme te introduceren om spookruis te onderdrukken, en een aanpak gebaseerd op Rayleigh-demping voor het modelleren van signaalverzwakking. In Hoofdstuk 4 wordt bovendien de modellering van sensorrespons geïntegreerd in dit kader, wat resulteert in een volledig systeem voor het simuleren van AE-signaalgeneratie ten gevolge van trek-scheurvorming.

Ten tweede onderzoekt het proefschrift de fundamentele mechanismen waarmee trek-scheurvorming AE-signalen genereert. Hoofdstuk 5 verkent deze mechanismen analytisch aan de hand van een vereenvoudigd één-vrijheidsgraden (1-DoF) systeem. Hoofdstuk 6 past het voorgestelde vakwerkmodel toe op een realistischer tweedimensionaal geval, waarbij de relatie tussen AE-signalen en zowel het lokale als globale mechanisch gedrag tijdens trek-scheurvorming wordt geanalyseerd.

Ten derde kwantificeert het onderzoek de AE-bronnen die worden gegenereerd door trek-scheurvorming in beton, met behulp van het ontwikkelde modelleringskader. Hoofdstuk 7 stelt kwantitatieve relaties vast tussen AE-bronparameters en het gedrag van trek-scheurvorming, waaronder een correlatie tussen AE-piekfrequentie en breukvolume, waarmee een fysisch onderbouwde AE-indicator wordt aangeboden. Hoofdstuk 8 geeft een fysische interpretatie van trends in AE-parameters die worden waargenomen tijdens scheurvoortplanting, ter ondersteuning van meer rationele, natuurkundige interpretaties van AE-signalen.

Samenvattend levert dit proefschrift een bijdrage aan het begrip van AE-bronmechanismen en aan betrouwbaardere AE-gebaseerde systemen voor vroegtijdige waarschuwing bij betonbreuk, door de volgende hoofdresultaten:

- Ontwikkeling van een uitgebreid vakwerk-modelleringskader dat in staat is om volledige AE-golfvormen te simuleren in quasi-brosse materialen (Hoofdstukken 3 en 4).
- Verklaring van de fysische mechanismen die AE genereren als gevolg van trek-scheurvorming in beton, en het bieden van een robuuste basis voor betrouwbare AE-toepassingen (Hoofdstukken 5 en 6).
- Introductie van een fysisch onderbouwde AE-indicator voor het kwantificeren van trek-scheurvorming, waarmee het breukvolume geschat kan worden op basis van gemeten AE-piekfrequentie, en die richtlijnen biedt voor sensorlay-out en -selectie (Hoofdstuk 7).
- Fysische interpretatie van de evolutie van AE-parameters tijdens scheurvoortplanting, wat bijdraagt aan een meer rationele, natuurkundige analyse van AE-data in experimentele breukmechanica (Hoofdstuk 8).

Table of Contents

1. Introduction

1.1 Reliable monitoring and early warnings on fracturing of concrete structures

Concrete structures are the major construction type for buildings and infrastructure. Throughout the world, a considerable share of concrete structures experience notable aging, compromising their functionality and performance (Hariri-Ardebili, Sanchez, and Rezakhani 2020). In the Netherlands, around 60% of bridges were built before 1975 among a total of around 3500 bridges in the road network (Lantsoght et al. 2013). It is essential to reliably monitor the health of aging concrete structures and provide early warnings against damages, enabling timely maintenance and repair.

Among various types of damage, fracturing of concrete is the most common damage type and is recognized as an effective indicator of structural failure. Reliable monitoring the fracturing processes of concrete structures has gained significant attention in the research community. Among others, tensile cracking constitutes the dominant fracture mechanism, especially during the early stages of concrete fracturing processes (Aggelis 2011).

Therefore, monitoring tensile cracking activities during the initial phases holds significant potential as an early warning indicator of impending structural failure in concrete. This is particularly important during load testing of concrete structures or during intensive monitoring of critical infrastructure. In such cases, tracking tensile cracking enables more effective assessment of structural performance and a deeper investigation into underlying fracturing (Zhang 2022).

To effectively monitor concrete tensile cracking activities in early fracturing stages, it is ideal to have a monitoring technique that possesses the following capabilities:

- Real-time monitoring
- Sensitive to microcracking at early fracturing stages
- Internal cracking detection

The first two capabilities are essential to provide an early warning of concrete fracture and enabling timely maintenance and repair. The third is critical for identifying structural failures that originate from internal damage (Tue, Theiler, and Tung 2014).

Although numerous non-destructive evaluation (NDT) techniques have been developed over the past decades (Gharehbaghi et al. 2022), most existing methods fail to meet the above requirements simultaneously. Specifically, traditional strain- and displacement-based techniques (e.g., strain gauges (Higson 1964), linear variable differential transformer (LVDT) (Nhung et al. 2023) and fibre optic sensors (Udd 1995) as well as vision-based methods (e.g., digital image correlation (DIC) (McCormick and Lord 2010) are

incapable of detecting internal cracks and/or are not sensitive to microcracks in the early stages of fracturing. Similarly, traditional ultrasonic monitoring techniques (e.g., external ultrasonic testing (Prassianakis and Prassianakis 2004) and embedded smart aggregates (Song, Gu, and Mo 2008) do not enable real-time monitoring; instead, they assess structural damage states only at specific time points.

Among various NDT methods, acoustic emission (AE) stands out as an ideal technique that simultaneously meets all three of the above-listed requirements, since the AE technique directly monitors the elastic waves generated by the rapid energy release of internal fracturing activities (Matthews 1983). This establishes the AE technique as an ideal monitoring method in concrete structures under loading. Much AE-related research has been conducted in literature for monitoring concrete fracture processes. For example, acoustic emission-based indicators have been recently proposed to provide early warnings of shear failure of reinforced concrete structures without shear reinforcement (Zhang 2022).

Although applications of the AE technique in the concrete field can be dated back to 1950s (Ajitesh 1956; Brun and Boucher 1956), many fundamental issues in acoustic emission (AE) remain unresolved. AE signals arise from a complex interplay of multiscale and multi-physical phenomena, including local material fracturing, global elastic wave propagation, and sensor response. To date, it is not yet possible to reliably link measured AE signals to fracture activities inside concrete structures.

1.2 Research goal and questions

This dissertation focuses on the acoustic emission induced by concrete tensile cracking, as it is dominant AE source type in concrete fracture processes and offers significant potential as early warning indicators of impending structural failure in concrete. The primary objective of this research is to understand the link between concrete tensile fracturing processes and induced AE signals.

Therefore, the central research question is: How can measured acoustic emission be linked to the tensile fracture processes in concrete?

The main question can be classified into sub-research questions, with the corresponding challenges.

The first discussed objective is development of AE modelling methods. Compared to experimental methods that cannot separate the individual components of the AE process, modelling is a promising tool to address the complicated multi-physics phenomena of AE. Nevertheless, there is currently no modelling method capable of accurately modelling the coupling between concrete fracture processes and induced elastic wave propagation, as well as sensor response. The inability to comprehensively capture all these interacting

components limits the predictive and interpretive capabilities of current AE modelling techniques.

Therefore, the first question is: (Q1) How can we accurately model the local material fracturing, global elastic wave propagation and sensor response simultaneously with one model?

The second discussed objective is mechanisms of AE sources. There is currently a lack of consistent understanding regarding the mechanisms underlying the monitored AE signals. Existing AE theories attribute the origin of AE phenomena to various mechanisms occurring at different scales and from diverse perspectives, resulting in fragmented and sometimes contradictory interpretations. Furthermore, these theories are generally unable to provide a physical explanation for many of the commonly used AE signal parameters, limiting their ability to support accurate, physics-based interpretation and modelling of AE data.

Therefore, we need to provide a physics-based interpretation of tensile cracking-induced AE phenomena. To achieve this, we need to figure out: (Q2) How does concrete tensile cracking generate acoustic emission?

The third discussed objective is understanding AE measurements. Currently, there is no reliable experimental AE characterization method capable of quantitatively linking recorded AE signals to concrete fracturing behaviour. Existing methods are largely developed through empirical calibration and experimental observations, often lacking a clear physical foundation. As a result, these phenomenological approaches fall short in providing quantitative insights into the actual fracture processes occurring within concrete, limiting their effectiveness for rigorous material characterization or predictive modelling.

For practical applications, we need to quantify concrete tensile cracking activities through AE measurements. Therefore, the research question is: (Q3) what is the quantitative relationship between concrete tensile fracturing parameters and induced AE signals?

Furthermore, to provide effective early warning for critical fracturing phases, we need to understand the effects of successive tensile fracturing processes on AE parameters. One following-up question is: (Q4) How does the successive tensile fracturing process effect the acoustic emission parameters?

The four sub-questions form three parts of work. Part 1 includes questions Q1, to develop AE modelling methods. Part 2 focuses on Q2, to fundamentally reveal the mechanisms underlying concrete tensile cracking-induced AE sources. Part 3 includes Q3-Q4, to develop physics-grounded AE indicators and to provide more reliable interpretation of AE measurements.

1.3 Thesis outline

The outline of this dissertation is illustrated in Figure 1.1. The main contents answer the three parts of research questions described in Section 1.2. The dissertation contains eight additional chapters, each briefly described as follows:

- Chapter 2 performs a literature review on AE phenomena induced by concrete fracturing processes. This chapter aims to explore cutting-edge knowledge on AE phenomena in concrete fracturing, and to compare different available AE theories and AE modelling methods.

Development of AE modelling methods, for research questions Part 1 (Q1)

- Chapter 3 addresses Q1, proposing a general lattice modelling framework for simulating the propagation and attenuation of elastic waves induced by concrete tensile cracking. The proposed model will be used to simulate complete AE waveforms induced by tensile cracking (Chapter 4) and to characterize the source mechanisms of tensile cracking-induced AE signals (Chapters 6, 7, and 8).
- Chapter 4 further addresses Q1, developing additional techniques for modelling AE sensor responses within the framework of the lattice model introduced in Chapter 3. This will allow for the simulation of complete AE waveforms induced by tensile cracking. The model will be experimentally validated through comparison with experimental results from a three-point bending test on a notched concrete beam.

Reveal of the mechanisms of AE sources, for research questions Part 2 (Q2)

- Chapter 5 analytically addresses Q2 in a simplified 1D case, using analytical modelling methods to understand the AE phenomena induced by concrete tensile cracking. The chapter identifies the factors that influence the parameters of AE signals during concrete tensile cracking process, and these factors are numerically quantified in Chapter 7.
- Chapter 6 numerically addresses Q2 in a realistic 2D case. This chapter employs the lattice model developed in Chapter 3 to reveal the source mechanisms of AE signals induced by concrete tensile cracking in a more realistic 2D scenario, providing clear explanations for the physical principles underlying AE phenomena in concrete tensile fracture processes.

Explanation of AE measurements, for research questions Part 3 (Q3-Q4)

- Chapter 7 addresses Q3, employing the lattice modelling framework (developed in Chapters 3 and 4) to quantify AE source parameters induced by concrete tensile cracking (identified in Chapter 5) through a numerical parametric study. Building

upon the parametric results, this chapter will select the dominant factors of concrete tensile cracking as physically grounded AE indicators.

- Chapter 8 addresses Q4, employing the lattice modelling framework developed in Chapters 3 and 4 to provide a fundamental interpretation the variation of typical AE parameters observed during successive concrete tensile cracking propagation processes, providing guidance for more reliable interpretation of AE measurements.
- Chapter 9 concludes the dissertation by summarizing the research findings and offering recommendations for future studies. These recommendations will focus on more reliable applications of the AE technique and more rational interpretation of AE measurements.

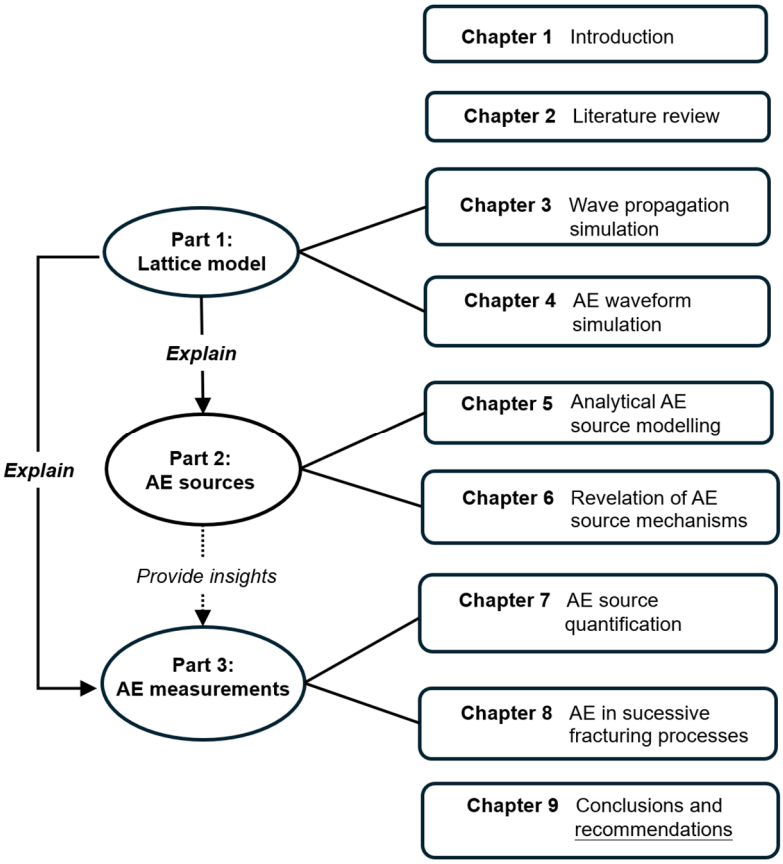

Figure 1.1 Outline of this dissertation.

2. Acoustic emission in concrete fracture processes: current understanding and available modelling methods in literature

2.1 Introduction

Acoustic emission (AE) is strongly linked to the fracturing process in various brittle and quasi-brittle materials like concrete; therefore, AE measurement is a promising technique that can monitor the health conditions of in-service concrete structures once the link between AE signals and the physical sources of the signals is clear. To reach that understanding, many experimental and modelling works have been conducted in literature. This chapter performs a literature review concerning the AE phenomena induced by concrete tensile fracturing processes, which is often considered as the major damaging process of concrete, with a focus on available theories and modelling methods.

It should be mentioned that the literature review performed in this chapter is not only restricted to concrete materials nor fracturing processes, although the focus of this dissertation is on AE phenomena in concrete fracturing processes. Some classical work in seismology is also referred in this section, as AE can be seen as a special type of microseismical activity (Wang 2014). A wider scope of reviewing on available theories and modelling methods for AE phenomena in various fields helps us to better understand the mechanisms of AE phenomena occurring in concrete fracture processes.

This chapter is organized as follows. Section 2.2 introduces the physical principles and technique bases of AE, and then briefly reviews available experimentally based AE characterization methods with a discussion on their limitations. Section 2.3 discusses concrete fracture theories related to AE phenomena and then reviews the AE source theories available in literature to explain AE phenomena induced by concrete fracturing processes. Section 2.4 reviews the available modelling methods of AE signals generated in concrete fracturing processes with a discussion on the pros and cons of each method. Based on the literature review, section 2.5 identifies the knowledge gap regarding mechanisms and modelling aspects of concrete fracture-induced AE phenomena.

2.2 Basics of acoustic emission

This section first introduces the general physical principals and technical bases of AE and then briefly describes available experimental-based AE source characterization methods with a discussion on their limitations.

2.2.1 Physical principals and technical bases of acoustic emission

The term of "acoustic emission" refers to both a class of physical phenomena and a monitoring technique. In this sub-section, we briefly introduced AE in these two aspects.

Physically, AE refers to a class of microscopic phenomena involving transient processes of stress redistribution at local level of a material (Ying 1973). Such transient processes lead to rapid energy release and further induce vibrations of the whole system, namely the propagation of elastic waves (Wang 2011; Eitzen and Wadley 1984).

For reinforced concrete structures, many deterioration processes involving transient local stress redistribution are likely to induce AE phenomena, such as hydration (Thirumalaiselvi and Sasmal 2019), creep (Zhao et al. 2024), fracture (Zhou et al. 2024), fatigue (Noorsuhada 2016) and corrosion of steel reinforcement (Zheng et al. 2020). Reader are referred to the book of (Grosse and Ohtsu 2008b) for more details of various AE source types in concrete.

Amongst various AE sources, the concrete fracturing is one of the major sources of AE signals and is often used to indicate the health conditions of concrete structures (Ohtsu, Isoda, and Tomoda 2007). Therefore, the scope of this dissertation is restricted to AE phenomena induced by fracturing processes of plain concrete. The fracture-induced AE phenomena has a similar physical base with earthquakes in seismology but at a smaller scale, and thus fracture-induced AE is also referred to as micro-seismicity in literature (Wang 2014; Zhu et al. 2024).

Technically, as shown Figure 2.1, the elastic waves induced by AE sources and travelling within structures can be captured and transformed into electrical signals (AE signals) by certain types of sensors (AE sensors) mounted on structure surfaces (Pollock 2018). The electrical signals are further stored and processed by an AE acquisition system (Scruby 1987b). This signal acquisition process is called AE technique, which aims at characterizing and localizing the signal sources through analysing measured AE signals.

AE is a passive and continuous monitoring technique that directly measures wave signals induced from the inside of the monitored structures. Such a passive nature brings the AE technique distinguished advantages in real-time monitoring (Pan et al. 2023) and the prompt detection of early cracking (Zheng et al. 2020).

Readers are referred to the classical work in literature for more details of the AE technique (Matthews 1983; Scruby 1987b; Nazarchuk, Skalskyi, and Serhiyenko 2017) and the AE phenomena of various source types in different materials (Ono 2011; Ohtsu 1996; Gholizadeh, Leman, and Baharudin 2015).

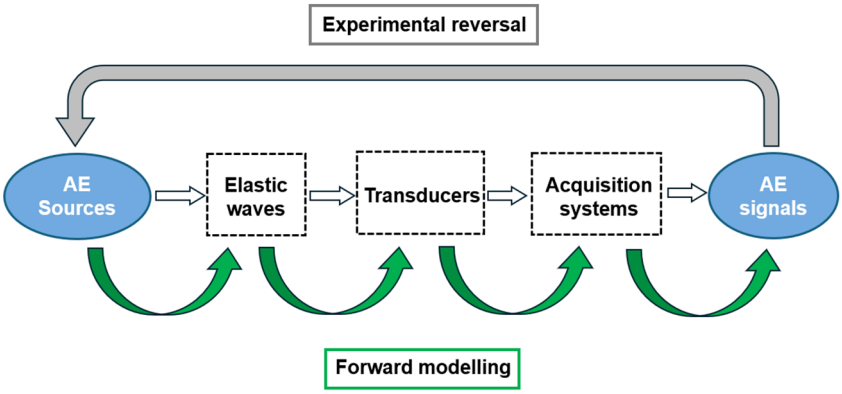

Figure 2.1 Illustration for the signal acquisition process of the AE technique and two options for establishing a source-to-signal relationship.

2.2.2 Available experimental-based AE characterization methods

The aim of AE technique is to characterize and localize signal sources inside structures through analysing signals received at structural surfaces. Therefore, reliable applications of AE technique rely upon a quantitative relationship between AE measurements and corresponding signal sources. As shown in Figure 2.1, inversion from experimental data and forward modelling provide two options to link the measured AE signals with the physical sources of the signals. Available AE methods are mostly established through experimental reversal. This sub-section briefly introduces available experimental-based AE source characterization methods. Readers are referred to the classical work in literature (Zhang 2022; Pollock 2018) for more comprehensive description in this regard.

Experimental-based AE source characterization methods aim to link AE measurements with concrete fracture behaviours through analysing measured AE parameters (or complete AE waveforms) (Zhao, Kang, and Yao 2018). The definition of AE parameters mentioned in this dissertation is illustrated in Appendix A (see also the work of Stone (Stone and Dingwall 1977)). Herein, we classify available AE methods into two categories according to the objects they aim to characterize, including methods for characterizing local AE sources and those for characterizing structural behaviours. In the following, these two categories of AE methods are briefly described, with a discussion on limitations of each mentioned method.

2.2.2.1 Methods for characterizing local AE sources

The first class of available AE methods is aimed at characterizing each AE source, including location and type of an AE source, through analysing waveforms/parameters of corresponding AE signals.

- *Source localization*:

Identifying the precise locations of damage/AE sources is essential for analysing potential cracking regions within structures and gaining a deeper understanding of the damage characteristics of monitored structures (Cheng et al. 2021). The mostly used AE localization methods are based on the arrival time of AE signals received by sensors at different locations. The location of each AE source is estimated by equalling the wave travel distances from the source to different sensors to the products of wave velocities multiplied by wave travel time. Different arrival time-based algorithms (Sedlak, Hirose, and Enoki 2013; Sedlak et al. 2009) have been developed following such a principal.

There are many other AE source localization algorithms available in literatures, such as zonal-based localization methods (Ai, Zhang, and Ziehl 2023) and machine learning methods (Ince et al. 2010), by analysing different AE parameters besides the first arrival time to estimate AE source locations. Readers are referred to the work of Hassan (Hassan et al. 2021) for more details of various AE source localization algorithms.

It should be noted that an accurate source localization is not possible in concrete structures, because many factors can lead to localization errors, such as picking error of arrival time, the presence of cracks in wave travel paths and wave scatters from concrete heterogeneity, which cannot be entirely removed (Zhang, Pahlavan, and Yang 2020).

- *Source type classification*:

The type of fracturing source is an important indicator of concrete fracturing processes. The RA-AF method (Aggelis 2011), a method given in the ISO 16838:2019 standard (ISO 2019), is the mostly used approach for classifying AE sources in concrete fracturing processes into two types of tensile cracking and friction. Two parameters of an AE signal, RA value and average frequency (AF) (see Appendix A for definition), are combined for analyses: AE signals from tensile cracking are characterized by higher average frequency and shorter rise time, while those from friction are characterized by lower average frequency and longer rise time.

There are many other classification methods available in literature, such as the moment tensor reversion methods (Shigeishi and Ohtsu 2001; Graham et al. 2010), the peak frequency-based criterion (Zhang et al. 2022) and the machine learning-based methods (Zhang, Yan, and Guo 2022), for classifying AE sources into different types in various

concrete deterioration processes. Readers are referred to the work of Sagar and Prasad (Sagar and Prasad 2012) for more details of various AE source type classification methods in concrete and reinforced concrete structures.

Nevertheless, it should be noted that all mentioned source classification methods are qualitative without a clear classification boundary. Moreover, they are all established based on experimental observations without clear physical meanings (Dong et al. 2023).

2.2.2.2 Methods for characterizing global structural behaviours

The second-class AE methods aim at characterizing the global behaviour of structures (e.g., structural damage degrees) through analysing the changes of measured AE signals/parameters during progressive failure processes.

The most forward AE method for characterizing structural integrity is by analysing the time history of AE rates or accumulated AE hit numbers in concrete fracturing processes: a sudden increase in AE rates/numbers means the change in structural damage degree (Zheng et al. 2020). There are several more advanced AE methods for a similar purpose. Herein, we describe two mostly used classical methods for exemplification:

- *AE intensity analysis*: this method is to evaluate the structural damage states analysing AE signal strength. Two statistical parameters are calculated from monitored AE signal strength data, historic index ($H(t)$) and severity index (S_r) (see the work of FOWLER (Fowler, Blessing, and Conlisk 1989) for the expressions of $H(t)$ and S_r). A sudden change in these two parameters indicates the deterioration of structural integrity (Zheng et al. 2020). This method has been applied to evaluate the integrity of different structure types subjected to various damage types (Abouhussien and Hassan 2020; Shahidan et al. 2011; Di Benedetti and Nanni 2014).

  However, the AE intensity analysis method provides only qualitative evaluation of structural damage states; there is no consistent and quantified relationship between two statistical parameters ($H(t)$ and S_r) and structural damage states.

- *B-value analysis*: this method originated from seismology by analysing the relationship between peak amplitude (magnitude) and occurrence frequency of earthquakes (Gutenberg and Richter 1954). The so-called b-value, calculated as the amplitude versus occurrence frequency distribution of AE hits (see the work of Main et al. (Main, Meredith, and Jones 1989) for the expression of b-value in AE field), is used to assess the fracturing scales inside structures. Since the occurrence frequency is inversely correlated with magnitude of AE hits (Colombo, Main, and Forde 2003), a decrease trend of b-value indicates the transformation from microcracking into macrocracking and thus the occurring of severe structural damage (Carpinteri, Lacidogna, and Puzzi 2009; Kurz et al. 2006). There is an improved version of b-value analysis

method, called improved b-value (Ib-value) method (Shiotani 1994), for minimizing influence of ambient noise signals by further considering the statistical distribution of AE signal amplitudes (Colombo, Main, and Forde 2003; Shiotani 2001; Shiotani 2006).

However, large fluctuations of b-values were observed in AE monitoring processes (Farhidzadeh et al. 2013), and it is difficult to find a critical b-value for reliably distinguishing macrocracking from microcracking (Zhang 2022).

There are several other AE methods available for characterizing structural behaviours, such as the load ratio-calm ratio method for characterizing structural behaviour under cyclic/fatigue loading conditions (Liu and Ziehl 2009) and the fractal dimension analysis calculated from AE hit numbers for assessing structural damage severity (Zheng et al. 2022). Readers are referred to the work of (Behnia, Chai, and Shiotani 2014) for more detailed description of various AE-based structural evaluation methods.

However, it should be mentioned that available AE-based structural damage evaluation methods are mainly established based on experimental observations without a clear physical basis, thus providing only qualitatively evaluation for structural damage states (Sagar and Prasad 2012).

2.2.2.3 Limitations of available experimental-based AE characterization methods

Characterizing local signal sources through AE measurements is a typical inverse problem. Although carrying the information of sources, the received AE signals are also influenced by many other factors, such as wave propagation and AE sensor response, as shown in Figure 2.1.

The aforementioned analysis methods of AE signals are mostly established through experimental observations. The physical basis behind these methods remains unclear. Therefore, they cannot provide reliable and quantified relationship between the source mechanism in the material/structure and received AE signals, because the influence from wave propagation and sensor response cannot be removed in experiments as shown in Figure 2.1 (Behnia, Chai, and Shiotani 2014).

Furthermore, the phenomenological models established through experimental reversal are usually case-dependent and can only provide a roughly qualitative description for AE sources due to the lack of clear physical bases (Sagar and Prasad 2012). Different or even conflicted conclusions can be drawn from the phenomenological methods when applied to different experimental cases (Dong et al. 2023).

2.3 Acoustic emission induced by concrete fracture processes in literature

In view of the limitations of available experimental-based analysis methods of AE signals, a rational understanding is needed to interpret the physical principals behind the measurable AE signals. Only based on that, it is possible to establish a solid model that can explain phenomenological observations of AE and develop new methods towards more reliable interpretation of AE measurements. In this section, we review and discuss available theories aimed at explaining AE phenomena induced by concrete fracture processes.

2.3.1 Concrete fracture theories associated with acoustic emission

As the scope of this dissertation is restricted to AE phenomena induced by concrete fracturing processes, this sub-section firstly briefly introduces concrete fracture theories.

Following the classical work of Griffith (Griffith 1921) for the fracture criterion of cracking extension in solids, several different theories have been proposed for explaining the fracturing processes of solids, such as stress intensity factor theory (Erdogan 1983), strain energy release theory (Hussain, Pu, and Underwood 1973) and J-integral theory (Schapery 1984). These fracture theories have been applied to solve different fracture-related problems in various solid materials (Anderson and Anderson 2005). Readers are referred to the classical work of Bažant and Cedolin (Bažant and Cedolin 1980) and of Carpinteri (Carpinteri 1982) for the applications of different fracture theories in brittle and quasi-brittle materials including concrete.

The difference between various concrete fracture theories mainly lies in the scale they focus on (Shah, Swartz, and Ouyang 1995). Macroscopically, the type of concrete fracture processes is usually defined by the external loading conditions, such as the failure types of tension, compression, shear and torsion, regardless of internal fracture mechanism (Van Mier 2017). The fracture theories formulated at mesoscale and microscale, which consider fracture mechanisms at local material regions, are more relevant to AE phenomena. In the following, we separately discuss mesoscopic and microscopic perspectives on independent basic fracture modes/mechanisms (namely AE source types) involved in the fracturing processes of concrete included quasi-brittle materials.

2.3.1.1 Mesoscopic perspective: classical fracture mechanics for solids

Mesoscopically, in the scale of macrocracks and under the framework of classical fracture mechanics (Gdoutos 2020; Sun and Jin 2011), the fracture of solids is traditionally classified into three basic modes based on the deformation types of cracks, including Mode I (opening cracks), Mode II (in-plane shear cracks) and Mode III (out-of-plane shear cracks), as illustrated in Figure 2.2. These three basic fracture modes and their combination can be used to explain all kinds of fracture processes of solids at macroscale (Kerlins

1987). Specifically, it is assumed that cracks under different fracture processes/loading states can be all reduced into a combination of stress intensity factors (Irwin 1957) or fracture energy (Ballatore et al. 1990) of the three independent basic fracture modes.

It should be noted that this viewpoint of three basic fracture modes at mesoscopic level is a universal principal that applies for diverse types of solids including concrete-like quasi-brittle materials and other ductile materials (e.g., metals and composites) (Kerlins 1987).

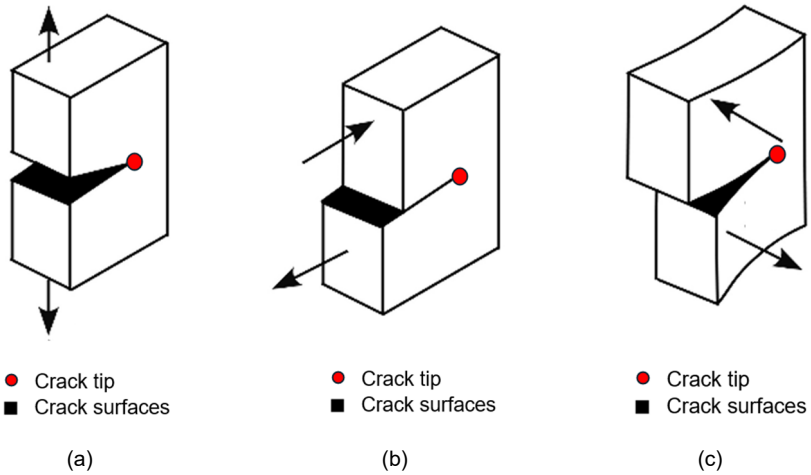

Figure 2.2 Illustration for three fracture modes of solids in classical fracture mechanics: (a) Mode-I fracture (opening crack); (b) Mode-II fracture (sliding crack); (c) Mode-III fracture (tearing crack) (adapted from (Sun and Jin 2011)).

2.3.1.2 Microscopic perspective: fracture mechanics specialized for quasi-brittle materials

The fracture processes of quasi-brittle materials are generally governed by two independent basic mechanisms, including tensile cracking at crack tip/front and friction along crack surfaces/planes (Carpinteri et al. 1993), as marked in Figure 2.2. Specifically, as illustrated in Figure 2.3, tensile cracking at crack tip is the dominant microscopic mechanisms that consumes fracture energy to create new fracture surfaces under different macroscopic fracture modes/loading states (see Figure 2.3a), while the friction along existed cracking surfaces due to roughness of cracking surfaces is the secondary microscopic mechanisms that provides additional resistance to fracture under various macroscopic fracture modes/loading states except pure tension (namely mixed-mode fracture) (see Figure 2.3b).

Such a viewpoint for the fracture of quais-brittle materials has been widely validated both numerically and experimentally (Ayatollahi, Moghaddam, and Berto 2015; Ayatollahi

and Saboori 2015; Carpinteri et al. 1993). It has been also demonstrated that by considering these two microscopic mechanisms it is possible to accurately simulate the macroscopic fracturing behaviours of quasi-brittle materials under different external loading states using different numerical methods, such as phase-field model (Fei and Choo 2020), lattice model (Place and Mora 1999), phantom node method (Komijani, Gracie, and Yuan 2020) and discrete element method (Torkan et al. 2019).

It should be noted that the term of "tensile cracking" mentioned herein is also referred to as "cohesive cracking" (Elices, Rocco, and Roselló 2009) or "cohesive fracture" (Park, Paulino, and Roesler 2010) in literature. Similarly, the term of "friction" is also referred to as "interlocking" (Walraven 1981) or "shear sliding" (Haskett et al. 2011) in literature. These different terminologies are same concepts that describe the two independent microscopical mechanisms governing the fracture processes of quasi-brittle materials shown in Figure 2.3.

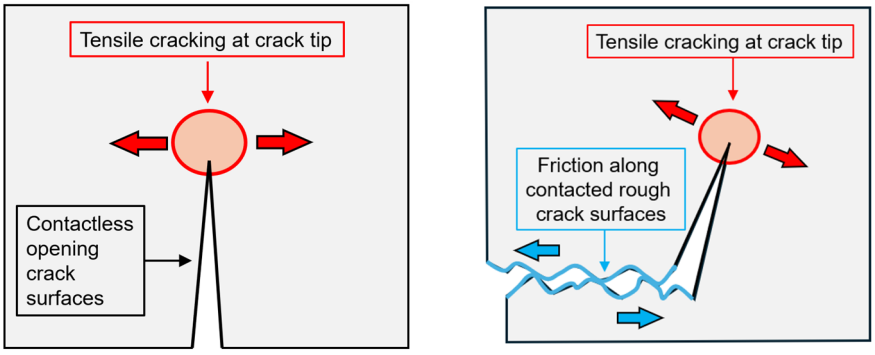

Figure 2.3 Illustration for two microscopic mechanisms governing different fracture modes of quasi-brittle materials like concrete: (a) tensile cracking at crack tip in Mode-I fracture (in pure tension); (b) tensile cracking at crack tip combined with friction along crack surfaces in mixed-mode fracture (adapted from (Xu, Hajibeygi, and Sluys 2024)).

2.3.1.3 AE source types in concrete fracture processes

Different perspectives on the independent basic fracture mechanisms largely influence the ways we look at AE phenomena in quasi-brittle materials, especially for the types of AE sources.

There are several AE theories and methods formulated following the macroscopic or mesoscopic viewpoints of fracture modes, where macroscopic failure modes defined by external loading conditions (i.e., tensile, shear and compressive failure) or mesoscopic fracture modes (i.e., Mode-I, -II and -III fracture) are regarded as independent AE source types involved in concrete fracturing process. For example, Chisari, Guarnaccia et al

(Chisari, Guarnaccia, and Rizzano 2020) proposed a numerical modelling strategy for simulating AE sources generated in fracturing processes of reinforced concrete structures, where tensile, shear and compressive failure of concrete elements are taken as three independent AE source types. Grosse, Reinhardt et al (Grosse, Reinhardt, and Dahm 1997) proposed a method to classify AE sources into three types corresponding to three independent fracture modes according to the radiation patterns of received AE waveforms. Ohno and Ohtsu (Ohno and Ohtsu 2010) developed a so-called SiGMA algorithm based on the moment tensor theory (MT) to classify AE sources generated by concrete fracture processes into three independent fracture modes.

Differently, most available AE theories and methods are formulated following the microscopic viewpoint of two governing fracture mechanisms, where tensile cracking friction are regarded as two basic AE source types in concrete fracturing process. As the AE induced in concrete fracture processes are microscopic phenomena, such a microscopic viewpoint is more reasonable for describing AE source types involved in concrete fracturing processes.

In the following, we review and discuss available AE theories and modelling methods for the two AE source types of tensile cracking and friction, while those formulated following the macroscopic or mesoscopic viewpoints of AE source types will not be further discussed in this dissertation.

2.3.2 Attempts on rational models of acoustic emission in concrete fracture processes

Although no general accepted rational models on acoustic emission during concrete fracturing process is available, there are several attempts in literature that form the basis of this research. This section reviews and discusses available theories in literature for explaining AE phenomena occurring in concrete fracturing processes. For a better illustration, the available theories are classified into three categories, including energy perspective, macroscopic perspective and microscopic perspective. For each category, theories for the two main AE source types involved in concrete fracturing processes, namely tensile cracking and friction as illustrated in previous section, are separately discussed.

2.3.2.1 Energy perspective: released energy

2.3.2.1.1 Tensile cracking-induced AE

The theories formulated from energy perspective to explain tensile cracking-induced AE in concrete included quasi-brittle materials are mainly contributed by Carpinteri and coauthors (Iturrioz, Lacidogna, and Carpinteri 2014; Bosia et al. 2008; Carpinteri, Corrado, and Lacidogna 2013) following the classical theories in seismology field (Scholz 2019).

This sub-section describes the energetic theory presented in the classical work (Iturrioz, Lacidogna, and Carpinteri 2013, 2014).

Consider a system consisted of single crack embedded in a 3D solid where inelastic material behaviour is assumed to be induced by propagation of tensile cracking at crack tip only. Ignoring the gravitational potential energy, the dynamic energy balance of considered system can be written as:

$$W_{total} = -W_{external} + W_{elastic} + W_{damage} + W_{kinetic} \tag{2.1}$$

where W_{total} is the total energy of the system; $W_{external}$ is the energy from external load; $W_{elastic}$ is the internal elastic strain energy of the system; W_{damage} is the internal energy dissipated by cracking extension (growth of tensile cracking at crack tips) in the fracturing process; $W_{kinetic}$ is the internal kinetic energy (released energy) in the fracture process.

The dynamic energy equilibrium given by Equation (2.1) can be written in rate form as (Scholz 2019):

$$\dot{W}_{total} = -\dot{W}_{external} + \dot{W}_{elastic} + \dot{W}_{damage} + \dot{W}_{kinetic} = 0 \tag{2.2}$$

where the superscript dot symbol "." represents the energy rate.

For an AE signal due to the extension (opening) of a crack occurring in a short period Δt, the AE energy, represented by W_{AE}, equals the sum of kinetic energy (released energy) during time Δt:

$$W_{AE} = \Delta W_{kinetic} = \int_{t_0}^{t_0+\Delta t} \dot{W}_{kinetic} \mathrm{d}t \tag{2.3}$$

where $\Delta W_{kinetic}$ is the change in kinetic energy in the duration Δt of the AE signal. t_0 is an arbitrary time moment.

By substituting Equation (2.2) into Equation (2.3), the AE energy W_{AE} is further expressed as:

$$W_{AE} = \Delta W_{kinetic} = \int \dot{W}_{kinetic} \mathrm{d}t = \int (\dot{W}_{external} - \dot{W}_{elastic} - \dot{W}_{damage}) \mathrm{d}t \tag{2.4}$$

Further consider very small change in external load during the transient time Δt (namely $\dot{W}_{external} \ll \dot{W}_{elastic}$ and $\dot{W}_{external} \ll \dot{W}_{damage}$) (Iturrioz, Lacidogna, and Carpinteri 2014), the AE energy W_{AE} is finally expressed as:

$$
\begin{aligned}
W_{AE} &= \Delta W_{kinetic} \\
&= \int \dot{W}_{kinetic} \mathrm{d}t = \int (\dot{W}_{external} - \dot{W}_{elastic} - \dot{W}_{damage}) \mathrm{d}t \\
&\approx \int (-\dot{W}_{elastic} - \dot{W}_{damage}) \mathrm{d}t \\
&= -\left(\Delta W_{elastic} + \Delta W_{damage}\right) \\
&= \left|\Delta W_{elastic}\right| - \left|\Delta W_{damage}\right|
\end{aligned}
\tag{2.5}
$$

where $\Delta W_{elastic}$ and ΔW_{damage} are changes in elastic strain energy and dissipated energy during tensile cracking process during the transient time Δt. $|*|$ is the absolute value sign.

To illustrate the energetical relationship given by Equation (2.5), Figure 2.4 shows the evolution of changes in elastic energy ($\Delta W_{elastic}$), dissipated energy (ΔW_{damage}) and AE (released) energy ($\Delta W_{kinetic}$) of the system during the propagation process of a tensile crack simulated by a lattice model (Iturrioz, Lacidogna, and Carpinteri 2014). When tensile cracking occurring, $\Delta W_{elastic}$ drops from positive into negative values while ΔW_{damage} increases from zero into positive values, leading to variations in the difference between their absolute values, namely $\Delta W_{kinetic}$. The AE energy (W_{AE}), defined as the change in system kinetic energy ($\Delta W_{kinetic}$) and standing for the released energy from an earthquake in seismology (Scholz 2019), represents the portion of energy resulting from elastic waves induced by the tensile cracking processes (Iturrioz, Lacidogna, and Carpinteri 2014).

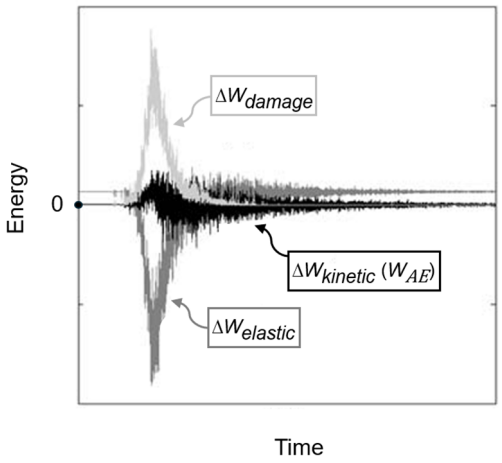

Figure 2.4 Evolution of elastic strain energy ($\Delta W_{elastic}$), dissipated energy (ΔW_{damage}) and AE/released energy ($\Delta W_{kinetic}$) during the propagation processes of a tensile crack simulated by a truss lattice model (adapted from (Iturrioz, Lacidogna, and Carpinteri 2014)).

As can be seen in Equation (2.5) and Figure 2.4, the AE energy comes from the variation of the difference between elastic strain energy and dissipated energy of the whole system

during tensile cracking processes (namely, AE energy comes from the surplus of elastic energy that cannot be fully dissipated by tensile cracking processes).

2.3.2.1.2 Friction-induced AE

For friction-induced AE in the fracture processes, the classical work for AE in tribology field is described in this subsection. The model describes the friction along two rough concrete cracking surfaces from an energy perspective.

Consider a pair of contacted rough cracking surfaces with asperity contact, as illustrated in Figure 2.5 (Baranov, Kudryavtsev, and Sarychev 1997). The amplitude (interference or deformation) of the asperity between two contact/rubbing surfaces is denoted by δ. A critical amplitude value of asperity, denoted as δ_c, is used to distinguish deformation modes of contacted asperity: the asperity undergoes elastic deformation when the contact amplitude larger than the critical value (i.e., $\delta > \delta_c$); otherwise, the asperity undergoes plastic deformation (i.e., $\delta \leq \delta_c$). Further consider two contacted surfaces sliding along each other for a sliding duration T and with a maximum interference amplitude of δ_{max} between two contact surfaces, the total energy stored by the deformations of the asperity during sliding in the sliding duration T, denoted as $W_{deformation}$, is expressed as (Hao et al. 2019):

$$\begin{aligned} W_{deformation} &= \int_0^{\delta_{\max}} P(\delta)\chi(\delta)\delta \mathrm{d}\delta \\ &= \begin{cases} \int_0^{\delta_{\max}} P_p(\delta)\chi(\delta)\delta \mathrm{d}\delta & \text{if } \delta_{\max} \leq \delta_c \\ \int_0^{\delta_c} P_p(\delta)\chi(\delta)\delta \mathrm{d}\delta + \int_{\delta_c}^{\delta_{\max}} P_e(\delta)\chi(\delta)\delta \mathrm{d}\delta & \text{if } \delta_{\max} > \delta_c \end{cases} \end{aligned} \tag{2.6}$$

where $P(\delta)$ is the contact force, for which the values depend on the interference amplitude δ. The subscript of e and p represent elastic and plastic deformation, respectively. $\chi(\delta)$ is a δ-dependent parameter characterizing the deformation degree of the asperity.

It is further assumed that a portion of the total energy of the contact surface ($W_{deformation}$) will be released into AE pulses. Furthermore, the released AE energy (W_{AE}) is considered linearly proportional to $W_{deformation}$ (Hao et al. 2019):

$$W_{AE} = gW_{deformation} \tag{2.7}$$

where g is empirical constant in the value range of 0-1; the value of g depends on the roughness of the contact surface (e.g., $g = 1$ in the case of pure slip friction and $g = 0$ in the case of pure stick friction) (Hao et al. 2019).

There are several different models (Fan, Gu, and Ball 2010; Hao et al. 2019; Baranov, Kudryavtsev, and Sarychev 1997) for sliding friction-induced AE in tribology field, all

formulated following the same energy concept that AE energy comes from the portions of deformation energy of asperity between contact surfaces. The difference between various AE-friction models mainly lies in the calculation involved parameters in Equation (2.6).

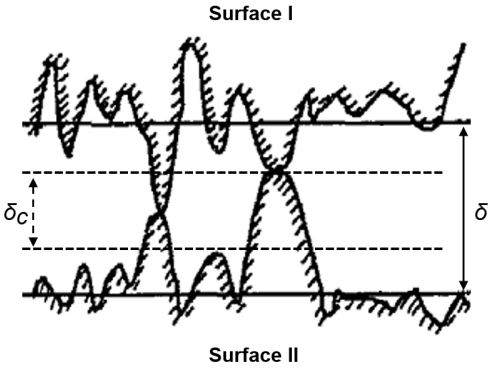

Figure 2.5 Illustration for a pair of rubbing surfaces and its characterizing parameters (adapted from (Baranov, Kudryavtsev, and Sarychev 1997)).

2.3.2.2 Macroscopic perspective: local instabilities in global load

2.3.2.2.1 Tensile cracking-induced AE

In this section, two theories are discussed which describe the global mechanical behaviours of concrete for explaining tensile cracking-induced AE phenomena, including the local snap-back instability theory and the local stress-drop instability theory, as follow:

- *Local snap-back instability*:

This theory was proposed by Carpinteri and co-authors explaining AE phenomena from tensile cracking of quasi-brittle materials (Carpinteri et al. 2016; Carpinteri 1989; Lacidogna, Accornero, and Carpinteri 2019; Carpinteri and Accornero 2018). Figure 2.6a illustrates a special type of catastrophic structural response of quasi-brittle materials under special conditions (e.g., large specimen slenderness and unstable loading processes), called snap-back or snap-through instability, which is characterized by a drop in both load and displacement in post-peak loading stages (Bocca and Carpinteri 1990). In more general conditions of quasi-brittle materials' fracturing processes, a more stable global behaviour is observed showing a post-peak softening behaviour perturbed by multiple local snap-back instabilities, with each local drop (snap) and recovering (back) in global load corresponding to sudden growth and arrest of a microcrack, as illustrated in Figure 2.6b (Carpinteri and Accornero 2018).

Such local phenomena, explained as a macroscopical evidence of the discontinuous manner of the growth of micro-cracks, is attributed to the source of tensile cracking-induced AE phenomena in quasi-brittle materials. Furthermore, the surplus of elastic energy that cannot be fully dissipated by material fracture, named as emitted as energy and denoted as “E” in Figure 2.6, are used as analogy to AE energy (Carpinteri et al. 2016). Such an energy-based explanation in the local snap-back theory is in line with the released energy theory discussed in Section 2.3.2.1.1.

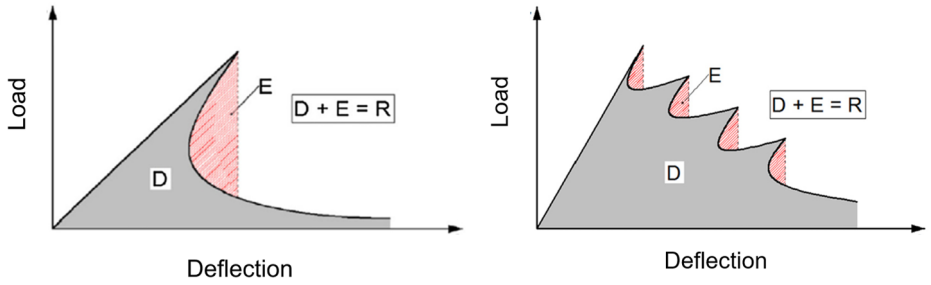

Figure 2.6 Illustration for snap-back instability theory: (a) a global snap-back catastrophic behaviour in a load-deflection curve and (b) a global post-peak softening behaviour characterized by multiple local snap-back instabilities, with D, E and R represent damage dissipated energy, emitted energy and total released energy, respectively. (adapted from (Carpinteri et al. 2016)).

- *Local stress-drop instability.*

This theory is proposed by Li, Ren et al. (Li, Ren, and Li 2024) to explain tensile cracking-induced AE phenomena in concrete. Figure 2.7 illustrates the basic concept of the local stress-drop instability theory, where a concrete sample is idealized by a bundle of paralleled micro-springs with random properties to represent the microscopic heterogeneity of concrete (see Figure 2.7a). When the external load gradually increases, the micro-springs break in sequence. Each broken spring, representing a microcrack, leads to a decrease in global stiffness (slope of stress-strain curve) and thus a local drop in global stress of the concrete sample. When the number of tensile yielded microcracks reaching a certain level, the saw-tooth shape of a stress-strain curve perturbed by multiple local stress drops turns into the smooth tensile softening curve as observed in experiments (Chen and Su 2013). Such local stress drops are considered as the source of AE phenomena induced by concrete tensile cracking.

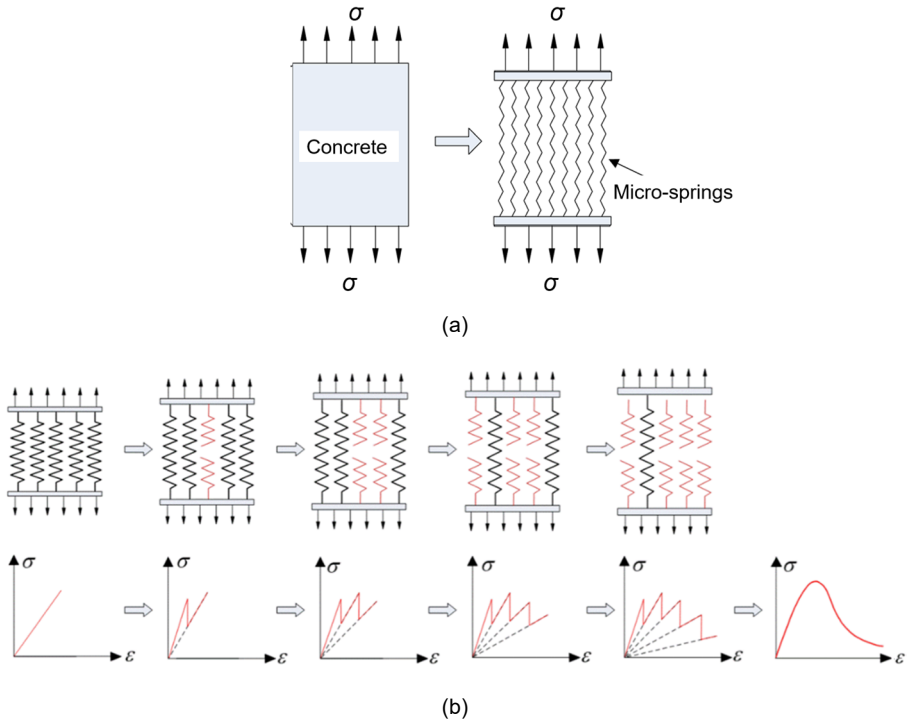

Figure 2.7 Illustration for the local stress-drop instability theory: (a) simplification of concrete into a system of micro springs and (b) a global strain-stress softening curve resulting from multiple stress drops (AE phenomena) induced by progressive failure of micro springs (adapted from (Li, Ren, and Li 2024)).

The local snap-back and stress-drop instability are similar theories, both attributing the origin of AE phenomena induced by tensile cracking of microcracks to local instabilities in global load/stress. The main difference between these two theories is that the local snap-back instability theory requires the decrease in global displacement/strain corresponding to the occurrence of local load/stress drops to emit AE energy (see Figure 2.6b). An example of experimental evidence for the correlation between AE phenomena and local stress drop is illustrated in Figure 2.8, where a burst of AE hits observed when local drops occurring in global load (see the blue circle in Figure 2.8) in a uniaxial compression test of a rock (gypsum) cylinder specimen under displacement control (Lacidogna, Accornero, and Carpinteri 2019).It should be mentioned the similar concept of stress drop is also used for earthquake source characterization in seismology field (Cocco, Tinti, and Cirella 2016; Baltay et al. 2011; Abercrombie 2021; Kanamori and Allen 1986).

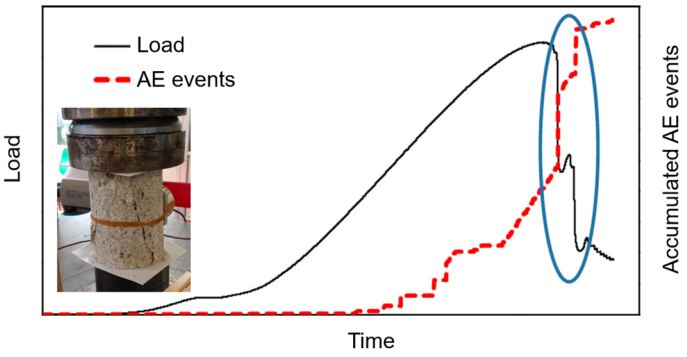

Figure 2.8 Evidence correlating AE phenomena to local instabilities in global load in post-peak regime in a compression test of a rock (gypsum) cylinder (adapted from (Lacidogna, Accornero, and Carpinteri 2019)).

2.3.2.2.2 Friction-induced AE

The stick-slip (or called stick-sliding) friction theory (Berman, Ducker, and Israelachvili 1996) provides explanation for friction-induced AE phenomena in concrete fracture processes.

Classically, the Coulomb friction is used to describe the contact (friction) mechanisms (Cull 1999). However, the Coulomb friction, where the contact is described as a constant opposing force independent of sliding velocity of contacted surfaces (see Figure 2.9a), is not suitable to describe the AE included dynamic friction processes.

The stick-slip/sliding friction model (Haessig Jr and Friedland 1991) (also referred to as "viscous friction" (Buttà, Cavallaro, and Marchioro 2015)) is a more accurate description of the dynamic friction processes. The basic concept of stick-sliding friction theory is illustrated in Figure 2.9b. The friction force between contact surfaces increases firstly when the relative velocity between two contact surfaces is smaller than a critical value, denoted as v_s in Figure 2.9b, during which the contact surfaces are in static states; when the relative velocity exceeds v_s, the states of contact surfaces start to transform from static to slip (sliding), characterized by a sharp decrease in friction force during a relative velocity range of (v_s, v_d) as marked in Figure 2.9b; with further increasing the relative velocity to a range larger than v_d, the contact surfaces are in steady sliding process and the friction force remains a constant, namely sliding friction force F_s in Figure 2.9b.

Following the applications of stick-sliding friction theory in seismology field for explaining and modelling the earthquakes from friction between earth faults (Dieterich 1978; Madariaga 1979; OHNAKA 1973), it has been used to study the friction-related vibrations of different dynamics systems in various fields, such as tribology (Gao, Kuhlmann-Wilsdorf, and Makel 1993), mechanical engineering (Galvanetto, Bishop, and Briseghella

1995) and rock mechanics (Yao et al. 2023). As a vibration-related phenomena, many modelling (Polycarpou and Soom 1995; Rozman, Urbakh, and Klafter 1997; Bengisu and Akay 1999) and experimental work (W. Goebel et al. 2013; Ferrer et al. 2010; Johnson et al. 2013) has been conducted to explain friction-induced AE phenomena in various materials by using the stick-slip friction theory.

The correlation between AE and the stick-slip phenomena of contact surfaces is marked by pink boxes in Figure 2.9b. AE phenomena occur mainly in the unstable stick-to-slip transformation process of contact surfaces, characterized by sharp drop in friction forces (in the velocity range of (v_s, v_d) as marked red in Figure 2.9b) (Ferrer et al. 2010). Secondary friction-related AE phenomena can be also observed in later steady sliding process depending on the roughness of contact surfaces (in the velocity range of $v > v_d$ in Figure 2.9b) (Bengisu and Akay 1999).

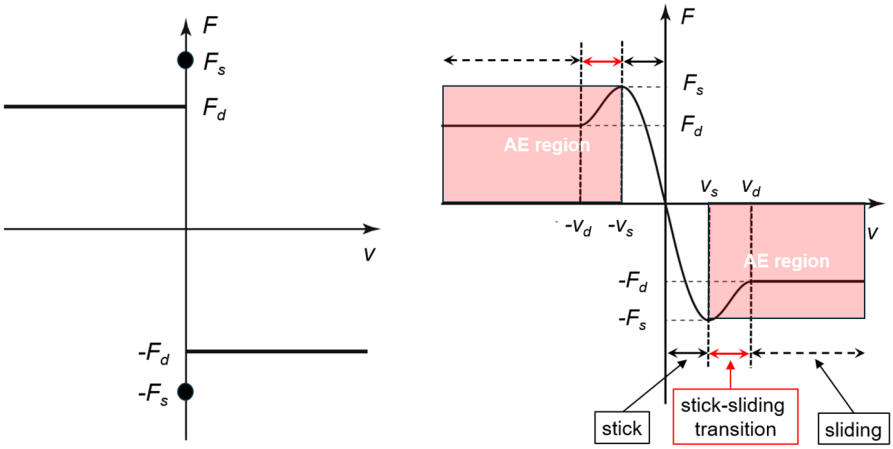

Figure 2.9 illustration for different friction models: (a) the classical Coulomb friction model and (b) a dynamic stick-sliding friction model (adapted from (Haessig Jr and Friedland 1991)).

An example of experimental evidence which shows the correlation between AE phenomena and local drop in global friction force is illustrated in Figure 2.8, where sliding-friction tests are performed on cracked surfaces of two types, rock-to-rock surfaces (Figure 2.8a) and glass-to-glass surfaces (Figure 2.8b), with the sliding driven force being prescribed by a constant velocity and lateral confinement being prescribed by a constant distributed force (McLaskey 2011). In both cases, similarly to the above stress-drop instabilities theory, AE events are observed when measured global friction force drops between contact surfaces. The burst of AE signals occurs mainly at the onset of sliding (namely the stick-sliding transition process as marked red in Figure 2.10b) for glass-to-glass surfaces, while AE signals are persistently observed in the whole sliding process for

rock-to-rock surfaces (see Figure 2.10a) which is explained by the damage (plastic deformation) of microscopical asperities (see Figure 2.5) along rougher rock-to-rock surfaces in later steady sliding process (McLaskey 2011; McLaskey et al. 2012; Sirorattanakul et al. 2025).

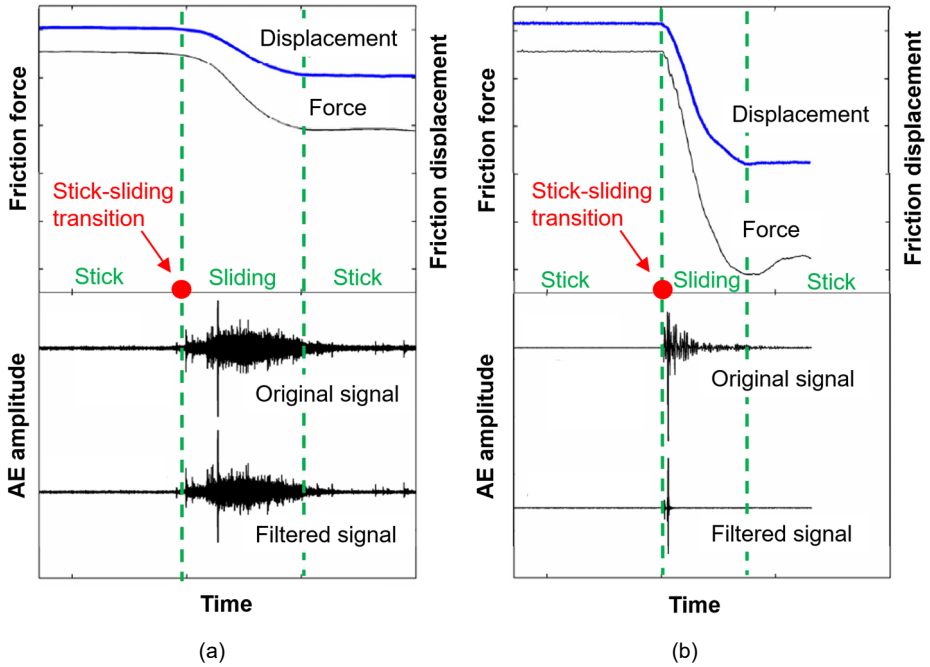

Figure 2.10 Correlation between stick-sliding friction instabilities and AE signals observed in sliding friction tests of contact surfaces of different materials: (a) friction along rock-to-rock surfaces and (b) friction along glass-to-glass surfaces (adapted from (McLaskey 2011)).

2.3.2.3 Microscopic perspective: local discontinuity/dislocation

In classical continuum mechanics, the physical cracks are mechanically described as displacement jumps at local material region, called dislocations or discontinuities (Mura 2013). Through such a idealization, the physical problem of fracturing in solids can be mathematically described (Friedel 2013). The explanation of AE phenomena (Eitzen and Wadley 1984; Ying 1973; Kao, Carvalho, and Labuz 2011) is mainly formulated following a continuum mechanics-based theory.

2.3.2.3.1 Tensile cracking-induced AE

As shown in Figure 2.11a, an opening of a microcrack due to tensile cracking is described by a normal (opening) dislocation (displacement jump) in a local material region following the classical continuum mechanics (Mura 2013), marked as Δu_n in Figure 2.11a. The dislocation Δu_n is further reassumed to occur during a period of T in a constant velocity.

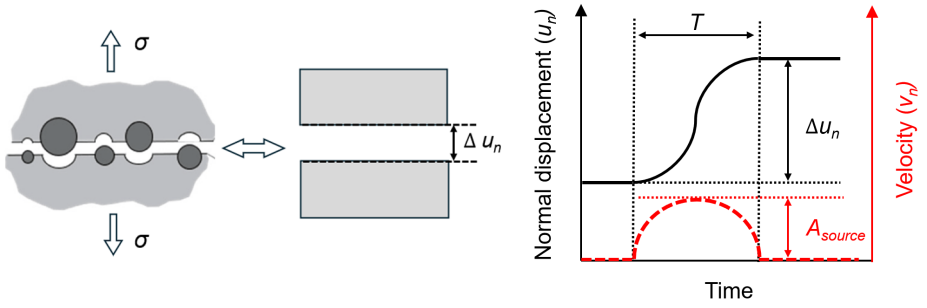

Figure 2.11 Illustration for (a) a local tensile cracking-induced dislocation (adapted from (Mura 2013)) and (b) its relationship with AE (adapted from (Sause and Richler 2015)).

The correlation between the dynamics of the microcracking process and AE phenomena is illustrated in Figure 2.11b. The dynamic history is assumed to be symmetric in time domain in the classical continuum mechanics (Mura 2013) (see Figure 2.11b). Therefore, the velocity of the microcracking, calculated as first-order derivative of displacement respect to time, is in the form of a pulse wave corresponding to the jump in displacements. Such a transient velocity pulse, further disturbing the whole system (i.e., elastic wave propagation), is considered as the source of AE signals. Following this assumption, the source parameters is determined by the velocity magnitude $\Delta \dot{u}_n$ and the duration T of the microcracking process. The properties of pulse waves (O'Rourke and Gallagher 1996), namely, the amplitude (denoted as A_{source}), the central frequency (denoted as f_{source}) of the AE sources are positively and negatively proportional to $\Delta \dot{u}_n$ and T:

$$A_{source} \propto \Delta \dot{u}_n \tag{2.8a}$$

$$f_{source} \propto \frac{1}{T} \tag{2.8b}$$

As the displacement jump duration T also describes the source pulse duration of AE signals, it is also referred as source rise time in classical AE theories (Eitzen and Wadley 1984; Ying 1973; Kao, Carvalho, and Labuz 2011)). It should be mentioned that the Δu_n and T, which fully determine time-domain amplitude and the frequency characteristics of

AE signals, respectively (see (Equation (2.8)), are based on a simplified fracturing model which neglects the nonlinear properties of concrete.

2.3.2.3.2 Friction-induced AE

Figure 2.12 illustrates the microscopical explanation for AE phenomena induced by friction along cracking surfaces (Sause and Richler 2015), which is similar to the above treatment of tensile cracking. The only difference is that the physical problem of friction along a pair of contacted cracking surfaces is mechanically represented as a different dislocation type (Mura 2013), namely a shear displacement jump (Δu_s) as shown in Figure 2.12a.

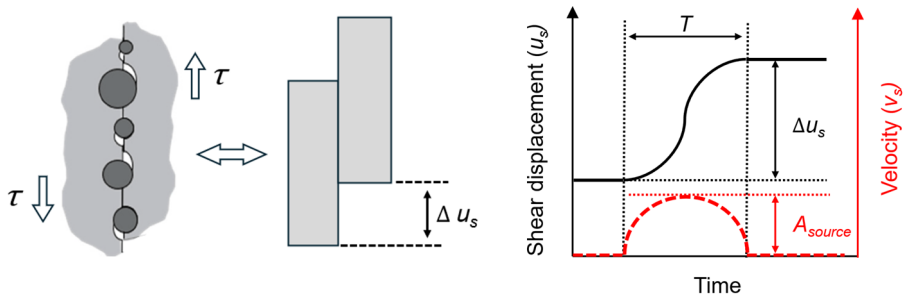

Figure 2.12 Illustration for (a) a friction (shear)-induced dislocation (adapted from (Mura 2013)) and (b) its relationship with AE (adapted from (Sause and Richler 2015)).

2.3.2.4 Summary and discussion on available AE theories

The above-mentioned AE theories are summarized in Table 2.1. Available AE theories provide quite limited explanation for AE phenomena in concrete fracture processes. Their limitations are summarized as follows:

- Available AE theories are inconsistent with each other, attributing the origin of AE phenomena to different mechanisms/phenomena at different scales from different perspectives.
- Available AE theories cannot quantify AE sources. Those formulated at macroscale (namely the snap-back instability, stress-drop instability, and stick-slip friction theories in Table 2.1) provide only qualitative description for AE phenomena induced by concrete fracture processes, although there has been experimental evidence for supporting them. Those established from energy perspective (namely the energy release theory in Table 2.1) or at microscale (namely the local dislocation theory in Table 2.1)) do provide relatively quantitative evaluation, which, however, introduce many assumptions and lack experimental validation.

- Available AE theories provide explanations for limited AE parameters, only the AE energy without experimental evidence and the AE source parameters involving strong assumptions; most of classical AE parameters (see Appendix A) cannot be physically explained by available AE theories.

Table 2.1 Summary of available theories for concrete fracture-induced AE.

Source types	Theories (reference)	Perspectives	Origin of AE	Quantitative ?	Explained parameters	Pros & Cons
Tensile cracking	Energy release (Iturrioz, Lacidogna, and Carpinteri 2013)	Energy	Released energy as the difference between elastic and dissipated energy	Yes	AE energy	*Pros*: Quantitative expressions for AE energy *Cons*: No experimental validation
	Snap-back instability (Carpinteri et al. 2016)	Macroscale	Local snap-back instabilities in global load-deflection curves	No	-	*Pros*: In line with classical snap-back and energy release theories *Cons*: No experimental validation Explaining no AE parameter
	Stress-drop instability (Li, Ren, and Li 2024)	Macroscale	Local drops in global load/stress	No	-	*Pros*: Experimentally validated *Cons*: Explain no AE parameter
	Local dislocation (Sause and Richler 2015)	Microscale	Transient jump of local normal displacements	Yes	AE source parameters	*Pros*: Quantifying AE source parameters *Cons*: Source parameters introduced by assumptions
Friction	Energy release (Baranov, Kudryavtsev, and Sarychev 1997)	Energy	Released energy from portions of deformation energy of microscopical asperities	Yes	AE energy	*Pros*: Quantitative expressions for AE energy *Cons*: A strong assumption that AE energy proportion to deformation energy of asperity
	Stick-slip friction (Haessig Jr and Friedland 1991)	Macroscale	Local drops in global friction force during stick-slip transition	No	-	*Pros*: Experimentally validated *Cons*: Explaining no AE parameters
	Local dislocation (Sause and Richler 2015)	Microscale	Transient jump of local shear displacements	Yes	AE source parameters	*Pros*: Quantifying AE source parameters *Cons*: Source parameters introduced by assumptions

2.4 Available modelling methods for acoustic emission induced by concrete fracturing processes

The limitations of available experimental-based AE characterization methods (see Section 2.2) and the lack of a deep and consistent understanding of AE mechanisms in available AE theories (see Section 2.3) highlight the need for forward modelling of AE phenomena in concrete fracture processes. Compared to the phenomenological models, forward-modelling methods are more reliable to understand and further establish reliable signal-to-source relationships for AE source characterization, in which the signal sources, wave propagation and sensor response can be explicitly modelled separately, as shown in Figure 2.1.

In this section, we review and discuss available forward AE modelling methods. Available AE modelling methods can be mainly classified into four categories, including analytical models, finite element methods (FEM), particle-based discrete element methods (DEM) and lattice models.

An AE signal is the result of a multi-physical and multiscale process, which has to include at least three sub-processes, namely the generation of AE source signals, the propagation of AE signal, and the measurement of AE signal at sensors. Because the sensor response and signal acquisition process can be separately considered through postprocessing the modelled wave signals (Hamam et al. 2021; Hamam et al. 2019) (see also Chapter 4), the last sub-process is not considered in this chapter. In the following, the pros and cons of each available method are discussed considering the generation of AE source signals, the propagation of AE signal.

2.4.1 Analytical approaches

There are several different analytical modelling methods of AE phenomena in literature, such as the analytical solution to surface waves derived from reciprocity theorem (Zhang and Lin 2023) and those to Lamb waves based on modal analysis (Seco and Jiménez 2012; Barat et al. 2019).

Among available analytical treatments, the moment tensor theory (MT) (Ohtsu and Ono 1986) is the most used method in the AE field. A brief description of the MT is given in sub-section. Readers are referred to the work of Ohtsu and co-authors (Ohtsu and Ono 1986; Ohtsu 1995) for more details of the MT.

2.4.1.1 Model description

The MT originates from seismology (Steketee 1958) and is formulated based on the classical elasodynamics (Eringen and Suhubi 1975). Its adaption for AE modelling is mainly

contributed by Ohtsu and co-authors (Ohtsu and Ono 1986; Ohtsu 1995). The MT is mathematically described under tensor notation as (Ohtsu 1995):

$$u_i(x,t) = G_{ij,k}(x,y,t)M_{jk} * S(t,T) \tag{2.9}$$

where $u_i(x,t)$ is a far-field displacement at location x and time t; M_{jk} and $S(t,T)$ are the so-called moment tensor and the source-time function, respectively, together describing the dynamics of an AE source at a local location y; $G_{ij,k}(x,y,t)$ is the first-order spatial deviation of the Green's function $G_{ij}(x,y,t)$; $|*|$ is the convolutional symbol.

The basic idea of Equation (2.9) is illustrated in Figure 2.13. The far-field displacement $u_i(x,t)$ is used to represent an AE signal in the MT, with its source and wave propagation being described by three terms in right side of Equation (2.9). The treatment of AE sources and wave propagation in the MT are described in the following.

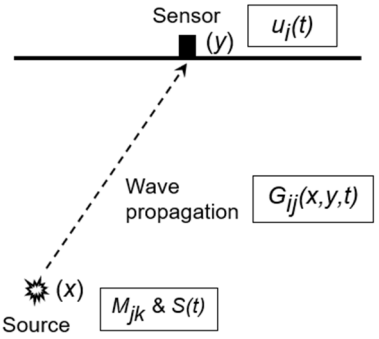

Figure 2.13 Illustration for the moment tensor theory.

- *AE source description*:

The magnitudes and types of AE sources are described by a second-order tensor, called moment tensor M_{jk} (Ohtsu 1995):

$$M_{jk} = C_{jkpq} l_p n_q \Delta V \tag{2.10}$$

where C_{jkpq} is the fourth-order elastic tensor; n_p is the unit normal vector of crack planes; l_p is a unit normal vector characterizing the movement direction of cracking (namely dislocation direction); ΔV is the volume of crack.

The moment tensor M_{jk} in seismology is similar to the concept of eigen stress in micromechanics (Kachanov 1980). The involved term of $l_p n_q \Delta V$ in Equation (2.10) can be seen as the eigen strain of cracks: the magnitude and dislocation direction of cracks are described by ΔV and $l_p n_q$, respectively. Such a treatment of AE sources in the MT is in

line with the microscopic understanding of AE as described in Section 2.3.2.3. The physical meanings of the nine elements in the moment tensor (Equation (2.11)) are illustrated in Figure 2.14. The MT treats fracture-induced AE sources as force dipoles/couples (dislocations). Each tensor element represents a different dislocation type: the tensile cracking sources are represented by diagonal elements (M_{xx}, M_{yy}, M_{zz}), while the friction sources are represented by the remaining elements (M_{xy}, M_{xz}, M_{yx}, M_{yz}, M_{zx}, M_{zy}).

$$M_{jk} = \begin{pmatrix} M_{xx} & M_{xy} & M_{xz} \\ M_{yx} & M_{yy} & M_{yz} \\ M_{zx} & M_{zy} & M_{zz} \end{pmatrix} \tag{2.11}$$

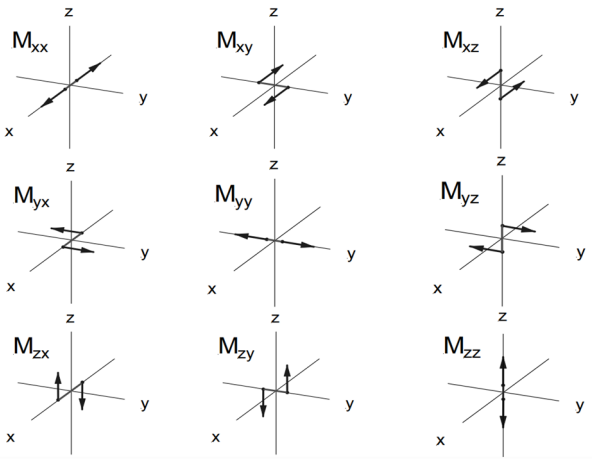

Figure 2.14 Nine elements of the moment tensor and their represented force dipole/dislocation types, with tensile cracking and friction AE sources represented by diagonal and orthogonal elements, respectively (adapted from (Grosse et al. 2021)).

It should be mentioned that there are several other analytical AE models similar to the MT, such as the models developed in the work (Hora and Červená 2010; Ohtsu, Yuyama, and Imanaka 1987). In these models the AE sources are treated as different force types, with the sources being treated as a point force (monopole) (Hora and Červená 2010) or the penny-shape cracks (Ohtsu, Yuyama, and Imanaka 1987) under the framework of micromechanics (Kachanov 1980), instead of the force dipoles used in the classical MT.

- *Wave propagation modelling*:

The propagation of elastic waves in the MT is modelled by solving the Green's function $G_{ij}(x, y, t)$. Mathematically, $G_{ij}(x, y, t)$ is a second-order tensor satisfying the following equations (Duffy 2015):

$$L[G_{jk}(x,y,t)] = -\delta_{jk}\delta(x,y)\delta(t) \tag{2.12}$$

where L is the differential operator associated with Navier-Cauchy's governing equation; δ_{jk} is the Kronecker's delta symbol; $\delta(x,y)$ and $\delta(t)$ are the spatial and temporal Dirac's delta functions.

Physically, the Green's function $G_{ij}(x,y,t)$ represents a i-direction far-field displacement at a location x and time t that is disturbed by a local j-direction displacement at a location x and time 0 (Grosse and Ohtsu 2008a).

2.4.1.2 Limitations

The MT has limitations for modelling both AE sources and wave propagation, as follows:

- *Wave propagation*: A close-form analytical solution to the Green's function $G_{ij}(x,y,t)$ (see Equation (2.13)) is, however, available only for special simplified cases under strong assumptions of an infinite space (Aki 1980), a semi-infinite half-space (Niwa, Ohtsu, and Shiomi 1982) or an infinite plate of isotropic medium (Wadley, Scruby, and Sinclair 1980). For more complicated cases, the solution relies on numerical approximations (Enoki, Kishi, and Kohara 1986; Hamstad, O'Gallagher, and Gary 1999). Moreover, the MT assumes a homogeneous medium, for which the applicability is limited because wave reflections, deflections, and velocity non-uniformity complicate the interpretation.

- *AE sources*: The moment tensor representation M_{jk} can only describe the crack magnitude and crack motion direction, while the dynamic history of cracking, which has a decisive effect on modeled AE waveforms especially the frequency characteristics, is based on an assumed source-time function $S(t,T)$ (see Equation (2.9)).

  An accurate description of $S(t,T)$ is not possible, as an AE signal occurs in a transient period in the magnitude of microsecond (Eitzen and Wadley 1984). One solution is to inverse $S(t,T)$ from an experimentally received AE signals (Kim and Sachse 1986; Ohtsu 1988); nevertheless, experimental reversion introduces many errors, as a AE signal received by a sensor is a result influenced by many other factors besides the sources, as shown in Figure 2.1.

  Another solution is to use an assumed mathematical function. According to the classical micromechanics (Kachanov 1980), the dynamic process of a crack dislocation (namely displacement jump) should start with a zero slope and smoothly approach to a constant displacement peak, as shown in Figure 2.15. Following such as a principal, many different mathematical expressions are assumed for $S(t,T)$ in literature. A mostly used $S(t,T)$ in the MT is given in Equation (2.13), which is first proposed in the classical work of NIWA, OHTSU et al. (Niwa, Ohtsu, and Shiomi 1982). As

discussed in Section 2.3.2.3, such a form of $S(t,T)$ leads to a pulse response of the velocity at source location, for which the source frequency characteristics are totally determined by the assumed value of source duration T (see Equation (2.8b)).

$$\frac{\mathrm{d}S(t,T)}{\mathrm{d}t} = \sin^4\left(\frac{\pi t}{T}\right) \quad 0 \le t \le T \tag{2.13}$$

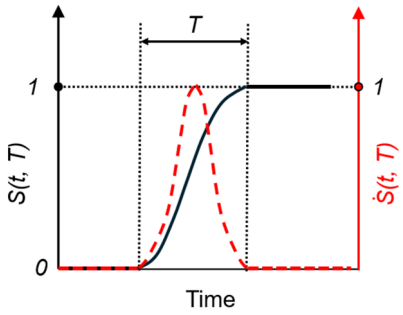

Figure 2.15 An example of source time function $S(t, T)$ and its first-order temporal derivative $\dot{S}(t, T)$ (adapted from (Niwa, Ohtsu, and Shiomi 1982)).

2.4.1.3 Advantages and applications

MT provides close-form solutions to both fractur-induced AE sources and wave propagation, which therefore can synthesize complete AE waveforms at a sensor location. It has been demonstrated that the AE waveforms synthesized by the MT can be comparable to those measured from experiments through properly selecting an assumed source time function $S(t)$ and an assumed moment tensor M_{jk} (Ohtsu and Ono 1986; Ohtsu 1995, 1989).

However, MT faces difficulties in forwardly model AE waveforms from sources due to the limitations of accurately describing both wave propagation and AE source as discussed above. Alternatively, in real applications, the MT theory is mainly used to characterize AE sources through measured waveforms inversely, called moment tensor inversion (MTI). Several attempts have been made to quantify concrete fracture sources using MT, such as fractured volume estimation (Chang and Lee 2004; Hazzard and Young 2002) and fracture source classification (Ohtsu 1991; Shigeishi and Ohtsu 2001) through different MTI algorithms (Kim and Sachse 1986; Ohtsu 1988; Kao, Carvalho, and Labuz 2011).

In the MTI, the limitations of source representation and wave propagation can both be minimized. For example, the so-called relative moment tensor inversion (rMTI) technique (Dahm 1996) provides a solution to the limitations of the Green's function (wave

propagation). In the rMTI, the Green's functions can be considered the same and thus be eliminated in Equation (2.9), for a set of acoustic emissions originating from a relatively small area compared to the travel distance. It has been demonstrated that the rMTI is providing an applicable approach concerning wave propagation in scattering and slightly heterogeneous materials (Cao et al. 2022). The rMTI also provides solutions to the source function in a reverse problem. Providing that the same source functions represent the same fracture type, it is easy to invert AE data onto the moment tensor using rMTI regarding a set of very different waveforms (Dahm 1996). A waveform comparison, such as the calculation of the Magnitude Squared Coherence Value, can then be used to quickly identify the fracture types for a large set of acoustic emissions (Malekpour, Gubner, and Sethares 2018). Additionally, there are other MTI-based methods to derive/approximate the source functions through measured waveforms in seismology, such as the higher-degree moment tensor representation (Dahm and Krüger 1999) and the MTI version developed by McLaskey et al to further account for sensor response (McLaskey and Kilgore 2013).

2.4.2 Traditional FEM included continuum mechanics-based numerical methods

The continuum theory-based numerical methods (Kukudzhanov 2012; Zhang and Cai 2010), especially the finite element method (FEM) (Cheung and Leung 1992; Hughes 2003), are the mostly used numerical tools for AE modelling.

2.4.2.1 Model description

The treatment of AE sources and elastic wave propagation in continuum theory-based numerical methods are discussed in the following.

- *AE source description*:

As illustrated in Figure 2.16, the most continuum theory based numerical methods use monopole force to represent a single concentrated nodal force/displacement (see Figure 2.16a) (Cheng et al. 2021; Zelenyak, Hamstad, and Sause 2015). Like the MT, the treatment of fracture-induced AE sources follow the microscopic dislocation theories (see Section 2.3.2.3): the tensile cracking and friction-induced AE sources are simulated by a tensile and shear force/displacement diploes, respectively, at different nodes (see Figure 2.16b and c) (Schubert and Schechinger 2002; Hamstad 2007a).

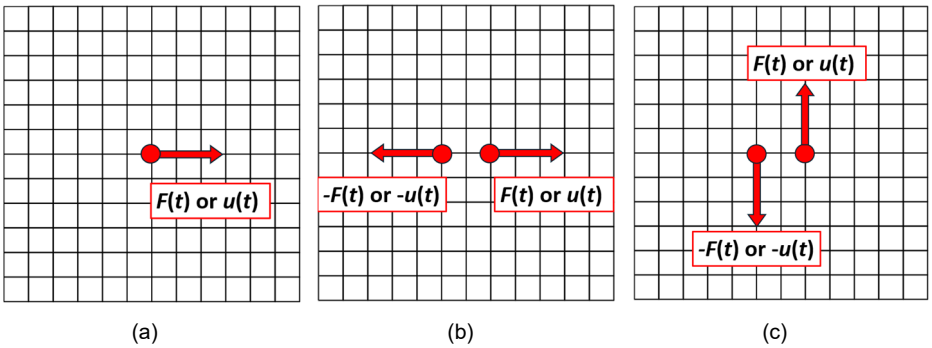

Figure 2.16 Description of AE sources in FEM included continuum theory-based numerical methods: (a) a point displacement/force (monopole), (b) a tensile cracking source represented by a displacement/force couple (dipole) and (c) friction source represented by a displacement/force couple (dipole) (adapted from (Schubert and Schechinger 2002; Hamstad 2007a)).

The above nodal forces/displacement introduced in the continuum theory-based numerical methods can be expressed in Equation (2.14). Like the MT, an assumed source time function $S(t,T)$ without clear physical meanings and irrelative to material fracture (see Figure 2.15), is needed to describe the dynamic history of sources, in which the frequency characteristics of modelled AE signals fully depend on the assumed source rise time T (see Equation (2.8a)).

$$F(t) = F_0 S(t,T) \tag{2.14a}$$

$$u(t) = u_0 S(t,T) \tag{2.14b}$$

where F_0 and u_0 are two constants that describe the magnitudes of source forces/displacements.

- *Wave propagation modelling*:

In continuum theory-based methods, the propagation of elastic wave propagation is modelled by solving motion equation (Equation (2.15a)) (Harris 2001) or wave equations (Equation (2.15b)) (Graff 2012):

$$\rho \frac{\partial^2 \boldsymbol{u}}{\partial t^2} = \nabla \cdot \boldsymbol{\sigma}(\boldsymbol{u}) + \boldsymbol{F_b} \tag{2.15a}$$

$$\frac{\partial^2 \boldsymbol{u}}{\partial t^2} = v^2 \nabla^2 \cdot \boldsymbol{u} \tag{2.15b}$$

where ρ is the density; $\boldsymbol{u}$ is the displacement tensor; ∇ is the del-operator; $\boldsymbol{F_b}$ is the body force tensor.

The motion or wave equations are then numerically solved to derive the approximated solutions to dynamic fields of the whole system at each time (namely elastic wave propagation) by using various mathematical approximation methods, such as the finite element method (FEM) (Serón et al. 1990; Zelenyak, Hamstad, and Sause 2014), finite difference method (FDM) (Marfurt 1984; Johnson 1987), finite boundary method (FBEM) (Ballandras et al. 2009; Ohtsu, Kaminaga, and Munwam 1999), finite volume method (FVM) (Dormy and Tarantola 1995; Xuan et al. 2014), spectral element methods (Komatitsch and Tromp 1999; Zhu, Qin, and Zhang 2011) and elastodynamic finite integration technique (EFIT) (Schubert and Schechinger 2002; Raley 2019), et al.

2.4.2.2 Advantages and applications

The FEM included continuum theory-based numerical methods are suitable for simulating elastic wave propagation processes. The motion equation (Equation (2.15a)) and wave equation (Equation (2.15b)) are partial differential equations (PDE), which are both derived in the framework of continuum mechanics (Spencer 2004) and can rigorously describe the dynamic force equilibrium of the entire system (field). The only difference is that the wave equation is a simplified form of the motion equation under certain conditions with a focus on describing wave propagation characteristics; the wave equation (Equation (2.15b)) can be derived from the motion equation (Equation (2.15a)) in the conditions of isotropic materials and without body force (Harris 2001). These two equations are both field equations that rigorously describe the wave (dynamic) field of solids.

Owing to the suitability to solve linear wave propagation problems in elastic and viscoelastic solids, the continuum theory-based numerical methods have been extensively implemented in simulating the propagation of AE waves induced by externally introduced source functions in varied materials (Sause and Richler 2015; Zelenyak, Hamstad, and Sause 2015; Hamstad 2007b; Sause and Horn 2010; Prosser et al. 1999).

2.4.2.3 limitations

The FEM included continuum theory-based numerical methods are, however, not suitable for describing fracture-induced AE sources. The fracture sources can be only indirectly introduced as assumed source functions with strong assumptions and without a clear fracture-related physical meaning (see Figure 2.16).

The FEM and other continuum theory-based methods established on the basis of continuity hypothesis and local contact principle cannot explicitly simulate the local displacement discontinuity (Dhatt, Lefrançois, and Touzot 2012). Specifically, there is a displacement spatial derivative term in the governing partial differential equations (the left-side term in Equation (2.15)) that reflects the internal force in governing equations, while the

displacement field in the crack tip region is discontinuous, and the spatial derivative does not exist (Javili et al. 2019).

2.4.3 Particle-base DEM

The particle-based discrete element method (also referred to as distinct element method (Hart 1993)) (DEM) are one of the mostly used numerical methods for modelling AE events induced during fracture processes of quasi-brittle materials.

2.4.3.1 Model description

As illustrated in Figure 2.17, particle-based DEM models represent a continuum material as an assembly of rigid or deformable spherical particles (or in other irregular shapes (Lu and McDowell 2007; Coetzee 2016)) that are bonded together at their contact points (Bićanić 2004). Two types of contact forces (also referred to as mechanical bonds (André et al. 2012)), normal and shear contact forces (marked as F_n and F_s in Figure 2.17b and c), are used to describe the particle interactions.

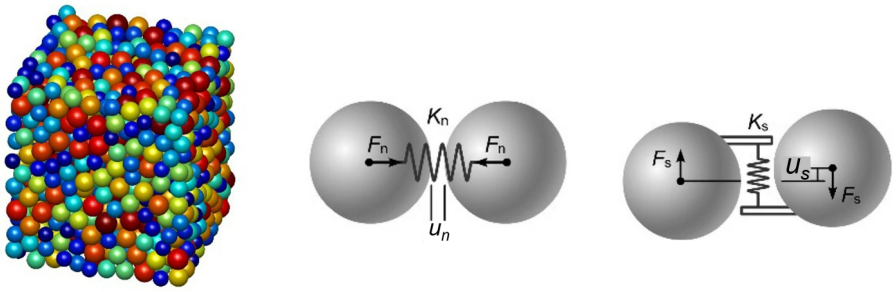

Figure 2.17 Illustration for the DEM: (a) discrete representation of a continuum; (b) normal contact forces between particles; (c) shear contact forces between particles (note: F_n and F_s represent normal and shear contact forces; K_n and K_s represent normal and shear stiffness; U_n and U_s represent normal and shear displacements) (adapted from (Qin et al. 2021)).

- *AE source description*:

In the particle-based DEM, the fracture-induced AE sources are described by failure of contact forces between particles by implementing nonlinear constitutive laws. As shown in Figure 2.18a, the tensile cracking is simulated by brittle (Hazzard and Young 2000) or softening (Li and Smith 2023a) failure of particle normal contact forces F_n governed by the relative normal displacement between particles u_n. Such a treatment of tensile cracking is in line with the local stress-drop theory (Li, Ren, and Li 2024) to explain tensile cracking-induced AE (see Figure 2.7).

As shown in Figure 2.18b, the friction-related AE sources are simulated by the shear-sliding failure of particle shear contact forces F_s that is governed by the relatively shear displacement u_s (namely the classical Coulomb friction law (see Figure 2.9a)) (Hazzard and Young 2000) or shear velocity $\dot{u}_s$ (namely the dynamic friction law (see Figure 2.9b)) (Horabik and Molenda 2016) between particles. Such a treatment of friction is in line with the local stick-sliding friction instability theory (McLaskey 2011) for explaining friction-induced AE (see Figure 2.10).

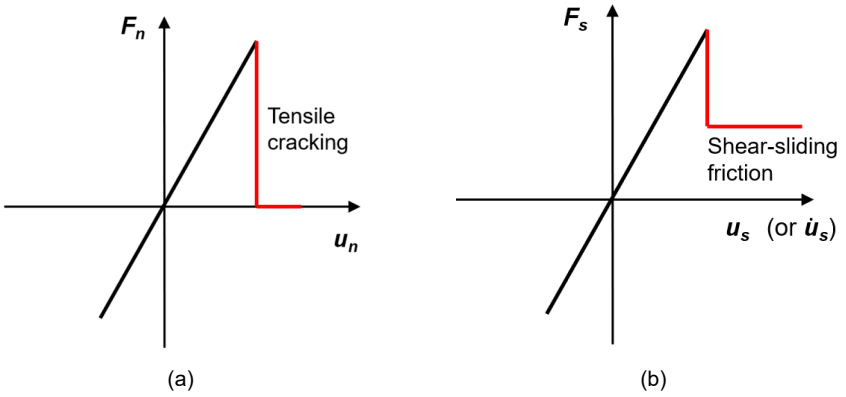

Figure 2.18 Nonlinear constitutive laws of contact forces for representing fracture-induced sources in the DEM: (a) tensile cracking and (b) shear-sliding friction (adapted from (Bićanić 2004)).

- *Wave propagation modelling*:

The wave propagation in particle-based DEM is simulated by solving the motion equations in terms of discrete equations assembled by the contacted forces between particles:

$$\boldsymbol{M}\ddot{\boldsymbol{u}}(t)+\boldsymbol{C}\dot{\boldsymbol{u}}(t)+\boldsymbol{F}(t)-\boldsymbol{P}(t)=0 \tag{2.16}$$

where $\boldsymbol{M}$ and $\boldsymbol{C}$ are mass and damping matrixes, respectively; $\ddot{\boldsymbol{u}}(t)$ and $\dot{\boldsymbol{u}}(t)$ are acceleration and velocity vectors, respectively; $\boldsymbol{F}(t)$ and $\boldsymbol{P}(t)$ are internal contact force and external force vectors.

2.4.3.2 Advantages and applications

DEM is suitable for fracture-induced AE source modelling. In DEM, the stress singularity at crack tip introduced by continuum theory is avoided in a straightforward way by using contact forces (see Equation (2.16)) to substitute the stress concept that involves a displacement spatial derivative term (see Equation (2.15)) in continuum-based methods for the description of internal forces (Tavarez and Plesha 2007). Although a relatively simple set of micromechanical interaction laws is used, these models can reproduce several typical features of macroscopic material behavior including elasticity, fracturing and damage

accumulation (Potyondy and Cundall 2004). Crack nucleation is simulated through breaking of internal bonds while fracture propagation is obtained by coalescence of multiple bond breakages (Lisjak et al. 2013a).

Owing to the ability for simulating microscopic fracturing activities during fracturing processes, the particle-based DEM models have been extensively employed to simulate the fracture-induced AE events in different brittle and quasi-brittle materials (Wu et al. 2023; Wang et al. 2021; Xie et al. 2020; Ji and Di 2013; Li and Smith 2022).

2.4.3.3 limitations

DEM cannot accurately simulate the propagation of elastic waves. The governing equations (Equation (2.16)) in particle-based DEM are established based on local contact forces between particles. Such discrete equations of local contact force equilibrium cannot rigorously describe the global wave field (Equation (2.15)), although there is an indirect connection between the local contact forces between discrete particles and the global properties of represented solids (Horabik and Molenda 2016).

Due to the inability of accurately simulating the elastodynamics of wave propagation induced by bond breakage, most work in literature is restricted to statistical characterization of AE events in the fracture process from different perspectives, such as the evolution of AE rate (bond breakage rate) in the fracture process (Li et al. 2017; Caulk 2020), the particle kinetic energy upon bond breakage (Hazzard and Young 2000; Li and Smith 2023b) and the b-value analysis considering the distribution of event amplitude and occurrence frequency (Zhang and Zhang 2017; Lisjak et al. 2013a). The explicit modelling of AE waveforms is not possible in particle-based DEM simulation.

2.4.4 Lattice model

The lattice models, also referred to as “central force model” in the physics community (Wang and Harris 1989), are another type of DEM that are particularly suitable for AE simulations.

2.4.4.1 Model description

As illustrated in Figure 2.19, in lattice modelling, a continuum is represented by a set of distributed nodes (lumped masses) interconnected by lattice elements. The bonded force between lumped masses is established by lattice elements that can be truss, spring or beam elements (Pan et al. 2018; Ostoja-Starzewski 2002).

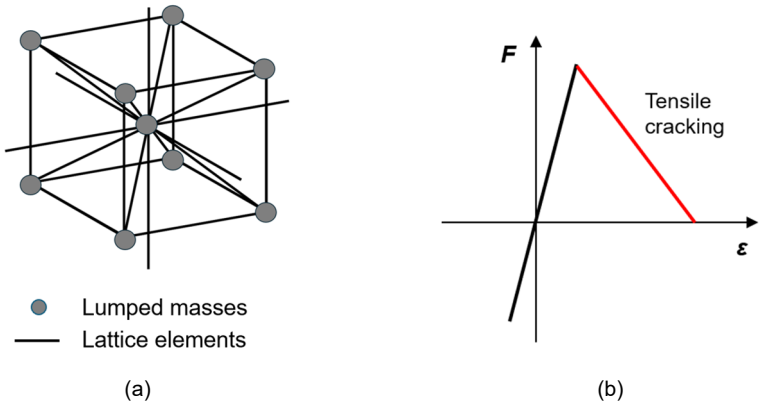

Figure 2.19 Illustration for a typical lattice model: (a) a basic lattice unit and (b) the nonlinear force-strain constitutive law for tensile cracking in a truss-element lattice model proposed by (Kosteski et al. 2011).

- *AE source description*:

The tensile cracking-related AE sources in lattice modelling is described by a brittle (Schlangen and Garboczi 1997; Chang et al. 2020) or softening (Kosteski et al. 2011; Zhou et al. 2024) nonlinear cohesive constitutive laws of lattice elements allowing element breakage upon reaching critical conditions.

Figure 2.19b exemplifies the nonlinear constitutive law for tensile cracking in a truss-element lattice model that has been widely used for AE simulations (Kosteski et al. 2011). Like the particle-based DEM, the nonlinear constitutive laws of the lattice elements can effectively simulate microcracking activities in fracture processes. Such a treatment of tensile cracking is in line with the local stress-drop theory (Li, Ren, and Li 2024) for explaining tensile cracking-induced AE (see Figure 2.7).

- *Wave propagation modelling*:

The wave propagation modelling in lattice models is like that in the particle-based DEM by solving the motion equations (Equation (2.16)). The main difference is that the discrete motion equations in lattice modelling is assembled by the bond forces between lumped masses that are established by lattice elements. Readers are referred to the classical review work (Pan et al. 2018; Ostoja-Starzewski 2002) for the establishment of force equilibrium using different lattice element types.

2.4.4.2 Advantages and applications

Lattice modelling combines the advantages of FEM and particle-based DEM and thus is suitable for modelling both AE sources and elastic wave propagation:

- For fracture-induced AE sources, like the particle-based DEM, the nonlinear constitutive laws of lattice elements for bond forces of lumped masses can effectively avoid stress singularity at crack tip introduced by continuum theory. The fracturing phenomena of crack nucleation, propagation, and coalescence to form macroscopic fracture can be reflected in lattice modelling through element breakage and the accumulation of broken elements (Nikolić et al. 2018). Therefore, the lattice modelling approach is suitable for describing fracture-induced AE sources.
- For wave propagation, the use of lattice elements enables it to accurately simulate the wave fields. Specifically, differently from the particle-based DEM that directly uses the contact forces between particles, the internal force (namely $\boldsymbol{F}(t)$ in Equation (2.16)) established by lattice elements are deduced from classical continuum mechanics in lattice models. Such discrete governing equations established by lattice elements are rigorously equivalent to the PDE of wave fields: the discrete motion equations in lattice models (Equation (2.15a)) can be seen as special forms of numerical discretization of the PDE of wave field (Equation (2.16)) (namely the discrete motion equations in lattice models and the particle-based DEM are mathematical and physical approximations, respectively, of the PDE in continuum theory) (Suiker, Metrikine, and De Borst 2001b). As a result, the elastodynamics of wave propagation induced by bond breakage can be accurately simulated by a lattice model.

Due to the aforementioned advantages of the lattice modelling approach, it is considered promising for simulating the complete AE process (Iturrioz, Lacidogna, and Carpinteri 2014). The first application of lattice modelling in AE simulation is contributed by Grabec & Petrišič (Grabec and Petrišič 1986) for the AE signals induced by tensile fracturing of polymeric materials. Subsequently, the lattice models have been applied in tensile cracking-induced AE simulations in various materials, such as crystal (Trochidis and Polyzos 1995), glass (Minozzi et al. 2003), wood (Nagy, Landis, and Davids 2010) and graphite (Barai and Mukherjee 2014).

Available work for simulating AE signals in tensile fracture process of different quasi-brittle materials was mainly contributed by Carpinteri and co-authors (Iturrioz, Lacidogna, and Carpinteri 2013; Friedrich et al. 2022; Iturrioz, Lacidogna, and Carpinteri 2014; Birck et al. 2016; Rodrigues, Birck, and Iturrioz 2016) by using a truss-based dynamic lattice model (the model shown in Figure 2.19).

2.4.4.3 Limitations

Although promising, the lattice modelling approach has limitations for AE simulation for modelling both AE sources and elastic wave propagation. The limitations and possible improvement are discussed as follows:

- *Treatment of friction-induced AE source*:

The study of friction-related AE sources in lattice modelling is quite limited in literature. In the above listed work for lattice modelling of AE, the tensile cracking is considered as the only fracture mechanisms. The mix-mode fracturing processes of quasi-brittle models is usually simulated as indirect tension failure by combing with a random lattice mesh to indirectly consider friction forces (Aydin, Binici, and Tuncay 2021; Schlangen and Garboczi 1997).

Although not yet applied for AE simulations, there have been several improved lattice models (Cusatis, Bažant, and Cedolin 2003; Mora and Place 1993; Abe et al. 2002; Place and Mora 1999) trying to incorporate friction mechanisms in simulating fracture processes of quasi-brittle materials by introducing additional shear type of lattice elements with various nonlinear constitutive laws to consider the stick-sliding behaviors between lumped masses (similar to the treatment of shear-sliding friction in the particle based-DEM, as shown in Figure 2.17c). These improved lattice models are promising for simulating friction-related AE sources in concrete fracturing processes.

- *Wave propagation:*

Although the lattice modelling approach is theoretically suitable for wave propagation simulation as discussed in Section 2.4.4.2, limited research was conducted in this regard. Available work is mainly restricted to statistical characterization of AE events in the fracture processes by analyzing released energy (Iturrioz, Lacidogna, and Carpinteri 2013), number of AE events (Iturrioz, Lacidogna, and Carpinteri 2014) and event amplitudes (Rodrigues, Birck, and Iturrioz 2016).

Several valuable attempts have also been made to explicitly model the fracture-induced AE waveforms (Iturrioz, Lacidogna, and Carpinteri 2014, 2013); nevertheless, an accurate simulation of transient complete AE waveforms has not yet been achieved. In listed literature, the simulated AE waveforms are largely different from the experimentally measured AE signals in both time and frequency domains.

2.4.5 Other numerical methods

Besides the above modelling strategies, there are several modelling strategies that have been adopted for AE modelling in literature. In this section, we briefly introduce three typical alternative types of numerical AE modelling methods, including two-step FEM, extended finite element method (XEFM) and finite discrete element method (FDEM).

2.4.5.1 Two-step FEM strategy

- *Model description*

The two-step FEM simulation strategy is proposed to overcome the limitations concerning explicit AE source description in traditional FEM-based AE simulations (see Section 2.4.2). The simulation strategy includes two independent steps:

The first step is to obtain two critical cracking displacement fields at the onset and end of a cracking growth step ($\boldsymbol{u_1}$ and $\boldsymbol{u_2}$ in Figure 2.20) through a static simulation using a FEM-based fracture model (e.g., those simulating the cracks as element stiffness degradation) (Cuadra et al. 2015; Cuadra 2015; Sause and Richler 2015; Mirgal, Singh, and Banerjee 2023) or through the digital image correlation (DIC) in experiments (Cuadra 2015).

Further assuming a source rise function to connect the obtained displacement fields $\boldsymbol{u_1}$ and $\boldsymbol{u_2}$ at two critical statuses of a cracking propagation step, the history of the displacement fields due to the cracking propagation can be completely described (see Figure 2.20b). A dynamic FEM simulation is then conducted using the displacement field history as boundary conditions to model the AE waveforms due to the change of the displacement fields in a transient fracturing process.

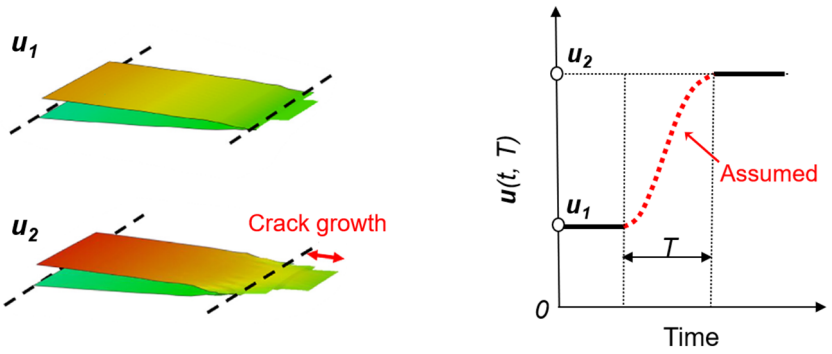

Figure 2.20 Illustration for the two-step FEM AE simulation strategy: (a) step one: obtaining the cracking displacement fields at the beginning and end of a cracking growth step; (b) step two: dynamic FEM simulation of AE waves due to the change of the obtained displacement fields with assumed source time function (adapted from (Cuadra 2015)).

- *Pros and cons for AE modelling*

Compared to the classical FEM-based AE simulations with fully assumed nodal force/displacement as AE sources (see Section 2.4.2.3), the use of cracking displacement fields to describe AE sources in such a two-step strategy enables a more realistic description of

fracture-induced AE sources and a simulation of the propagation of AE waves in a structural stress state that is closer to real fracturing processes.

Nevertheless, an assumed source rise time function still needed to describe the complete history of cracking displacement fields (see Figure 2.20b), which determines the amplitudes and frequency characteristics of simulated waves, as discussed in Section 2.3.2.3.1 (see Equation (2.8)). Moreover, this method can only simulate a single AE signal in one step of crack propagation and is not suitable for studying the changes of multiple AE signals during progressive fracturing processes.

2.4.5.2 XFEM

- *Model description*

The extended finite element method (XFEM) (also referred to as generalized finite element method (GFEM) (Strouboulis, Copps, and Babuška 2001)) is a numerical method proposed specially to address the discontinuity problems of conventional FEM when modelling the fracturing process (Fries and Belytschko 2010).

The basic concept of the XFEM is illustrated in Figure 2.21. It extends the traditional continuous finite element shape functions by using enrichment functions (jump functions) (marked as *H (x)* in Figure 2.21) in a grid containing discontinuous elements to simulate discontinuous physical fields (marked as Ω^+ and Ω^- in Figure 2.21) (Fries and Belytschko 2010). After numerically describing the fracture planes (discontinuity) by the enrichment functions, the tensile cracking and friction related microscopic fracture mechanisms (fracture induced-AE sources) are then described by a crack propagation criterion (e.g., energy release rate (Xu, Hajibeygi, and Sluys 2024)) at crack tip and contact laws along fracture surfaces, respectively. Such a treatment of fracture-related AE sources is similar to those in the DEM as shown in Figure 2.18 and is in line with macroscopic theories for explaining AE phenomena in Section 2.3.2.2. Readers are referred to the classical work (Datta 2013; Khoei 2015) for more details of the XFEM.

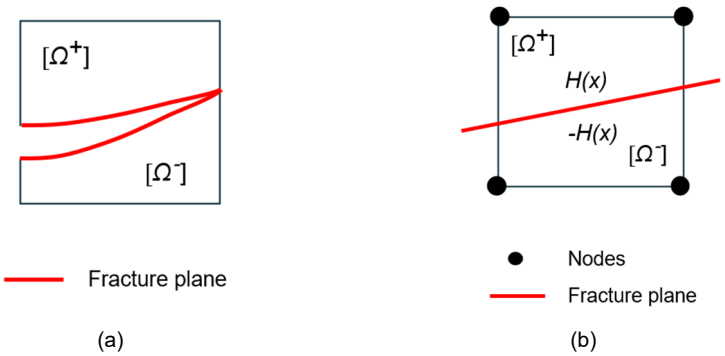

Figure 2.21 Illustration of the XFEM: (a) a physical fracturing plane characterized by displacement discontinuity and (b) numerical treatment of discontinuity by enrichment function *H(x)* in XFEM (note: Ω^+ and Ω^- represent two portions divided by a fracture in a discontinuous field) (adapted from (Khoei 2015)).

- *Pros and cons for AE modelling*

The XFEM overcomes the limitation of traditional FEM for describing the microscopic fracturing mechanisms (AE sources) and at the same time keeps the advantage of traditional FEM in simulating elastic wave propagation (see Section 2.4.2.2); therefore, it is capable of simulating the fracture-induced AE signals. The applications of the XFEM in AE simulation is mainly contributed by Komijani and co-authors for the AE source types of both tensile cracking and stick-sliding friction in different fracturing processes under various external loading conditions in porous solids (Komijani and Gracie 2017; Komijani and Gracie 2019; Komijani, Gracie, and Yuan 2020; Komijani, Wriggers, and Goudarzi 2023; Komijani 2018).

However, the XFEM has limitations in simulating fracture-induced AE. First, the enrichment functions themselves (besides the implemented fracturing criterion and contact laws) introduce additional assumptions on microscopic fracturing behaviours (AE sources) (Fries and Belytschko 2010). Second, the used of enrichment functions also largely increase the computational costs especially in combination with the dynamic solution to elastic wave propagation problem (Xu, Hajibeygi, and Sluys 2024); the above listed available XFEM-based AE simulations are restricted in modelling a single AE event induced by one cracking propagation/sliding step and cannot simulate multiple AE events during progressive fracturing processes.

2.4.5.3 FDEM

- *Model description*

The finite-discrete element method (FDEM) (also referred to as combined discrete finite element method (DEM/FEM) (Munjiza 2004)) is another numerical method that particularly suitable for AE simulation. The DEM is used to describe local fracturing areas while the FEM is used to describe the elasticity and wave propagation away from the fracture areas. There are two types FDEM available for AE simulation, as illustrated in Figure 2.22, with the fractured areas being simulated by the particle-based discrete elements (Gao et al. 2019) or interface (cohesive) elements (Lisjak et al. 2013a) while the unfractured areas being described by the FEM in both cases.

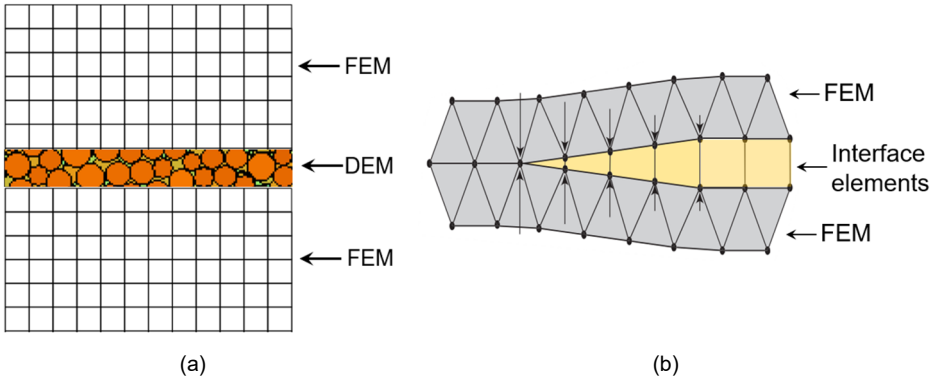

Figure 2.22 Illustration for two types of FDEM available for AE simulation: (a) FEM combined with particle-based DEM (adapted from (Gao et al. 2019)) and (b) FEM combined with interface elements (adapted from (Lisjak et al. 2013a)).

- *Pros and cons for AE modelling*

Unlike the XEFM relying on complicated mathematical implementation of enrichment functions that largely increase computational costs, the FDEM efficiently addresses the discontinuity of fracture in a simple way by directly combining the DEM and FEM. The computational efficiency makes the FDEM suitable for simulating multiple AE signals during fracturing processes. The particle discrete element-based (Ferdowsi et al. 2013; Wang, Elsworth, and Fang 2017; Ciamarra et al. 2011; Gao et al. 2019) and interface element-based (Zhao 2013; Wu et al. 2019; Bu et al. 2022; Xia et al. 2023; Zhao et al. ; Lisjak et al. 2013a) FDEM has been used to simulate the AE signals from both tensile cracking and friction in fracturing processes of various materials.

However, the XFEM has limitations in simulating fracture-induced AE. First, the FDEM needs to pre-define possible fracturing areas, for which the fracture paths are fixed in predefined DEM zones and the elastic wave propagation is restricted to the elastic FEM

zones away from the fracture areas (Munjiza 2004). Second, although theoretically suitable for elastic wave propagation simulation, the research of AE wave modelling by the FDEM is limited in literature; the above listed literature is mainly restricted to analysing AE event (broken element) numbers during fracturing processes. In few available works considering the wave propagation (Zhao et al. ; Lisjak et al. 2013a), the simulated AE waveforms are largely different from the experimentally measured AE signals in both time and frequency domains.

2.4.6 Summary and discussion on available AE modelling methods

The above-mentioned AE modelling methods are summarized in Table 2.2.

To date, it is a formidable challenge to model AE signals occurring in concrete processes. The traditional continuum theory-based methods (the MT and FEM) and the DEM face challenges in simultaneously modelling fracture-induced AE sources and elastic wave propagation, which is, therefore, not suitable for describing the whole AE processes due to their rooted limitations.

It should be mentioned that there are other numerical methods in literature for AE simulations besides the mentioned ones, such as the molecular dynamics (MD) method (Landa et al. 2003; Marasanov and Sharko 2017) and the peridynamics method (Ma et al. 2022; Cottica et al. 2020). Nevertheless, like those exemplified in Section 2.4.5, all these methods are formulated following a methodology like either the FEM (see Section 2.4.2) or DEM (see Section 2.4.3), facing the similar challenges in simulating AE.

Amongst the available modelling methods, the lattice models, XFEM and FDEM are three promising methods for AE modelling, as they can model both the discontinuity of local material fracturing and the global continuity of elastic wave propagation within a same modelling approach in one step. However, an accurate simulation of fracture-induced AE signals by these methods has not been achieved due to limited research in literature: available work is mainly restricted to analysing AE event (broken element) numbers during fracture processes. In few available works considering the wave propagation, the simulated AE waveforms are largely different from the experimentally measured AE signals in both time and frequency domains. Without accurately modelling the complete waveform, most of AE parameters cannot be obtained for understanding their relationships with concrete fracturing behaviors.

Table 2.2 Summary of available modelling methods for concrete fracture-induced AE.

Method names	AE source modelling			Elastic wave propagation modelling			AE modelling aspects in literature
	Description ways	Consider fracture?	Limitations	Description ways	Accurate?	Limitations	
MT	Moment tensor representation	No	Assumed source-time functions	Green functions	No	Simplified analytical solutions unable to describe complicated wave propagation processes	A single AE waveform due to an assumed source
FEM	Displacement/force-time functions	No	Assumed source-time functions	Motion/wave equations	Yes	Ignoring structural stress states in real fracturing situations	A single AE waveform due to an assumed source
DEM	Nonlinear constitutive laws	Yes	Calibrated fracture parameters without clear physical meanings	Motion equations	No	Motion equations assembled by contact forces unable to accurately describe the wave field	Multiple AE hits in fracture processes (without waveforms)
Lattice model	Nonlinear constitutive laws	Yes	Limited research in defining friction-related constitutive behaviors	Motion equations	Yes	Limited research (not yet achieving accurate wave simulation in literature)	Multiple AE waveforms in tensile cracking processes (inaccurate waveforms)
Two-step FEM	Displacement/force-time functions	Indirectly	Assumed source-time functions	Motion equations	Yes	Heavy computational costs introduced by two-step simulations	A single AE waveform due to an assumed source
XFEM	Nonlinear constitutive laws	Yes	Assumptions introduced by enrichment functions	Motion equations	Yes	Heavy computational costs introduced by enrichment functions	A single AE waveform due to one fracture propagation step (inaccurate waveforms)
FDEM	Nonlinear constitutive laws	Yes	Fixed fracture paths only in predefined DEM zones	Motion equations	Yes	Wave propagation only in predefined FEM zones	Multiple AE waveforms in fracture processes (inaccurate waveforms)

2.5 Knowledge gap

Bazant (Bazant 2009) pointed out in his speech at the award ceremony of Timusinko Medal in 2009: "The problem of damage and fracture of solids and structures, along with turbulence in fluid dynamics, is one of the two major problems of engineering science in the 21st century". As an attendant physical phenomenon associated with solid fracture, AE occurring in concrete fracturing process is even more complicated than fracture itself because we need consider other aspects besides fracture such as elastic wave propagation and sensor response.

In view of the complexity of fracture-induced AE phenomena in concrete, limited work is available in literature on how AE signals are linked to the physical fracturing processes of concrete. The knowledge gap regarding AE induced in concrete fracturing processes are summarized as follows:

Knowledge Gap 1: lacking accurate AE modelling methods. Although many methods are available for modelling AE phenomena, none of them can accurately model the complicated multiscale coupling process of fracture-induced AE between the discontinuity of local material fracturing and the global continuity of elastic wave propagation.

Knowledge Gap 2: lacking consistent and reliable AE source theories.

- Knowledge Gap *2.1: lacking consistent understanding of the origin of concrete fracture-induced AE phenomena*. Available AE theories are inconsistent with each other for explaining the origin of AE phenomena. They attribute the origin of AE phenomena to different mechanisms/phenomena at different scales from different perspectives.
- Knowledge Gap *2.2: lacking physical bases for measured AE signals*. Available theories provide mainly qualitatively description with strong assumptions for fracture-induced AE phenomena and cannot physically explain most parameters of AE measurements.

Knowledge Gap 3: lacking reliable and quantified AE characterization methods. Available experimental-based AE characterization methods are mostly established through experimental observations without clear physical bases. Therefore, they cannot provide reliable and quantified relationships between signal sources and received AE signals.

Among the three listed knowledge gaps, the knowledge gap 1 is the principal one. The lack of accurate AE modelling methods leads to the lack of reliable AE characterization methods and AE theories. This dissertation aims to fill in these identifies knowledge gaps, as follows:

- This dissertation first attempts to develop an accurate modelling framework for concrete-fracture AE phenomena based on one of the three promising AE modelling methods identified in Section 2.4.6, namely the lattice model. The developed modelling framework is expected to accurate simulate the whole multiscale and multi-physical process of concrete fracture-induced AE phenomena as shown in Figure 2.1, by extending the lattice modelling approach dedicated for concrete fracturing simulation with additional techniques that can accurately simulate the propagation of elastic waves (Chapter 3) and the sensor response (chapter 4) (for knowledge gap 1).
- With the developed AE modelling method, this dissertation expects to reveal the source mechanisms of tensile cracking-induced AE phenomena (Chapter 5 and 6) (for knowledge gaps 2).
- Building upon the understanding of AE source mechanisms, this dissertation expects to develop new AE indicator for quantifying the tensile cracking behaviour of concrete through AE measurements (Chapter 7), and to physically explain the evolution trends of AE parameters during tensile cracking propagation processes (Chapter 8). (for knowledge gaps 3).

3. A lattice modelling framework for acoustic emission wave propagation in concrete

3.1 Introduction

As reviewed in chapter 2, it remains a challenge to relate the local fracturing phenomena of concrete to the received acoustic emission (AE) signals after propagation in concrete structures, therefore, resulting in a lack of fundamental understanding and physically based explanation for most parameters of measured AE signals. In view of the complexity of AE phenomenon, forward modelling is a promising option to establish quantitative AE source characterization models. To achieve this, accurately modelling the complete transient waveforms of fracture-induced AE signals is a prerequisite. Nevertheless, to date, there is no comprehensive approach available that can explicitly model the complete transient waveforms of acoustic emissions induced by concrete fracture processes.

Among available modelling methods, the lattice type models are promising approaches, as they are known to be a matured modelling approach to simulate the fracturing processes in concrete-included quasi-brittle materials. However, limited explorations have been reported in literature on simulation of elastic waves propagation using the framework of lattice modelling. Consequently, modelling of wave generation and propagation cannot be done using the same approach. This chapter presents a lattice modelling framework to simulate the propagation of fracture-induced AE waves (elastic waves) in concrete.

This chapter is organized as follows. Section 3.2 describes the basic concept of lattice modelling approach, and the new techniques implemented in this study. Section 3.3 verifies the feasibility of proposed methods against theoretical solutions for simulating undamped elastic wave propagation using a simple externally inputted wave source function. Section 3.4 investigates the undamped numerical elastodynamic response of wave propagation induced by the breakage of a lattice element. Section 3.5 investigates the influence of numerical damping on simulated AE waves and then introduces a systematic test-based calibration procedure for simulating the attenuation of fracture-induced AE waves. Section 3.6 discusses the choices of representing an AE signal in numerical modelling, and the limitations and possible improvement of proposed methods for simulating elastic wave propagation.

3.2 Description of proposed lattice modelling framework

This section describes the proposed lattice modelling framework for AE wave simulations. Section 3.2.1 briefly describes the adopted approach of lattice modelling. Section 3.2.2 and Section 3.2.3 show two new implemented techniques to incorporate wave propagation and attenuation simulation in lattice modelling, including a proportional-integral-derivative (PID) control algorithm in an explicit time integration scheme for numerical noise reduction and a Rayleigh damping-bases theoretical method for AE wave attenuation simulation.

3.2.1 Description of adopted lattice model

This sub-section gives a brief description for the lattice model adopted in this thesis. This study uses a two-dimensional truss-based lattice model. The adopted approach for the lattice model was initially developed by Aydin and co-authors (Aydin, Tuncay, and Binici 2018), which has been extended in order to simulate the fracturing behaviour of plain concrete structures subject to tension (Aydin, Tuncay, and Binici 2018) and compression (Aydin, Binici, and Tuncay 2021) and the structural response of different reinforced concrete members (Aydin, Tuncay, and Binici 2019; Aydin et al. 2022).

In the adopted lattice model, a continuum is represented by a set of uniformly distributed nodes (lumped masses) interconnected by unidimensional truss elements. A two-dimensional squared lattice network is used in this study, corresponding to the classical lattice geometry proposed by Hrennikoff (Hrennikoff 1941). A basic unit of the adopted lattice network is shown in Figure 3.1a. The minimum spacing between two neighbouring nodes is called grid size, denoted as d. The total mass of an area with the size of $d \times d$ (in 2D case) around a node is lumped into a dimensionless mass at the node. The lumped mass of each node, denoted as m_n, is calculated as:

$$m_n = \rho \phi_n \tag{3.1a}$$

$$\phi_n = p d^2 w \tag{3.1b}$$

Where ϕ_n is the material volume represented by a node (a lumped mass). w and ρ denote the specimen thickness and material density. The values of ϕ_n is calculated by Equation (3.1b), where p is a coefficient to adjust ϕ_n for nodes at different locations. The value of p is 1 for internal nodes, while the value of p is adjusted into 0.75, 0.5 and 0.25 for nodes at outer corners, edges and inner corners, respectively, to match their actual representing area (see Figure 3.1b).

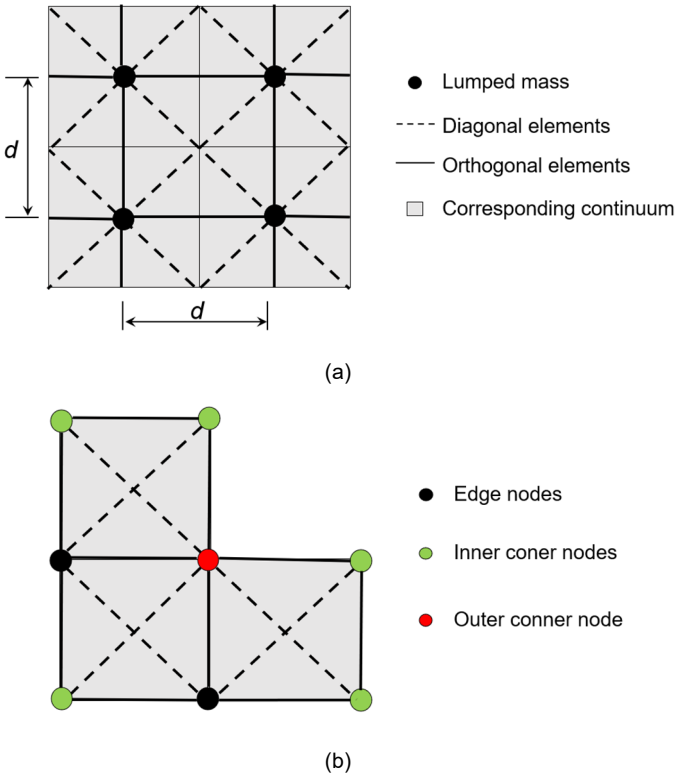

Figure 3.1 Illustration for the adopted two-dimensional truss-based lattice network: (a) A basic unit and (b) the nodes at edges and corners with adjusted masses to match their actual representing area.

Two types of elements are employed at grid level, including the orthogonal elements with size $l = d$ and diagonal elements with size $l = \sqrt{2}d$ (see Figure 3.1a). The force-strain constitutive law of the truss elements is shown in Figure 3.2, where F_e and ε represent the axial force and strain of truss elements. The elastic rigidity of orthogonal and diagonal elements is taken the same value as ES^*, where E and $S^*(d)$ are concrete modulus of elasticity and effective cross-sectional area of the truss elements, respectively, in which the latter is a function of the lattice grid size d. $S^*(d)$ acts as a bridge linking the elastic properties of discrete lattice elements to those of represented continuum. Specifically, the $ES^*(d)$ value can be viewed as the slope of the linear range of constitutive force-strain diagram (Figure 3.2a) and is determined by equalling the total elastic energy of a continuum to that of the equivalent lattice model under a uniform strain field. The effective cross-sectional area $S^*(d)$ of all truss elements involved in a lattice grid level d is calculated as:

$$S^*(d) = \frac{3}{2(1+\sqrt{2})} dw \tag{3.2}$$

where w is the specimen thickness. The derivation procedure of Equation (3.2) is detailed in Appendix B.

The compressive force in the truss elements is assumed to be linear elastic. The tensile force in the truss elements is assumed to be linear until the critical tensile strain ε_{cr} is reached, followed by a tri-linear softening curve (Muralidhara et al. 2011). The value of ε_{cr} is taken as a material property and determined as $\varepsilon_{cr} = f_t/E$, where f_t is concrete tensile strength.

To minimize the difference in fracture energy between orthogonal and diagonal elements involved in a chosen grid size, the fracture energy regularization concept (Bažant and Oh 1983) is implemented. Denoting the three tensile softening parameters of orthogonal elements of length $l = d$ as a_1, a_2 and a_3, the softening parameters of diagonal elements with length of $l = \sqrt{2}d$ are then divided by $\sqrt{2}$ (Figure 3.2a), to assure a same stress-displacement relationship (i.e., fracture energy) for different element sizes (Figure 3.2b). In Figure 3.2, two force coefficients b_1 and b_2, corresponding to two softening parameters a_1 and a_2 are selected as fixed values of 0.6 and 0.2, respectively (Muralidhara et al. 2011).

Moreover, different from the classical continuum theory-based numerical methods (e.g., FEM) that the element size mainly affects the computational accuracy mathematically, the element size of the lattice model as a discrete element method has a clear physical meaning. A fractured lattice element (with strain larger than ε_{cr}) physically corresponds to certain fracture volume, denoted as ϕ_f, induced by a crack propagation step. According to Figure 3.1, ϕ_f is the sum of two sub-volumes represented by two nodes (lumped mass), denoted as $\phi_{n,1}$ and $\phi_{n,2}$, that are linked by a broken element:

$$\phi_f = \phi_{n,1} + \phi_{n,2} \tag{3.3}$$

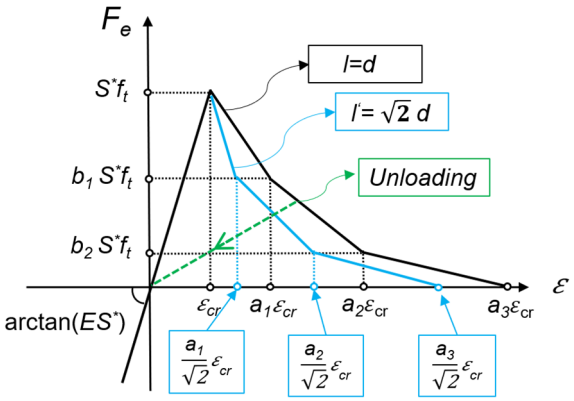

(a)

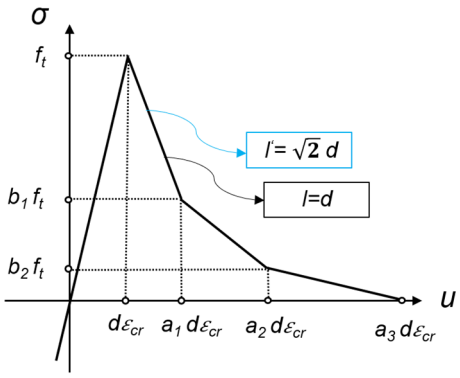

(b)

Figure 3.2 Constitutive law of truss elements: (a) constitutive force-strain diagrams for different element sizes; (b) regularized stress-displacement relationships for different element sizes (b_1=0.6 and b_2=0.2) (Aydin, Tuncay, and Binici 2018).

The softening parameters a_1, a_2 and a_3 are calibrated by a procedure as shown in Figure 3.3 to match the uniaxial stress–average displacement response of a "representative" direct tension test. Specifically, the stress-displacement model proposed by Cornelissen et al. (Reinhardt, Cornelissen, and Hordijk 1986) is selected as the "representative" test result and used as a benchmark for the lattice model. Lattice simulations are conducted using different trial values for softening parameters and a comparison in fracture energy (area under stress-displacement curve) is conducted between the numerical and benchmark results in each trial simulation. The tension softening parameters of lattice elements are updated until the difference between simulated and experimental fracture energy is reduced to a chosen tolerance (5%). This calibration procedure is conducted prior to the formal simulation case of tested specimen which is then conducted as a blind prediction based on the calibrated parameters.

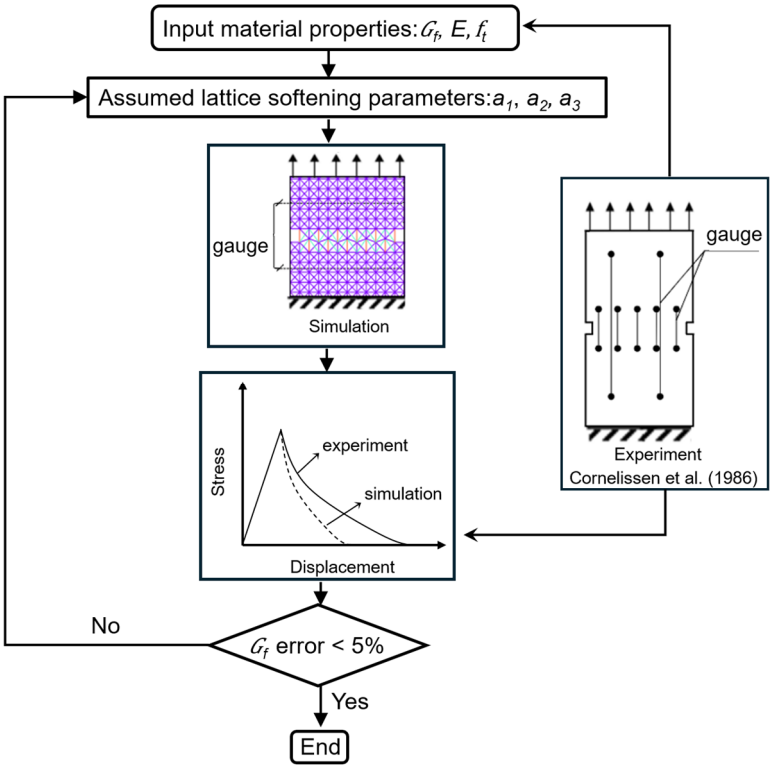

Figure 3.3 Calibration procedure of tension softening parameters (Aydin, Tuncay, and Binici 2018).

Figure 3.4 shows the solution flowchart of the adopted lattice model. In each time step, the strain in each lattice element is first computed according to the computed nodal displacement in a previous step and prescribed boundary conditions. The element forces are then computed according to the constitutive law shown in Figure 3.1. The resultant force F in a node (lumped) is then obtained as the vector summation of the forces of all elements connected to the node:

$$F = \sum_{i=1}^{n} F_e(i) \tag{3.4}$$

where $F_e(i)$ is the force in i-th element. n is the number of elements connected to a node ($n = 8$ for the adopted 2D squared lattice network as shown in Figure 3.2). The equations of motion are then obtained from equilibrium conditions of all the forces acting on the nodal masses:

$$\boldsymbol{M}\ddot{\boldsymbol{u}}(t) + \boldsymbol{C}\dot{\boldsymbol{u}}(t) + \boldsymbol{F}(t) - \boldsymbol{P}(t) = 0 \tag{3.5}$$

where $\ddot{\boldsymbol{u}}(\boldsymbol{t})$ and $\dot{\boldsymbol{u}}(\boldsymbol{t})$ are the acceleration and velocity vectors, respectively. $\boldsymbol{M}$ and $\boldsymbol{C}$ are

the diagonal mass and damping matrices. $\boldsymbol{F(t)}$ and $\boldsymbol{P(t)}$ are the internal and external force vectors.

In this study, the damping matrix $\boldsymbol{C}$ is approximated by the Rayleigh damping (Caughey 1960):

$$\boldsymbol{C} = \alpha \boldsymbol{M} + \beta \boldsymbol{K} \tag{3.6}$$

where $\boldsymbol{K}$ is the stiffness matrix. α and β are the mass-proportional and stiffness-proportional Rayleigh damping coefficients, respectively.

The explicit time integration method proposed by Chung & Lee (Chung and Lee 1994) is adopted to solve the equations of motion (Equation (3.5)). A more detailed description of the solutions strategy adapted by the lattice model is discussed in previous works of the authors (Aydin, Tuncay, and Binici 2018; Aydin, Tuncay, and Binici 2019).

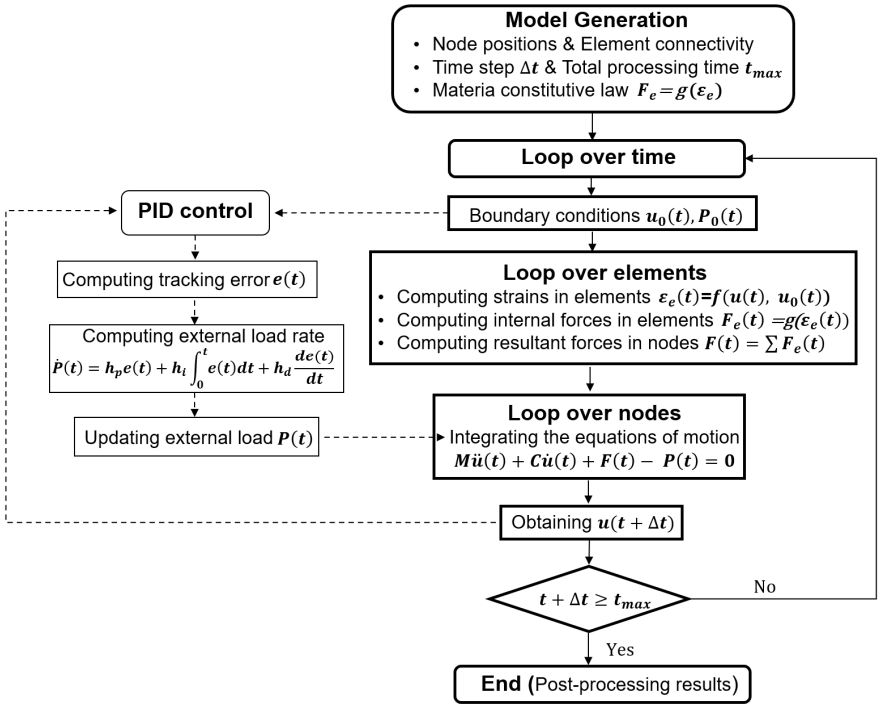

Figure 3.4 Solution flowchart of the adopted lattice model (Aydin, Tuncay, and Binici 2018).

3.2.2 PID control for noise signal reduction

In the lattice modeling approach, the fracture-induced AE signals are assumed to be the elastodynamic response of concrete induced by breakage of elements locally. This effect can be simulated directly in lattice models by solving the motion equations (Equation (3.5)) using an explicit time integration scheme. This scheme, however, also introduces dynamic noises, called spurious oscillations (Schmicker et al. 2014). The spurious oscillations are largely amplified in case of unstable external loading (Mirbagheri et al. 2015). In a direct solver, external loading bias is inevitable, and it amplifies the spurious oscillations into high-amplitude dynamic noise in the system (see also Section 3.4.1). This can be suppressed by controlling the external loading bias.

In this paper, we propose to minimize noise signals caused by external loading bias by implementing a proportional-integral-derivative (PID) control scheme in the lattice model. The PID algorithm serves as a feedback loop controller and can be mathematically describe as follows:

$$\dot{P}(t) = h_p e(t) + h_i \int_0^t e(t)\,dt + h_d \frac{de}{dt} \tag{3.7}$$

where $\dot{P}(t)$ and $e(t)$ are the external loading rate and tracking error, respectively. h_p, h_i and h_d are three coefficients controlling the proportional gain, integral gain and derivative gain of $e(t)$, respectively. Considering an arbitrary system (Figure 3.5), the loading rate function $\dot{P}(t)$ can be controlled in multiple ways by controlling the displacement rate at Point A, relative displacement rate between Points A and B, crack width opening rate at Point C, or stress/strain rate at Point D.

The flowchart of the PID control algorithm is shown in dash lines in Figure 3.4. Assuming that the targeted control variable is the displacement of loading point $u_0(t)$, and the actual calculated displacement is $u(t)$, the tracking error is calculated as $e(t) = u_0(t) - u(t)$. The rate of external load $\dot{P}(t)$ defined by the integro-differential equation (Eqution (3.7)) is solved to update the value of $P(t)$ as feedback in each calculation step (Equation (3.5)).

The bias in nodal velocity or acceleration induced by external loading $P(t)$ (i.e., noise signals) can be sufficiently reduced by keeping the values of error function at a low level. Values of PID constants used in this study are chosen according to the recommendation from Ziegler and Nichols (Ziegler and Nichols 1942). Integrating PID control within the explicit time integration methodology avoids additional dynamic effects from external loading bias. The effect of the implemented PID control will be demonstrated in Section 3.4.1.

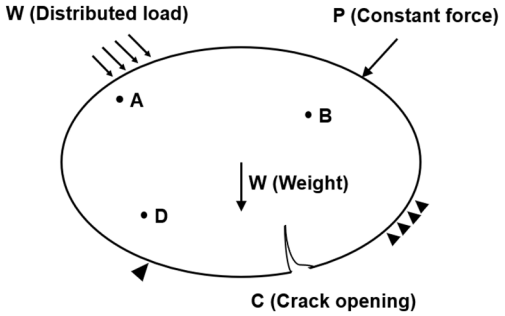

Figure 3.5 An arbitrary system with PID control.

3.2.3 A Rayleigh damping calculation method for AE signal attenuation

To properly simulate the propagation of elastic waves in concrete, it is essential that the modelling approach can consider the attenuation of AE signals. The attenuation of AE signals (elastic waves) in concrete is caused by many factors (Gresil and Giurgiutiu 2015; Schubert and Herrmann 2011; Pollock 1986). Among others, two main factors can be distinguished, namely, geometric spreading loss (or called geometric attenuation) and material damping (Zhang 2022). The geometric spreading loss is the loss of wave amplitude due to the radiation of a wave front departing from a point source into all directions (Gresil and Giurgiutiu 2015). The material damping (also referred to as viscous damping (Yang, Cascante, and Polak 2011) or absorbing damping (Tian et al. 2017a)) describes the energy stored in a wave that is dissipated due to viscoelastic material behaviours, which further includes the intrinsic damping and scattering damping (Zhang 2022). The intrinsic damping is associated with the internal friction between particles (Lambri 2000), while the scattering damping is associated with the fact that wave with certain wavelength scatters in the media when it travels through scatters of comparable sizes (e.g., aggregates or pores in concrete) (Lai and Tu 2020).

The wave attenuation due to spreading loss has been inherently considered in the adopted lattice model (this will be demonstrated in Section 3.3.2), as the system energy conservation is accurately considered in the establishment of force equilibrium (Equation (3.5)). A Rayleigh damping-based method is proposed in this paper to consider the wave attenuation due to material damping. Derivation of the proposed method is described in the following.

As the intrinsic damping and scattering damping are hard to be distinguished from each other, they are often described together by a frequency-dependent material damping factor (Philippidis and Aggelis 2005), herein denoted as $\eta(\omega)$. $\eta(\omega)$ depends on the frequency and the type of a wave: a wave of higher frequency attenuates faster because the wave involves more cycles of particle movements during the same travel time (Bormann,

Engdahl, and Kind 2012); shear and Rayleigh waves attenuate more than pressure wave owing to more friction between motion particles in shear deformation (Gaydeck et al. 1992). For a single-frequency and single-mode wave with angular frequency ω, the ratio between two wave peak amplitudes, $A_i(\omega)$ and $A_j(\omega)$, received at two different locations i and j, respectively, with distances of r_i and r_j to the wave source is described as (Yang, Cascante, and Polak 2011; Zerwer, Cascante, and Hutchinson 2002):

$$\frac{A_i(\omega)}{A_j(\omega)} = \left(\frac{r_j}{r_i}\right)^{\eta_0} \exp\left[-\eta(\omega)\left(r_i - r_j\right)\right] \tag{3.8}$$

where $\left(\frac{r_j}{r_i}\right)^{\eta_0}$ is the wave attenuation considering geometric spreading loss and η_0 is a controlling variable with $\eta_0 = 0$ for plane wavefront, $\eta_0 = 0.5$ for cylindrical and circular wavefronts and $\eta_0 = 1.0$ for spherical wavefronts propagating in isotropic and homogeneous media (Yang, Cascante, and Polak 2011). $\exp\left[-\eta(\omega)\left(r_i - r_j\right)\right]$ represents the wave attenuation due to material damping. Based on Equation (3.8), the frequency-dependent material damping factor $\eta(\omega)$ can be expressed as:

$$\eta(\omega) = \frac{1}{r_i - r_j}\left(\ln\frac{A_j(\omega)}{A_i(\omega)} - \eta_0 ln\frac{r_i}{r_j}\right) \tag{3.9}$$

According to Equation (3.9), the attenuation of wave amplitudes excluding the geometric spreading loss between locations i and j, denoted as $\gamma(\omega)$, can be expressed as:

$$\gamma(\omega) = \ln\frac{A_j(\omega)}{A_i(\omega)} - \eta_0 ln\frac{r_i}{r_j} = (r_i - r_j)\eta(\omega) = \Delta r\eta(\omega) \tag{3.10}$$

where $\Delta r = r_i - r_j$ is the distance between two receiving locations i and j. If $V(\omega)$ is the velocity of the considered single-mode wave, the arrival time difference of waves received at locations i and j, denoted as $\Delta t = t_i - t_j$, can be expressed as:

$$\Delta t = t_i - t_j = \frac{r_i - r_j}{V(\omega)} = \frac{\Delta r}{V(\omega)} \tag{3.11}$$

Assuming the two locations i and j are chosen in such a way that Δt can be expressed as the product of the number of wave cycles n and the wave period $T = \frac{2\pi}{\omega}$, Equation (3.11) can be further expressed as (Gresil and Giurgiutiu 2015):

$$\Delta t = \frac{\Delta r}{V(\omega)} = nT = \frac{2\pi n}{\omega} \tag{3.12}$$

By substituting Equation (3.12) into Equation (3.10), $\gamma(\omega)$ is then expressed as:

$$\gamma(\omega)=\frac{2\pi n}{\omega}V(\omega)\eta(\omega) \tag{3.13}$$

Alternatively, consider the motion of a wave particle involved in the single-frequency and single-mode wave. The vibration amplitude of the wave particles attenuates in the time domain following a logarithmic decrement law. The logarithmic decrement, denoted as $\gamma_{\text{logarithmic}}(\omega)$, is given by the following equation (Meirovitch 2010):

$$\gamma_{\text{logarithmic}}(\omega)=ln\frac{A_1}{A_n}=\frac{2n\pi\xi(\omega)}{\sqrt{1-\xi(\omega)^2}} \tag{3.14}$$

where A_1 and A_n are the vibration amplitudes of the wave particle at first cycle and after n cycles, respectively. $\xi(\omega)$ is damping ratio. In a low-damping system, $\xi(\omega)\ll 1$, Eq. (3.14) can be approximated to:

$$\gamma_{\text{logarithmic}}(\omega)=ln\frac{A_1}{A_n}\approx 2n\pi\xi(\omega) \tag{3.15}$$

The damping ratio $\xi(\omega)$ can be expressed in the form of Rayleigh damping $c=\alpha m+\beta k$ as proposed by Caughey (Caughey 1960):

$$\xi(\omega)=\frac{c}{c_0}=\frac{\alpha m+\beta k}{2\sqrt{km}}=\frac{1}{2}\left(\alpha\sqrt{\frac{m}{k}}+\beta\sqrt{\frac{k}{m}}\right)=\frac{1}{2}\left(\frac{\alpha}{\omega}+\beta\omega\right) \tag{3.16}$$

where m, k and $\omega=\sqrt{k/m}$ are mass, stiffness and natural angular frequency of the wave particle. $c_0=2\sqrt{km}$ is the critical damping. Furthermore, it is assumed that in the case of a single-frequency and single-mode wave propagating in isotropic and homogeneous media, the attenuation of the motion of an involved wave particle in time domain, $\gamma_{\text{logarithmic}}(\omega)$, is equivalent to the spatial attenuation of the wave excluding geometric spreading loss, $\gamma(\omega)$, both caused by the material damping (Tian et al. 2017b; Ramadas et al. 2011; Gresil and Giurgiutiu 2015). Accordingly, Equation (3.13) is equal to Equation (3.15), as follows:

$$\gamma(\omega)=\frac{2\pi n}{\omega}V(\omega)\eta(\omega)=\gamma_{\text{logarithmic}}(\omega)=2n\pi\xi(\omega) \tag{3.17}$$

By substituting Equation (3.16) into Equation (3.17), the relationship between the material damping factor $\eta(\omega)$ and Rayleigh damping coefficients α and β is established as:

$$\eta(\omega)=\frac{2\pi f\xi(\omega)}{V(\omega)}=\frac{\omega}{2V(\omega)}\left(\frac{\alpha}{\omega}+\beta\omega\right)=\frac{1}{2V(\omega)}\left(\alpha+\beta\omega^2\right) \tag{3.18}$$

Equation (3.18) is derived based on the assumption of a single-frequency and single-mode

wave. An AE signal is however composed of waves of multiple modes and a wide frequency range. To model the attenuation of an AE signal, we assume the AE signal is dominated by certain wave modes and the attenuation of the dominating mode can represent the attenuation of the entire AE signal. The attenuation of an AE signal in an interested frequency range (ω_{min}, ω_{max}) can then be described by one set of suitable Rayleigh damping coefficients using an average concept. Specifically, by substituting the low- and high-bound frequency ω_{min} and ω_{max}, corresponding material damping factors $\eta(\omega_{min})$ and $\eta(\omega_{max})$, and wave velocities $V(\omega_{min})$ and $V(\omega_{max})$ of a dominating wave mode into Equation (3.18), we get the following equation set:

$$\begin{cases} \eta(\omega_{\min}) = \dfrac{1}{2V(\omega_{\min})}\left(\alpha + \beta{\omega_{\min}}^2\right) \\ \eta(\omega_{\max}) = \dfrac{1}{2V(\omega_{\max})}\left(\alpha + \beta{\omega_{\max}}^2\right) \end{cases} \tag{3.19}$$

By solving Equation (3.19), average Rayleigh damping coefficients covering an interested frequency range (ω_{min}, ω_{max}) of an AE signal with certain dominating wave mode, denoted as $\alpha(\omega_{min}, \omega_{max})$ and $\beta(\omega_{min}, \omega_{max})$, can be determined as:

$$\alpha(\omega_{\min},\omega_{\max}) = \frac{2\left[V(\omega_{\max})\eta(\omega_{\max}){\omega_{\min}}^2 - V(\omega_{\min})\eta(\omega_{\min}){\omega_{\max}}^2\right]}{{\omega_{\min}}^2 - {\omega_{\max}}^2} \tag{3.20a}$$

$$\beta(\omega_{\min},\omega_{\max}) = \frac{2\left[V(\omega_{\min})\eta(\omega_{\min}) - V(\omega_{\max})\eta(\omega_{\max})\right]}{{\omega_{\min}}^2 - {\omega_{\max}}^2} \tag{3.20b}$$

3.3 Verification of undamped elastic wave propagation in lattice model

In this section, the proposed lattice model is verified using four simplified cases of two different signal source forms, namely, plane waves and point-source waves. In the verification cases, the models assume undamped elastic wave propagation, so that one may compare the simulated results with classical theoretical solutions. A concrete beam specimen with dimensions of 550×150×40 (length×width×thickness) mm^3 is modelled with 1-mm lattice grid size (d = 1 mm). For a clear discussion, a Cartesian frame is defined with the coordinate origin located at the bottom left corner of the numerical model, see Figure 3.5. The adopted material properties are listed in Table 3.1.

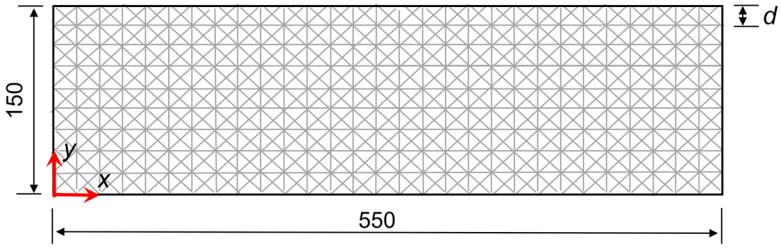

Figure 3.6 Numerical model for simulating undamped elastic wave propagation (unit: mm).

Table 3.1 Concrete material properties.

Properties (unit)	Density ρ (kg/m^3)	Elastic modulus E (GPa)	Compressive strength f_c (MPa)	Tensile strength f_t (MPa)	Fracture energy G_f (N/m)	Dynamic Poisson's ratio υ (-)
Values	2310	35.20	33.95	3.15	58.82	0.24

A nodal displacement $u_i(t)$ is defined as the wave source function at the corresponding source location. The adopted wave source function $u_i(t)$ was initially proposed in Bruna & Riera (Bruna and Riera 1988) as a typical numerical representation of hypocentres:

$$u_i(t) = u_0 \sin(\omega_0) \sin(\pi \frac{t - t_a}{t_a - t_b}), \quad t_a < t < t_b \tag{3.21}$$

where the subscript $i = x,\ y$ of $u_i(t)$ denotes the nodal displacement directions in x or y directions. $u_0 = 2.5 \times 10^{-6}$ mm, $t_a = 0$, $t_b = 0.01$ ms and $\omega_0 = 2\pi \times 200$ kHz. These parameters result in a Gaussian pulse (Bauer et al. 1984b) with a central frequency 200 kHz and a duration of 0.01 ms.

A time step of 2×10^{-4} ms (5 MHz sampling rate) and zero numerical damping ($\alpha = \beta = 0$) are used in the explicit integration procedure when solved the model.

3.3.1 Plane waves

The propagation of the plane pressure (P) and shear (S) waves is examined in this subsection through two simulation cases. The plane waves are considered propagating from left ($x = 0$ mm) to right plane ($x = 550$ mm) in x direction. The applied boundary conditions are summarized in Table 3.2, where Case 1 and Case 2 correspond to the simulation of P wave and S wave, respectively. The source displacements $u_i(t)$ are applied to all the nodes at plane $x = 0$ mm in the x and y directions for P wave and S wave, respectively. The symmetric or antisymmetric boundary conditions are introduced at planes $y =$

0 mm and $y = 150$ mm to simulate an infinite space in y direction that allows the unrestricted propagation of plane waves without altering the waveforms (Iturrioz and Riera 2021). In addition, a nonreflexive boundary is implemented on the right edge to avoid wave reflection. Various methods can be used to create such a nonreflexive boundary, as discussed in (Givoli 1991). Herein, a simple method was implemented by providing nodes from $x = 540$ mm to $x = 550$ mm with smoothly increased viscous dampers, with their stiffness proportional damping coefficients β linearly increasing from 0 (nodes at $x = 540$ mm) to a critical value β_0 (nodes at $x = 550$ mm). β_0 is determined by the central angular frequency ω_0 of simulated source wave as (Semblat, Lenti, and Gandomzadeh 2011):

$$\beta_0 = \frac{2}{\omega_0} \tag{3.22}$$

Table 3.2 Boundary conditions used for plane wave simulations.

Case number	Wave type	Plane at x=0	Planes at y=0, y=150 mm	Planes at x=540~550 mm	Plane at x=550 mm
1	P-wave	$u_x(t)$	Symmetry plane	Nonreflexive boundary	$u_x = 0$
2	S-wave	$u_y(t)$	Anti-symmetry plane	Nonreflexive boundary	$u_x = u_y = 0$

For Case 1, a typical x direction displacement field at simulation time $t = 0.1$ ms is illustrated in Figure 3.7a. Figure 3.7b shows the evolution of displacements in x direction of the two recorded nodes at ($x = 0,\ y = 75$ mm) and ($x = 100$ mm, $y = 75$ mm). The P-wave velocity in the lattice model can be estimated using the distance and arrival time difference of two recorded nodes. The arrival time of P-wave at $x = 100$ mm is 22.7 μs and the numerical P-wave velocity is estimated as $V_{P\ (numerical)} = 100\ \text{mm}/22.7\ \mu\text{s} = 4405\ \text{m/s}$.

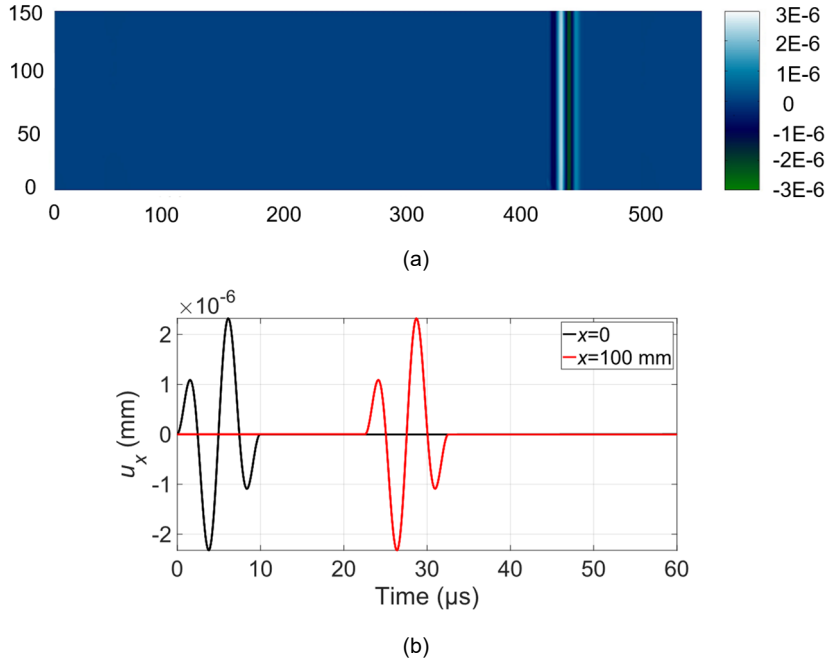

Figure 3.7 Simulation results for plane P-wave: (a) a typical *x* direction displacement filed at simulation time *t*=0.1 ms (unit: mm); (b) evolution of *x* direction displacements of two recorded nodes at (*x*=0, *y*=75 mm) and (*x*=100 mm, *y*=75 mm).

For Case 2, a typical y direction displacement field at simulation time $t = 0.1$ ms is illustrated in Figure 3.8a. Figure 3.8b shows the evolution of displacements in y direction of the two recorded nodes at $(x = 0,\ y = 75\ \text{mm})$ and $(x = 100\ \text{mm},\ y = 75\ \text{mm})$. The arrival time of S-wave at $x = 100$ mm is 41.8 μs and accordingly the numerical S-wave velocity is estimated as $V_{S\ (numerical)} = 100\ \text{mm}/41.8\ \mu\text{s} = 2395\ \text{m/s}$.

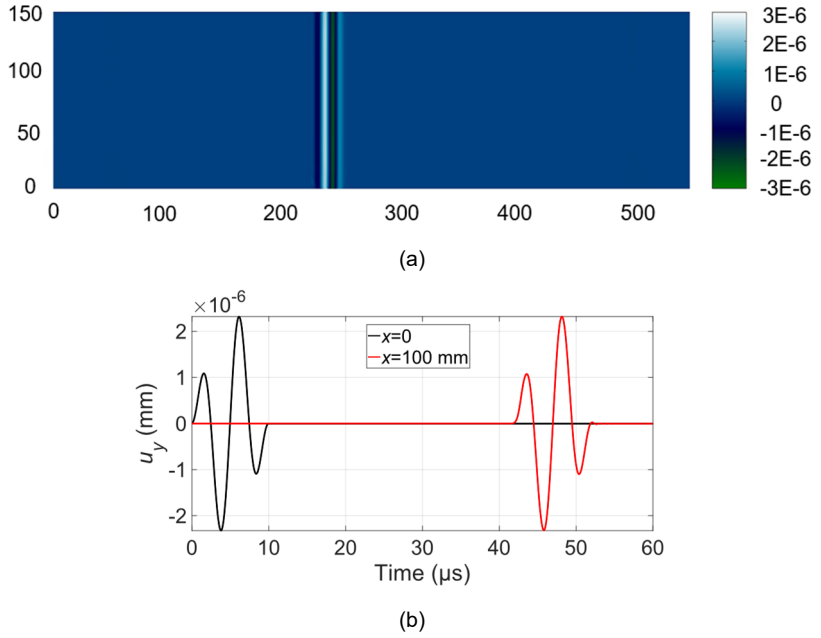

Figure 3.8 Simulation results for plane S-wave: (a) a typical *y*-direction displacement filed at simulation time *t*=0.1 ms (unit: mm); (b) evolution of *y*-direction displacements of two recorded nodes at (x=0, y=75 mm) and (x=100 mm, y=75 mm).

For isotropic and homogeneous solids, the theoretical P- and S-wave velocities are calculated by (Morelli and Dziewonski 1993):

$$V_{P\,(theoretical)} = \sqrt{\frac{(1-\upsilon)E}{(1+\upsilon)(1-2\upsilon)\rho}} \tag{3.23a}$$

$$V_{S\,(theoretical)} = \sqrt{\frac{E}{2(1+\upsilon)\rho}} \tag{3.23b}$$

Using the material properties listed in Table 3.1, the theoretical P- and S-wave velocities are calculated as 4238 and 2479 m/s, respectively. The differences between theoretical and numerical wave velocities are 4.2% and 3.4% for P- and S-waves, respectively.

3.3.2 Point-source waves

As the sources of acoustic emission signals can be regarded as point excitations considering the much smaller fracture scale than that of concrete structures, two additional simulation cases are conducted to investigate the propagation of body wave and Rayleigh wave (R-wave) induced by a point source. The applied boundary conditions are summarized in Table 3.3. A source displacement $u_y(t)$ (Equation (3.21)) is applied in y direction on a single node at ($x = 275$ mm, $y = 75\ mm$) and at ($x = 275$ mm, $y = 150$ mm),

respectively. Case 3 simulates the propagation of a point-source body wave while Case 4 simulates a point source R-wave. The boundary conditions defined at the four edges of both models are given in Table 3.3. The nonreflexive boundaries are applied using the same method described above for plane wave simulations.

Table 3.3 Boundary conditions used for point-source wave simulation (unit: mm).

Case number	Wave type	Node at (x=275, y=75)	Node at (x=275, y=150)	Planes at x=0~10, x=540~550, y=0~10	Planes at y=140~150	Plane at y=0
3	Body wave	$u_y(t)$	-	Nonreflexive boundary	Nonreflexive boundary	u_y=0
4	Rayleigh wave	-	$u_y(t)$	Nonreflexive boundary	-	u_y=0

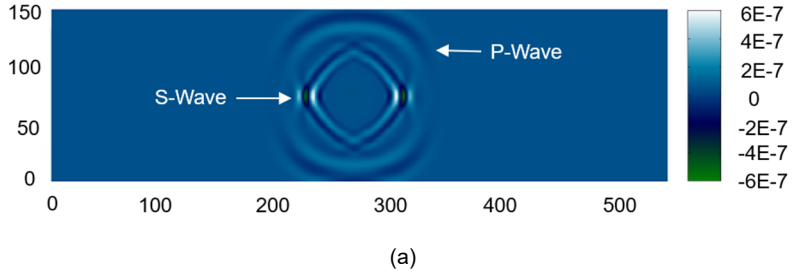

(a)

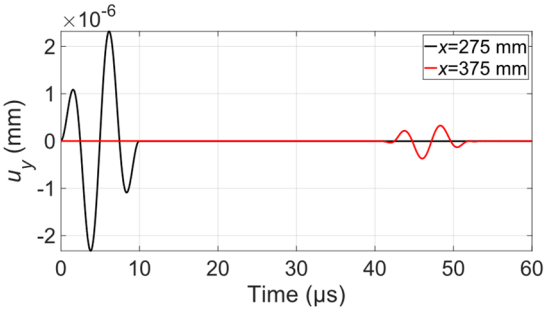

(b)

Figure 3.9 Simulation results for point-source body wave: (a) a typical y direction displacement filed at simulation time t=0.02 ms (unit: mm); (b) evolution of y direction displacements of two recorded nodes at (x=275 mm, y=75 mm) and (x=375 mm, y=75 mm).

For Case 3, a typical y direction displacement field at simulation time $t = 0.02$ ms is illustrated in Figure 3.9a. Due to the directivity of the applied wave source (applied in y direction), the intensity of the wave front is biased in different propagation directions. The P- and S-waves are dominant in y and x directions, respectively. Figure 3.9b shows the evolution of displacements in y direction of two recorded nodes at ($x = 275$ mm, $y = 75$ mm) and ($x = 375$ mm, $y = 75$ mm). It can be seen that the amplitudes of point-source wave decrease with increasing the wave travel distance due to geometric spreading loss (or wave radiation) (Gresil and Giurgiutiu 2015). Moreover, the waveform is slightly altered due to the directional dependency of Poisson's ratio in the lattice model. A more detailed discussion about the influence of material anisotropy on the waveform alternation can be found in (Iturrioz and Riera 2021).

For Case 4, a typical y direction displacement field at simulation time $t = 0.04$ ms is illustrated in Figure 3.10a. P-, S- and R-waves are coexisted in this case with the intensity of R-wave being dominant. Figure 3.10b shows the evolution of displacements in y direction of two recorded nodes at ($x = 275$ mm, $y = 150$ mm) and ($x = 375$ mm, $y = 150$ mm). The R- and S-waves are superposed due to their similar velocities, which brings the difficulty in determining the arrival time and thus velocity of R-wave. Moreover, the amplitude of R-wave decreases with increasing of the wave travelling distance due to the geometric spreading loss. In isotropic and homogeneous media, R-wave follows a circular and cylindrical spreading loss for 2D and 3D cases, respectively (Yang, Cascante, and Polak 2011). For the undamped R-waves modelled here ($\alpha = \beta = 0$), by substituting $\eta_0 = 0.5$ and $\eta(\omega) = 0$ into Equation (3.8), the ratio between two R-wave peak amplitudes, $A_i(\omega)$ and $A_j(\omega)$, received at two different locations i and j, respectively, with distances of r_i and r_j to the wave source is described as:

$$\frac{A_i(\omega)}{A_j(\omega)} = \sqrt{\frac{r_j}{r_i}} \tag{3.24}$$

Figure 3.10c shows the numerical results for the peak amplitudes of R-waves received at different recorded nodes versus the distances to source, where the peak amplitudes are normalized with respect to that of a reference node at ($x = 300$ mm, $y = 150$ mm). It can be found that the numerical results fit well the theoretical curve given by Equation (3.24). Despite the consistency with the theoretical solutions, limitation of the lattice model for simulating the propagation of point-source waves should be mentioned as well. Theoretically, a circular wave front is expected for the point-source body waves propagating in two-dimensional isotropic and homogeneous media (same wave velocity in all propagation directions) (Schubert and Schechinger 2002). However, due to the variation of Poisson's ratio values in the adopted two-dimensional lattice model, the simulated wave velocities are slightly different in different propagation directions. As can be observed in Figure 3.9a and Figure 3.10a, the simulated wave fronts are distorted circles,

especially for S-waves.

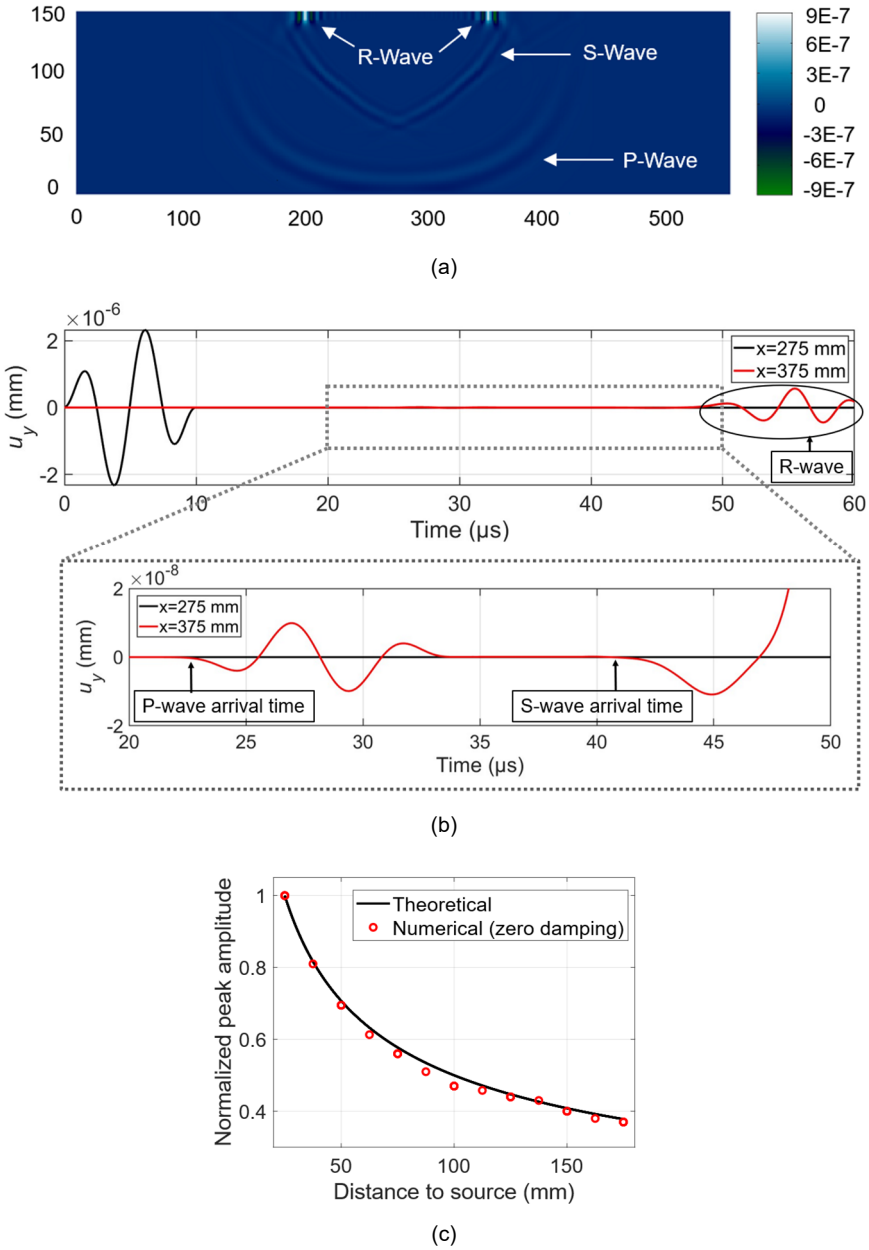

Figure 3.10 Simulation results for point-source Rayleigh wave: (a) a typical *y* direction displacement filed at simulation time *t*=0.04 ms (unit: mm); (b) evolution of *y* direction displacements of two recorded nodes at (*x*=275 mm, *y*=150 mm) and (*x*=375 mm, *y*=150 mm); (c) a comparison of geometric spreading loss of Rayleigh waves between theoretical calculations and numerical results with zero damping (α=β=0).

3.4 Influence factors on simulating undamped fracture-induced AE signals in lattice modelling

This section considers the propagation of fracture induced acoustic emission signals generated by the breakage of a lattice element. The effect of the implemented PID control algorithm and the influence of lattice grid sizes on the simulated AE waveforms are investigated. This chapter focuses on simulating elastic wave propagation, and thus a simplified simulation case is considered for demonstration. The simulation of AE waveforms in real concrete fracturing processes implementing the proposed model will be reported in next chapter.

The studied numerical model and its boundary conditions are given in Figure 3.11 and is named as simulation Case 5. The material properties listed in Table 3.1 are adopted as inputs for the numerical model. An additional 1-mm vertical element is placed at location $x = 50$ mm, $y = 150$ mm as the fracture source ($l_{(s)} = 1$ mm). The tensile softening parameters a_1, a_2 and a_3 of the fracturing element are calibrated as 5.5, 120 and 620, respectively, using listed material properties following the calibration procedure described in Figure 3.3. A positive y direction displacement $u_y(t)$ in terms of a constant velocity of 1×10^{-3} mm/s ($\mathrm{d}u_y(t)/\mathrm{d}t = 1 \times 10^{-3}$ mm$/s$) is applied at the upper node of the fracture source element to induce the fracturing of the element. The bottom nodes are fixed ($u_x = u_y = 0$) to assure force equilibrium of the system.

The PID control algorithm is implemented in the simulations. The controlling variable is the velocity of the loading node (upper node of the fracture source element) to minimize the loading bias (computational errors). The PID constants are selected as: $h_p = 0.01$, $h_i = 0.01$ and $h_d = 0.05$.

The node located at $x = 130$ mm, $y = 150$ mm is considered as a virtual AE sensor (marked as S1 in Figure 3.11). The other virtual sensors marked in Figure 3.11 (S2-S6) will be used in the simulation cases in later sections. The vertical (y direction) accelerations recorded at S1 are used to mimic the received AE signals, as received AE signals in reality are the stress waves perpendicular to AE sensor surface (Matthews 1983). A more detailed discussion about the numerical representation of AE signals will be given in Section 3.6.1. The adopted time step and numerical damping coefficients are 5×10^{-5} ms (20 MHz sampling rate) and zero ($\alpha = \beta = 0$), respectively.

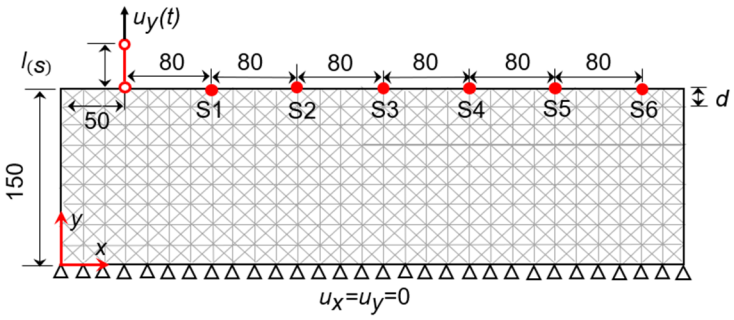

Figure 3.11 Numerical model and boundary conditions of Case 5 for simulating the AE signals induced by a fractured lattice element (unit: mm).

3.4.1 Effect of implemented PID control algorithm

This sub-section aims to to illustrate the effect of the implemented PID algorithm described in Section 3.2.2. Two simulation cases are performed with and without the PID control. The grid size is selected as 1 mm ($d = 1$ mm in Figure 3.11).

The evolution of vertical accelerations of virtual AE sensor S1 in the two simulation cases are shown in Figure 3.12, where the presented period is from the beginning of the loading process to a moment before fracturing of the source element. It can be found that by introducing the PID algorithm a stable loading process is observed and the dynamic noise in nodal accelerations is effectively suppressed comparing to the simulation case without PID control in which the nodal accelerations have a bias induced by the external loading, with non-vanishing noise signals of high amplitudes existing even in the absence of a lattice element fracture (Figure 3.12a). Similar phenomenon was also reported in the work of Minozzi et al. (Minozzi et al. 2003), where a 2D lattice model without PID control was used to simulate the dynamic fracture of quasi-brittle materials. The dynamic noises influence the computational accuracy of targeted dynamic response due to a fracturing lattice element; it also leads to the difficulty in identifying the fracture-induced AE signals with relatively low amplitudes, which is mixed by the non-vanishing noises.

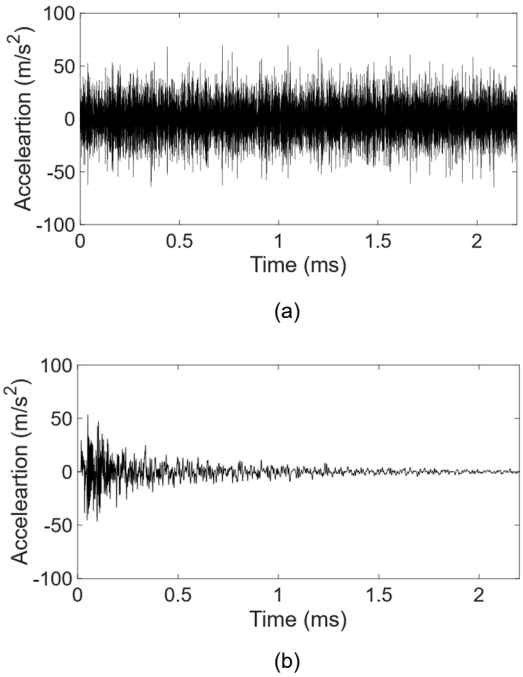

Figure 3.12 Vertical accelerations of the virtual AE sensor S1 before fracture occurring for two simulation cases: (a) without PID control and (b) with PID control.

3.4.2 Lattice model grid size & AE signal frequency resolution

As a discrete modelling approach, the grid size has a clear influence of the propagation of AE signals. To demonstrate this, several simulations are performed with varied grid sizes ($d = 1{\sim}10$ mm). The AE signal source is controlled by keeping the size of the fracture source element constant ($l_{(s)} = 1$ mm).

Figure 3.13 shows typical simulated AE signals from models with grid sizes of 1 and 10 mm. The starting time zero of AE signal presented in Figure 3.13 is not the actual simulation time but has been normalized to represent a typical pre-trigger time of 256 us (Scruby 1987a) (see Appendix A for the definition of pre-trigger time). It can be observed that the obtained AE signals are largely influenced by the grid sizes. In models with smaller grid sizes higher frequency components of an AE signal are observed. A theoretical explanation of this observation is given below.

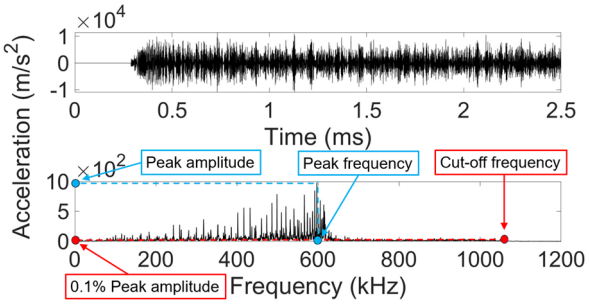

(a)

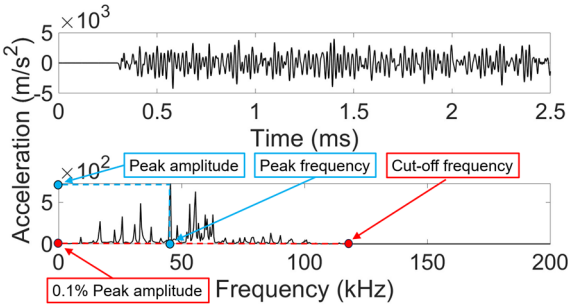

(b)

Figure 3.13 Simulated AE signals received at virtual sensor S1 for simulation cases with: (a) 1 mm and (b) 10 mm grid sizes *d* and a fixed 1 mm fracture source element size $l_{(source)}$.

The maximum frequency that a lattice model with given grid size can simulate is herein defined as cut-off frequency, denoted as f_{max}. The minimum pressure wavelength corresponding to f_{max} is denoted as $\lambda_{p(min)}$. In Figure 3.13, it should be noted that the signal amplitudes corresponding to frequencies higher than around half of the cut-off frequencies f_{max} are sharply decreased. According to the Nyquist criteria (Desoer and Wang 1980), the frequency components higher than half of the maximum frequency that can be produced by a given temporal or spatial sampling rate will lose their information (Howell, de Weck, and Miller 2008). This phenomenon is called the aliasing (Haldorsen 2020). The highest frequency without signal aliasing, herein called Nyquist frequency and denoted as f_{Ny}, is equal to half of the cut-off frequency f_{max}:

$$f_{Ny} = 0.5\, f_{max} \tag{3.25}$$

The minimum pressure wavelength without signal aliasing, herein called Nyquist pressure wavelength and denoted as λ_{P_Ny}, corresponding to the Nyquist frequency f_{Ny} is then calculated as:

$$\lambda_{P\_Ny} = \frac{V_P}{f_{Ny}} = \frac{V_P}{0.5 f_{max}} = 2\lambda_{P(min)} \tag{3.26}$$

Physically, the adopted truss elements have constant axial deformations (without bending moment), resulting in linear variation of displacement only at their nodes. Therefore, as shown in Figure 3.14a, at least four element (5 nodes) are needed to approximate (or spatially sample) a minimum pressure sine wave with wavelength $\lambda_{P(min)}$. Accordingly, as shown in Figure 3.14b, at least eight element (9 nodes) are needed to approximate the Nyquist pressure wavelength λ_{P_Ny}:

$$\lambda_{P\_Ny} = 2\lambda_{P(min)} = 8d \tag{3.27}$$

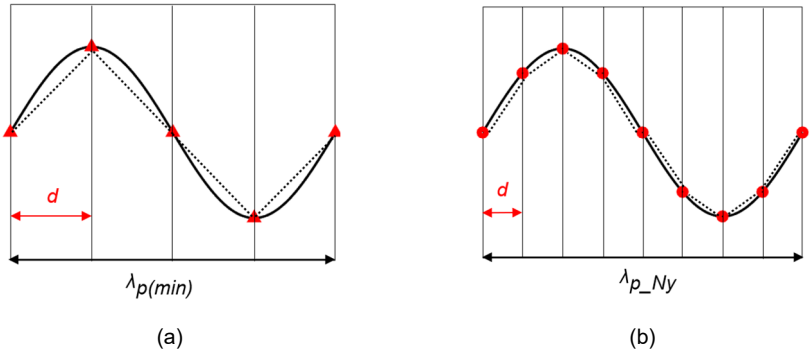

Figure 3.14 Physical interpretation for the relationships between: (a) lattice grid size *d* and the minimum pressure wavelength $\lambda_{P(min)}$ and (b) lattice grid size *d* and the Nyquist pressure wavelength λ_{P_Ny}.

By substituting Equation (3.26) into Equation (3.27), a relationship between the Nyquist frequency f_{Ny} and lattice grid size d can be established as:

$$f_{Ny} = \frac{V_P}{8d} \tag{3.28}$$

The relationship between the lattice grid sizes d and the Nyquist frequency f_{Ny} obtained from both Equation (3.28) and from lattice simulations are compared in Figure 3.15. The numerical value of f_{Ny} is calculated as half of f_{max} (Equation 3.25). The values of f_{max} from the lattice model selected as the frequency in the upper frequency range with an amplitude equal to 0.1% of the peak amplitude, as shown in Figure 3.13. It can be found that the proposed function fits well the simulation data.

The requirement defined by Equation (3.28) can be a recommendation for the selection of lattice grid size: an appropriate lattice grid size d should be selected according to the

maximum targeted AE signal frequency, denoted as $f_{\max\_targeted}$, or the minimum targeted pressure wave length, denoted as $\lambda_{P(min\_targeted)}$.

$$d \le \frac{V_p}{8 f_{max\_targeted}} \text{ or } d \le \frac{\lambda_{p(min\_targeted)}}{8} \tag{3.29}$$

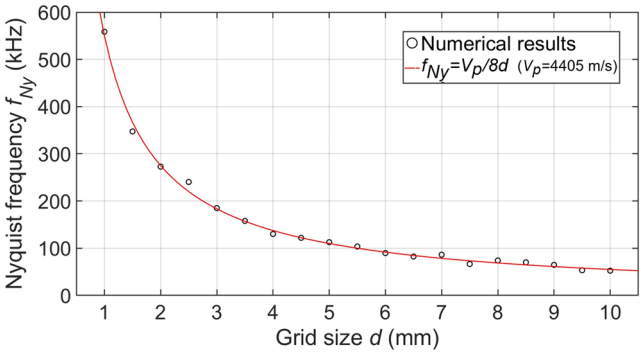

Figure 3.15 Relationship between lattice grid size d and Nyquist frequency f_{Ny} of the simulated AE signals.

3.5 Numerical damping & AE signal attenuation

In previous section, all presented numerical cases adopt a zero damping ($\alpha = \beta = 0$) to illustrate the effect of factors other than numerical damping. This section shows the relationship between numerical damping and the attenuation characteristics of simulated AE signals. The influence of Rayleigh damping coefficients on simulated AE signals is discussed in Section 3.5.1. Section 3.5.2 demonstrates the calibration and calculation procedure of the Rayleigh damping-based method for AE signal attenuation proposed in Section 3.2.3 through an experimental example.

3.5.1 Influence of numerical damping on simulated AE signals

The influence of numerical damping on the simulated AE signals is investigated with several simulation cases adopting different values of Rayleigh damping coefficients α and β. The adopted numerical model and model inputs are same with previous section (see Figure 3.11). The influence of mass proportional damping coefficients α and stiffness proportional damping coefficients β is shown in Figure 3.16 and Figure 3.17, respectively. Compared to the undamped case shown in Figure 3.13a, the simulated AE signals with various α and β values are attenuated to different extents showing a lower amplitude in time domain and less high-frequency contents in time domain.

Moreover, it is noted that the mass proportional damping coefficients α has less influence

on the simulated AE signals, while the influence of stiffness proportional damping coefficients β is more significant. Specifically, in the simulation cases with various α values and a zero β (Figure 3.16), the simulated AE signals are attenuated in time-domain showing a slightly lower amplitudes and a shorter duration, while their frequency characteristics remain similar. In the simulation cases with various β values and a zero α (Figure 3.17), the simulated AE signals are largely attenuated in both time and frequency domains, with a higher β value leading to lower amplitudes and lower upper-bound frequencies.

Traditionally, Rayleigh damping is used to describe the time-domain vibration attenuation of macroscopic structures. In such case, the mass-proportional coefficient α and stiffness-proportional Rayleigh damping coefficient β are both significant, because mass and stiffness are both structural properties that determine the structural vibration attenuation characteristics (Chowdhury and Dasgupta 2003). When applied to the case of wave propagation in current study, the situation is changed. In such case, mass is a material property of a single wave particle, while stiffness describes the interactions between different wave particles. Physically, the attenuation of elastic waves is mainly a result of interactions between microscopic wave particles (Gresil and Giurgiutiu 2015; Schubert and Herrmann 2011; Pollock 1986) and is less relevant with the mass of each wave particle. As a result, the stiffness-proportional Rayleigh damping coefficient β show a larger effect on the attenuation of high-frequency elastic waves as the case of acoustic emission.

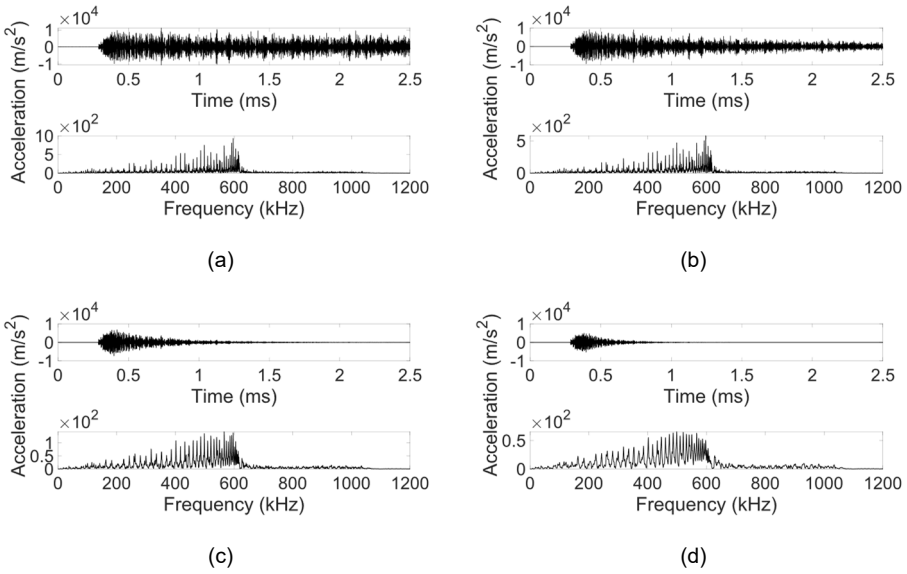

Figure 3.16 Simulated AE signals received at virtual sensor S1 with different α values and a zero β value (β =0): (a) α=100 rad/s; (b) α=1000 rad/s; (c) α=5000 rad/s and (d) α=10000 rad/s.

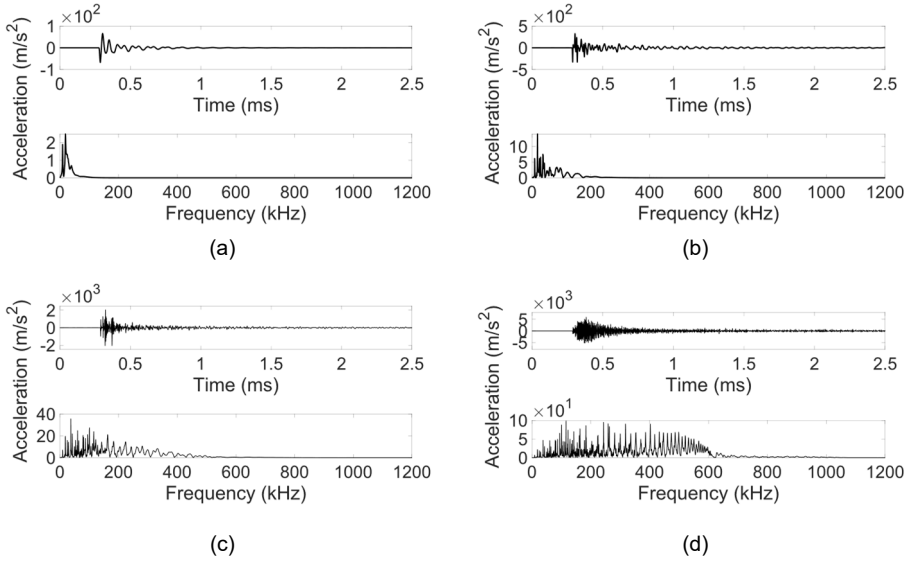

Figure 3.17 Simulated AE signals received at virtual sensor S1 with different β values and a zero α value (α=0): (a) β=1×10^{-6} s/rad; (b) β=1×10^{-7} s/rad; (c) β=1×10^{-8} s/rad and (d) β=1×10^{-9} s/rad.

3.5.2 A Rayleigh damping calibration procedure for AE signal attenuation

As shown in previous section, the values of numerical damping largely influence the attenuation characteristics and thus the waveforms of simulated AE signals. This section is dedicated to introducing a systematic test-based calibration procedure for incorporating numerical damping in the lattice modelling approach. The theoretical Rayleigh damping-based calculation method for AE wave attenuation proposed in Section 3.2.3 is demonstrated through an experiment. The Rayleigh damping coefficients α and β are determined by the experimentally obtained material damping factor $\eta(\omega)$ and the wave velocity $V(\omega)$ (Equation (3.16-3.17)). Experimental procedure for evaluating these two parameters is described in the following.

The measurement setup and the calibration specimen are given in Figure 3.18. The specimen has the same dimensions of the numerical model discussed in Section 3.4 (Figure 3.11), namely 550×150×40 mm^3. Different from the simplified model, a notch of 5-mm width and 30-mm depth is present at mid-length of the specimen. A three-point bending test will be applied on the specimen and the results of the test will be reported in next chapter of this thesis. The material properties of the specimen are the same with those used in the simulations (Table 3.1). The details of concrete mix proportions are listed in Table 3.4. The concrete has a maximum aggregate size of 8 mm and a designed strength class of C35. The modulus of elasticity E is obtained averaging measurements on three

prism specimens (100×100×400 mm^3) from the same concrete batch. The cube compressive strength $f_{c,cube}$ and mass density ρ are obtained from averaging measurements on three cubic specimens (150×150×150 mm^3) from the same concrete batch. The cylinder compressive strength f_c is converted from measured $f_{c,cube}$ according to *fib* Model Code 2010 (MC2010) (Walraven 2012). The tensile strength f_t and tensile fracture energy G_f are estimated based on the value of compressive strength f_c according to MC2010. The dynamic Poisson's ratio value of 0.24 is selected based the measurement for C35-class concrete (Pal 2019).

Table 3.4. Details of concrete mix proportions.

Material	Water	Cement	Sand	Gravel	Superplasticizer
Density (kg/m^3)	156	260	848	1123	0.25

The measurement setup consists of a transducer (marked as S0) as signal source and six R15α AE sensors with operating frequency range of 50-400 kHz (MISTRAS 2011b) (marked as S1-S6) as receivers. The signal source S0 is placed at the location ($x = 50$ mm, $y = 150$ mm) and connected to a Pundit-200 wave generator (Pundit 2021). Two types of transducers with different wavebands are used to generate source signals of different frequencies, including a dry-point-contact (DPC) S1803 transducer (10-160 kHz band width) (ACS 2023a) and a DPC S1820 transducer (150-400 kHz band width) (ACS 2023b). The receivers are installed on the top surface of the specimen with a spacing of 80 mm and are connected to a AE acquisition system (Micro-II Express Digital AE (MISTRAS 2011a)). Steel holders and silicone grease coupling agent are used for AE sensor installation to assure tight coupling between sensor and specimen. The positions of the DPC transducer and the six AE sensors on the specimen are consistent with those of the fracture source element and virtual AE sensors in the lattice model shown in Figure

To calibrate suitable Rayleigh damping coefficients that cover the operating frequency range of used R15α AE sensors (50-400 kHz), wave attenuation characteristics of lower- and upper-bound frequencies (namely 50 and 400 kHz) are tested. Specifically, squared waves of two different central frequency, namely 50 kHz and 400 kHz, were generated by the wave generator. The signals are received by the AE sensors and recorded by the AE acquisition system.

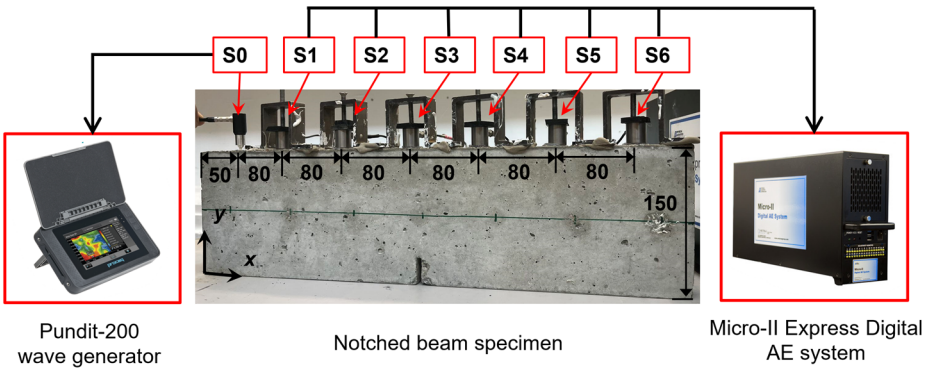

Figure 3.18 Experimental setup for AE signal attenuation tests (unit: mm).

According to the simulation case 4 in Section 3.2.3 (Figure 3.10), the AE signals received in experiments are dominated by R-waves. Its wave velocity $V_R(\omega)$ and material damping factor $\eta_R(\omega)$ are used to calculate the Rayleigh damping coefficients α and β in Equation (3.18-3.19). The values of $V_R(\omega)$ and $\eta_R(\omega)$ are evaluated based on the received AE signals. The evaluation procedure is given in the following:

A typical AE signal with 50 kHz central frequency received by AE sensor S1 is given in Figure 3.19. Two parameters can be directly obtained from the received AE signals, including the first arrival time and signal peak amplitude. The first arrival time of the signal corresponding to P-wave components is picked using the Akaike information criterion (AIC) method (Liu et al. 2017). The P-wave velocity $V_P(\omega)$ is then estimated by a linear regression between the picked first arrival time and the distances from AE sensor to source (Equation (3.21)). To reduce the picking error of AE signal peak amplitude, the amplitudes of the original signals are transformed into effective amplitudes using the average energy concept (Weaver and Sachse 1995). The effective amplitude at time t_i, denoted as $A^*_{t_i}(\omega)$, is calculated as the average squared root energy of the original amplitudes $A_{t_j}(\omega)$ in the time interval $t_j \in [t_i - \frac{\Delta t}{2},\ t_i + \frac{\Delta t}{2}]$ (Weaver and Sachse 1995):

$$A^*_{t_i}(\omega) = \sqrt{\frac{\sum_{t_j = t_i - \frac{\Delta t}{2}}^{t_j = t_i + \frac{\Delta t}{2}} \left[A_{t_j}(\omega) \right]^2}{f_{sp} \Delta t}} \tag{3.30}$$

where f_{sp} is the sampling rate. Δt is the length of predefined time interval, which is selected as twice the wave period in this study (Weaver and Sachse 1995). The effective peak amplitude of an AE signal received by an AE sensor S_i ($i = 1 \sim 6$), denoted as $A^*_i(\omega)$, is then picked as the maximum amplitude.

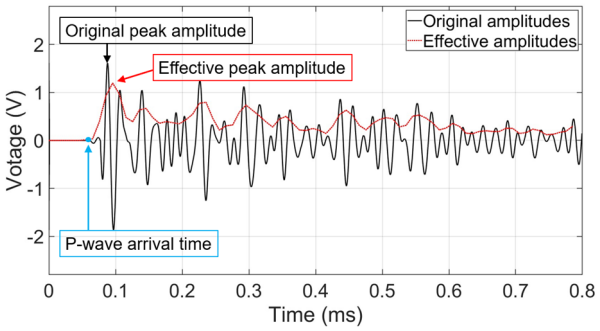

Figure 3.19 A typical 50-kHz AE signal received by AE sensor S1.

Wave velocity $V_R(\omega)$ and material damping factor $\eta_R(\omega)$ of dominating R-waves are then indirectly evaluated using the experimentally obtained P-wave velocity $V_P(\omega)$ and the effective peak amplitudes $A_i^*(\omega)$.

Since the Rayleigh wave velocity $V_R(\omega)$ cannot be accurately determined from experiments (see Figure 3.10b), it is estimated by Equation (3.31) (Morelli and Dziewonski 1993) based on the measured $V_P(\omega)$. The $V_R(\omega)$ are estimated as: $V_R(\omega_{min}) = 2285\ \mathrm{m}/s$ for $\omega_{min} = 2\pi \times 50$ kHz and $V_R(\omega_{max}) = 2349\ \mathrm{m}/s$ for $\omega_{max} = 2\pi \times 400$ kHz.

$$V_S = V_P\sqrt{\frac{1-2\upsilon}{2(1-\upsilon)}} \tag{3.31a}$$

$$V_R = \frac{0.87+1.12\upsilon}{1+\upsilon}V_S \tag{3.31b}$$

The frequency-dependent material damping factor of Rayleigh waves $\eta_R(\omega)$ is calibrated using Equation (3.9). Specifically, by selecting AE sensor S1 as a reference, the relative drop of peak amplitude due to material damping received by an AE sensor $\mathrm{S_i}$ ($i = 1\sim6$), denoted as $\tilde{\gamma}_i(\omega)$, is normalized in Nepers (Np) as:

$$\tilde{\gamma}_i(\omega) = \ln\left[\frac{A_1^*(\omega)}{A_i^*(\omega)}\right] - 0.5ln\frac{r_i}{r_1} \tag{3.32}$$

In Figure 3.20, the total peak amplitude drop measured in experiments (first term in left side of Equation (3.30)) and theoretical values of the peak amplitude drop due to geometric spreading losses (second term in left side of Equation (3.32)) are plot in cross and triangle markers, respectively. The values of $\tilde{\gamma}_i(\omega)$ calculated as their difference are marked as circle symbols in Figure 3.20. The value of $\eta_R(\omega)$ is then estimated by finding

the best fitted line between the $\tilde{\gamma}_i(\omega)$ values and the distances from sensor S_i to reference S_1, $\Delta r_i = r_i - r_1$. The $\eta_R(\omega)$ values are estimated as: $\eta_R(\omega_{min}) = 1.05$ Np/m for $\omega_{min} = 2\pi \times 50$ kHz and $\eta_R(\omega_{max}) = 4.03$ Np/m for $\omega_{max} = 2\pi \times 400$ kHz. Substituting the estimated values of $V_R(\omega_{min})$, $V_R(\omega_{min})$, $\eta_R(\omega_{max})$ and $\eta_R(\omega_{max})$ into Equation (3.20), the Rayleigh damping coefficients covering a interested frequency range of $(\omega_{min} = 50$ kHz, $\omega_{max} = 400$ kHz) are calculated as: $\alpha(\omega_{min}, \omega_{max}) = 4574.1$ rad/s and $\beta(\omega_{min}, \omega_{max}) = 2.28 \times 10^{-9}$ s/rad.

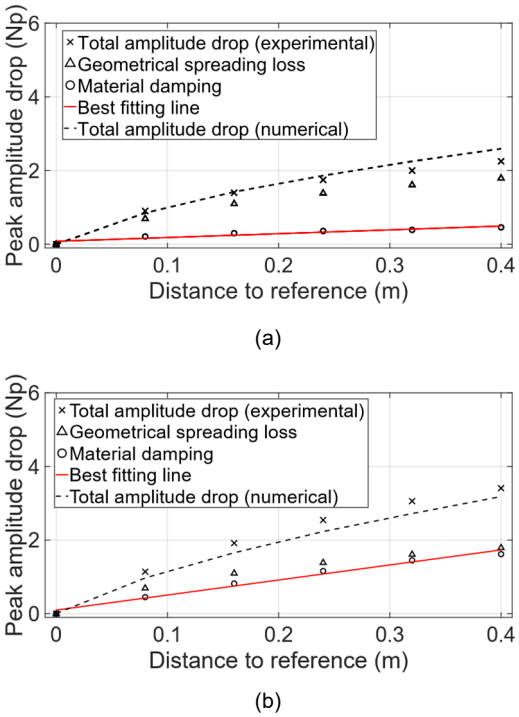

Figure 3.20 Normalized amplitude drops versus sensor distances to reference S1: (a) 50 kHz central frequency AE signals and (b) 400 kHz central frequency AE signals.

A simulation is performed adopting the Rayleigh damping coefficients obtained from the calibration process described above. The configurations of the model are similar to that of Case 5 (see Figure 3.11). The only difference is that a notch of 5-mm width and 30-mm depth is created at mid-length in the numerical model to be consistent with the physical notched beam specimen.

Figure 3.21a shows typical simulated AE signals received at virtual sensor S1 to demonstrate the effectiveness of proposed method in modelling the temporal attenuation of AE waves. In frequency domain, the high-amplitude wave components are concentrated in the frequency range of 37-446 kHz that is close to the targeted frequency range of 50-400

kHz. The amplitudes of other frequency components are largely attenuated.

The effectiveness of the proposed method in modelling the spatial attenuation of AE waveforms is further examined by examining the attenuation of narrow-banded wave components at 50 and 400 kHz respectively. The two wave components with 50 and 400 kHz as their central frequencies are extracted using the second-order Butterworth band-pass filter (Hussin, Birasamy, and Hamid 2016) with a 10-kHz bandwidth, as shown in Figure 3.21b. The peak amplitudes of these two extracted waves are marked in dashed line in Figure 3.20a and b. With the damping coefficients calibrated from experiments, the spatial attenuation of simulated AE signal turns out to be comparable to experimental results.

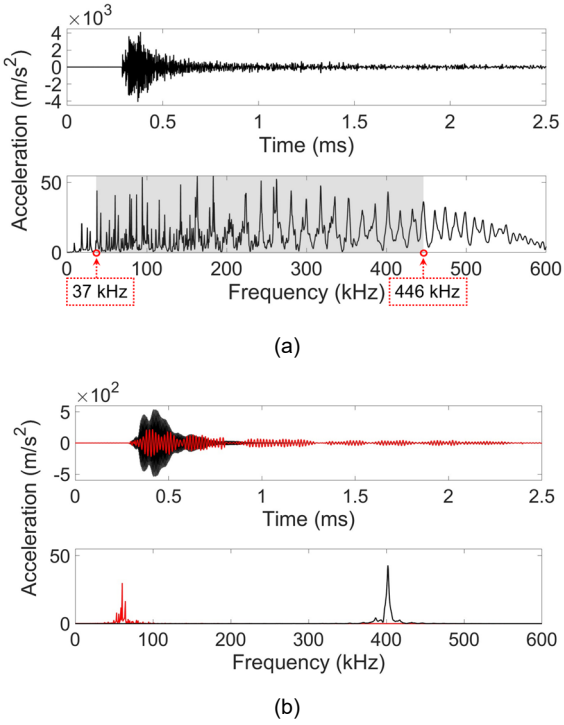

Figure 3.21 Simulated AE signals received at virtual sensor S1 with calibrated Raleigh damping coefficients: (a) original signals and (b) filtered signals (50 kHz and 400 kHz central frequency components are marked in red and black lines, respectively).

3.6 Discussion and recommendation

3.6.1 Numerical representation of acoustic emission signals: displacement, velocity or acceleration?

There is no consensus in literature on how to represent an AE signal in numerical modelling. Nodal displacement (Prosser et al. 1999), velocity (Lisjak et al. 2013a) and acceleration (Iturrioz, Lacidogna, and Carpinteri 2014) were all used to numerically represent an AE signal in literature. Figure 3.19 shows the displacements, velocities and accelerations of virtual AE sensor S1 in simulation case 5 adopting a 1-mm grid size d (see Figure 3 10). It can be observed that the nodal acceleration of the same signal contains more high-frequency components than the nodal velocity response, and the displacement response has the least.

A similar phenomenon was observed in literature that high-frequency vibration signals cannot be obtained when using displacement or velocity to represent a fracture-induced AE signal (Minozzi et al. 2003; Iturrioz, Lacidogna, and Carpinteri 2014). Different explanations were proposed for this phenomenon, e.g., attributing to the low fracture velocity of the adopted model (Lisjak et al. 2013a) or the large numerical damping values used in the simulation (Minozzi et al. 2003). A more reasonable explanation is given in the following. Consider a dynamic displacement $u(t)$ defined as a simple sine function of time t:

$$u(t) = A\sin(\omega t + \varphi) \tag{3.33a}$$

where A, ω and φ are the amplitude, angular frequency and initial phase angle. The velocity $\dot{u}(t)$ and acceleration $\ddot{u}(t)$ are expressed as:

$$\dot{u}(t) = A\omega\sin\left(\omega t + \varphi + \frac{\pi}{2}\right) \tag{3.33b}$$

$$\ddot{u}(t) = A\omega^2\sin(\omega t + \varphi + \pi) \tag{3.33c}$$

As can be seen in Equation (3.33), when the frequency of the signal increases, the amplitudes of the velocity and acceleration are proportional to ω and ω^2 times of those of the displacement, respectively. In an AE signal with multiple frequency components, it means that an acceleration signal is more sensitive to the higher frequency components than a displacement signal.

Moreover, AE sensors, whether wideband- or resonant-type, are made from piezoelectric ceramic or crystal which charges electrically in response to applied mechanical force (stress) (Matthews 1983). The electrical signals measured by an AE sensor are directly transformed from the dynamic forces (stress waves) of structure surface where the sensor is attached through piezoelectric effect. The dynamic forces measured by AE sensors are

mainly contributed by the acceleration-related inertia force, due to the much higher magnitude of acceleration than those of displacement and velocity for high-frequency vibrations. Accordingly, we suggest using accelerations to represent AE signals in lattice models. However, it should be mentioned that this is a simplified representation method, as both velocity and acceleration of particles contribute to the measured signals (e.g., wideband and resonant-type sensors measure mainly the acceleration and velocity, respectively (Grosse et al. 2021)). A more rigorous method in future studies is to explicitly model the transition process from particle motions to electric signals through implementing the piezoelectric equations.

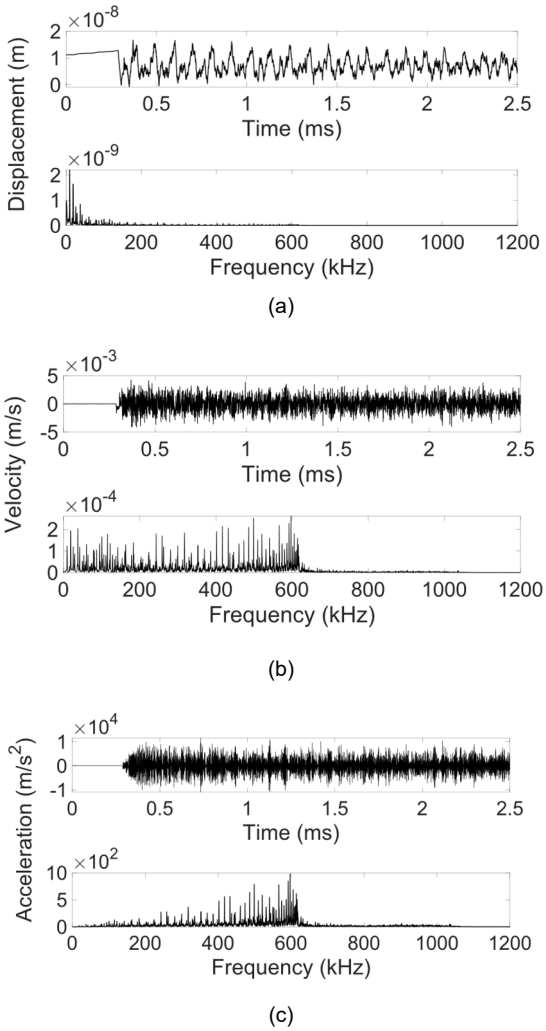

Figure 3.22 Different representation choices for AE signals: (a) displacements, (b) velocities and (c) accelerations of virtual AE sensor S1 of simulation Case 5.

3.6.2 Limitations of current study and recommendations for future study

The model developed in this study is based on a 2D truss-based square lattice network. This lattice network has inherent Poisson's ratios varying from 0.26 to 0.42 depending on loading directions, resulting in unequal velocities of elastic waves in different propagation directions (Figure 3.9). Many alternative lattice configurations have been proposed to address the constraints associated with Poisson's ratio, by using additional shear springs (Griffiths and Mustoe 2001; Cusatis, Bažant, and Cedolin 2003), beam elements (Karihaloo, Shao, and Xiao 2003; Lilliu and van Mier 2003), spring birth (Parisi and Caldarelli 2000), Kirkwood–Keating springs (Monette and Anderson 1994; Ostoja-Starzewski, Sheng, and Alzebdeh 1996) and the artificial force concepts (Baudet et al. 2007). As shown by Gerstle (Gerstle 2015), it is feasible to achieve various Poisson's ratios using a hexagonal mesh. An example of wave propagation simulation using a hexagonal lattice mesh can be found in (Suiker, Metrikine, and de Borst 2001a). In a future study, these advanced lattice networks can be adopted to better simulate the propagation of fracture-induced AE waves in the fracture process of concrete.

Additionally, this study adopts a 2D version of lattice model that cannot well simulate the wave propagation in real 3D concrete structures. In a future study, the proposed modelling framework can be adapted into a 3D lattice model (such as that developed in the work of Kosteski (Kosteski et al. 2011)) to better simulate the 3D wave propagation induced by concrete fracture process.

3.7 Summary

Developing deterministic models for quantitative AE source characterization relies upon accurately modelling the whole AE process, including the fracture sources and the induced elastic waves. Nevertheless, there is currently no available method that can simulate the complete transient waveforms of fracture-induced AE signals including their propagation. This chapter proposes a lattice modelling framework to fill this research gap with a focus on simulating the wave propagation and attenuation. The proposed approach includes the following new features:

- A proportional-integral-derivative (PID) control algorithm to control the dynamic noises other than fracture-induced response (i.e., fracture-induced AE signals) in an explicit time integration procedure.
- A Rayleigh damping-based theoretical method which has been experimentally validated to model the attenuation of AE signals.

Using the developed approach, we systematically investigate the feasibility and limitation

of lattice models for simulating propagation of AE included elastic waves. The principal findings are synthesized as follows:

- Feasibility of the lattice model for simulating elastic wave propagation is examined. The simulated pressure and shear wave velocities agree well with theoretical results. The geometric spreading loss of point-source wave can be accurately captured by the lattice model. Limitation of the adopted lattice model is that the simulated wave velocities are unequal in different propagation directions due to the variation of Poisson's ratio in the adopted two-dimensional squared lattice network.
- Effect of the implemented proportional-integral-derivative (PID) control algorithm has been demonstrated. Without the PID control, non-vanishing noise signals of high amplitudes persistently exist even in the absence of a lattice element fracturing. The PID control algorithm effectively reduces the noise signals due to external loading bias in nodal accelerations.
- A relationship is established between the lattice grid size and the frequency resolution of simulated AE signals: an appropriate lattice grid size should be no more than one eighth of the minimum targeted pressure wavelength to avoid signal aliasing.
- A theoretical method and corresponding experimental calibration procedure are proposed to determine the Rayleigh damping coefficients for modelling the attenuation of AE signals due to material damping. The proposed method has been demonstrated by an experiment; a comparison between the numerical and experimental results shows that the proposed method is able to capture the spatial and temporal attenuation of AE waveforms. The proposed method has the potential to be used in other numerical methods besides lattice modelling (e.g., finite element methods) for modelling the attenuation of AE signals generated by various sources besides fracture (e.g., stick-sliding friction along crack surfaces) in different materials besides concrete (e.g., rocks, composites or metals).

The proposed lattice modelling framework will be used in the rest of this thesis to model the complete AE waveforms in concrete progressive tensile fracturing process (Chapter 4) and to reveal the source mechanisms of AE induced by concrete tensile fracture (Chapters 6,7 and 8).

4. Lattice modelling of complete acoustic emission waveforms in the concrete tensile fracturing process

4.1 Introduction

In the previous chapter, we have proposed a framework to simulate the acoustic emission (AE) wave propagation with attenuation through a dynamic lattice modelling approach. However, as illustrated in Section 2.2, the monitored AE signals in experiments are also affected by the response of AE sensors. It is necessary to further explicitly model the sensor response to physically interpret experimental AE measurements. Therefore, this chapter develops modelling methods to further include the effect of sensor response in the proposed lattice modelling framework, leading to a completed numerical modelling framework for the whole process of tensile fracture-induced AE phenomena, including the tensile cracking-related AE sources, induced elastic wave propagation and sensor response.

The enhanced lattice modelling approach is then applied to simulate the full waveforms of AE signals measured during a tensile cracking process in concrete. Using a three-point bending test of an unreinforced concrete beam as a benchmark, this chapter further aims to validate the effectiveness of the proposed modelling framework for AE waveform simulation through comparing the simulated AE waveforms against experimental measurements.

This chapter is organized as follows. Section 4.2 introduces the proposed methods for explicitly modelling the AE sensor response. Section 4.3 details the experimental setup of the three-point bending test used for model validation. Section 4.4 describes the numerical model configuration, including the setup and input parameters for simulating the bending test, as well as the postprocessing techniques employed to extract AE hits. Section 4.5 presents a comparison between numerical and experimental results in terms of mechanical behaviour, AE hit distribution during loading, representative AE waveforms, statistical patterns, and spatial variation of AE parameters. Section 4.6 discusses the observed discrepancies in certain AE parameters between numerical and experimental results, outlines limitations of the current model, and suggests possible improvements for more accurate simulation of tensile fracture-induced AE waveforms.

4.2 Modelling methods for sensor response

As reviewed in Chapter 2, the AE sources-induced elastic waves travelling within structures are transformed into electric AE signals through AE sensors. To interpret the AE signals measured in experiments, this section proposes methods to explicitly model the sensor response. The effects of sensor response include the sensor geometry and sensor frequency-response sensitivity, which both affect the monitored AE signals. In the following, we introduce modelling techniques for considering these two aspects.

4.2.1 Modelling of sensor geometry

A typical AE sensor is illustrated in Figure 4.1a. The output of AE sensors comes from the average disturbance over the entire sensor surface, which is called "aperture" effect (Grosse et al. 2021) (see Appendix C for more detail). Therefore, the basic idea of explicitly modelling the effect of sensor geometry is to calculate the average amplitudes over the sensor covering surface in time domain.

As shown in Figure 4.1b, a monitored AE signal is the out-of-plane response (y direction in Figure 4.1a) of a 2D covering area of an AE sensor (x-z plane in Figure 4.1b), which cannot be strictly modelled in the proposed 2D lattice model. Alternatively, we use a 1D line in lattice model (x direction in Figure 4.1b) to represent the 2D sensor area (x-z plane in Figure 4.1b). The average y-direction response of the nodes in the x-direction 1D line is then used to numerically represent AE signals.

Moreover, as shown in Figure 4.1c, the nodes included in the 1D line have varied sizes of represented 2D areas (gray area in Figure 4.1c) due to the circular shape of sensor surface. Therefore, to account for the 2D circular geometry of AE sensor bottom surface, an area-based weight function is further assigned to each selected bottom node distributed in a 1D line. Specifically, the weighted average accelerations in y-direction of each selected bottom node group, denoted as $\bar{A}$, are used as a numerical representation of AE signals and calculated as follows:

$$\bar{A} = \sum_{i=1}^{n} q_i A_i \tag{4.1a}$$

$$q_i = \frac{s_i}{S} = \frac{2\int_{x_i-\frac{d}{2}}^{\min(x_i+\frac{d}{2},\ \frac{D}{2})} \sqrt{\left(\frac{D}{2}\right)^2 - x^2}\,\mathrm{d}x}{\pi\left(\frac{D}{2}\right)^2} \tag{4.1b}$$

where n is the number of selected nodes included in each virtual sensor. q_i and A_i are the weight and y-direction accelerations of node i, respectively. s_i is the representing area of

node i in the circular sensor surface. S and D are the area and diameter of sensor bottom surface. d is the distance between two neighboring nodes (namely lattice grid size). x_i is the distance from node i to the center of sensor surface.

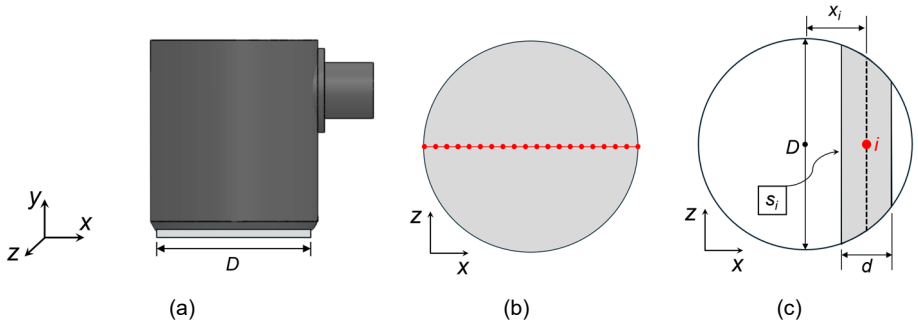

Figure 4.1 Illustration for modelling of sensor geometry: (a) a typical AE sensor with diameter of D, (b) selection of nodes to represent a sensor surface and (c) parameters to calculate numerical AE signals.

4.2.2 Modelling of sensor frequency-response sensitivity

In the experiments, the original elastic waves induced by concrete fracture are further transmitted into electrical signals by AE sensors through piezoelectric effect (Manbachi and Cobbold 2011). In the transformation process, the information of original elastic waves is partially lost and thus altering the waveforms, due to the frequency-response sensitivity of AE sensors, herein called "sensor effect" (Hamam et al. 2021; Hamam et al. 2019).

To more accurately model the waveforms of monitored AE signals, the "sensor effect" should be considered in the lattice modelling. In the following, we use a typical AE sensor type, R15α AE sensors (MISTRAS 2011b), to exemplify the modelling procedure of the "sensor effect".

Figure 4.2a shows the frequency-response sensitivity spectrum of the R15α AE sensors, where the red and blue curves are the frequency-response sensitivity of R15α sensor in response to pressure (acceleration)- and velocity-type of surface motions, respectively (McLaskey and Glaser 2012). As we consider nodal acceleration as numerical representation of AE signals (see also Section 3.6.1), the red frequency-response sensitivity curve in Figure 4.2a is considered herein.

We then transform the frequency-response sensitivity spectrum into a normalized sensitivity function $I_{sensor}(\omega)$, as shown in Figure 4.2b. The maximum function value 1 (maximum sensitivity) of $I_{sensor}(\omega)$ is achieved at the central frequency of the R15α sensors and the function values are reduced for other frequency components.

To accounting for the "sensor effect", the numerical AE waveforms considering only the normalized sensor geometry $\bar{A}(\omega)$ calculated by Equation (4.1) are further convoluted with the normalized sensor sensitivity function $I_{sensor}(\omega)$ in frequency domain as:

$$A_{sensor}(\omega) = \bar{A}(\omega) \times I_{sensor}(\omega) \tag{4.2}$$

where $A_{sensor}(\omega)$ denotes the amplitude of numerical AE waveforms with complete "sensor effect", namely considering both sensor geometry and sensor frequency-response sensitivity.

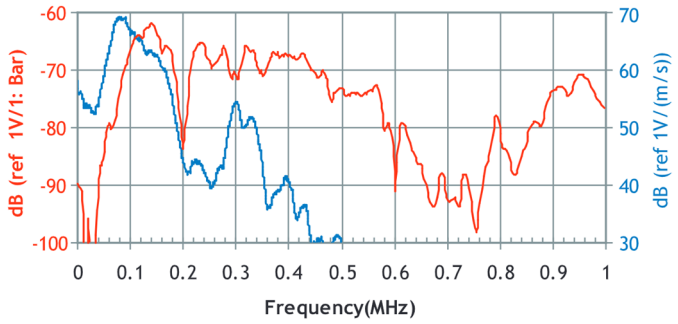

(a)

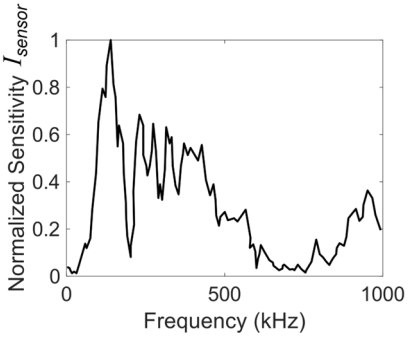

(b)

Figure 4.2 An example for obtaining $S(\omega)$: (a) frequency-response sensitivity of used R15α AE (adapted from (MISTRAS 2011b)) and (b) normalized sensor sensitivity function $I(\omega)$.

4.3 Experimental benchmark

The enhanced lattice model is benchmarked by a three-point bending test. The experimental setup is described in this section.

A three-point bending test is conducted on the same notched beam specimen that has been used for wave attenuation tests in Section 3.5.2, with dimensions of 550×150×40 (length × width × thickness) mm^3 and a notch of 5-mm width and 30-mm depth at mid-length (see Figure 3.18). The small thickness value of 40 mm is designed to minimize the difference of wave propagation in thickness direction between the physical and corresponding numerical specimens, as the lattice model is currently restricted to 2D simulation. Only waves with wavelength longer than 40 mm are considered in the measurement.

Material properties and concrete mixture design of the considered beam specimen are listed in Table 3.1 and Table 3.4, respectively. Tests and calculation of listed material properties have been detailed in Section 3.5.2.

The setup of three-point bending test is shown in Figure 4.3. Two linear variable differential transducers (LVDT) are installed across the notch on front and back surfaces (marked as LVDT1 and LVDT2 in Figure 4.3) to measure the crack mouth opening displacements (CMOD). The test is conducted under CMOD control at a prescribed CMOD rate of 1×10^{-6} m/s using the average measurements from LVDT1 and LVDT2 as feedback. The mid-span deflection of the beam specimen is measured by another LVDT, marked as LVDT3 in Figure 4.3.

The AE sensor layout is shown in Figure 4.3b. A total of seven sensors are used to record the AE signals in the whole three-point bending test, including three R15a AE sensors (MISTRAS 2011b) (marked as S1-S3 in Figure 4.3b) and four R15a AE sensors on the specimen front side (marked as S4-S7 in Figure 4.3b). All sensors are glued by hot melted adhesive due to lacking additional space for installing sensor holders.

The acquisition of AE signals is performed using a 32-channel Micro-II Express Digital AE system (MISTRAS 2023). Pencil-leak break (PLB) tests are conducted for each sensor before the main tests to assure sensor sensitivity and the proper settings of AE monitoring system. The threshold and sampling rate for AE acquisition are initialized as 45 dB and 5 MHz, respectively. The peak definition time (PDT), hit definition time (HDT) and hit lockout time (HLT) are set as 300, 600 and 1000 µs, respectively (PAC 2005). The waveforms corresponding to each AE hit are saved by the acquisition system for further analysis, with a 256 µs pre-trigger time and a 1.6 ms waveform recording length. The definition of AE parameters mentioned in this dissertation is given in Appendix A.

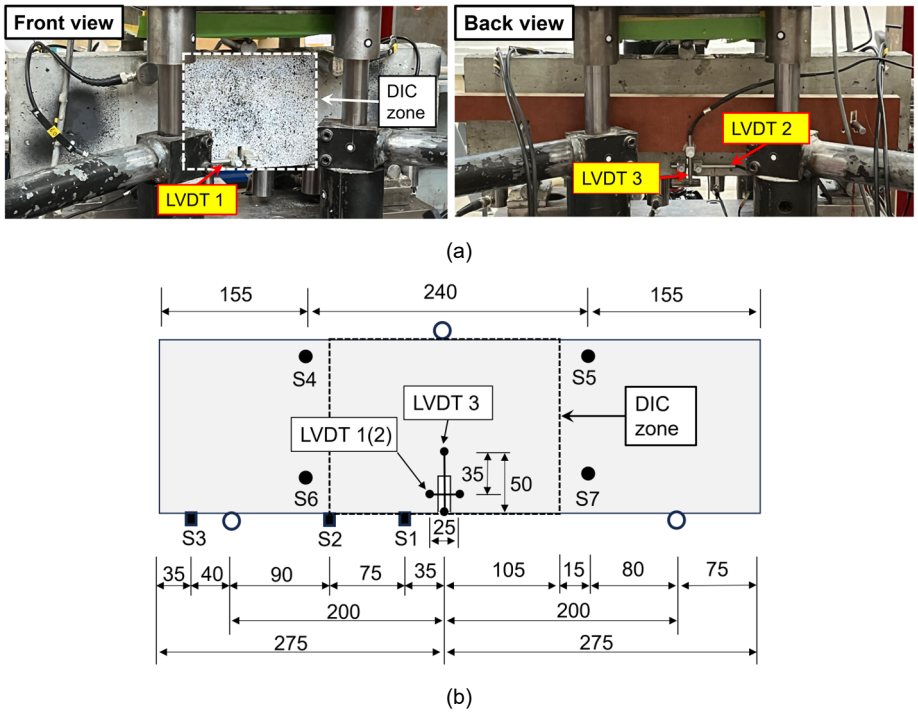

Figure 4.3 Three-point bending test: (a) experimental setup; (b) schematic view of sensor locations (unit: mm).

The digital image correlation (DIC) technique is applied in the three-point bending test to record images of specimen surface in the loading process, which are further processed to obtain surface cracking patterns. The area painted with speckles on the front surface of the notched beam, marked by dash lines in Figure 4.3, is selected as the DIC measuring zone. The DIC setup is shown in Figure 4.4, which is consisted of a flash and a 51 Megapixel camera with 8688 × 5792 pixels to record images with a resolution of 0.125 mm/pixel. The DIC sampling rate is selected as 1 Hz (1 image per second) to capture crack kinematics. The principle of DIC technique is to obtain the displacement filed through the correlation between images recorded at different loading time. The displacements are further processed to calculate the strain fields. The calculation process of strain fields from images measured by DIC technique can be found in the work of Pan (Pan 2011).

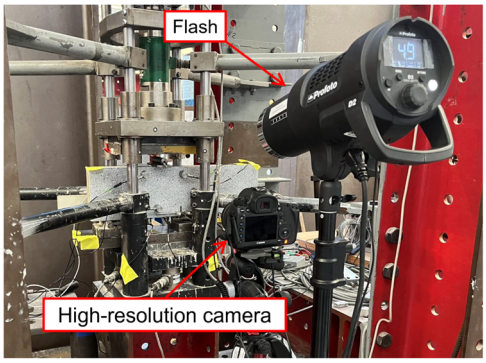

Figure 4.4 DIC measuring setup.

4.4 Description of adopted numerical model

This section describes the setup and input parameters of built numerical model, and the output setting and postprocessing methods for numerical AE signals.

4.4.1 Model overview

The geometry and boundary conditions of built numerical models are shown in Figure 4.5. The grid size d is selected as 1 mm to achieve a frequency resolution up to 512.5 kHz, which is wider than the 50-400 kHz operating frequency range of experimentally used R15a AE sensors. This estimation is based on Equation (3.27) for the relationship between lattice grid size d and maximum targeted AE signal frequency $f_{\max\_targeted}$. 5

The material properties listed in Table 3.1 are adopted as inputs for the numerical model. The tensile softening parameters a_1, a_2 and a_3 are calibrated as 5.5, 120 and 620, respectively, for 1 mm orthogonal lattice elements following the calibration procedure described in Figure 3.3 (see also the work of Aydin et al. (2018)). The softening parameters of $\sqrt{2}$ mm diagonal elements are regularized by dividing $\sqrt{2}$ according to Figure 3.2a, to assure a same fracture energy of orthogonal and diagonal elements (see Section 3.2.1 for more details about fracture energy regularization in adopted lattice model).

The Rayleigh damping coefficients are calibrated as: $\alpha(2\pi \times 50\text{kHz}, 2\pi \times 400\text{kHz}) = 4574.1\ \text{rad/s}$ and $\beta(2\pi \times 50\text{kHz}, 2\pi \times 400\text{kHz}) = 2.28 \times 10^{-9}\ \text{s/rad}$, to cover the 50-400 kHz operating frequency range of experimentally used R15a AE sensors. The calculation method and experimental calibration procedure of adopted Rayleigh damping coefficients are detailed in Section 3.2.3 and Section 3.5.2, respectively.

The left and right supports are pinned ($u_x = u_y = 0$) and hinged ($u_y = 0$) boundary conditions, respectively. The CMOD loading condition in the experiment is reproduced in

the simulation by implementing the PID control algorithm (see Section 3.2.2 for details about implemented PID control). Two nodes (marked red in Figure 4.5) with same coordinates of the centers of two installation holders of LVDT1(2) in the experiment (Figure 4.3) are selected as controlling nodes. The rate of horizontal (x-direction) displacement difference between two controlling nodes, namely CMOD rate, is used as PID control variable. The load is applied according to the selected PID control variable which is prescribed as the same value used in experiment, namely the CMOD rate of 1×10^{-6} m/s. The PID constants are selected as the same values used in experiment: $h_p = 0.01$, $h_i = 0.01$ and $h_d = 0.05$. The time step is selected as 2×10^{-7} s in the explicit integration procedure to be consistent with the 5 MHz sampling rate used in experiments.

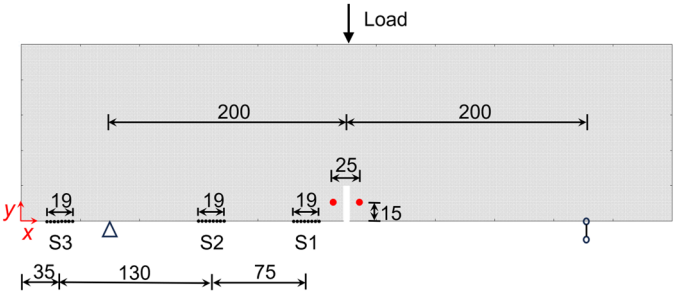

Figure 4.5 Overview of numerical model (unit: mm).

4.4.2 Postprocessing of simulated AE signals

Herein, we explicitly model the waveforms of sensors S1-S3 for experimental validation, while the results of the remaining sensors S4-S7 will be used for AE event localization.

For sensors S1-S3, the y-direction accelerations of bottom nodes located in the covering area of experimentally used AE sensors (see Figure 4.5) are used to represent numerical AE signals, as AE signals received in experiments are the stress waves perpendicular to sensor surfaces (see Section 3.6.1 for details about numerical representation of AE signals).

For sensors S4-S7, the x-direction (horizontal) accelerations of nodes located in the covering surfaces of AE sensors are considered as numerical AE signals. The reason to select x-direction nodal motions as numerical AE representation herein is that there is no out-of-plane direction (the direction perpendicular to sensor surface) response in 2D simulation, and the x-direction deformation is dominant compared to that of y direction (vertical) in the three-point bending test.

The simulated AE signals represented by nodal accelerations are continuous waveform flows in time domain. A numerical waveform flow in terms of y-direction accelerations of a single node located in the center of AE sensor S1 is shown in Figure 4.6, where each

sudden jump in accelerations (vertical lines) is an AE hit induced by the breakage of lattice elements. A typical numerical AE waveform (the last AE hit in the loading process) is shown in the zoomed-in subfigure of Figure 4.6.

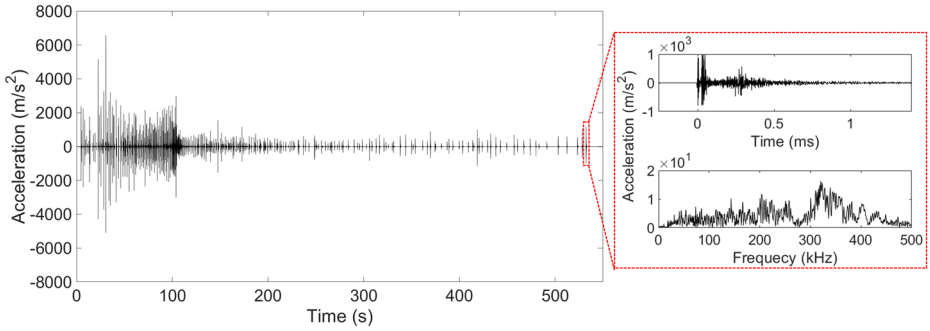

Figure 4.6 Simulated AE signals (represented by *y*-direction nodal accelerations) received by a single node located in the centre of AE sensor S1.

In the following, we describe the output setting for modelling the geometry and sensitivity response of AE sensors and introduce methods for extracting AE hits.

4.4.2.1 Sensor response

The sensor response, including sensor geometry and frequency-response sensitivity, is explicitly modelled following the procedure detailed in Section 4.2.

The parameters for modeling sensor geometry are specified here. The dimensions of experimentally used R15α AE sensor are 19 mm × 22.4 mm (diameter × height) (MISTRAS 2011b), namely D =19 mm in Equation (4.1). Accordingly, a total of 20 bottom nodes are included in the covering surface of each virtual AE sensor (Figure 4.5b) in the adopted 1-mm lattice grid level, namely n =20 in Equation (4.1). Throughout the main text of this chapter, we only consider the geometry of used R15α AE sensor to compare with the experimental benchmark. A detailed parametric analysis on more sensor geometry cases and corresponding physical interpretation is given in Appendix C.

An example of the numerical AE waveforms (corresponding to the last AE hit in the loading process in Figure 4.6) recorded by sensor S1 is given in Figure 4.7, in terms of the accelerations of a single node in sensor centre (Figure 4.7a), the weighted average accelerations of multiple nodes calculated by Equation (4.1) considering only sensor geometry (Figure 4.7b) and those calculated by Equation (4.2) with complete "sensor effect" (Figure 4.7c).

It can be observed that the time- and frequency-domain characteristics of the numerical waveform are both altered by the geometry and frequency-response sensitivity of AE

sensors. The sensor geometry reduces time-domain amplitudes and filters high-frequency contents of the numerical waveform. Such influence of sensor geometry on time- and frequency domain responses are both physically explained in Appendix C (see Figure C.2). The frequency-response sensitivity of sensors alters the wide-band frequency response into a narrowed-band one due to the inherent characteristics of used resonant-type sensors (the R15α AE sensors).

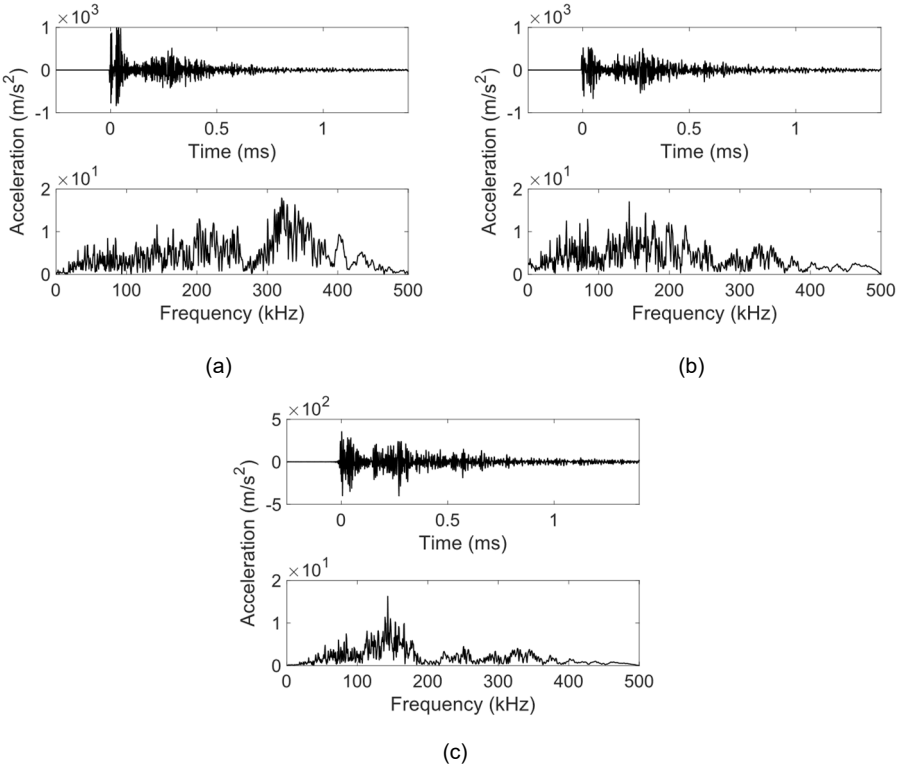

Figure 4.7 Typical simulated AE signals: (a) a raw AE signal recorded by a single node; (b) a postprocessed AE signal considering sensor geometry (b) a postprocessed AE signal with complete "sensor effect".

4.4.2.2 AE hit extraction

To isolate hit-based discrete numerical AE waveforms and calculate corresponding numerical AE characteristic parameters, the AE waveform extraction process conducted in the AE acquisition system in experiment is applied on the simulated waveform flows (see Figure 4.4). Numerical AE hits are identified in a simulated waveform flow through defining four hit definition parameters, namely threshold, PDT, HDT and HLT (PAC 2005). The numerical hit definition parameters PDT, HDT and HLT are selected as the same

values used in experiments, i.e., 300, 600 and 1000 μs, respectively. See Appendix B for the definition of the AE parameters mentioned.

For the values of numerical threshold, a trial value of $0.15\ \mathrm{m/s^2}$, which is chosen as twice the peak amplitude of numerical noises (i.e., the maximum value of accelerations in the absence of lattice element breakage in lattice simulations), is first applied to the continuous numerical waveform flows to isolate AE hits. The average values of peak amplitudes of isolated numerical AE hits recorded by virtual sensor S1 are calculated as: $753.5\ \mathrm{m/s^2}$, $626.4\ \mathrm{m/s^2}$ and $431.2\ \mathrm{m/s^2}$, respectively, for the numerical AE signals represented by a single node located in sensor center, the numerical AE hits considering only sensor geometry (obtained by Equation (4.1)) and the numerical AE hits with completed "sensor effect" (obtained by Equation (4.2)). The numerical threshold values are then evaluated by equalizing numerical and experimental ratios between threshold and average peak amplitude. Specifically, the experimental threshold and average peak amplitudes of experimental AE hits received by AE sensor S1 are 45 dB and 58.4 dB, respectively. The numerical threshold values are then calculated as: $753.5\ \mathrm{m/s^2}/(58.4-45)\mathrm{dB} = 161.0\ \mathrm{m/s^2}$, $626.4\ \mathrm{m/s^2}/(58.4-45)\mathrm{dB} = 133.8\ \mathrm{m/s^2}$ and $431.2\ \mathrm{m/s^2}/(58.4-45)\mathrm{dB} = 92.1\ \mathrm{m/s^2}$, respectively, for the three different numerical representation choices.

After identifying the numerical AE hits, numerical AE waveforms are isolated from the numerical waveform flows by adopting the same values of waveform recording parameters used in experiments, namely 256 μs and 1.6 ms, respectively, for pre-trigger time and waveform recording length. Numerical AE characteristic parameters are then calculated based on the isolated waveforms. See Appendix A for the definition of the AE parameters mentioned.

4.5 Model validation

This section compares the numerical and experimental results in various aspects, including mechanical behaviour, AE hits, typical AE waveforms, statistical distributions and spatial variation of typical AE parameters.

4.5.1 Mechanical behaviour

Figure 4.8 presents load-deflection curves of the three-point bending test obtained from both the experiment and the simulation. It can be observed that the numerical curve obtained by the lattice modelling is close to the experimental one.

The zoom-in subfigure with a gray dashed border in Figure 4.8 shows the detailed mechanical behavior around peak force, where many small fluctuations can be observed in the numerical load-deflection curve, called local snap-back instability (Carpinteri and Accornero 2018) or local stress drop (Madariaga 1977). This observation is in line with the experimental observation from Carpinteri and co-authors (Carpinteri et al. 2016).

Such local fluctuations are not obvious in the experimental load-deflection curve in Figure 4.8, which may be attributed to the much smaller sampling rate of 10 Hz used to record loading data in our experiment (the sampling rate used in the lattice simulation is 5 MHz). The relationship between AE phenomena and such local instabilities will be discussed in detail in chapter 6.

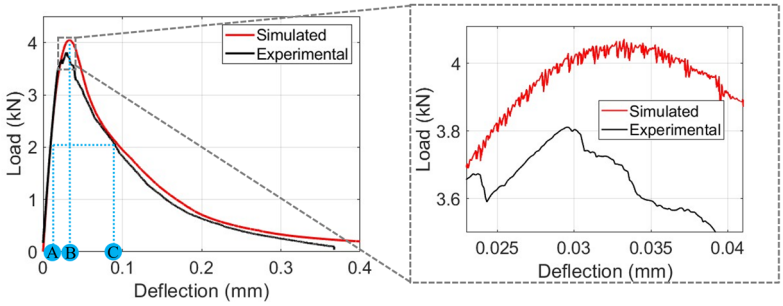

Figure 4.8 Comparison between experimental and numerical load-deflection curves.

The crack trajectory in the experiment and the simulation is shown in Figure 4.9. The numerical results are presented in terms of the x-direction strain filed (Figure 4.9a) and the distribution of broken elements (Figure 4.9b) in the loading stage corresponding to 0.4 mm mid-span deflection in Figure 4.8.

In Figure 4.9b, we use scatter diagram to represent the distribution of broken elements, with each dot representing the centre of a broken element, in order to make the broken element distribution pattern more visible and to compare with following AE event localization results. Moreover, the broken element configuration shown in Figure 4.9b are the accumulated results; an element is marked as broken once its strain exceeding ε_{cr} in certain loading stage even if it is unloaded in later loading stages. This is because that the strains of already broken elements are likely to be reduced to linear range due to locally unloading processes, since the adopted constitutive force-strain law follows an unloading path back to zero strain (see Figure 3.2a) and cannot consider the residual strains in unloading process.

It can be observed that the numerical and experimental results both show a curved crack trajectory. Such cracking trajectory is often attributed to the heterogeneity of concrete material (Ghosh, Dhang, and Deb 2020), i.e., cracks mainly developing along the mortar paste between randomly distributed aggregates in experiment. Nevertheless, the curved crack trajectory is observed in the lattice modelling without considering the concrete heterogeneity (differentiation between mortar paste and aggregates) in mesh generation.

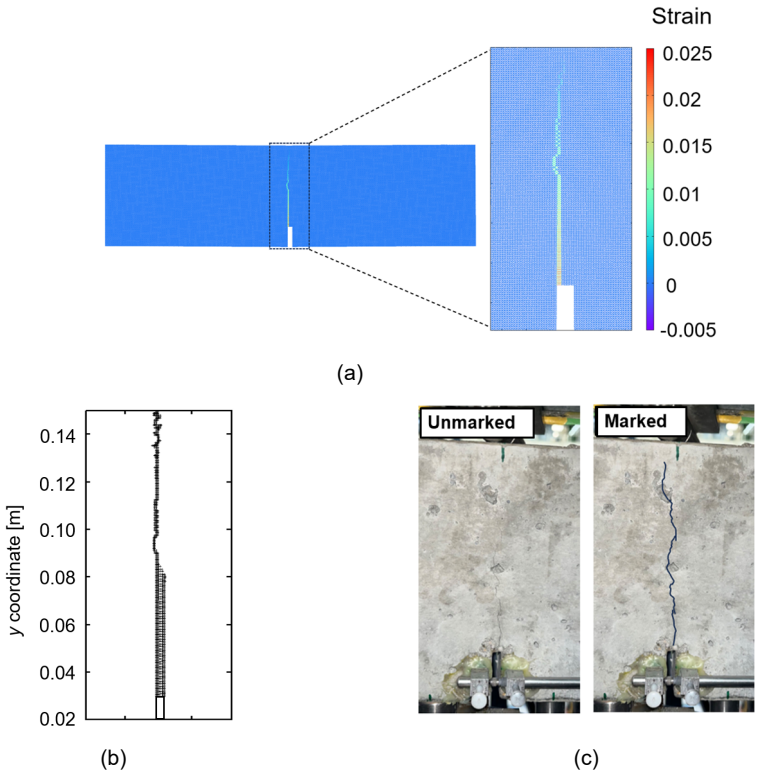

Figure 4.9 Comparison in cracking patterns: (a) final numerical cracking configuration in terms of strain field; (b) final numerical cracking configuration in terms of broken element distribution; (c) final experimental cracking configuration.

To understand the curved crack trajectory in lattice modelling, Figure 4.10 presents the evolution of numerical cracking patterns at different stages compared to the experimental results. The cracking patterns are represented in terms of *x*-direction strain fields at four different loading stages, including 50% pre-peak load, peak load, 50% post-peak load and 10% post-peak load. The experimental strain fields shown are obtained based on DIC measurements described in Section 4.3 using the GOM Correlation software (GOM 2016).

From a general point of view, the numerical and experimental results show different widths of cracking bands. The wider cracking bands in experiment are due to the restriction from the resolution of recorded images and the size of patterns painted on the specimen surface (see Figure 4.3a). The influence of DIC resolution on widths of calculated cracking bands is detailed in the work of Carroll (Carroll et al. 2013). However, it can be observed that fracture morphology and strain values are similar for experimental and numerical results in all presented loading stages.

In early loading stages, as shown in the sub-figures in last two rows of Figure 4.10, the cracks initiate at the corners of the notch due to stress concentration. It should be noted that only one crack initiate at left corner of the notch in the experiment following a curved cracking path, while two symmetric vertical cracks are observed in both corners of the notch in numerical results. This can be attributed to the imperfect loading condition and concrete heterogeneous material properties in the experiment, leading to the curved cracking shape and asymmetrical cracking distribution.

In later loading stages, as shown in the sub-figures in last two rows of Figure 4.10, the straight numerical cracking path turns into curved shapes. This can be attributed to the large displacements occurring in later loading stages. Specifically, large displacements are accounted for naturally in the proposed lattice model by adopting a Lagrangian-type solver proposed by Chung & Lee (Chung and Lee 1994) for solving motion equations (see Section 3.2.1). The iterative operation is carried out by means of coordinate updating, i.e., the deformed coordinates of the mesh after each iteration are used as the new starting coordinates, to simulate the actual deformation more realistically. Moreover, to account for the effect of stress states on local cracking behaviour, we set a same value of elastic rigidity ES^* and thus slightly different values of elastic stiffness ES^*/l for orthogonal and diagonal elements with different sizes l (see Section 3.2.1). In this way, when large displacements occurring in certain stress states in the loading process, strains are localized in the weaker diagonal elements and then the cracking propagation direction is deviated, although without considering the concrete heterogeneity (differentiation between mortar paste and aggregates) in mesh generation.

It also be noted that the numerical cracks on right side of the notch appearing in early loading stages disappear in later loading stages. This is due to locally unloading process. Specifically, during late loading stages, the strains are localized at the left side of the notch in numerical results due to different support conditions applied at two sides: the pinned support ($u_x = u_y = 0$) on left side has less degrees of freedom than the hinged support ($u_y = 0$) on right side (see Figure 4.5). The right support that is unconstrained in x direction allows the right half of the specimen to deform freely in same direction. Therefore, the already cracked elements on the right side of the notch are then locally unloaded in later loading stages when large deformation occurring, since the adopted constitutive force-strain law cannot consider the residual strains in unloading process (see Figure 3.2a).

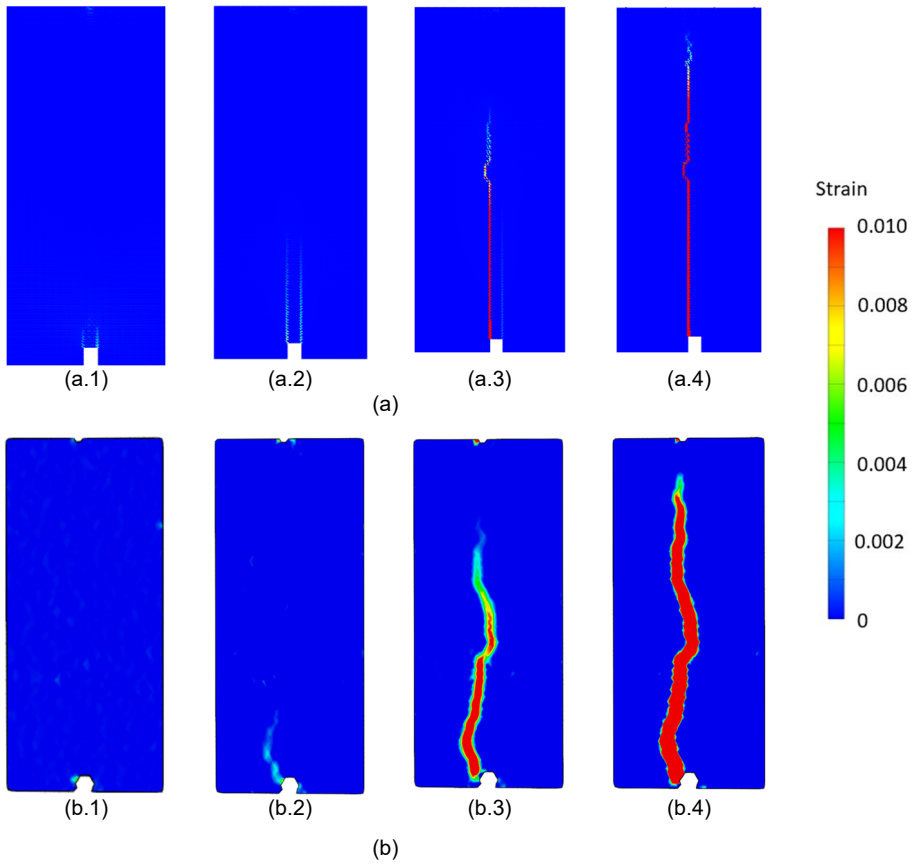

Figure. 4.10 The evolution *x*-direction strain fields at different loading stages: (a) numerical results and (b) experimental results, with (a.1) (b.1) at 50% pre-peak load, (a.2) (b.2) at peak load, (a.3) (b.3) at 50% post-peak load, (a.4) (b.4) at 10% post-peak load.

4.5.2 AE events

This sub-section compares the numerical and experimental results of AE hits and events. The numerical AE hits for different AE sensors are extracted from the simulation by following the procedure discussed in Section 4.2.2.2.

Figure 4.11 and Figure 4.12 present numerical and experimental distributions of AE hit rates and accumulated AE hit numbers, respectively, in the loading process. The analyses are based on the AE signals received by sensor S1 which has a closest distance to the crack (see Figure 4.5). Herein, AE hit rate is defined as the number of AE hits per second. A good agreement is observed between the experimental and numerical results: high AE rates and thus rapid increasement in accumulated AE hit numbers mainly occur in the loading stage of 0.01~0.15 mm mid-span deflection, with the peak values of AE rate being distributed at around the peak load. The AE activities are then gradually suppressed in

later post-peak loading stage. Such evolution trends of AE hits will be physically explained in Chapter 8.

The total number of experimental and numerical AE hits received by AE/virtual sensor S1 are 1617 and 833, respectively. The 2D lattice model produced a smaller number of numerical AE hits because the sizes of microcracks (AE sources) in the model is limited by the size of the lattice elements. It should be mentioned that it is possible to generate more numerical AE hits by using a smaller lattice grid size, due to the dependence of broken lattice element number on the lattice discretization level. The influence of lattice discretization level on AE sources and their evolution in fracturing process will be reported in Chapter 7 and 8, respectively.

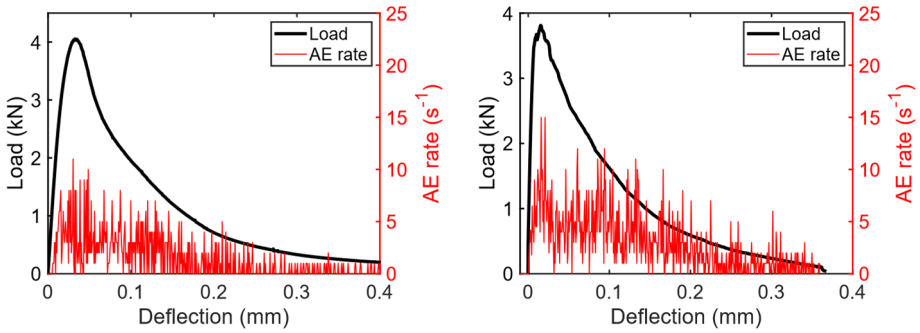

Figure 4.11 AE rate received by AE/virtual sensor S1: (a) numerical results and (b) experimental results.

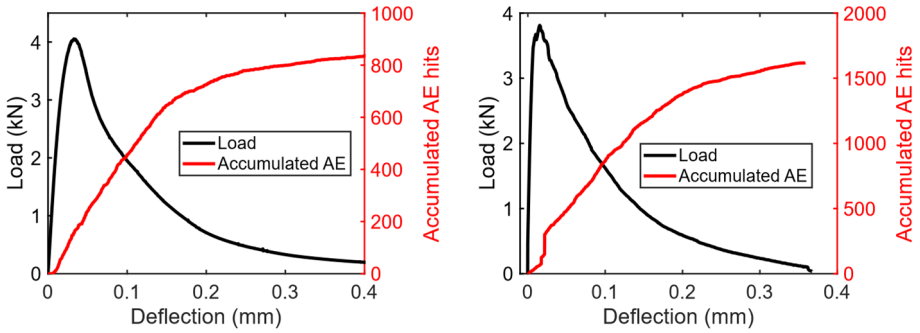

Figure 4.12 Accumulated AE hits received by AE/virtual sensor S1: (a) numerical results and (b) experimental results.

AE event localization is performed for both experimental and numerical results based on AE signals received by four AE sensors S4~S7 (see Figure 4.3). The arrival time of experimentally and numerically obtained AE signals are both determined using the Akaike information criterion (AIC) method (Liu et al. 2017). The obtained AE hits are then clustered into AE events according to their arrival time differences 139.0 μs ($\Delta t_{max} = \Delta d_{max}/V_p = 570\ \text{mm}/4100\ \text{m/s} = 139.0\ \mu\text{s}$, where Δd_{max} is the maximum sensor spacing distance) are classified into a same AE event. Only the AE events that are received by at least three sensors among S4~S7 are kept for source localization (a minimum number of three signals received at different locations are required for 2D source localization). The grid search method (Kundu 2014) is then used to determine the locations of each AE event based on the arrival time received by sensors S4~S7.

Figure 4.13 compares the numerical and experimental AE event localization results, where each dot represents the location of an AE event. The experimental and numerical results show a similar distribution pattern: larger numbers and a wider distribution width of AE events are observed along the lower height range of around 0.03~0.08 m, which is consistent with the distribution patterns of broken elements in Figure 4.9b.

Nevertheless, the experimental results exhibit a more scattered distribution than numerical results. This may be partially explained by the concrete material heterogeneity and the presence of cracks in wave travel paths in the experiment, both leading to changes in wave velocity and thus larger localization errors (the material is considered as isotropic with a constant wave velocity in the adopted AE event localization algorithm). Moreover, the scattered AE event distribution in the experiment may be caused by a wider width of experimental fracture process zone, since the width of numerical fracture process zone (broken element distribution) is restricted by the lattice discretization level (this will be detailed in Chapter 8).

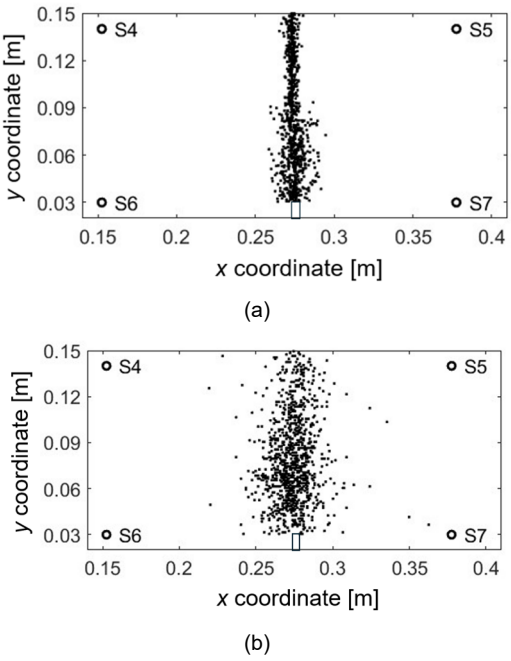

Figure 4.13 AE event localization results (unit: m): (a) numerical results and (d) experiment results.

4.5.3 AE waveforms

This sub-section compares typical AE waveforms and statistical distributions of AE parameters obtained in the experiment and lattice simulation, based on the results received by AE/virtual sensor S1.

A selection of typical numerical and experimental AE waveforms obtained by sensor S1 are shown in Figure 4.14. Three presented signals are randomly selected at around 50% pre-peak load, the peak load and 50% post-peak load (corresponding to blue circles A, B and C marked in Figure 4.8), respectively. In the main test, we only show final numerical waveform obtained by Equation (4.2) considering complete "sensor effect". Corresponding numerical waveforms in intermediate steps are given in Appendix D, including raw waveforms recorded by a single node located in sensor centre and those calculated by Equation (4.1) considering only the sensor geometry.

In Figure 4.14, it can be observed that the numerical AE waveforms with complete "sensor effect" show high similarity to experimental waveforms. In time domain, the signals show high amplitudes from 0 to around 0.2 ms and then are gradually attenuated in amplitudes. In frequency domain, the numerical and experimental waveforms both show a main frequency peak at around 150 kHz (marked red in Figure 4.14) and secondary peak at around 300 kHz (marked blue in Figure 4.14).

A comparison between Figure 4.14 and Figure D.1 (see Appendix D) reveals the role of sensor response in obtained signals. The time-domain characteristics of waveforms are mainly influenced by sensor geometry: the numerical AE signals recorded by a single node (sub-figures in first column of Figure D.1) have a shorter duration; after considering only the geometry of AE sensors, the numerical waveforms (sub-figures second column of Figure D.1) are already like experimental ones in time domain.

The frequency-domain characteristics of waveforms are largely influenced by both sensor geometry and sensor frequency-response sensitivity: the sensor geometry filters high-frequency wave components, while sensor frequency-response sensitivity narrows the response to a band around the 150-kHz central frequency of used R15α sensors. The secondary peak at around 300 kHz in numerical AE waveforms is also due to sensor frequency-response sensitivity; as shown in Figure 4.2, there is a secondary peak at 300 kHz in the frequency-response sensitivity curve of used R15α sensors.

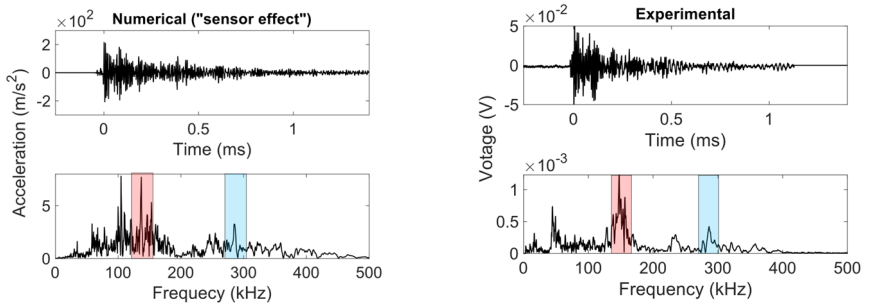

(a)

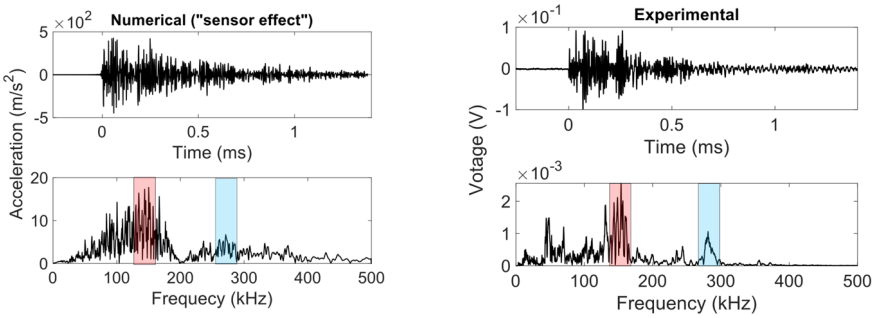

(b)

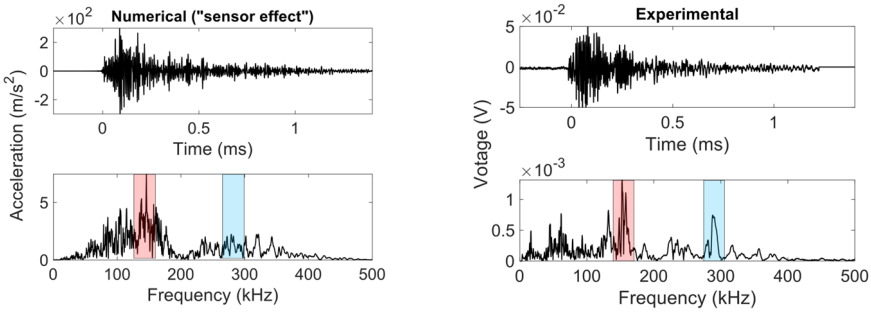

(c)

Figure 4.14 Typical experimental and numerical AE waveforms received by AE/virtual sensor S1 at (a) 50% pre-peak load; (b) peak load; (c) 50% post-peak load.

It is meaningless to conduct a point-to-point comparison between numerical and experimental signals, because even the experimental AE signals show large discrepancy in waveforms from each other, as shown in three sub-figures in second column of Figure 4.12. A statistical comparison is then conducted between all numerical and experimental AE signals obtained in the whole loading process of the three-point bending test, in terms of typical AE characteristic parameters, to further validate the effectiveness of proposed model for AE waveform simulation. The definition of AE parameters used herein can be found in Appendix A. It should be mentioned that, throughout this chapter, the statistical analyses ignore the occurrence sequence of AE signals in the loading process. The evolution of AE parameters during tensile cracking propagation processes will be analysed in Chapter 8.

Figure 4.15 compares the statistical results of typical AE parameters calculated from experimental waveforms and the numerical AE waveforms with complete “sensor effect”. The distributions of numerical AE parameters are like those of experimental ones. As shown in Figure 4.15a and b, two time-domain parameters both show a wide distribution pattern, with the percentages of two parameters descend with the increase of parameter values. The duration and rise time values are mainly distributed in the ranges of 100~500 and 0~50 μs, respectively, for both numerical and experimental results. Three frequency-domain parameters all show a similar concentrated distribution pattern, as shown in Figure 4.15c-e. The distributions of average frequency, peak frequency and frequency centroid are mainly concentrated at around 40-100 kHz, 150 kHz and 100-220 kHz, respectively, for both numerical and experimental results.

The distributions of AE parameters corresponding to numerical waveform without “sensor effect” are given in Figure D.2 in Appendix D. It can be observed that two time-domain parameters are mainly influenced by sensor geometry: the duration and rise time of raw numerical results represented by a single node (subfigure in first column of Figure D.2) are more narrowed in the ranges of smaller values, while those only considering

sensor geometry (subfigure in second column of Figure D.2) are similar to those with complete "sensor effect" (subfigure in first column of Figure 4.15). For three frequency characteristic parameters, larger difference can be observed between the numerical results using the three different representation methods. The statistical results of those represented by a single node show a much wider distribution along frequencies. The concentrated distribution pattern of frequency-domain parameters in experiments are due to the geometry and frequency response of sensors.

However, it should be noted that there is an obvious difference in three frequency parameters between experimental and numerical results. About 20% experimental signals show low values of average frequency, peak frequency and frequency centroid in the ranges of 0~40, 0~75 and 50~100 kHz (marked in red dash boxes in Figure 4.15c-e), respectively, while such low-frequency signals are not observed in the numerical simulation. A detailed discussion on possible reasons for this discrepancy is given in Section 4.6.1.

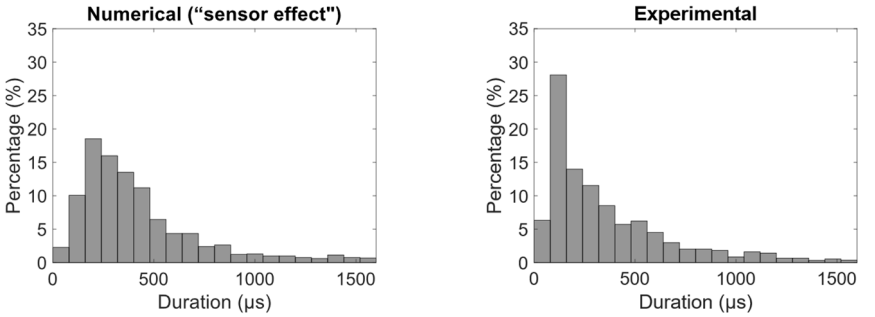

(a)

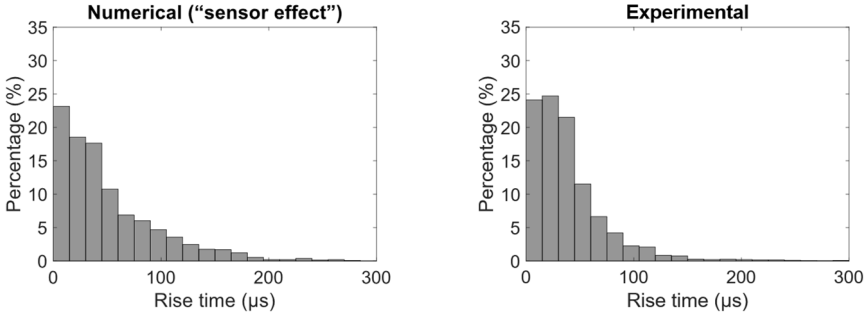

(b)

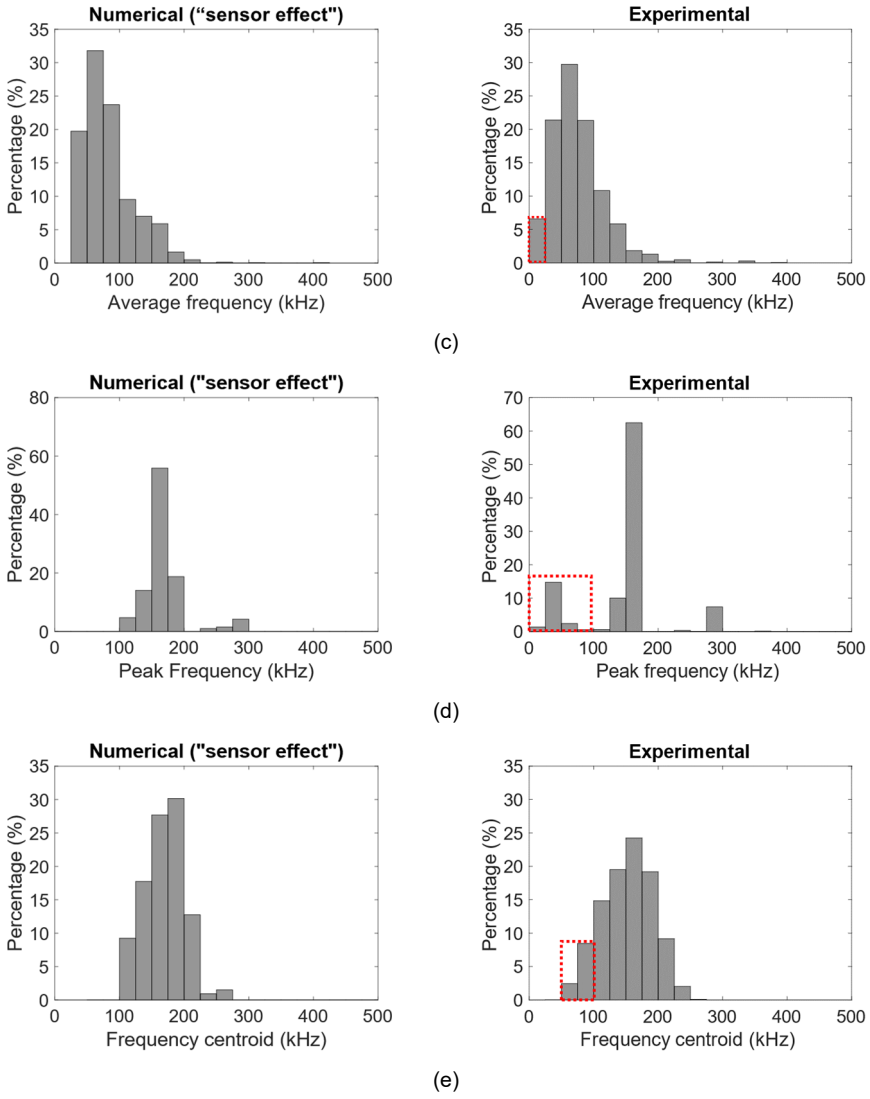

Figure 4.15 Statistical comparison between experimental and numerical AE parameters received by AE/virtual sensor S1: (a) duration; (b) rise time; (c) average frequency (d) peak frequency; (e) frequency centroid.

4.5.4 Spatial variation of acoustic emission parameters

This sub-section compares numerical and experimental results in terms of spatial variation of AE waveforms. To further evaluate the effectiveness of the developed lattice model in simulating the attenuation of AE signals propagating in concrete structures, a comparison is conducted between numerical and experimental AE signals received by

three AE/virtual sensors (S1, S2 and S3 in Figure 4.5) with various distances to fracturing sources.

Figure 4.16 shows experimental signals and the numerical waveforms with complete "sensor effect" received by three AE sensors from a typical AE event randomly selected at around the peak load (corresponding to blue circle B marked in Figure 4.8).

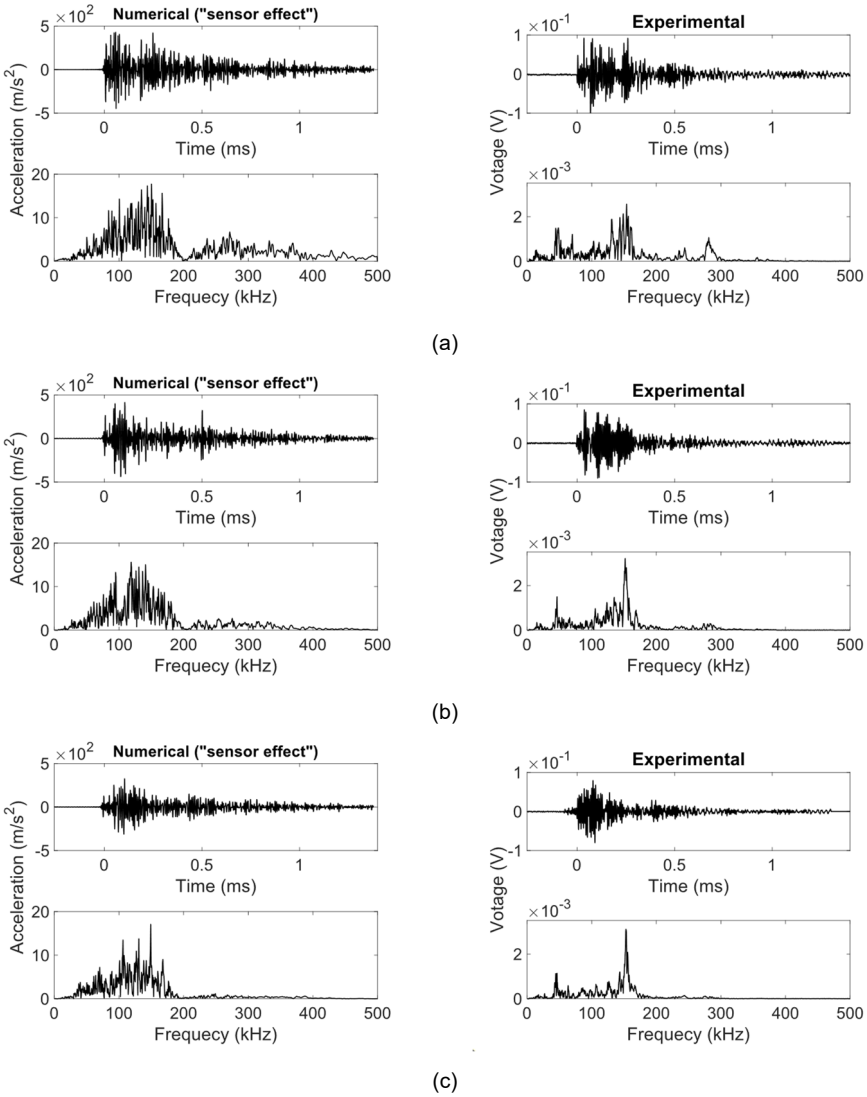

Figure 4.16 Comparison between numerical and experimental waveforms of a typical AE event received at different sensor locations: (a) sensor S1; (b) sensor S2; (c) sensor S3.

With increasing the distance from sensor to cracking source, a decreasing trend is observed in peak amplitudes in time domain and the amplitudes of high-frequency components (200~500 kHz) in frequency domain for both numerical and experimental waveforms. Moreover, it should be noted that the waveforms of sensor S3 with longest distance to source show longer rise time than sensors S1 and S2.

The numerical results in intermediate steps corresponding to those shown in Figure 4.16 are given in Figure D.3 in appendix D, including original waveforms recorded by a single node located in sensor centre and the waveforms obtained by Equation (4.1) considering only the sensor geometry. The attenuation characteristics of numerical waveforms in three different representation ways are similar, all showing a decrease in time-domain peak amplitudes and in high-frequency wave components with the increase of wave travel distance.

According to the above observations in the attenuation characteristics of typical waveforms, statistical analyses are conducted considering the changes in distributions of peak amplitudes, peak frequency and rise time of numerical and experimental AE waveforms received by sensors S1, S2 and S3.

Figure 4.17 shows the statistical change in signal time-domain peak amplitudes received at different sensor locations, for experimental signals and the numerical waveforms with complete "sensor effect". To compare numerical and experimental peak amplitudes in different units, the peak amplitude values are normalized. Specifically, the peak amplitudes of sensors S2 and S3 are both normalized relative to those of S1 in dB as:

$$\tilde{A}_{p,k} = 20\log\left(\frac{A_{p,k}}{A_{p,1}}\right) \tag{4.3}$$

where $\tilde{A}_{p,k}$ and $A_{p,k}$ are the normalized and original peak amplitudes for an AE event received by sensor S_k ($k = 2, 3$). A_1 the original peak amplitudes for an AE event received by sensor S1.

Corresponding numerical results in intermediate steps are given in Figure D.4 in Appendix D. It can be observed that the statistical distributions of numerical and experimental results are similar, and there is no large difference between the numerical results using three different representation methods. The drop in normalized peak amplitudes of waveforms received by sensor S2 and S3 are mainly distributed in the ranges of 0~6 and 3~12 dB, respectively, for both the numerical and experimental AE signals.

The major difference in time-domain amplitude attenuation between numerical and experimental waveforms is that some negative values of peak amplitude drop are observed in numerical results (those in red dash boxes in Figure 4.17). Such negative values of peak amplitude drop mean that their AE sources are closer to sensors S2 and S3 than

sensor S1, and thus corresponding signals received at S1 attenuate more due to a longer travel distance. The sources of such signals can be attributed to the friction between specimens and left support in experiments (see Figure 4.5), which are closer to sensors S2 and S3.

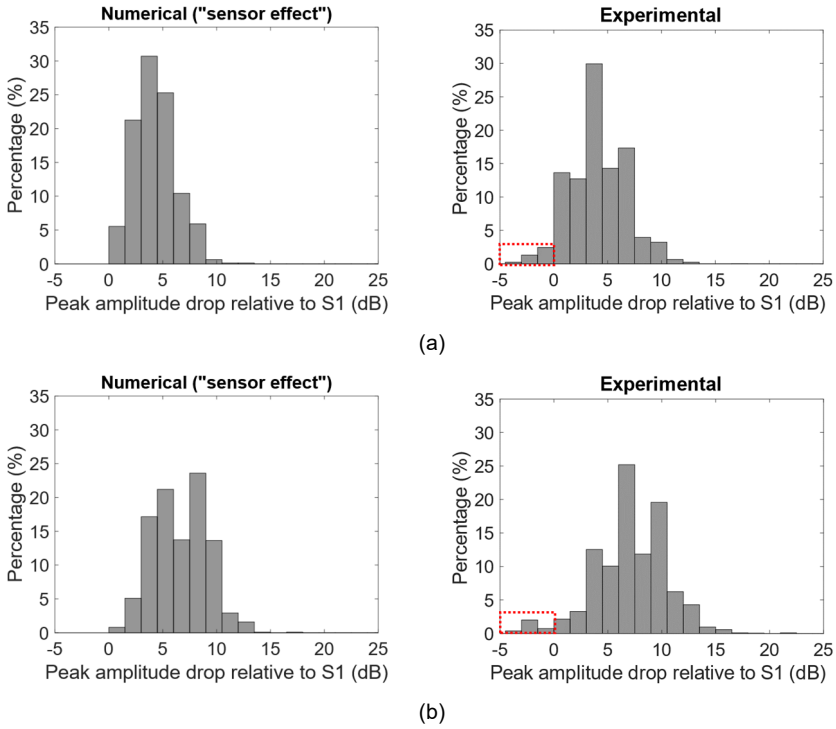

Figure 4.17 Statistical distribution of peak amplitudes of AE signals received at different sensor locations relative to sensor S1: (a) S2 and (b) S3.

Figure 4.18 shows the statistical distributions of signal rise time at different sensor locations for experimental signals and the numerical waveforms with complete "sensor effect". Corresponding numerical results in intermediate steps are given in Figure D.5 in appendix D. The experimental results and the numerical results in three different representation ways show similar variation characteristics for the rise time: the proportion of signals with longer rise time increase with increasing the wave travel distance.

Such relationship between AE rise time and wave travel distance is also observed in several experimental works reported in literature (Dong et al. 2023; Zhang et al. 2022). This can be explained by the difference in wave velocities between different wave modes. Specifically, in an AE signals, shear and surface wave components have higher amplitudes (energy) but slower wave velocities than pressure wave (see Figure 3.9 and 3.10).

The starting point of the rise time defined as first threshold crossing corresponds to pressure wave components with earlier arrival time but lower amplitudes, while ending point of the rise time defined as arrival time of signal peak amplitude corresponds to shear and/or surface wave components with latter arrival time but higher amplitudes (see Appendix A for the definition of AE rise time). Therefore, a longer signal travel distance leads to a larger difference in arrival time between different wave modes and thus a longer signal rise time.

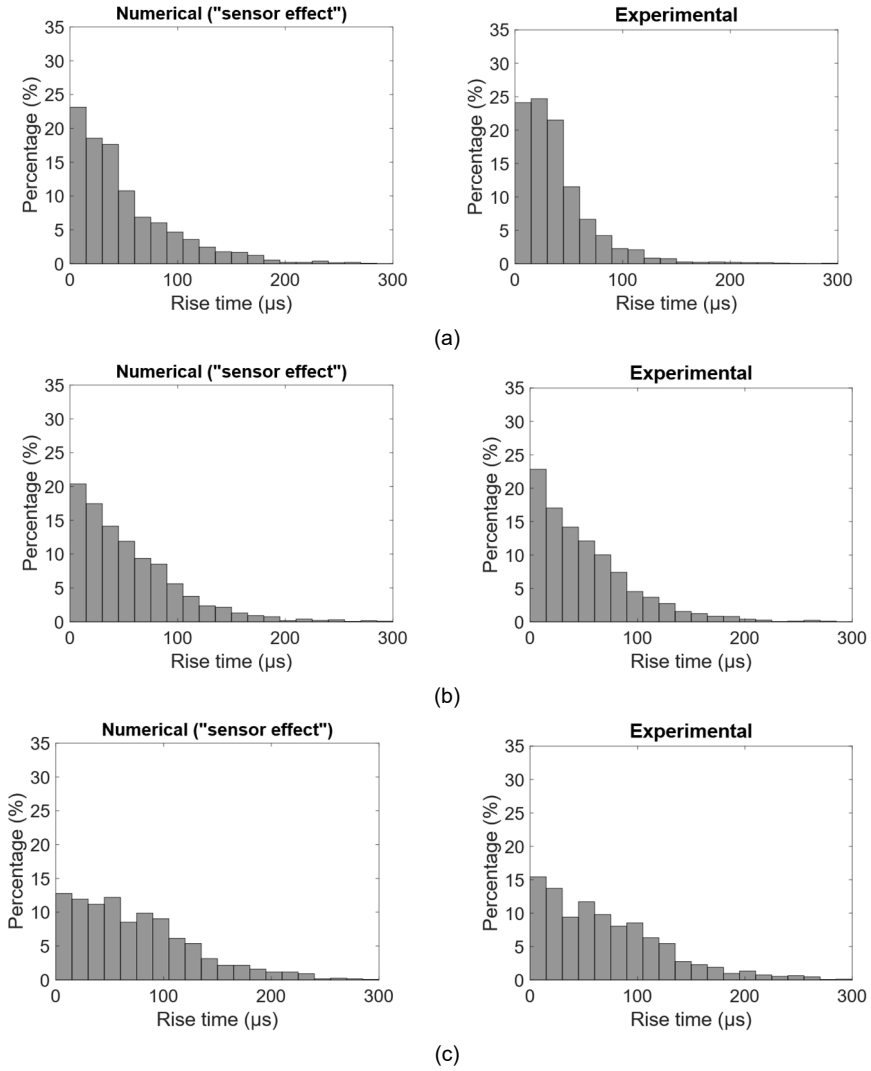

Figure 4.18 Statistical distribution of rise time of AE signals received at different sensor locations: (a) S1; (b) S2 and (b) S3.

Figure 4.19 shows the statistical results of peak frequency at different sensor locations for experimental signals and the numerical waveforms with complete "sensor effect". The variation characteristics of numerical and experimental peak frequency are similar: the percentages of AE signals with peak frequency values concentrated at around 150-kHz sensor central frequency slightly increase with increasing the distance from sensor to sources, while the percentages of signals with higher peak frequency (those at around 300 kHz marked by blue dash boxes in Figure 19a and b) are significantly reduced with increasing the sensor-to-source distance. Herein, we do not distinguish the AE signals in different loading stages; the evolution of AE peak frequency values in the loading processes will be reported in Chapter 8.

The statistical results of the peak frequency values corresponding to numerical waveforms without complete "sensor effect" are given in Figure D.6 in appendix D. Compared to above little influence of "sensor effect" on the attenuation characteristics of time-domain peak amplitudes, the geometry and frequency response of sensor show large effect on the distributions of signal peak frequency. Specifically, the numerical AE signals represented by a single node at sensor center (subfigures in first column of Figure D.6) show a larger spread discrepancy from the experimental signals. After accounting for the sensor geometry, the peak frequencies of all three sensors are narrowed to the frequency range of 100~200 kHz (second-column subfigures in Figure D.6). Such effect of sensor geometry one signals frequency characteristics is physically explained in Appendix C (see Figure C.2b).

Nevertheless, numerical waveforms obtained with three different representation choices show similar attenuation characteristics of peak frequency: the proportions of signals with high- and low- peak frequency decrease and increase, respectively, with the increase in wave travel distance.

Additionally, it should be mentioned that there is an obvious difference in peak frequency distribution between numerical and experimental AE signals for all the three sensor locations and for all the three numerical representation choices: the low-frequency signals with peak frequency at around 50 kHz (marked by red dash boxes in Figure 4.19) in experimental results do not exist in the simulations. Corresponding explanations are given in Section 4.6.1.

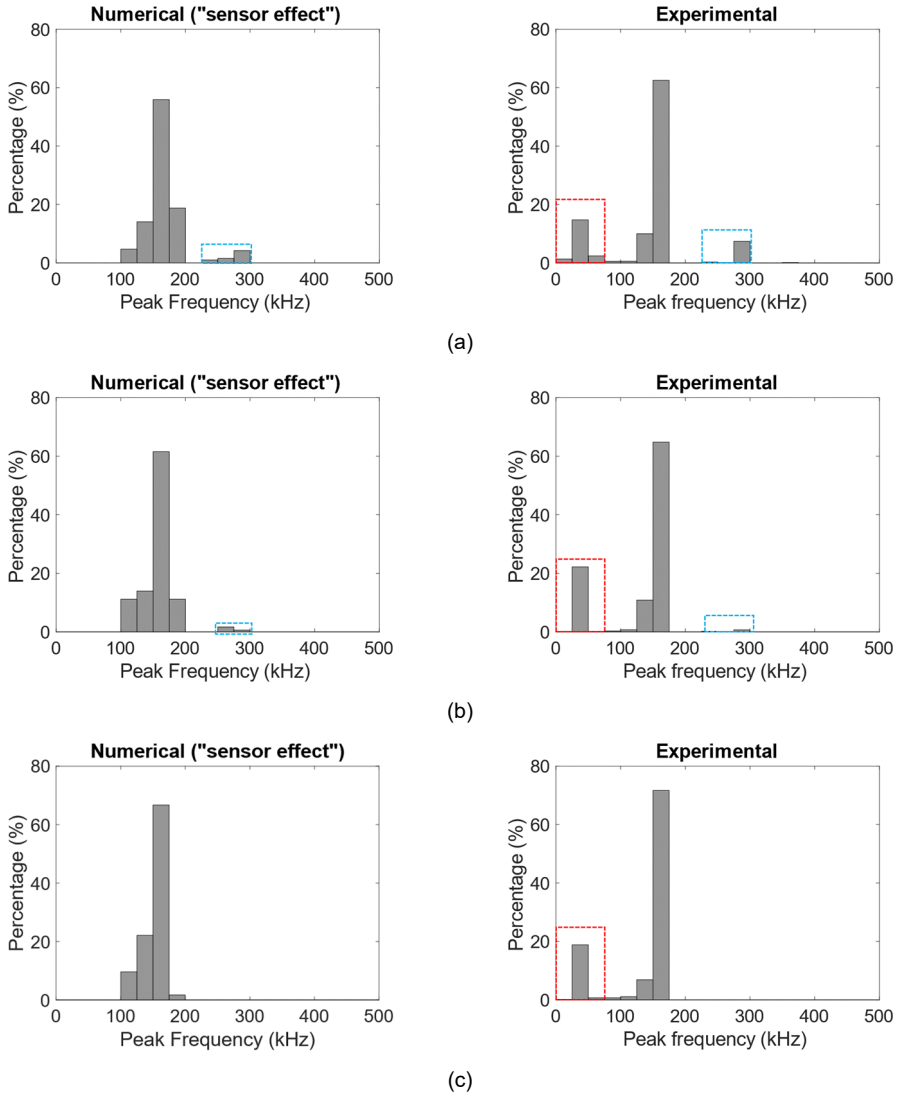

Figure 4.19 Statistical distribution of peak frequency of signals received by different AE sensors: (a) S1; (b) S2; (c) S3

4.6 Discussion

This chapter experimentally validates the effectiveness of the proposed lattice model for full-waveform simulation of tensile cracking induced AE signals. To the best knowledge of the authors, to date, the proposed method is the first model in literature that can explicitly simulate both the mechanical responses of concrete fracture processes, and the AE waveforms measured during the fracturing processes with one model and with relatively simple modelling and calibrating process.

The proposed model has distinguished advantages among available AE modelling methods. It relies only on the concrete mechanical properties with clear physical meanings as model inputs; AE signals are automatically generated as a direct result of concrete fracturing process and do not require additional inputs for AE phenomenon itself. Compared to traditional continuum-based analytical models and numerical FEM, the proposed model does not need additional assumptions (external inputs) for the description of AE sources. With respect to other DEM, the proposed model can explicitly simulate the transient elastodynamic effects of elastic wave propagation and attenuation triggered by element breakage, and thus the complete fracture-induced AE waveforms.

To date, we have no clue about how AE signals are linked to the physical fracturing processes inside concrete. As a most dominant AE source in quasi-brittle materials like concrete, the AE source of tensile cracking is often used to indicate the health conditions of concrete structures. The experimentally validated lattice model is promising to uncover AE sources mechanisms induced by concrete tensile fracturing (this will be addressed in Chapter 6 and 7). Additionally, the fracturing phenomena of crack nucleation, propagation and coalescence to form macroscopic fracture can be reflected in lattice modelling through element breakage and the accumulation of broken elements (Nikolić et al. 2018). Therefore, the developed model also has great potential to investigate the evolution of fracture sources and resultant change in AE parameters in different fracturing stages, thus towards developing reliable AE indicators for concrete structural damage states (this will be addressed in Chapter 8).

The proposed model however has its limitations. In the following, we discuss the model limitations and possible improvements.

4.6.1 Explanations for the difference in frequency characteristics between experimental and numerical AE signals

The As can be seen in Figure 4.15c-e and Figure 4.19, there are differences in frequency characteristics between numerical and experimental AE waveforms. The experimental results include around 20% AE signals with frequency values, while such low-frequency

signals are not observed in the numerical simulation. Possible explanations for this discrepancy are given in the following:

① Fracturing scale. The numerical discretization level (grid size) in the lattice model has a clear physical meaning. As shown in Figure 3.1, different lattice grid size corresponds to different areas of represented continuum, and thus broken elements of different sizes represent different sizes of fractured areas. As will be discussed in Chapter 7, the frequency characteristics of generated AE signals is related to corresponding fractured area. The numerical simulation case presented in this chapter adopts a fixed grid size of 1-mm and thus low-frequency signals from fractured area of larger sizes in the experiment may not be reproduced in the simulation case.

② Friction. In plain concrete, AE signals are mainly from two sources, tensile cracking (Mode-I fracture) and stick-sliding friction along existing crack surfaces (Zhang et al. 2022). AE signals from these two mechanisms show different waveform characteristics. It is well-known that the AE signals from tensile cracking are characterized by higher average frequency and shorter rise time. The AE signals from friction are characterized by lower average frequency and longer rise time (Ohno and Ohtsu 2010; Shiotani 2006; Shiotani, Ohtsu, and Ikeda 2001). This explanation is in line with the observation in the research of Zhang et al. (Zhang et al. 2022), in which it was proposed that the cracking-induced AE signals have peak frequency values higher than 70 kHz, while friction induced AE signals may have peak frequency lower than 70 kHz. As shown in Figure 4.9c, the surface cracks in the three-point bending test are not perfectly straight involving sliding along the crack surfaces. The low-frequency signals observed in the experiments may be caused by the friction along crack surfaces, which cannot be considered in current lattice modelling framework. In addition, parts of the experimental low-frequency AE signals can be attributed to the noises from the friction between specimen and loading devices (i.e., loading and support plates).

Such an observed discrepancy will be further explained in Section 8.4.1.

4.6.2 Limitations of current research and recommendations for future study

The limitations of current research and corresponding recommendations for future study are discussed in this section.

4.6.2.1 Influence of existed cracks on wave propagation

In the proposed lattice model, the implemented numerical Rayleigh damping can simulate the intrinsic wave attenuation of the undamaged concrete, while the attenuation and reflection of AE waveforms caused by cracks cannot be correctly simulated. Specifically,

to ensure the reduction of the mechanical properties, the stiffness of the cracked elements must be reduced in the lattice model. However, following the Rayleigh damping formulation (see Equation (3.4)), this reduction of stiffness will lead to a lower damping, as the damping values of nodes linked by a broken element are reduced when its stiffness degrades. On the contrary, the damping value at a cracked region shall increase towards an infinitely large value (the cracking surfaces can be seen as additional boundaries). This challenge can be resolved by two possible solutions; one option is to remove the broken elements to create cracking boundaries in each calculation step or set an increasing damping value for the nodes linked by broken elements. Here, the damping value of cracked elements will not be linearly linked to the stiffness of the element, a dedicate calibration of the damping effect of cracked concrete with respect to the crack width, wave propagation angle and polarization shall be carried out (Caleap, Aristégui, and Angel 2009).

4.6.2.2 Concrete heterogeneity

In microscopic level, concrete is a highly heterogeneous material. The heterogeneity may influence both source mechanisms and AE wave propagation: the AE sources from the fracture of mortar, aggregates or their interface may be different; the presence of aggregates or pores in concrete leads to wave scattering of AE signals. In this study, concrete is modelled as homogeneous material without considering the differentiation between mortar paste and aggregates in mesh generation. In a future study, the influence of concrete heterogeneity on simulated AE signals should be investigated. In lattice modelling, the concrete material heterogeneity can be simulated by either applying random distribution of element material parameters, e.g., fracture energy (Iturrioz, Lacidogna, and Carpinteri 2013) or by adopting a random lattice mesh (i.e., perturbing lattice grids with small random displacements or random angles (Aydin, Binici, and Tuncay 2021)). The material disorder has been considered in classical lattice modelling work and is seen as an essential part to simulate an AE test (Iturrioz, Lacidogna, and Carpinteri 2013, 2014; Minozzi et al. 2003).

4.6.2.3 Limitation of 2D simulation

The developed lattice model is currently restricted to 2D simulation and thus cannot simulate the propagation of AE waves and the fracturing process inside concrete in 3D. To ensure enough temporal and spatial sampling rates of simulated AE signals, small values were used for both the mesh size and time step in the simulation, leading to more computational resources. Although the vectorization and parallelization computing techniques have been applied in the lattice modelling platform, the computation time is still around 10 days for the simulation case presented in this study even using a high-performance workstation.

In a future study, a more efficient 3D lattice model is necessary for a better simulation of wave propagation process and internal fracturing process in real structures. One possible solution is to use varied time steps in the explicit integration procedure, adopting a much larger time step when no lattice element is broken. The second possible solution is to combine the lattice model with high-order finite element methods (i.e., combined finite-discrete element method (Lisjak et al. 2013b)). The possible cracking region is still modelled by lattice elements, and the remaining undamaged parts can be modelled by elastic finite elements.

4.7 Summary

To establish a clear relationship between the AE signals measured during the fracturing process and the physical sources that induces the signal, it is ideal to establish a forward model that can explicitly model the fracturing process of concrete, the propagation of AE waves and the response of AE sensor. In this chapter, additional techniques for modelling AE sensor response are introduced to the proposed lattice model presented previous chapter, forming a complete lattice modelling framework for complete AE processes.

The effect of sensor response on AE signals has been revealed through lattice modelling. The sensor geometry reduces time-domain amplitudes and filters high-frequency contents of the numerical waveform, while the frequency-response sensitivity of sensors narrows a wide-band frequency response to certain narrowed bands with higher sensor sensitivity.

The feasibility of the proposed model for tensile fracture-induced AE waveform simulation has been demonstrated through a comparison against experimental results. In this chapter, the proposed lattice model is implemented concrete tensile cracking process in a three-point bending test of notched concrete beam. Besides mechanical behaviours and AE hits, a comparison is conducted between typical numerical and experimental waveforms. The simulated AE waveforms show a high degree of similarity statistically to the measured AE signals in terms of typical AE parameters.

The proposed lattice model that has been experimentally validated in this chapter will be adopted to uncover the source mechanisms of concrete tensile fracture-induced AE signals in Chapter 6, Chapter 7 and Chapter 8.

5. Understanding the tensile cracking-induced acoustic emission phenomena in concrete: 1D analytical modelling

5.1 Introduction

To date, the source mechanisms of acoustic emission (AE) signals generated during concrete fracturing processes remain unclear. As reviewed in Section 2.3, existing AE theories provide inconsistent explanations for the origin of AE phenomena, attributing them to different mechanisms or phenomena across various scales and perspectives. Moreover, these theories fail to explain most parameters of AE measurements due to the absence of a clear physical foundation. Therefore, a deeper understanding of the physical principles underlying AE phenomena in concrete fracture processes is essential.

This chapter aims to elucidate the source mechanisms of acoustic emission (AE) induced by concrete tensile cracking, as it represents the primary AE source in concrete fracturing processes, yet its physical basis for generating AE signals remains unclear. While previous chapters introduced a numerical lattice model capable of explicitly simulating the entire AE process induced by concrete tensile fracture, an analytical approach is necessary to first understand the fundamental mechanisms of AE signal generation before numerically investigating the AE sources through the proposed lattice model. To achieve this, a simplified one-degree-of-freedom (1-DoF) dynamic system is employed to study a localized concrete tensile cracking area. By analysing this model, the chapter seeks to enhance the understanding of tensile cracking-induced AE phenomena and identify key factors influencing AE source characteristics.

This chapter is structured as follows. Section 5.2 explores the physical phenomena associated with tensile cracking-induced acoustic emission (AE) sources in concrete fracturing processes. Section 5.3 introduces the simplified one-degree-of-freedom (1-DoF) dynamic system to describe AE phenomena induced by concrete tensile cracking. In Section 5.4, a closed-form expression for the dynamic response of this system is derived. Section 5.5 illustrate a typical example of the system dynamic response. Based on the obtained expressions, Section 5.6 examines the relationship between concrete tensile cracking behaviour and the resulting AE phenomena, while Section 5.7 identifies key factors influencing the parameters of tensile cracking-induced AE sources. Finally, Section 5.8 discussed how the observations from the simplified 1-DoF dynamic system can be extended to more realistic cases of AE phenomena induced by concrete tensile cracking.

5.2 Description of physical phenomena

Figure 5.1a illustrates an idealized straight macro-crack of concrete under tension where the crack tip is characterized by many micro-cracks. We follow the assumption that the micro-cracks as well as their interactions (e.g., coalescence of micro-cracks) are the physical sources of tensile cracking-induced AE signals in quasi-brittle materials like concrete (Ohtsu 1996). The micro-cracking area ahead of a visible macro-crack is defined as the fracturing process zone (FPZ) (Bažant and Lin 1988), or called plastic zone (Besel and Breitbarth 2016). From the mechanics perspective, the FPZ is an area where irreversible cracking strain (plastic strain) is localised and is characterised by progressive nonlinear inelastic tensile softening behaviour, for which the stress decreases at increasing deformation/strain, as shown in Figure 5.1b.

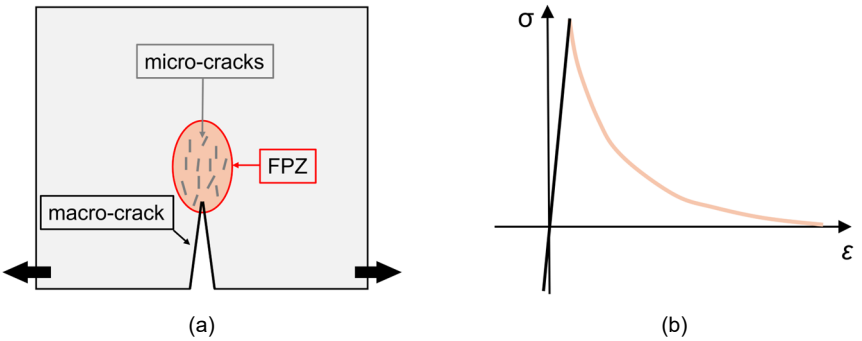

Figure 5.1. Illustration for physical mechanisms of tensile cracking-induced AE sources in concrete: (a) a FPZ at cracking tip and (b) nonlinear tensile softening behaviour of the FPZ.

As the micro-cracking activities in the FPZ is considered as the physical sources of tensile cracking-induced AE phenomena in concrete, in the following we derive the closed-form expressions of dynamic response of the FPZ under tension to understand the tensile cracking-induced AE phenomena in concrete.

5.3 Model description and assumptions

To understand the complicated physical problem of concrete FPZ dynamic response in 2D as shown in Figure 5.1, we first analytically address the 1D case in this chapter. The more complicated 2D case will be numerically studied in next chapter through the proposed lattice model.

Let we consider the case of a 1D bar of length $(2L + l)$, cross-section area S^*, Young's modulus E and density ρ. The considered 1D bar is subjected to uniformed tractions at two edges in terms of a constant velocity v_0 (v_0 is considered as a small value so that the 1D bar is restricted to quasi-static loading conditions globally), as shown in Figure 5.2a. We assume that the applied tension load results in a localised cracking zone of length $2l$

in the mid (marked red in Figure 5.2a) showing tensile softening (plastic) behaviour as illustrated in Figure 5.1b. Here the localized cracking zone is considered as the FPZ in 1D case.

Even for the considered a 1D bar in Figure 5.2a, describing its force equilibrium relies on nonlinear partial differential equations (PDE) with respect to time and space under the framework of classical continuum mechanics theory (Spencer 2004), for which a closed-form analytical solution is not possible because the material properties (coefficients of the PDE) are not constants but vary in both space (nonlinear tensile softening occurs only in the FPZ while other parts remain elastic as shown in Figure 5.2a) and time (stiffness of the FPZ continuously degrades during loading process as shown in Figure 5.1b).

To derive a closed-form solution to the dynamic response of the FPZ for revealing AE source mechanisms, we need to first perform spatial discretization on the considered 1D bar as a continuum to simplify the time- and space-dependent PDEs for describing its force equilibrium into the ordinary differential equations (ODE) only with respect to time that can be analytically solved. Specifically, we discretize the considered 1D continuum bar into a simplified spring-mass system, as shown in Figure 5.2b. The FPZ is divided into two equal symmetric areas, and each area is represented by a lumped mass located in the area centroid, denoted as m:

$$m = \frac{\rho \phi_{FPZ}}{2} = \rho S^* l \tag{5.1}$$

where $\phi_{FPZ} = 2S^* l$ is the volume of the FPZ.

The two symmetric lumped masses m representing the FPZ are then connected by three springs to establish the force interactions. As shown in Figure 5.2b, two types of springs are used. One nonlinear spring of length l (the spring 2 in Figure 5.2b) connects the two symmetrical portions of the PFZ for describing the tensile softening behaviors of the FPZ. Two linear elastic springs (denoted as springs 1 and $1'$ in Figure 5.2b) of length L are used for describing the elastic behaviors of the elastic zone surrounding the PFZ. Tensile displacements in terms of constant velocity v_0 are applied at the ends of linear springs 1 and $1'$ to induce the tensile failure of nonlinear spring 2.

It should be noted that the simplified spring-mass system shown in Figure 5.2b is not a strict discretization of the 1D continuum bar shown in Figure 5.2a, because we do not consider the mass of the elastic zone surrounding the PFZ. This will be further discussed in Section 5.8. Nevertheless, the focus of this study is the dynamic response of the FPZ under global quasi-static loading conditions, for which the surrounding elastic zone provides mainly the elastic force interactions that are considered by elastic springs 1 and $1'$ (namely we ignore the (global) inertia force of the surrounding elastic zone on the FPZ).

Therefore, the simplified model is still able to uncover the basic physical principles underlying tensile cracking-induced AE phenomena.

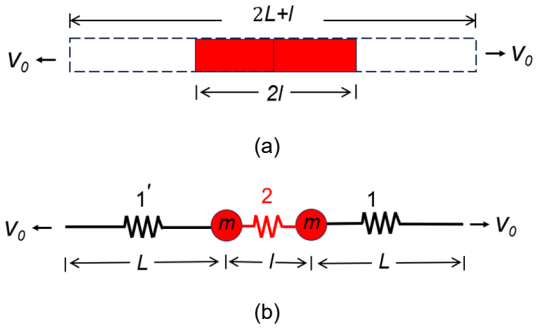

Figure 5.2. Illustration for the considered model: (b) a 1D bar with a mid-span localized fracture zone under tension and (b) a simplified dynamic system for analysing.

Figure 5.3 shows the constitutive laws of the three springs defined in Figure 5.2b. Herein, we use the force-strain relationships for describing constitutive behaviors. Specifically, linear elastic force-strain constitutive law is considered in elastic springs 1 and $1'$ (see Figure 5.3a), as all areas except the FPZ remain elastic in the whole loading process. For the ease of analyses, a bilinear softening force-strain relationship (Park, Paulino, and Roesler 2008) is considered in the nonlinear spring 2 for mathematically describing tensile softening behavior of the FPZ, as shown in Figure 5.3b. The effect of different nonlinear constitutive laws will be discussed in Section 5.6.

Considering the physical properties of the 1D bar in Figure 5.2a (namely cross-section area $S^*$and Young's modulus E) represented by the simplified spring-mass system in Figure 5.2b, the rigidity of both linear and nonlinear springs (slop of the linear parts in the force-strain curves in Figure 5.3) is calculated as ES^* (Troyer, Griffis, and Shackelford 2005) (see also Section 3.2.1 and Appendix B). The linear limit of the FPZ (nonlinear spring 2) is characterized by its tensile strength f_t amd cracking strain ε_{cr} shown in Figure 5.3b. The first-stage nonlinear behavior of the FPZ is characterized by a tensile softening strain coefficient a_1 and corresponding force reduction coefficient b_1. The angle between the adopted bilinear force-strain curve and the force-axis direction in the first tensile softening stage (ε_{cr}~$a_1\varepsilon_{cr}$) is denoted as θ_0. Constitutive behavior of the FPZ after $a_1\varepsilon_{cr}$ is described by an angle between the force-strain curve and force-axis direction, marked as θ_1 in Figure 5.3b.

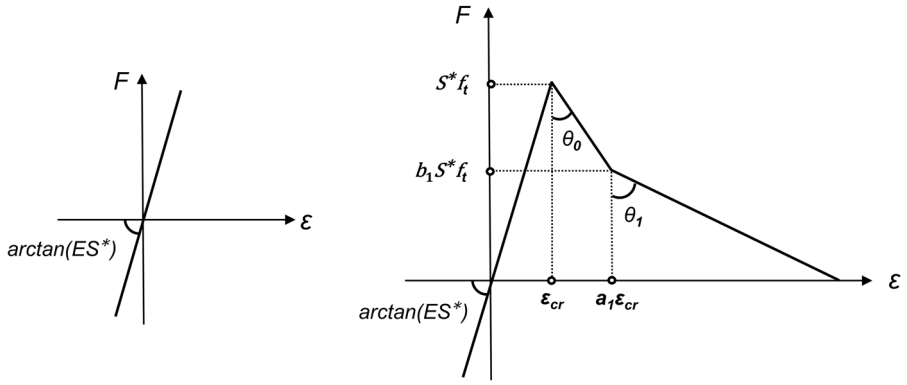

Figure 5.3. Constitutive law for springs: (a) linear elastic behaviour of springs 1 and 1′ and (b) bi-linear tensile softening behaviour of spring 2 (Park, Paulino, and Roesler 2008).

According to the physical characteristics of concrete FPZ (Park, Paulino, and Roesler 2008), the defined tensile fracturing parameters satisfy the following mathematical conditions:

$$a_1 \geq 1 \tag{5.2a}$$

$$0 \leq b_1 \leq 1 \tag{5.2b}$$

$$0 \leq \theta_0 \leq \frac{\pi}{2} \tag{5.2c}$$

$$\theta_0 < \theta_1 \leq \frac{\pi}{2} \tag{5.2d}$$

The displacements of left and right lumped masses m representing the FPZ are denoted as $u'(t)$ and $u(t)$, respectively, with $u'(t) = -u(t)$ due to the symmetry of the problem (t is the loading time). The strains of linear springs (springs 1 and 1′ in Figure 5.2b) and nonlinear springs (spring 2 in Figure 5.2b), denoted as $\varepsilon_1(t)$ and $\varepsilon_2(t)$, respectively, are then expressed as:

$$\varepsilon_1(t) = \frac{v_0 t - u(t)}{L} \tag{5.3a}$$

$$\varepsilon_2(t) = \frac{u(t) - u'(t)}{l} = \frac{2u(t)}{l} \tag{5.3b}$$

The force in linear spring 1 (1') and nonlinear spring 2 (see Figure 5.2) are denoted as $F_{e1}(t)$ and $F_{e2}(t)$ respectively. According to the strain-force constitutive laws of springs defined in Figure 5.3, $F_{e1}(t)$ and $F_{e2}(t)$ are expressed as:

$$F_{e1}(t) = \varepsilon_1(t) ES^* \tag{5.4}$$

$$F_{e2}(t) = \begin{cases} \varepsilon_2(t) ES^* & \text{if } 0 < \varepsilon_2(t) \le \varepsilon_{cr} \quad (5.5a) \\ \dfrac{\varepsilon_{cr} - \varepsilon_2(t)}{\tan\theta_0} + ES^* \varepsilon_{cr} & \text{if } \varepsilon_{cr} \le \varepsilon_2(t) < a_1 \varepsilon_{cr} \quad (5.5b) \\ \dfrac{a_1\varepsilon_{cr} - \varepsilon_2(t)}{\tan\theta_1} + b_1 ES^* \varepsilon_{cr} & \text{if } \varepsilon_2(t) \ge a_1 \varepsilon_{cr} \quad (5.5c) \end{cases}$$

$$\text{with } \varepsilon_{cr} = \frac{f_t}{E} \tag{5.5d}$$

5.4 Model formulation

Under the above model simplification, the physical problem described in Section 5.2 is then transformed into an inverse modelling problem. Specifically, the classical elastodynamics theory (Achenbach 2012) and MT theory (see Section 2.3.1) available for AE modelling only provide the solution to the forward problem of far-filed dynamic response due to a local disturbance (source) with known expressions of source dynamic response, namely the problem of wave propagation excited by known sources. Differently, the model established herein is to inversely solve the dynamic response of the FPZ (source) during tensile softening process, namely displacement $u(t)$, under a far-field displacement prescribed by a constant velocity v_0.

To solve this problem, force analysis is conducted on one lumped mass m representing half of the FPZ (see Figure 5.2), as shown in Figure 5.4.

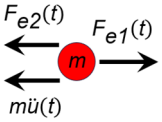

Figure 5.4. Undamped dynamic force equilibrium of the FPZ.

Furthermore, for the problem of high-frequency elastic wave propagation as the case of acoustic emission considered herein, the solids can be treated as a low-damping system with low values of damping ratio (Meirovitch 2010) (see also Section 3.5.1). Therefore, further ignoring the damping force for the simplicity of analyses, the undamped dynamic force equilibrium (motion equation) of lumped mass m is established as:

$$m\ddot{u}(t) + F_{e2}(t) = F_{e1}(t) \tag{5.6}$$

where $\ddot{u}(t)$ are the acceleration of the lumped mass m.

The mathematical model established by Equation (5.6) is in line with the classical dynamics problem of undamped forced vibration of a 1-DoF system (Humar 2012), but has a changed stiffness that varies with loading time t. $F_{e1}(t)$ and $F_{e2}(t)$ in Equation (5.6) can be regarded as external and stiffness-related internal force in a 1-DoF dynamic system, respectively, as shown in Figure 5.4.

By substituting Equation (5.3), Equation (5.4) and (5.5) into Equation (5.6), the undamped dynamic force equilibrium of the FPZ (lumped mass m) is further expressed as:

$$\begin{cases} \dfrac{m}{ES^*}\ddot{u}(t)+\left(\dfrac{2}{l}+\dfrac{1}{L}\right)u(t)=\dfrac{v_0}{L}t & \text{if } 0<\varepsilon_2(t)\le\varepsilon_{cr} \quad (5.7a) \\ \dfrac{m}{ES^*}\ddot{u}(t)+K^*(\theta_0)u(t)=\dfrac{v_0}{L}t-(1+\dfrac{1}{\tan\theta_0 ES^*})\varepsilon_{cr} & \text{if } \varepsilon_{cr}\le\varepsilon_2(t)<a_1\varepsilon_{cr} \quad (5.7b) \\ \dfrac{m}{ES^*}\ddot{u}(t)+K^*(\theta_1)u(t)=\dfrac{v_0}{L}t-(b_1+\dfrac{a_1}{\tan\theta_1 ES^*})\varepsilon_{cr} & \text{if } \varepsilon_2(t)\ge a_1\varepsilon_{cr} \quad (5.7c) \end{cases}$$

$$\text{with} \quad \begin{cases} K^*(\theta_0)=\dfrac{1}{L}-\dfrac{2}{\tan\theta_0 ES^* l}=\dfrac{1}{L}-\dfrac{2(1-b_1)}{l(a_1-1)} & (5.7d) \\ K^*(\theta_1)=\dfrac{1}{L}-\dfrac{2}{\tan\theta_1 ES^* l} & (5.7e) \end{cases}$$

where K^* is the effective stiffness of the 1-DoF system (i.e., the coefficient of all displacement-related terms).

Equation (5.7) includes three second-order linear differential equations with constant coefficients. Appendix E gives the standard solution procedure to a generalized second order linear differential equation with constant coefficients. In the following, the solution process to Equation (5.7) is divided into three stages according to the three different strain phases of the FPZ, namely $\varepsilon_2(t)$.

5.4.1 Stage 1: linear elastic stage of the fracture process zone

The force equilibrium of the FPZ in linear elastic stage ($0<\varepsilon_2(t)\le\varepsilon_{cr}$) is described by Equation (5.7a). The solution to Equation (5.7a) is as follows (see Appendix E):

$$u(t)=C_1\cos\left[\sqrt{\left(\frac{2}{l}+\frac{1}{L}\right)\frac{ES^*}{m}}t\right]+C_2\sin\left[\sqrt{\left(\frac{2}{l}+\frac{1}{L}\right)\frac{ES^*}{m}}t\right]+\frac{v_0 l}{2L+l}t \quad (5.8)$$

where C_1 and C_2 are two constant coefficients to be decided by initial conditions. Considering the constant strain rate $\dot{\varepsilon}$ in the whole domain in the elastic stage of the PFZ, the initial conditions of Equation (5.8) are expressed as:

$$u(0) = 0 \tag{5.9a}$$

$$\dot{u}(0) = \frac{\dot{\varepsilon} l}{2} = \left(\frac{2v_0}{2L + l} \right) \frac{l}{2} = \frac{v_0 l}{2L + l} \tag{5.9b}$$

$$\ddot{u}(0) = 0 \tag{5.9c}$$

Substituting the initial values in Equation (5.9) into Equation (5.8), two constant coefficients are determined as:

$$C_1 = C_2 = 0 \tag{5.10}$$

Moreover, because the expression of $u(t)$ is a linear increasing function of both time t (Equation (5.8)) and strain $\varepsilon_2(t)$ (Equation (5.3b)) when $0 < \varepsilon_2(t) \leq \varepsilon_{cr}$ (namely displacement and thus strain of the FPZ monotonically increase with increasing loading time in this strain stage), the strain condition $0 < \varepsilon_2(t) \leq \varepsilon_{cr}$ can then be transformed into time condition as:

$$0 < t \leq t_1 \tag{5.11}$$

where t_1 is the ending time of this stage corresponding to cracking strain ε_{cr} of the FPZ and thus satisfying the following equation:

$$\varepsilon_2(t_1) = \frac{2u(t_1)}{l} = \varepsilon_{cr} \tag{5.12}$$

By substituting Equation (5.8) and Equation (5.10) into Equation (5.12), the expression of t_1 is derived as:

$$t_1 = \frac{2L + l}{2v_0} \varepsilon_{cr} \tag{5.13}$$

5.4.2 Stage 2: first nonlinear softening stage of the fracture zone

The force equilibrium of the FPZ in first nonlinear tensile softening stage ($\varepsilon_{cr} \leq \varepsilon_2(t) < a_1 \varepsilon_{cr}$) is described by Equation (5.7b). Mathematically, the solution to Equation (5.7b) can be in different forms depends on the value of the involved term $K^*(\theta_0)$ (see Appendix E). Physically, considering the brittle behavior of concrete in early tensile softening stage (Chen and Su 2013), θ_0 is a small positive value (see Figure 5.3) and thus only the case of negative value of $K^*(\theta_0)$ is taken into consideration herein ($K^*(\theta_0)$ is positively correlated with θ_0 (see Equation (5.7d))). This will be further discussed in Section 5.6 in more detail. Accordingly, Equation (5.7b) is solved as:

$$u(t)=C_1^{'}e^{t\sqrt{-\frac{K^*(\theta_0)ES^*}{m}}}+C_2^{'}e^{-t\sqrt{-\frac{K^*(\theta_0)ES^*}{m}}}+\frac{v_0}{LK^*(\theta_0)}t-\left(1+\frac{1}{\tan\theta_0 ES^*}\right)\frac{\varepsilon_{cr}}{K^*(\theta_0)} \tag{5.14}$$

where C_1' and C_2' are two constant coefficients to be determined by the initial conditions. Considering the time-domain continuity of displacements of lumped mass m, the initial values of Equation (5.14) equal to the end values of Equation (5.8) at time t_1. By substituting the expression of t_1 in Equation (5.13) and Equation (5.10) into Equation (5.8), the initial conditions of Equation (5.14) at time t_1 are expressed as:

$$u(t_1)=\frac{l\varepsilon_{cr}}{2} \tag{5.15a}$$

$$\dot{u}(t_1)=\frac{v_0 l}{2L+l} \tag{5.15b}$$

$$\ddot{u}(t_1)=0 \tag{5.15c}$$

Substituting Equation (5.15) into Equation (5.14), the two constant coefficients are determined as:

$$C_1^{'}=-\left(1+\frac{1}{\tan\theta_0 ES^*}\right)\frac{v_0}{(2L+l)K^*(\theta_0)\sqrt{-\frac{K^*(\theta_0)ES^*}{m}}}e^{-t_1\sqrt{-\frac{K^*(\theta_0)ES^*}{m}}} \tag{5.16a}$$

$$C_2^{'}=\left(1+\frac{1}{\tan\theta_0 ES^*}\right)\frac{v_0}{(2L+l)K^*(\theta_0)\sqrt{-\frac{K^*(\theta_0)ES^*}{m}}}e^{t_1\sqrt{-\frac{K^*(\theta_0)ES^*}{m}}} \tag{5.16b}$$

Substituting Equation (5.16) and Equation (5.13) into Equation (5.14), Equation (5.14) is further organized as:

$$u(t)=C_0^{'}\left[e^{(t-t_1)\sqrt{-\frac{K^*(\theta_0)ES^*}{m}}}-e^{-(t-t_1)\sqrt{-\frac{K^*(\theta_0)ES^*}{m}}}\right]+\frac{v_0}{K^*(\theta_0)L}(t-t_1)+\frac{l}{2}\varepsilon_{cr} \tag{5.17a}$$

$$\text{with } C_0^{'} = -\left(1+\frac{1}{\tan\theta_0 ES^*}\right)\frac{v_0}{(2L+l)K^*(\theta_0)\sqrt{-\dfrac{X(\theta_0)ES^*}{m}}} \tag{5.17b}$$

$u(t)$ in this strain stage ($\varepsilon_{cr} \le \varepsilon_2(t) < a_1\varepsilon_{cr}$) is an increasing function of both time t (Equation (5.17)) and strain $\varepsilon_2(t)$ (Equation (5.3b)). The proof procedure that Equation (5.17) is an increasing function of time t is given in Appendix F. This means the displacement and thus strain of the FPZ monotonically increase with increasing loading time in this stage. Therefore, the strain condition, $\varepsilon_{cr} \le \varepsilon_2(t) < a_1\varepsilon_{cr}$, can be transformed into time condition as:

$$t_1 \le t < t_2 \tag{5.18}$$

where time t_2 corresponds to the moment that the strain of the FPZ reaching $a_1\varepsilon_{cr}$:

$$\varepsilon_2(t_2) = \frac{2u(t_2)}{l} = a_1\varepsilon_{cr} \tag{5.19}$$

By substituting Equation (5.17) into Equation (5.19), we derive the following equation for t_2:

$$\begin{aligned} u(t_2) = \frac{l}{2}a_1\varepsilon_{cr} = C_0^{'}e^{(t_2-t_1)\sqrt{-\frac{K^*(\theta_0)ES^*}{m}}} - C_0^{'}e^{-(t_2-t_1)\sqrt{-\frac{K^*(\theta_0)ES^*}{m}}} \\ + \frac{v_0}{K^*(\theta_0)L}(t_2-t_1) + \frac{l}{2}\varepsilon_{cr} \end{aligned} \tag{5.20}$$

Equation (5.20) has no explicit solution for t_2, but an approximate solution of t_2 is given as:

$$t_2 \approx t_1 + \frac{\ln\left\{-\dfrac{\varepsilon_{cr}(a_1-1)(2L+l)K^*(\theta_0)}{2v_0}\left(1+\dfrac{1}{\tan\theta_0 ES^*}\right)\sqrt{-\dfrac{K^*(\theta_0)ES^*}{m}}\right\}}{\sqrt{-\dfrac{K^*(\theta_0)ES^*}{m}}} \tag{5.21}$$

The derivation process of Equation (5.21) is detailed in Appendix G.

5.4.3 Stage 3: second nonlinear softening stage of the fracture zone

The force equilibrium of the FPZ in second nonlinear tensile softening stage ($\varepsilon_2(t) \ge a_1\varepsilon_{cr}$) is described by Equation (5.7c). Mathematically, the solution to Equation (5.7c) can be in different forms according to the value of the term $K^*(\theta_1)$ (see Appendix E). Physically, considering the ductile behavior of concrete in late tensile softening stage

(Chen and Su 2013), the value of $\tan\theta_1$ is relatively large and thus only the case of positive value of $K^*(\theta_1)$ is taken into consideration here ($K^*(\theta_1)$ is positively correlated with θ_1 (see Equation (5.7e))). This will be further discussed in Section 5.6. Accordingly, Equation (5.7c) is solved as:

$$u(t)=\sqrt{C_1''^2+C_2''^2}\sin\left(\sqrt{\frac{K^*(\theta_1)ES^*}{mL}}t+\varphi\right)+\frac{v_0}{LK^*(\theta_1)}t-\frac{\varepsilon_{cr}}{K^*(\theta_1)}\left(b_1+\frac{a_1}{\tan\theta_1 ES^*}\right) \tag{5.22a}$$

$$\text{with}\quad \varphi=\arctan\frac{C_1''}{C_2''} \tag{5.22b}$$

where $C_1''$and C_2'' are two constant coefficients to be decided by the initial conditions. Considering the time-domain continuity of displacements of lumped mass m, the initial values of Equation (5.22) equal to the end values of Equation (5.17) at time t_2. By substituting the expression of t_2 in Equation (5.21) into Equation (5.17), the initial conditions of Equation (5.22) at time t_2 are expressed as:

$$u(t_2)=\frac{a_1 l\varepsilon_{cr}}{2} \tag{5.23a}$$

$$\dot{u}(t_2)\approx\frac{(a_1-1)l\varepsilon_{cr}}{2}\sqrt{-\frac{K^*(\theta_0)ES^*}{m}} \tag{5.23b}$$

$$\ddot{u}(t_2)\approx-\frac{(a_1-1)l\varepsilon_{cr}K^*(\theta_0)ES^*}{2m} \tag{5.23c}$$

The detailed derivation processes of Equation (5.23b) and Equation (5.23c) are given in Appendix H. Substituting Equation (5.23) into Equation (5.22), two constant coefficients are determined as:

$$C_1''=\left[u(t_2)-\frac{v_0}{LK^*(\theta_1)}t_2+\frac{\varepsilon_{cr}}{K^*(\theta_1)}\left(b_1+\frac{a_1}{\tan\theta_1 ES^*}\right)\right]\cos\left(\sqrt{\frac{K^*(\theta_1)ES^*}{mL}}t_2\right)-\left(\dot{u}(t_2)-\frac{v_0}{LK^*(\theta_1)}\right)\frac{mL}{K^*(\theta_1)ES^*}\sin\left(\sqrt{\frac{K^*(\theta_1)ES^*}{mL}}t_2\right) \tag{5.24a}$$

$$C_2^{''} = \left[u(t_2) - \frac{v_0}{LK^*(\theta_1)} t_2 + \frac{\varepsilon_{cr}}{K^*(\theta_1)} \left(b_1 + \frac{a_1}{\tan\theta_1 ES^*} \right) \right] \sin\left(\sqrt{\frac{K^*(\theta_1)ES^*}{mL}} t_2 \right)$$
$$+ \left(\dot{u}(t_2) - \frac{v_0}{LK^*(\theta_1)} \right) \frac{mL}{K^*(\theta_1)ES^*} \cos\left(\sqrt{\frac{K^*(\theta_1)ES^*}{mL}} t_2 \right) \tag{5.24b}$$

5.5 Model illustration

The above derived dynamic displacement $u(t)$ of the FPZ in response to tensile cracking is summarized as follows:

$$u(t) = \begin{cases} \dfrac{v_0 l}{2L + l} t & 0 < t \le t_1 \quad (5.8) \\ C_0^{'} \left[e^{(t-t_1)\sqrt{-\frac{K^*(\theta_0)ES^*}{m}}} - e^{-(t-t_1)\sqrt{-\frac{K^*(\theta_0)ES^*}{m}}} \right] + \dfrac{v_0}{LK^*(\theta_0)} (t - t_1) + \dfrac{l}{2} \varepsilon_{cr} & t_1 < t \le t_2 \quad (5.17) \\ \sqrt{C_1^{''2} + C_2^{''2}} \sin\left(\sqrt{\dfrac{K^*(\theta_1)ES^*}{mL}} t + \arctan\dfrac{C_1^{''}}{C_2^{''}} \right) + \dfrac{v_0}{LK^*(\theta_1)} t - \left(b_1 + \dfrac{a_1}{\tan\theta_1 ES^*} \right) \dfrac{\varepsilon_{cr}}{K^*(\theta_1)} & t > t_2 \quad (5.22) \end{cases}$$

The acceleration $\ddot{u}(t)$ of the FPZ is used for the representation of AE sources, as AE signals are stress waves in nature (see also Section 3.6.1). Taking the second-order derivative of displacement $u(t)$ with respect to time t, the expression of $\ddot{u}(t)$ is derived as:

$$\ddot{u}(t) = \begin{cases} 0 & 0 < t \le t_1 \quad (5.25a) \\ -C_0^{'} \dfrac{K^*(\theta_0)ES^*}{m} \left[e^{(t-t_1)\sqrt{-\frac{K^*(\theta_0)ES^*}{m}}} - e^{-(t-t_1)\sqrt{-\frac{K^*(\theta_0)ES^*}{m}}} \right] & t_1 < t \le t_2 \quad (5.25b) \\ -\sqrt{C_1^{''2} + C_2^{''2}} \dfrac{K^*(\theta_1)ES^*}{mL} \sin\left(\sqrt{\dfrac{K^*(\theta_1)ES^*}{mL}} t + \arctan\dfrac{C_1^{''}}{C_2^{''}} \right) & t > t_2 \quad (5.25c) \end{cases}$$

The expressions of parameters involved in Equation (5.25) are not listed again in this section to avoid repetition. Readers are referred to the previous section for the expressions of involved parameters: t_1 (Equation (5.13)), $C_0^{'}$ (Equation (5.17b)), $K^*(\theta_0)$ (Equation

(5.7d)), m (Equation (5.1)), t_2 (Equation (5.21)), C_1'' (Equation (5.24a)), C_2'' (Equation (5.24b)) and $K^*(\theta_1)$ (Equation (5.7e)).

Figure 5.5 illustrates an example of the displacement $u(t)$ and accretion $\ddot{u}(t)$ (Equation (5.25)) of the FPZ in response to tensile cracking. The concrete properties listed in Table 3.1 are adopted for the calculation. The values of other involved parameters are selected as: $l = 1$ mm, $S^* = 5$ mm^2, $L = 100$ mm, $a_1 = 7.5$, $b_1 = 0.6$, $\tan\theta_1 = 2 \times 10^{-4}$ N^{-1} and $v_0 = 1 \times 10^{-3}$ mm/s.

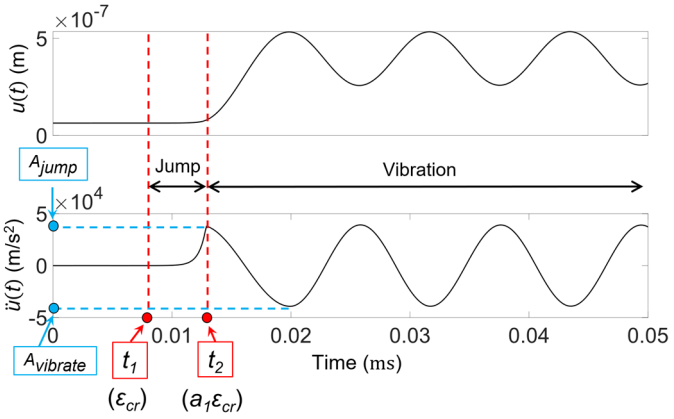

Figure 5.5. An example of the analytically derived dynamic responses of the FPZ in tensile cracking process.

It can be observed that the dynamic response of the FPZ under tension is a two-stage dynamic process. Starting from time t_1 corresponding to cracking strain ε_{cr} (tensile strength f_t) of the FPZ in Figure 5.3b, an acceleration jump occurs in the FPZ. The acceleration of the mass at FPZ increases continuously following an exponential trend (Equation (5.25b)) until reaching time t_2. In the simplified constitution relationship, this time t_2 corresponds to the first tensile strain limit $a_1\varepsilon_{cr}$ of the FPZ in Figure 5.3b. After the strain firstly reaching $a_1\varepsilon_{cr}$, the FPZ starts to vibrate (Equation (5.24c)).

5.6 Model analyses I: AE phenomena & concrete tensile softening behaviour

This section aims to understand the tensile cracking-induced AE phenomena. As shown in Figure 5.5, the dynamic response of the FPZ (AE sources) under tension is a two-stage process. In this section, we describe such a dynamic process mathematically and then provide corresponding physical interpretations. The analysis focuses on revealing the connection between concrete tensile softening behavior and AE source response.

The difference in the forms of dynamic response of the FPZ in the two strain softening stages in Figure 5.5 lies in the mathematical solution forms to its dynamic force equilibrium (Equation (5.7b) and Equation (5.7c)). The solution forms of these two similar equations depend on the values of involved terms of $K^*(\theta_0)$ (Equation (5.7d)) and $K^*(\theta_1)$ (Equation (5.7e)) (see Appendix E).

According to the physical characteristics of concrete tensile softening behavior (Chen and Su 2013), we have considered the following conditions to derive the expressions of the dynamic response $u(t)$ of the FPZ (see Section 5.4.2 and Section 5.4.3):

$$K^*(\theta_0) = \frac{1}{L} - \frac{2}{\tan\theta_0 ES^* l} < 0 \tag{5.26a}$$

$$K^*(\theta_1) = \frac{1}{L} - \frac{2}{\tan\theta_1 ES^* l} > 0 \tag{5.26b}$$

The negative $K^*(\theta_0)$ and positive $K^*(\theta_1)$ lead to the solution forms of exponential functions (corresponding to displacement jump stage of the FPZ in Figure 5.5) and of trigonometric functions (corresponding to vibration stage of the FPZ in Figure 5.5), respectively. This indicates that the angle between the force-strain curve and force-axis direction (namely θ_0 and θ_1 in Figure 5.3b) is a criterion for distinguishing different dynamic stages of the FPZ. Physically, this angle describes how rapid the stiffness of concrete degradation at the FPZ is with the increase of strain. In early tensile softening stage $\varepsilon_{cr}\sim a_1\varepsilon_{cr}$ (the period $t_1\sim t_2$ in Figure 5.5), the dynamic response of the FPZ is in the displacement/acceleration-jump stage in terms of an exponential function due to the rapid stiffness degradation characterized by a small angle θ_0. When the strain of the FPZ larger than $a_1\varepsilon_{cr}$ (the period after time t_2 in Figure 5.5), the dynamic response of the FPZ is then in the vibration stage in terms of a trigonometric function when the stiffness degradation rate slows down corresponding to a large angle θ_1.

In the above analysis, the nonlinear tensile softening behavior of the FPZ is approximated by two linear segments (see Figure 5.3b), where only two angle values, namely θ_0 and θ_1, are involved in the nonlinear softening curve. Now we consider a more general case with multi-linear segments to approximate an exponential tensile softening curve of the FPZ, as shown in Figure 5.6a, where a *i*-th linear segment is characterized by the stain values of $a_i\varepsilon_{cr}$ and $a_{i+1}\varepsilon_{cr}$ and force values of $b_iS^*f_t$ and $b_{i+1}S^*f_t$ at its starting and ending points. θ_i is the angle between the *i*-th linear segment and the force-axis direction. When the number of segments increase, the force-strain curve approaches towards the classical exponential tensile softening constitutive law of concrete (Reinhardt, Cornelissen, and Hordijk 1986), as shown in Figure 5.6b. According to the tensile softening behavior of concrete, θ_i satisfy the following mathematical conditions in the nonlinear stages:

$$0 \le \theta_i \le \frac{\pi}{2} \tag{5.27}$$

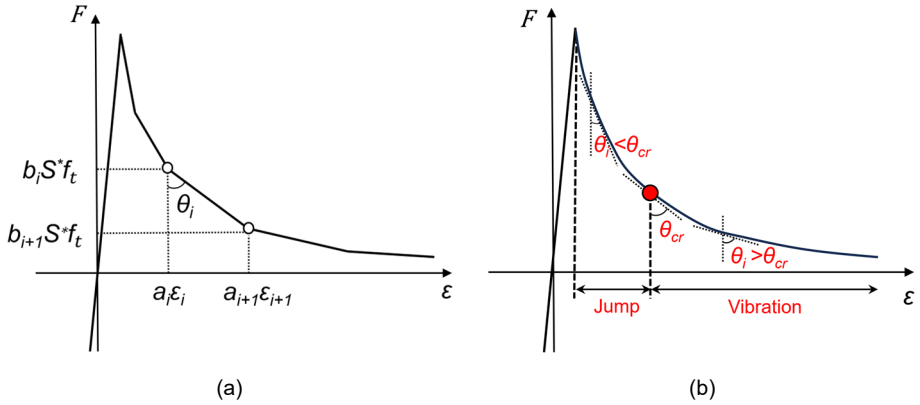

Figure 5.6. Illustration for occurrence conditions of different dynamic response phases of the FPZ: (a) a tensile softening curve approximated by multiple linear segments and (b) classical exponential tensile softening curve of concrete (Reinhardt, Cornelissen, and Hordijk 1986).

Following the procedure described in Section 5.4, the force equilibrium of the FPZ (the lumped mass m in Figure 5.2b) in the i-th strain softening range is established as:

$$\frac{m}{ES^*}\ddot{u}(t)+K^*(\theta_i)u(t)=\frac{v_0}{L}t-\left(b_i+\frac{a_i}{\tan\theta_i ES^*}\right)\varepsilon_{cr} \quad \text{if } a_i\varepsilon_{cr}\le\varepsilon_2(t)<a_{i+1}\varepsilon_{cr} \tag{5.28a}$$

$$\text{with } K^*(\theta_i)=\left(\frac{1}{L}-\frac{2}{\tan\theta_i ES^* l}\right) \tag{5.28b}$$

According to Appendix E (see also the work of Sibuya (Sibuya 1975)), the value of $K^*(\theta_i)$ defined by Equation (5.28b) governs the solution forms of Equation (5.28a). Specifically, the characteristic equation of Equation (5.28a) is expressed as:

$$\frac{m}{ES^*}\mu^2+K^*(\theta_i)=0 \tag{5.29}$$

where μ is the eigen root of Equation (5.28a). The value types of μ govern the solution forms of Equation (5.28a), as follows:

① When $K^*(\theta_i)<0$, Equation (5.28a) has two real eigen roots μ_1 and μ_2 as:

$$\mu_1=\sqrt{-\frac{K^*(\theta_i)ES^*}{m}} \tag{5.30a}$$

$$\mu_2 = -\sqrt{-\frac{K^*(\theta_i)ES^*}{m}} \tag{5.30b}$$

In such a case the solution form to Equation (5.28a) is an exponential function, corresponding to a dynamic response form of displacement/acceleration jump for the FPZ, as follows:

$$\begin{aligned} u(t) = C_1^i e^{t\sqrt{-\frac{K^*(\theta_i)ES^*}{m}}} + C_2^i e^{-t\sqrt{-\frac{K^*(\theta_i)ES^*}{m}}} \\ + \frac{v_0}{LK^*(\theta_i)}t - \left(b_i + \frac{a_i}{\tan\theta_i ES^*}\right)\frac{\varepsilon_{cr}}{K^*(\theta_i)} \end{aligned} \tag{5.31}$$

where C_1^i and C_2^i are two constant coefficients to be determined by the initial conditions.

② When $K^*(\theta_i) > 0$, Equation (5.28a) has two wo complex eigen roots μ_1 and μ_2 as:

$$\mu_1 = \chi\sqrt{\frac{K^*(\theta_i)ES^*}{m}} \tag{5.32a}$$

$$\mu_2 = -\chi\sqrt{\frac{K^*(\theta_i)ES^*}{m}} \tag{5.32b}$$

where $\chi = \sqrt{-1}$ denotes the imaginary unit.

In such a case, the solution form to Equation (5.28a) is a trigonometric function, corresponding to a dynamic response form of vibrations for the FPZ, as follows:

$$\begin{aligned} u(t) = \sqrt{C_1^{i2} + C_2^{i2}}\sin\left(\sqrt{\frac{K^*(\theta_i)ES^*}{mL}}t + \arctan\frac{C_1^i}{C_2^i}\right) \\ + \frac{v_0}{LK^*(\theta_i)}t - \left(b_i + \frac{a_i}{\tan\theta_i ES^*}\right)\frac{\varepsilon_{cr}}{K^*(\theta_i)} \end{aligned} \tag{5.33}$$

where C_1^i and C_2^i are two constant coefficients to be determined by the initial conditions.

From an energy perspective, $K^*(\theta_i)$, representing the effective stiffness of the 1-DoF system (i.e., the coefficient of all displacement-related terms), governs the form of energy dissipation within the system. In a typical linear dynamic system, the inertial, damping, and stiffness coefficients are all positive (i.e., $K^*(\theta_i) > 0$ as shown in Equation (5.32)). This configuration describes a dissipative system, where all internal force components work to absorb external energy, resulting in either balanced undamped vibration amplitudes (see Equation (5.33)) or attenuated amplitudes when damping is considered. However, if one or more internal force terms become negative (namely $K^*(\theta_i) < 0$ as Equation (5.30)), those internal forces no longer absorb energy. Instead, they contribute energy

to the system, effectively acting as additional external inputs. This transformation occurs because negative internal force terms on the left-hand side of the motion equation become positive external forces when moved to the right-hand side (refer to Equation (5.28)). In this scenario, the system is characterized as unstable or even divergent and exhibits energy emission, leading to amplified vibration amplitudes (see Equation (5.31)).

As shown in Figure 5.6, the value of θ_i monotonically increases with the increase of strain ε during the tensile softening process of the FPZ. Furthermore, as can be seen from Equation (5.28b), $K^*(\theta_i)$ is positively correlated with θ_i when $0 \leq \theta_i \leq \frac{\pi}{2}$ (Equation (5.27)). This means $K^*(\theta_i)$ also monotonically increases with the increase of strain ε during the tensile softening process of the FPZ. Further considering the brittle fracture behavior of the FPZ in early tensile softening stages, the value of $K^*(\theta_i)$ can be negative in early tensile softening stages, e.g., $K^*(\theta_i)$ approaches negative infinity for ideal brittle failure when θ_i approaches zero (see Equation (5.28b)). Such negative values of $K^*(\theta_i)$ in early tensile softening stages then monotonically increase to positive values with the increase of strain ε during the tensile softening process of the FPZ, e.g., $K^*(\theta_i)$ approaches the positive value of $\frac{1}{L}$ for ideal plateau ductile failure when θ_i approaches $\frac{\pi}{2}$ (see Equation (5.28b)).

Corresponding to such an evolution trend of $K^*(\theta_i)$ during the tensile softening process of the FPZ , the dynamic response of the FPZ involves a first stage of displacement/acceleration jump (exponential solution forms of FPZ response) when the values of $K^*(\theta_i)$ increase from negative to zero (Equation (5.31)), and a second stage of vibrations (trigonometric solution forms of FPZ response) when $K^*(\theta_i)$ further increases from zero to positive values Equation (5.33). Therefore, the zero value of $K^*(\theta_i)$ is a critical value that distinguishes such two different dynamic forms of the FPZ. The critical value of $K^*(\theta_i)$, denoted as $K^*(\theta_{cr})$, is then expressed as:

$$K^*(\theta_{cr}) = \frac{1}{L} - \frac{2}{\tan\theta_{cr} ES^* l} = 0 \tag{5.34}$$

By solving Equation (5.34), a critical value of θ_i, denoted as θ_{cr}, that distinguishes the two different dynamic forms of the FPZ (displacement jump or vibrations) is expressed as:

$$\theta_{cr} = \arctan\frac{2}{K_{structure} l} \tag{5.35a}$$

$$K_{structure} = \frac{ES^*}{L} \tag{5.35b}$$

where $K_{structure}$ defined by Equation (5.35b) is the stiffness of the linear elastic springs 1 and 1' illustrated in Figure 5.2b, physically being the stiffness of the elastic parts surrounding the FPZ, namely structural stiffness, as shown in Figure 5.2a.

The dynamic process of the FPZ (namely the tensile cracking-induced AE source) and corresponding occurrence conditions in the concrete tensile softening curve are marked red in Figure 5.6b. According to the above analyses, the occurrence conditions of concrete tensile cracking-induced AE phenomena is the rapid stiffness degradation in the FPZ at the starting of nonlinear softening stage. The degree of FPZ stiffness degradation should satisfy the mathematical condition of $\theta_i < \theta_{cr}$, as shown in Figure 5.6b, to allow the occurrence of AE phenomena; such a rapid stiffness degradation triggers a transient jump of displacement/acceleration and later vibrations in the FPZ.

Considering the physical meaning of θ_i in Figure 5.6, it is associated with the (tangent) stiffness of the FPZ, denoted as $K_{FPZ,i}$, as follows:

$$K_{FPZ,i} = \frac{\mathrm{d}F_i}{\mathrm{d}u_i} = \frac{\mathrm{d}F_i}{\frac{l}{2}\mathrm{d}\varepsilon_i} = -\frac{2}{l\tan\theta_i} \tag{5.36}$$

where $\mathrm{d}F_i$, $\mathrm{d}u_i$ and $\mathrm{d}\varepsilon_i$ are the increments of the force, displacement and strain of the FPZ in the i-th strain softening range (see Figure 5.6).

By substituting Equation (5.36) into Equation (5.35), a critical value of $K_{FPZ,i}$, denoted as $K_{FPZ,cr}$, that distinguishes the two different dynamic forms of the FPZ (displacement jump or vibrations) is expressed as:

$$K_{FPZ,cr} = -\frac{2}{l\tan\theta_{cr}} = -K_{structure} \tag{5.37}$$

Equation (5.37) means that the FPZ should have an inelastic (tangent) stiffness ($K_{FPZ,i}$) at the starting of nonlinear softening stage with a value less than the negative value of the structural elastic stiffness of the elastic parts surrounding the FPZ ($K_{structure}$) to allow a transient jump of displacement/acceleration in the FPZ that triggers the AE phenomena.

The above occurrence conditions of the tensile cracking-induced AE phenomena are physically explained in the following. The tensile softening curve shown in Figure 5.6b is a mechanical description at mesoscale for an assembly of microscopical phenomena occurring in the PFZ (Ritchie 2011). Figure 5.7 illustrates microscopical fracture phenomena involved in different stages of the strain-stress constitutive curve of the FPZ (Morgan 2015).

After reaching elastic limit (cracking strain ε_{cr}), micro-cracks occur in the FPZ, leading to a rapid stiffness degradation of the FPZ and manifesting as a sharp stress drop in the strain-stress curve. The micro-cracking develops and lasts for a certain strain range until

θ_{cr} in Figure 5.7, during which more microcracks appear and then gradually coalesce to form cracks of larger sizes in the FPZ, manifesting as continuous stress drops but with gradually reduced degrees of stiffness degradation in the constitutive curve.

With further increasing in strains of the FPZ after θ_{cr} in Figure 5.7, the micro-cracks fully develop into macro-cracks where secondary fracturing phenomena dominate the response. In the case of concrete tensile fracture, the secondary fracturing phenomena are mainly the bridging effect of aggregates (namely the FPZ cannot be fully separated at once due to concrete material heterogeneity with aggregates bridging the cracking paths, as marked brown in Figure 5.7) (Van Mier 1991) and the interlocking between rough surfaces of macro-cracks (namely friction forces between aggregates or at interfaces between aggregates mortar, as marked green in Figure 5.7) (Walraven 1981). Such secondary phenomena provide residual stress in the FPZ, manifesting as continuous stress drops but with very slow rate of stiffness degradation.

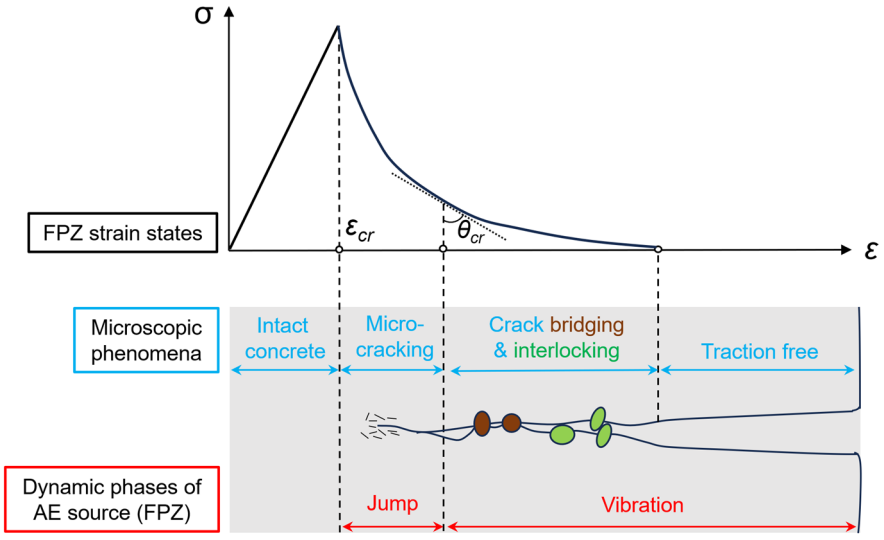

Figure 5.7. Physical interpretation for dynamic process of AE sources (the FPZ) in response to tensile cracking.

A comparison between Figure 5.6b and Figure 5.6 reveals the physical mechanism of the above mathematical conditions for dynamic response of the FPZ (namely tensile cracking-induced AE sources). Specifically, the sources of tensile cracking-induced AE phenomena in concrete are the micro-cracks at cracking tips, which mechanically manifest as sharp stress drops in the FPZ at meso-scale. Such a sharp stress drop triggers transient displacement/acceleration jumps (or called displacement discontinuity/dislocation in classical continuum theory (Chen et al. 2018)) in the FPZ. The jumps last for a short period of time until the micro-cracks develop into macro-cracks, which mechanically

manifest residual stress with slower stiffness degradation rates in the FPZ due to secondary fracturing phenomena. With further decreasing in stiffness degradation rates, the FPZ mathematically follows a dynamic response of trigonometric forms, which physically manifests as vibrations of the FPZ.

5.7 Model analyses II: Influencing factors of tensile cracking-induced AE sources

With the analytical 1D model, it is already possible to analyze, from the perspective of a dynamic system, what are the influencing factors that can affect the parameters of AE signals. In this section, based on the closed-form expressions given by Equation (5.25), we analyze the factors that influence tensile cracking induced AE sources. Three important parameters of AE source signals are selected for analyses, including the source rise time, amplitude and frequency of source signals.

5.7.1 Source rise time

As reviewed in Section 2.3.2.3, the source rise time is an important parameter in classical AE modelling theories (the MT (Ohtsu 1995) and FEM based models (Sause and Richler 2015)), which has decisive effects on the frequency characteristics of modelled AE waves (see Equation (2.8) and Figure 2.11) but is however introduced as assumed values in available theories. As we have obtained closed-form expressions of complete dynamic response of AE sources, the source rise time is analyzed in this sub-section.

The source rise time, denoted as T_{rise}, is defined as the duration of local displacement jump (Ohtsu 1995). Therefore, herein, it is calculated as the time difference between t_1 and t_2 in Equation (5.25) (see also Figure (5.5)). To generalize the results, we transform the external loading conditions of prescribed velocity v_0 (see Figure 5.2) into average strain rate $\dot{\varepsilon}$ of the whole domain as (see Figure 5.2):

$$\dot{\varepsilon} = \frac{2v_0}{2L + l} \tag{5.38}$$

By substituting Equation (5.1), Equation (5.3c), Equation (5.5d), Equation (5.7d) and Equation (5.38) into Equation (5.21), T_{rise} is expressed as:

$$\begin{aligned} T_{rise} &\approx t_2 - t_1 \\ &\approx \frac{1}{\sqrt{\left[\frac{2(1-b_1)}{l(a_1-1)} - \frac{1}{L}\right]\frac{E}{\rho l}}} \ln\left\{ \frac{f_t\left[2L(1-b_1) - l(a_1-1)\right]\sqrt{\left[\frac{2(1-b_1)}{l(a_1-1)} - \frac{1}{L}\right]\frac{1}{E\rho l}}}{\left(1 + \frac{1-b_1}{a_1-1}\right)\dot{\varepsilon}L} \right\} \end{aligned} \tag{5.39}$$

It can be easily found that T_{rise} is positively correlated with concrete tensile strength f_t, and is negatively correlated with the strain rate $\dot{\varepsilon}$ and concrete elasticity modulus E. Further considering the definition of concrete cracking strain ε_{cr} given in Equation (5.5d), T_{rise} is then negatively correlated with ε_{cr}. This means T_{rise} is affected by both concrete inherent material properties and external loading conditions.

More importantly, it should be mentioned that, in Equation (5.39), T_{rise} is positively correlated with both fracture scale l and fracture early-stage ductility coefficient a_1 (proof process for this is detailed in Appendix I). This indicates that the fracture at a relatively larger scale and with more ductility leads to a longer duration of the displacement/ acceleration jump.

5.7.2 Source amplitudes

As the time-domain amplitude is an import AE parameter, it is analyzed in this sub-section. Herein, we consider two amplitudes involved in a source signal: the amplitude at the end of displacement/acceleration-jump stage and the amplitude in the vibration stage, denoted as A_{jump} and $A_{vibrate}$, respectively, as marked in Figure 5.5.

The expression of A_{jump}, namely $\ddot{u}(t_2)$ in Equation (5.25b), is given by Equation (5.23c) (its detailed derivation process can be found in Appendix H). By further substituting Equation (5.1), Equation (5.5d) and Equation (5.7d) into Equation (5.23c), an equivalent expression is derived as:

$$A_{jump} = \ddot{u}(t_2) \approx \frac{(a_1-1)l\varepsilon_{cr}}{2}\left[\frac{2(1-b_1)}{l(a_1-1)} - \frac{1}{L}\right]\frac{ES^*}{m} = \frac{f_t}{2\rho}\left[\frac{2(1-b_1)}{l} - \frac{(a_1-1)}{L}\right] \tag{5.40}$$

It is interesting to note that A_{jump} is independent of external loading conditions. Among other involved parameters, it should be noted that the value of A_{jump} is linearly proportional to concrete strength f_t and the structural scale of undamaged portion L (see Figure 5.2), and is in linearly inverse proportion to fracture early-stage ductility coefficient a_1, density ρ and fracture scale l. This indicates higher amplitudes of displacement/ acceleration jump of the FPZ will be induced in the cases of higher concrete strength, larger structural scale, more brittle fracture, lighter-weight materials and smaller fracture scales.

By substituting Equation (5.24) to Equation (5.25c), the amplitude of AE source at vibration stage, $A_{vibrate}$, is derived as:

$$A_{vibrate} = \left|\sqrt{C_1''^2 + C_2''^2}\left(\frac{2}{\tan\theta_1 ml} - \frac{ES^*}{mL}\right)\right| = \left(\frac{ES^*}{mL} - \frac{2}{\tan\theta_1 ml}\right)\sqrt{\left[u(t_2) - \frac{v_0 ES^* l t_2 - \left(\frac{a_1}{\tan\theta_1} + b_1 ES^*\right) Ll\varepsilon_{cr}}{lES^* - \frac{2L}{\tan\theta_1}}\right]^2 + \frac{mLl\left[\dot{u}(t_2) - \frac{v_0 ES^* l}{lES^* - \frac{2L}{\tan\theta_1}}\right]}{lES^* - \frac{2L}{\tan\theta_1}}} \quad (5.41)$$

where $|*|$ is the absolute value symbol. It can be easily found that the value of $A_{vibrate}$ is positively correlated with the displacement $u(t_2)$ and velocity $\dot{u}(t_2)$ of fracture sources at the end of displacement/acceleration jumps stage. Moreover, there are many other parameters involved in the expression of $A_{vibrate}$, including both concrete material properties (m and E), fracture properties (a_1, b_1 and θ_1), fracturing source scale (S^* and l), structural dimensions (L) and external loading rate (v_0). This indicates that the displacement/acceleration jump at the source performs like a trigger for the AE process. Subsequent vibration of the source is a complicated system response to the trigger, which is further governed by the geometry and properties of the system and external loading conditions.

5.7.3 Source frequency

The frequency characteristics are important AE parameters for characterizing fracturing sources. The peak frequency and average frequency are considered as classical AE indicators for classifying fracturing source types in various quasi-brittle materials (Zheng et al. 2020; Aggelis 2011). The source frequency is analyzed in this sub-section.

Based on Equation (5.25c), the angular frequency of the AE source signals in the vibration stage ($t > t_2$ in Figure 5.5), denoted as ω, is expressed in:

$$\omega = \sqrt{\frac{ES^*}{mL} - \frac{2}{\tan\theta_1 ml}} = \sqrt{\frac{1}{m}\left(\frac{ES^*}{L} - \frac{2}{\tan\theta_1 l}\right)} = \sqrt{\frac{2}{\rho\phi_{FPZ}}\left(K_{structure} - \frac{2}{\tan\theta_1 l}\right)} \quad (5.42)$$

where $K_{structure}$ is the stiffness of elements 1 and 1′ in Figure 5.2b (namely the structural stiffness of elastic area surrounding the FPZ in Figure 5.2a). $\phi_{FPZ} = 2A^* l$ is the volume of the FPZ (see Figure 5.2a).

It can be seen that ω mainly depends on volume of the FPZ (namely mobilised fracture volume), the density ρ and the stiffness of unfractured concrete surrounding the FPZ. This indicates that the smaller fracture scale, lighter-weight material and stiffer structures leads to higher AE source frequency. Moreover, the values of $K_{structure}$ and ρ are similar within a same concrete structure, and thus the frequencies of different tensile-cracking

sources generated in a same structure are mainly determined by fracture scales ϕ (the FPZ size). It can be also inferred that a degraded structural stiffness $K_{structure}$ results to a lower AE source frequency, which may partitially explain the experimental observations that the average frequency of AE signals tends to be gradually reduced in progressive loading processes (Aggelis 2011), because the structural stiffness $K_{structure}$ is gradually degradated during fracture processes.

5.8 Discussion

This section discusses how the above observations from the simplified 1-DoF system can be generalized to more realistic cases of multiple DoF systems.

To derive closed-form expressions for AE sources, the dynamic response of the FPZ (tensile cracking-induced AE sources) is derived by addressing a 1-DoF system in this chapter (see Figure 5.2). This leads to large discrepancy from the dynamic response of the FPZ in real concrete fracturing processes, especially for the vibration stage of the FPZ (the response stage after time t_2 in Figure 5.5), as follows:

First, due to omitting the damping force in establishing the force equilibrium of the FPZ Equation (5.6), there is no amplitude attenuation in the vibration stage (after time t_2 in Figure 5.5). In real concrete fracturing processes, vibration amplitudes of the FPZ should attenuate to zero in a short period after t_2 due to the existence of damping force and the geometric spreading loss of vibration energy (see Section 3.2.3). This will be further illustrated in Chapter 6.

Second, only one vibration mode and thus one frequency and one vibration amplitude can be considered in the adopted simplified 1-DoF system. A concrete structure is an infinite-DoF system. If the 1D bar shown in Figure 5.2a could be discretized into more DoFs, the expressions of the AE sources (namely dynamic response of the FPZ) in vibration stage would be in following form according to modal superposition principle (Nickell 1976):

$$\ddot{u}(t) = \sum_{i=1}^{n\to\infty} A_{vibrate}(i)\sin\left[\omega(i)t + \varphi(i)\right] \quad t > t_2 \tag{5.43a}$$

$$\text{with } \omega(i) = \sqrt{\frac{iES^*}{Lm} - \frac{2}{\tan\theta_1 ml}} \tag{5.43b}$$

where n is the DOF number of the system, namely the number of vibration modes. $A_{vibrate}(i)$, $\omega(i)$ and $\varphi(i)$ are the amplitudes, angular frequency and phase position of i-th vibration mode.

A closed-form expression of involved parameters in Equation (5.41) cannot be analytically obtained. Nevertheless, the analytical modelling has illuminated the mechanism of

a tensile cracking-induced AE process and has identified factors that influence source response. Moreover, it should be mentioned that analytical modelling conducted in this chapter is a simple analytical version of the numerical lattice model proposed in Chapter 3. Therefore, in the next two chapters, we will numerically quantify AE sources induced by concrete tensile cracking through the proposed lattice model.

5.9 Summary

This chapter analytically addresses the long-term standing problem of AE source mechanisms induced by concrete tensile cracking in a 1D case. A simplified one-degree-of-freedom (1-DoF) dynamic system is employed to study the dynamic response of a localized concrete tensile cracking area (namely fracture process zone (FPZ)). Such a dynamic response of the FPZ is considered as a tensile cracking-induced AE source. By analysing such a simple dynamic system, we uncover the physical principles underlying the tensile cracking-induced AE phenomena. The main conclusions are as follows:

- Mathematical and physical occurrence conditions of tensile cracking-induced AE phenomena: we quantify the relationship between concrete tensile softening behavior and AE source response. It is found that a tensile cracking-induced AE source is induced by rapid degradation of the FPZ stiffness due to sudden propagation of microcracks in early softening stages. Such a rapid stiffness degradation should meet a quantitative condition that the tangent stiffness of the inelastic FPZ is less than the negative of the structural stiffness of the elastic parts surrounding the FPZ, which mathematically leads to an exponential solution form of FPZ dynamic response and physically manifests as a local displacement jump in the FPZ.

  When the degradation degree of the FPZ stiffness is reduced in later-stage softening stages where the secondary fracturing activities of macrocracks dominate the FPZ fracturing behaviours, the tangent stiffness of the inelastic FPZ gradually increases to a level higher than the negative of the structural stiffness of the elastic parts surrounding the FPZ. Such an increased tangent stiffness then mathematically leads to a trigonometric solution form of FPZ dynamic response and physically manifests as vibrations of the FPZ.

- Influence factors of tensile cracking-induced AE sources: we identify the key factors that influence different typical AE source parameters. Among various source parameters, we found that the source frequency is mainly determined by the volume of the FPZ (namely the volume of mobilised areas), the material density ρ and the stiffness of unfractured concrete surrounding the FPZ (namely structural stiffness). This indicates that a smaller fracture scale, lighter-weight material and stiffer structures leads to higher AE source frequency.

The source mechanisms of concrete tensile cracking-induced AE phenomena revealed in the simplified 1-DoF system will be further discussed in a more realistic 2D case in Chapter 6. The identified influencing factors of AE source parameters will be further quantified in Chapter 7 through the lattice model presented in previous chapters.

6. Revealing the source mechanisms of concrete tensile cracking-induced acoustic emission: 2D lattice modelling

6.1 Introduction

In the previous chapter, we examined the acoustic emission (AE) phenomena induced by concrete tensile cracking through the analysis of a fracture area in a one-dimensional (1D) scenario, which is further treated as a simplified one-degree-of-freedom (1-DoF) system, with large discrepancy from reality. Therefore, this chapter further investigates the source mechanisms underlying the AE phenomena associated with concrete tensile cracking in a more realistic two-dimensional (2D) context, utilizing the lattice model proposed in Section 3.2.

In addition, as reviewed in Chapter 2, the correlations between concrete tensile cracking behaviour and the resulting AE phenomena are still controversial in the literature. First, existing AE source theories present inconsistencies, attributing the origin of AE phenomena to various mechanisms and processes occurring at different scales. Second, the relationship between concrete fracture energy and AE phenomena are controversial in the literature. Accordingly, this chapter seeks to critically examine the available AE source theories and the relationship between concrete fracture energy and AE phenomena in light of the observations obtained through lattice modelling.

The structure of this chapter is as follows: Section 6.2 outlines the numerical model adopted for the analyses. Section 6.3 explores the source mechanisms of AE phenomena induced by concrete tensile cracking by analysing a representative numerical source signal (defined herein as a vibration signal recorded directly at the fracture location). Section 6.4 discusses the connection between available AE source theories and the relationship between concrete fracture energy and AE phenomena based on the numerical findings.

6.2 Description of adopted numerical model

As discussed in Chapter 2, the AE signals received in experiments are influenced by many factors including AE sources, wave propagation and sensor response, which cannot be decoupled in experimental measurements. To clearly uncover the relationship between concrete tensile cracking behaviors and induced AE signals, we numerically investigate the AE source signals in lattice modelling by excluding the influence from wave propagation and sensor response. Note that this is impossible with experimental methods. Herein, a numerical source signal is defined as the acceleration signal of a node directly linked by a broken lattice element, for which the influence from spatial wave propagation and sensor response are minimized.

Throughout this chapter, the same lattice simulation case of three-point bending test of a notched unreinforced concrete beam that has been tested and simulated in Chapter 4 is

adopted for numerical analyses. The adopted numerical model is illustrated in Figure 6.1. The first numerical source signal in the loading process is selected as a representative example for the analysis. This signal is triggered by the tensile failure of a lattice element positioned at the upper left corner of the notch, noted as E0 and marked red in Figure 6.1. The accelerations in x direction (dominant deformation direction) of a node located at (x = 272.5 mm, y = 30 mm) (namely the left-side node of the source element E0), labeled as S0 and marked green in Figure 6.1, are used to mimic a tensile cracking-induced AE source signal.

The model inputs are the same as those described in Section 4.3.1. The only difference is that a smaller time step of 2×10^{-8} s is used to achieve a higher sampling rate of 50 MHz, since this chapter focuses on the AE source signals directly at fracture areas with a response of higher frequency than corresponding signals after spatial wave propagation (this will be further demonstrated in Section 6.3).

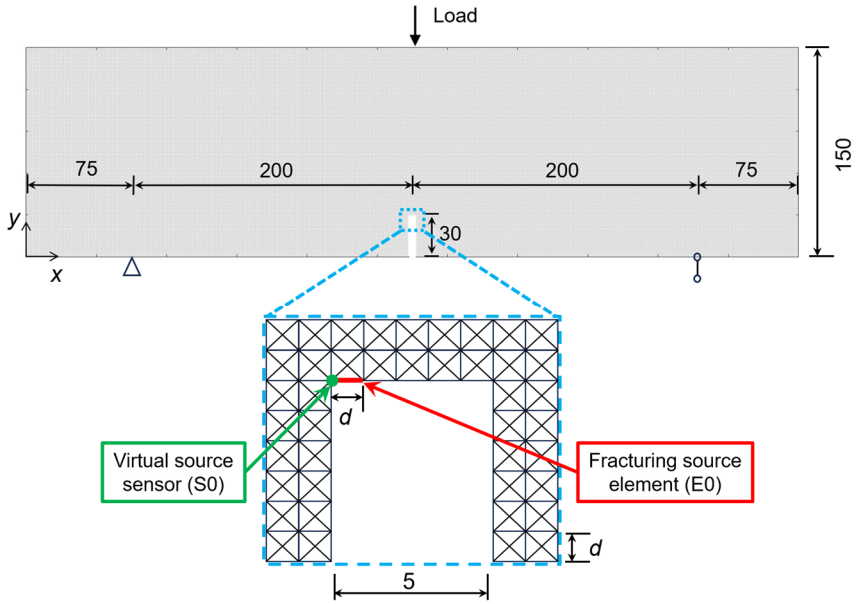

Figure 6.1 Numerical model adopted for analysing concrete tensile cracking-induced AE sources (unit: mm).

6.3 Source mechanisms of tensile cracking-induced AE

In the previous chapter, we analysed how concrete tensile cracking behaviour is linked to AE phenomena in a simplified one-degree-of-freedom (1-DoF) system (see Section 5.6); nevertheless, the analysis of a 1-DoF case leads to large discrepancy from tensile cracking-induced AE phenomena in real concrete fracturing processes (see Section 5.8).

Therefore, this section seeks to further elucidate the source mechanisms underlying AE phenomena associated with concrete tensile cracking in a more realistic 2D case, through the analysis of a representative numerical source signal derived from lattice modelling.

Figure 6.2 shows a typical AE source signal induced by the tensile fracture of source element E0 and recorded by virtual source sensor S0 (see Figure 6.2). It should be mentioned that the time of presented AE source signal is not the actual simulation time but has been normalized to represent a signal pre-trigger time of 0.01 ms (see appendix A for definition of pre-trigger time). The source signal is in the form of Gaussian pulses (Bauer et al. 1984a), with a short duration of around 10 μs in time domain and a wide frequency range up to 2 MHz with peak frequency at around 600 kHz.

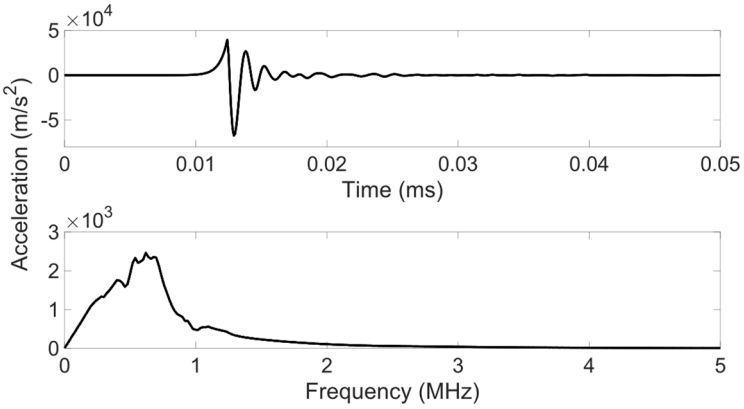

Figure 6.2 The first tensile cracking-induced AE source signal induced by source element E0 and received by virtual sensor S0.

Compared to those received at a far-field sensor as shown in Figure 4.7, due to the excluding of spatial wave attenuation, the source signal shows higher amplitudes and shorter duration in time domain and a wider frequency range.

Compared to the analytical source signal of a 1-DoF system shown in Figure 5.5 (the numerical and analytical models have similar inputs), the numerical source signal shows a similar two-phase dynamic response including a first stage of acceleration jump in terms of an exponential shape and then a second stage of vibrations in terms of a trigonometric shape. Nevertheless, the numerical dynamic response in the later vibration stage is largely different from that of the analytical one. The modelled 2D case with more DoFs are closer to a real concrete specimen and thus the numerical source signal contains more vibration modes manifesting as a wide range of frequency response. Moreover, as the damping force has been included in the lattice simulation, the numerical time-domain amplitudes gradually attenuate and disappear in a short period in the vibration stage.

In the following, the source mechanisms of AE signals induced by concrete tensile cracking are investigated by analysing both the local dynamic responses and the global mechanical behaviour of the numerical model (see Figure 6.1), in relation to the occurrence of the AE source signal presented in Figure 6.2.

6.3.1 Micro-mechanical behaviors associated with AE phenomena

Figure 6.3 shows the local behaviors induced by tensile failure of the source element E0, including the dynamic response of the source node S0 (in terms of displacement, velocity and acceleration) and the evolution of strain and stress of corresponding fracturing source element E0. The cracking strain ε_{cr} and first tensile softening strain limit $a_1\varepsilon_{cr}$ defined in the constitutive law (see Figure 3.2) are marked red and blue, respectively, in Figure 6.3a. The occurrence time corresponding to ε_{cr} and $a_1\varepsilon_{cr}$ are marked as t_1 and t_2, respectively, in Figure 6.3e.

Similar to the 1-DoF case shown in Figure 5.5, during $t_1 \sim t_2$ corresponding to early strain softening stage of E0 characterized by a rapid stiffness degradation ($\varepsilon_{cr} \sim a_1\varepsilon_{cr}$), there is a drop in stress of fracturing source element E0 (Figure 6.3b) and a jump in both displacement (Figure 6.3c), velocity (Figure 6.3d) and acceleration (Figure 6.3e) of source node S0. Physically, a broken lattice element with tensile softening behavior represents a fracturing area as part of the whole FPZ at crack tip as illustrated in Section 3.2 (this will be discussed in detail in Chapter 7). According to the relationship between the FPZ strain states and microscopic fracturing activities as shown in Figure 5.7, such a rapid stiffness degradation of source element E0 in early softening stage is physically attributed to the sudden propagation of microcracks in the fracturing area represented by element E0.

After t_2 when the strain of E0 exceeds its first tensile softening strain limit $a_1\varepsilon_{cr}$ characterized by a reduced stiffness degradation rate, the source node S0 starts to vibrate. The vibration trend is more obvious in the acceleration (Figure 6.3e) than the velocity (Figure 6.3c) and displacement (Figure 6.3d), because the acceleration is more sensitive to high-frequency signals as discussed in Section 3.6.1. This stage physically corresponds to the arrest of microcracking and the occurrence of secondary fracturing phenomena of macrocracks in the fracturing area represented by element E0 (see Figure 5.7).

The vibrations of S0 are then rapidly attenuated in a short period due to the implemented numerical Rayleigh damping. The strain value of source element E0 and corresponding occurrence time (denoted as t_3) at the end of source vibration stage are marked gray in Figure 6.3a and Figure 6.3e, respectively. At the end of source vibrations, the strain value of source element E0 is far less than its second tensile softening strain limit $a_2\varepsilon_{cr}$ defined in Figure 3.2.

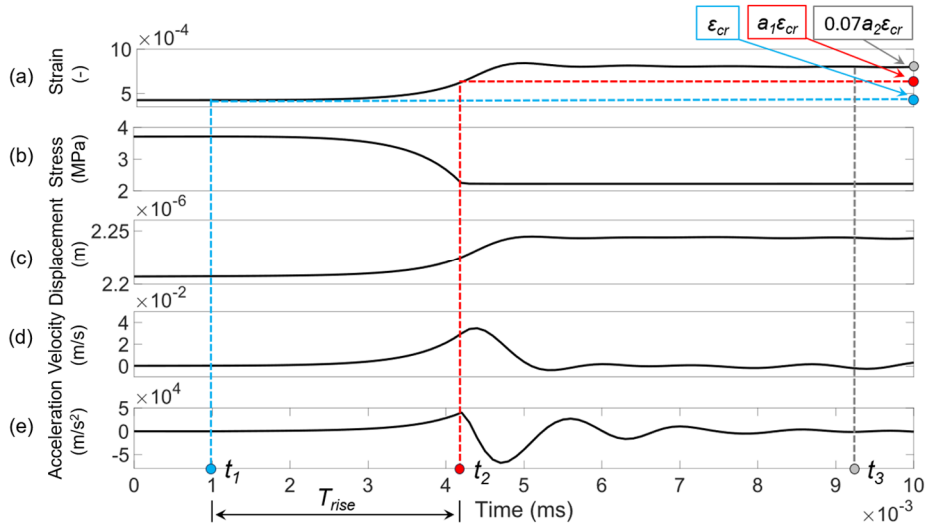

Figure 6.3 Local behaviour of source node S0 and fracturing source element E0: (a) strain of fracturing source element E0; (b) stress of fracturing source element E0 (MPa); (c) *x*-direction displacement of source node S0 (m); (d) *x*-direction velocity of source node S0 (m/s); (e) *x*-direction acceleration of source node S0 (m/s^2).

6.3.2 Macro-mechanical behaviors associated with AE phenomena

Figure 6.4 shows the global mechanical response of the notched beam specimen corresponding to the fracturing moment of source element E0. The load-deflection curve in a strain stage of source element E0 from ε_{cr} to $0.07a_2\varepsilon_{cr}$ is zoomed in in Figure 6.4, corresponding to the occurrence period of the source signal shown in Figure 6.2 (namely the period of $t_1 \sim t_3$ marked in Figure 6.3). Three critical strain values of fracturing source element E0, ε_{cr}, $a_1\varepsilon_{cr}$ and $0.07a_2\varepsilon_{cr}$, are marked red in Figure 6.4.

It can be observed that there is a sharp drop in global load and a sudden increase in global mid-span displacement in the strain stage $\varepsilon_{cr} \sim a_1\varepsilon_{cr}$ of E0 corresponding to the jump stage of source node S0 during $t_1 \sim t_2$ (see Figure 6.3). In later tensile softening stages when the strain of E0 exceeding $a_1\varepsilon_{cr}$, the global load is then gradually recovered following a path with small fluctuations (vibrations). Such global behavior is physically explained as follows:

In early tensile softening stage of fracturing element E0, physically corresponding to the sudden propagation of microcracks (see Figure 5.7), the rapid stiffness degradation of E0 at the microscale leads to a sharp global stiffness degradation of the structure, because global stiffness of the whole specimen is determined by local stiffness of each involved sub-area (namely each lattice element). Such a sharp degradation of structural stiffness mechanically manifests a sharp drop in global load.

In later tensile softening stages, when the strain of fractured element E0 is larger than $a_1\varepsilon_{cr}$, physically corresponding to arrest of micro-crack propagation and the occurrence of secondary fracturing phenomena of macro-cracks (cracking bridging and interlocking in Figure 5.7), the reduction in stiffness degradation rates of a local fracturing area leads to a decreased rate of global stiffness degradation of the whole structure, during which the global load is then partially recovered following a path with reduced global stiffness. The reduction in global stiffness due to tensile failure of source element E0 is illustrated by an intersection angle $\theta_{reduced}$ between original and recovered load-deflection curves as marked blue in Figure 6.4. The recovered load then further increases until new micrcrack suddenly propagates (new lattice element breakage) when the material fracture toughness is reached again.

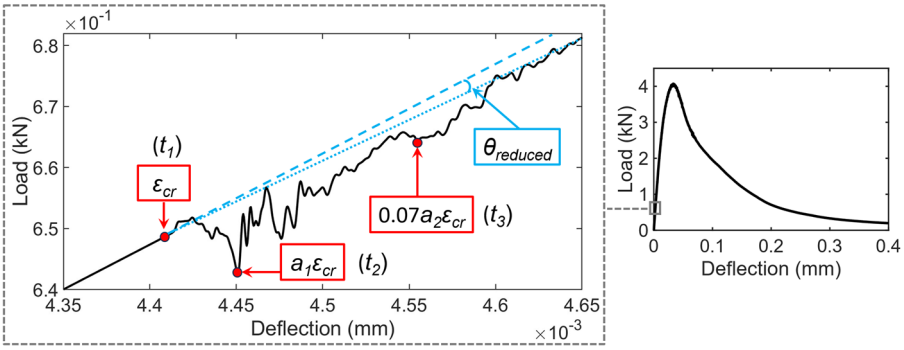

Figure 6.4 Global load-deflection behavior at the fracturing moment of source element E0.

6.4 Discussion on the correlations between concrete tensile cracking behaviour and the resulting AE phenomena

This section discusses available theories proposed in literature that explains the relationships between concrete tensile cracking behaviour and induced AE phenomena in various aspects based on the numerical results.

6.4.1 Connection between available AE source theories across different scales

This sub-section discusses the connection between available theories in literature for explaining the tensile cracking-induced AE phenomena. Readers are referred to Section 2.3.2 for details of mentioned AE source theories.

As illustrated in Figure 5.6, the physical nature of tensile cracking-induced AE signals is the sudden propagation of micro-cracks at crack tips. Such a physical phenomenon is mechanically described as sharp stiffness degradation locally, which results in a microscopic displacement discontinuity (jump) in a local fracturing area (see Figure 6.3). This

microscopic observation is consistent with the AE source explanation provided by the continuum mechanics-based local dislocation theories, e.g., the MT (Ohtsu 1995) (see Section 2.3.2.3). In addition, a local stiffness degradation weakens the global stiffness of the whole structure, and thus dynamically leads to a small drop in global load in the macroscopic load-deflection curve (see Figure 6.4). This macroscopic observation is consistent with the local load-drop instability theory for explaining AE sources (Li, Ren, and Li 2024) (see Section 2.3.2.2).

Therefore, the local dislocation theory and the local load-drop instability theory are the mechanical description for a same physical phenomenon of tensile cracking-induced AE at microscopic and macroscopic scales, respectively.

The local snap-back instability theory (Carpinteri et al. 2016) (see Section 2.3.2.2) explains AE phenomena in a similar way to the local stress-drop instability theory. The only difference lies in the need for a drop in global displacement together with the drop in global load to emit AE energy in the local snap-back instability theory (see Figure 2.6 and 2.7). As shown in Figure 6.4, no drop in mid-span displacement is observed when the source element E0 is fractured in the lattice simulation. This means the local snap-back instability (local drop in both global load and global deflection) might not be a necessary condition for the occurrence of AE phenomenon. The local stress-drop instability theory could be a more generalized explanation for AE source mechanism at macroscopic level.

6.4.2 AE phenomenon & concrete fracture energy

The relationship between concrete fracture energy and AE energy is still controversial in the research community. Positive (Landis and Baillon 2002; Han, Yang, and Xu 2018) and negative (Carpinteri and Accornero 2018; Carpinteri et al. 2016) correlations are proposed in literature between concrete fracture energy and AE energy, both established by fitting experimental data. The relationship between concrete fracture energy and AE phenomenon is discussed in this sub-section.

To illustrate the relationship between fracture energy and AE phenomena, additional simulation cases are performed by varying the values of the second and third tensile softening parameters a_2 and a_3 in the adopted tensile softening constitutive law (see Section 3.2.1). In these numerical cases, all model inputs are kept the same as those described in Section 6.2 except a_2 and a_3. Figure 6.5 shows typical simulated AE source signals received at source node S0 with different values of a_2 and a_3. The simulated source signals are identical when varying a_2 and a_3.

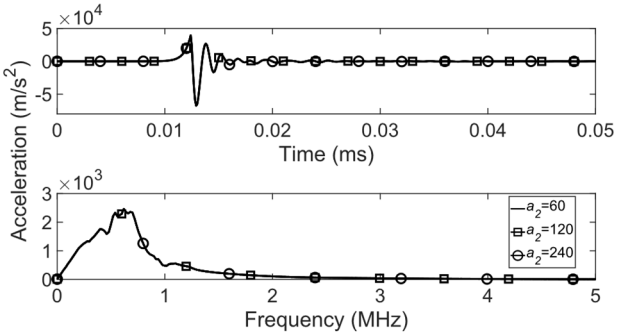

(a)

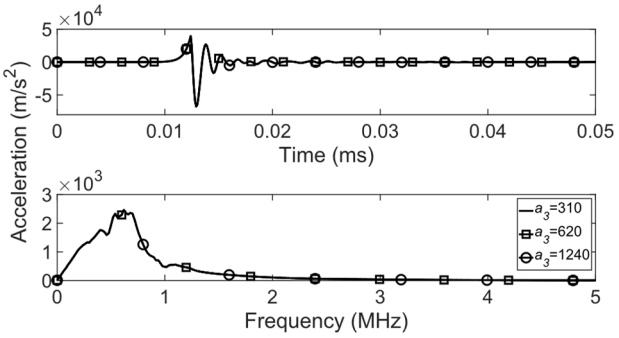

(b)

Figure 6.5 Typical fracture-induced AE source signals received by virtual sensor S0 in: (a) simulation case 5 with various a_2 values and (b) simulation case 6 with various a_3 values.

As shown in Figure 6.6a, the microscopic concrete tensile fracture energy at element level is calculated as the area under the stress-displacement curve in the whole nonlinear stage ($d\varepsilon_{cr}$~$a_3 d\varepsilon_{cr}$). As demonstrated in Figure 6.5, an AE source signal is only associated to concrete early-stage tensile softening behavior (area marked by red cross in displacement stage of $d\varepsilon_{cr}$~$a_1 d\varepsilon_{cr}$ in Figure 6.6a), while it is irrelative to the later-stage fracture behavior ($a_1 d\varepsilon_{cr}$~$a_3 d\varepsilon_{cr}$ in Figure 6.6a). This indicates that there is no direct correlation between microscopic concrete fracture energy and AE phenomenon.

At macroscopic level, the concrete tensile fracture energy is positively related to the whole area under the global load-deflection curve. The standard calculation procedure of concrete fracture energy using the load-deflection curve in a three-point test can be found in the work of Peterson (Peterson 1980). However, as discussed in Section 6.3.2, the tensile cracking-induced AE phenomena are only related to the local load-drop instabilities in a global load-deflection curve, namely the areas marked by red cross in Figure 6.6b. This indicates that there is no direct connection between macroscopic concrete fracture

energy and AE phenomenon. It should be mentioned that the local load-drop instabilities are plotted exaggeratively in Figure 6.6b for better illustration, while such local load-drop instabilities in lattice simulation are on a much smaller scale as shown in Figure 6.4 (see also Figure 4.8).

Physically, the Mode-I (tensile) fracture energy is the total energy dissipated by all fracturing activities occurring in a concrete tensile fracturing process (see Figure 5.7). Nevertheless, AE phenomena in concrete tensile fracturing processes are only related to sudden propagation and arrest of microcracks among various fracturing activities. Such AE-related microcracking activities are only related to a small portion of the total dissipated energy, namely fracture energy. Therefore, AE phenomena should not have a direct relationship with concrete Mode-I fracture energy.

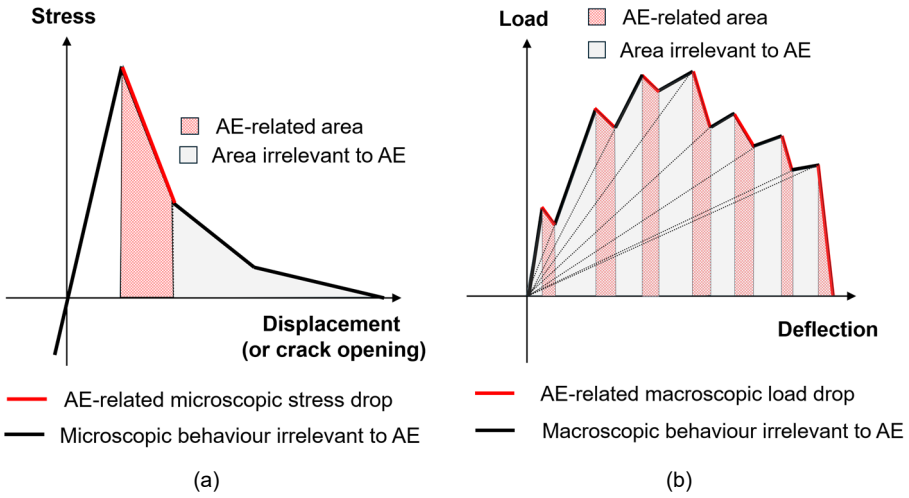

Figure 6.6 Illustration for the relationship between concrete fracture energy and AE phenomenon: (a) micro-scale and (b) macro-scale.

6.5 Summary

This chapter numerically investigates the mechanisms underlying the AE phenomena associated with concrete tensile cracking in a more realistic 2D case by utilizing the lattice model that has been proposed and validated in chapters 3 and 4.

Through analysing a typical numerical AE source signal directly recorded at a local tensile fracture area, as well as the local and global mechanical behaviour associated with the source AE signal, we derive the following conclusions:

- The dynamic response of a concrete tensile cracking area consists of a first dynamic stage of exponential-shape acceleration jump and a second stage of attenuated vibrations. Such a two-stage dynamic response forms a Gaussian pulse in acceleration of a local fracture area that generates acoustic emission signals.
- The physical origin of tensile cracking-induced AE phenomena is the sudden propagation microcracks, mechanically leading to a rapid stiffness degradation of both local fracturing area and the whole structure. Such a rapid stiffness degradation simultaneously induces a sudden displacement jump of the local fracturing area at microscopic level and a sharp drop in global load at macroscopic level.

Based on the numerical analyses, we then discuss the classical theories available in literature for explain AE phenomena in various aspects and derive the following conclusions:

- The local dislocation theory and the local load-drop instability theory are the mechanical description for a same physical phenomenon of tensile cracking-induced AE at microscopic and macroscopic levels, respectively.
- There is no direct relationship between AE phenomena and concrete Mode-I (tensile) fracture energy, as tensile cracking-induced AE phenomena is only related to the sudden propagation and arrest of microcracks among various fracturing activities. AE phenomena are only associated with a small portion of all dissipated fracture energy.

7. Quantifying concrete tensile cracking-induced acoustic emission sources through lattice modelling

7.1 Introduction

Building on the qualitative analysis of acoustic emission (AE) sources generated by concrete tensile cracking presented in the previous chapter, this chapter shifts the focus toward a quantitative evaluation of AE source characteristics.

As discussed in Chapter 2, there is currently no reliable method for quantitatively assessing tensile cracking behaviour in concrete using AE measurements. This limitation stems from the complex interactions among AE source mechanisms, wave propagation phenomena, and sensor responses in experimental observations. To address this challenge, it is essential to establish case-independent, quantitative relationships between concrete tensile cracking behaviour and AE source characteristics, which are isolated from the uncertainties introduced by wave propagation and sensor effects. Numerical modelling offers a promising approach for achieving this objective.

This chapter conducts a numerical sensitivity analysis using the lattice modelling framework introduced in Chapters 3 and 4. This analysis quantifies the relationships between tensile cracking characteristics and corresponding AE source parameters. The primary goal is to identify key deterministic factors that govern AE source behaviour and to develop these into quantitative AE indicators linked to tensile cracking. These indicators are then applied to practical AE monitoring scenarios to assess their effectiveness in evaluating concrete cracking.

This chapter is organized as follows: Section 7.2 presents a numerical sensitivity study using lattice modelling to quantify the influence of various tensile cracking factors on typical AE source parameters. Section 7.3 evaluates the significance of each influencing factor and identifies the key parameters that deterministically govern AE source behaviour. A quantitative AE indicator is proposed based on the relationship between these factors and the AE source characteristics. Section 7.4 demonstrates the practical application of the proposed AE indicator through several case studies. Section 7.5 provides a critical discussion comparing the current findings with classical AE source theories, particularly focusing on the determinants of AE frequency characteristics.

7.2 Numerical sensitivity study on AE source parameters

To develop reliable AE characterization methods for concrete tensile cracking behaviour, we need first to assess different influencing factors associated with concrete tensile cracking behaviour on the generated AE source parameters, isolating the uncertainties introduced by wave propagation and sensor effect in experiments. In Chapter 5, the influencing factors of AE sources induced by concrete tensile cracking were identified through the analysis of a single degree-of-freedom (DoF) system (see Section 5.7). However, the insights derived from the single DoF system are limited in their generalizability and quantitative applicability to AE source characterization. Therefore, this section seeks to quantify the previously identified influencing factors through a numerical parametric study within a more realistic two-dimensional (2D) framework, employing the lattice model introduced in Section 3.2.

Throughout this chapter, the same lattice simulation case of the three-point bending test of a notched concrete beam used in chapter 6 (see Section 6.2) that has been experimentally validated in Chapter 4 is adopted for numerical analyses. The effects of the influencing factors of concrete tensile cracking-induced AE sources that have been identified by analytical modelling in Section 5.7 are investigated through six numerical cases. The parameters adopted in different numerical cases are detailed in Table 7.1. Simulation case 0 serves as a benchmark corresponding to the case presented in Chapter 6, for which the parameters correspond to properties of the physical notched specimen listed in Table 3.1. Model parameters are changed in the remaining numerical cases (cases 1-6) to investigate the effect of changed parameters on generated AE sources. The model parameter investigated in each case is highlighted gray in Table 7.1.

A uniform lattice network is adopted for all the simulation cases, namely all the elements are kept at the same grid level in each simulation case. It should be mentioned that the numerical case 5 in Table 7.1 involves various lattice grid levels d. In Section 3.2.1, we have introduced the fracture energy regularization technique for the tensile softening parameters of diagonal and orthogonal elements with different element sizes l involved in a same lattice grid level d (see Figure 3.2). Herein, the same concept is extended to lattice elements involved in different lattice grid level d. The softening parameters only calibrated once for orthogonal elements involved in a certain lattice grid level d_0 with $l = d_0$, following the calibration procedure shown in Figure 3.3; other elements with different sizes ($l \neq d_0$), including diagonal elements involved in a same grid d_0 and all elements involved in different grid levels, are obtained by regularizing their fracture energy. Specifically, denoting the calibrated softening parameters of element size $l = d_0$ as $a_i(d_0)$ with $i = 1, 2, 3$ (see Figure 3.2), the tensile softening parameters of other element sizes $l \neq d_0$, denoted as $a_i(l)$, are regularized as:

$$a_i(l) = \frac{a_i(d_0)d_0}{l} \tag{7.1}$$

Herein, the softening parameters are calibrated based on orthogonal elements involved in a 1-mm grid size (namely d_0=1 mm) and those of all other elements are regularized by Equation (7.1). As shown in Figure 3.2, after being regularized by Equation (7.1), lattice elements of different sizes have a same stress-displacement (stress-crack opening) constitutive law and thus a same fracture energy. The effects of fracture energy regularization on modelling AE source signals are detailed in Appendix J, while its effects on simulating concrete mechanical response are demonstrated in Appendix K(see also the work of Aydin (Aydin, Tuncay, and Binici 2018)).

Table 7.1 Model parameters of different simulation cases.

Case number	Material density ρ	Elastic modulus E	Tensile strength f_t	*Fracture parameter $a_1(d_0)$	Grid size d	CMOD rate $\Delta\dot{u}$
(unit)	(kg/m^3)	(GPa)	(MPa)	(-)	(mm)	(m/s)
[factor]	[×10^3]	[-]	[-]	[-]	[-]	[×10^{-6}]
0	2.31	35.2	3.15	5.5	1	1
1	1.5~3.0	35.2	3.15	5.5	1	1
2	2.31	27~44	3.15	5.5	1	1
3	2.31	35.2	1.5~5	5.5	1	1
4	2.31	35.2	3.15	1~10	1	1
5	2.31	35.2	3.15	5.5	0.05~5	1
6	2.31	35.2	3.15	5.5	1	0.01~10

* The listed values of tensile softening parameters are calibration results for lattice elements of 1 mm size ($l = d_0$=1 mm). Tensile softening parameters of elements with sizes different than d_0 ($l \neq d_0$) are regularized by Equation (7.1).

In the following, we separately investigate the effect of each influencing factor on the AE source response. The accelerations in x direction of source node S1 triggered by the tensile failure of critical element E0 are used to present an AE source signal for analyses (see Figure 6.1). As illustrated in chapter 6, a concrete tensile cracking-induced AE source signal is in the form of Gaussian pulses (see Figure 6.2), for which the peak (central) frequency and time-domain peak amplitude are two most important signal parameters (Bauer et al. 1984a). Moreover, the source rise time T_{rise}, defined as the duration of local displacement jump/discontinuity (dislocation), is an important parameter in classical AE

modelling theories, as reviewed in Section 2.3.2.3. Therefore, these three parameters are selected as typical parameters of AE source signals for the following analyses.

Readers are referred to Appendix A for the definition of peak frequency and time-domain peak amplitude. Since the source rise time T_{rise} is defined as the duration of local dislocation (displacement jump) (Ohtsu 1995), it is herein calculated as the time interval corresponding to the strain stage ε_{cr}~$a_1\varepsilon_{cr}$ of the critical element E0 (see Figure 6.3).

7.2.1 Material properties

This subsection investigates the influence of concrete material properties on AE source signals, corresponding to simulation Cases 1–3 presented in Table 7.1. The selected parametric range for concrete density ρ encompasses various concrete types, including both high-density (Khalaf, Ban, and Ramli 2019) and lightweight concrete (Newman and Owens 2003). The studied parametric ranges for elastic modulus E and tensile strength f_t are selected covering common concrete classes (C12~C90) according to fib Model Code 2010 (MC2010) (Walraven 2012).

Figure 7.1 shows the effects of concrete density ρ on three selected typical AE source parameters. Within the investigated parameter ranges, concrete density ρ is linearly proportional to source rise time T_{rise} and is inversely proportional to peak frequency and peak amplitude. This indicates that concrete with lighter weights generates AE source signals of higher amplitudes and higher-frequency contents.

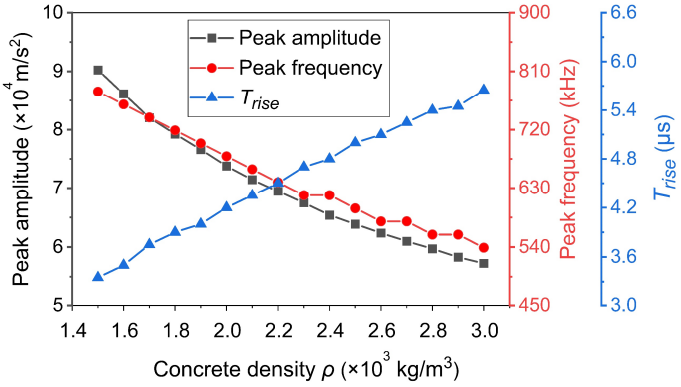

Figure 7.1 Effects of concrete density ρ on three AE source parameters in simulation case 1.

Figure 7.2 shows the effects of Young's modulus E on three selected typical AE source parameters. Within the investigated parameter ranges, Young's modulus E is positively correlated with peak frequency and peak amplitude and is negatively correlated with

source rise time T_{rise}. This indicates that concrete of higher elasticity generates AE source signals of higher amplitudes and higher-frequency contents.

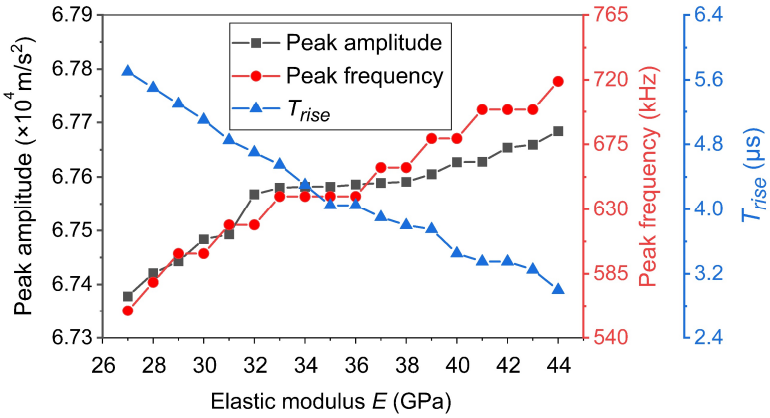

Figure 7.2 Effects of Young's modulus E on three AE source parameters in simulation case 2.

Figure 7.3 shows the effects of concrete tensile strength f_t on three selected typical AE source parameters. Within the investigated parameter ranges, tensile strength f_t is positively correlated with peak amplitude and source rise time T_{rise}, while the peak frequency remains the same value when varying f_t. This indicates that concrete of higher strength generates AE source signals of higher amplitudes.

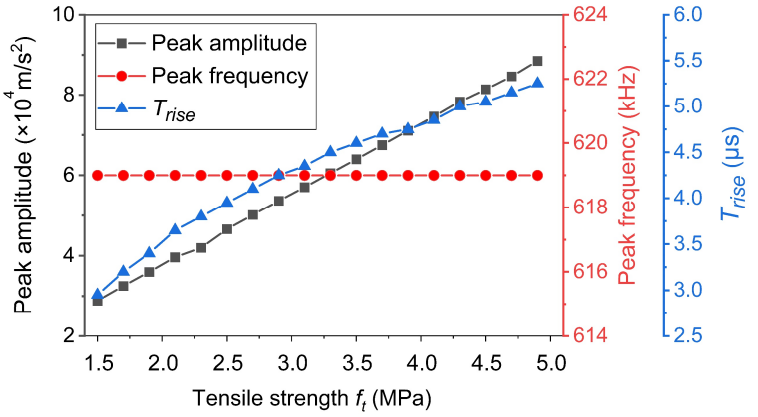

Figure 7.3 Effects of concrete tensile strength f_t on three AE source parameters in simulation case 3.

7.2.2 Fracture parameters

This sub-section studies the influence of the first tensile softening parameters a_1 defined in the constructive law of lattice elements (see Figure 3.2) on induced AE source signals,

corresponding to simulation Cases 4 in Table 7.1. We do not further consider the other two softening parameters involved in the adopted tensile constitutive law (a_2 and a_3 in Figure 3.2), because they are irrelevant to AE phenomena as demonstrated in both Section 5.7 and Section 6.4.

Figure 7.4 shows the effects of the first tensile softening parameter a_1 on three selected typical AE source parameters. The peak frequency is independent of a_1. The source rise time T_{rise} is positively correlative with a_1, because a larger a_1 value leads to a wider strain range of ε_{cr}~$a_1\varepsilon_{cr}$ and thus a longer duration of source jump stage (see Figure 5.6). Moreover, the peak amplitude is negatively correlative with a_1. This indicates that more brittle fracture results in higher source amplitudes, as a_1 physically characterizes the brittleness of concrete fracture in an early softening stage as illustrated in Figure 5.7.

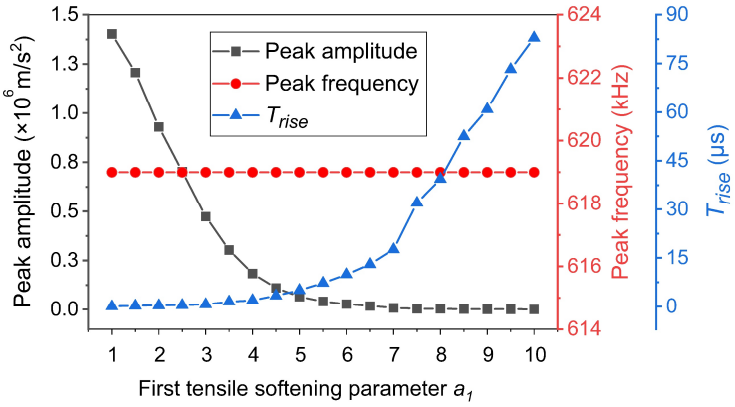

Figure 7.4 Effects of concrete tensile fracture parameter a_1 on three AE source parameters in simulation case 4.

7.2.3 Mesh size

This sub-section discusses the mesh size sensitivity of simulated AE source signals corresponding to Case 5 in Table 7.1. For different discretization levels *d*, dimensions of the notch in the specimen are kept the same, namely 5-mm width and 30-mm depth (see Figure 6.1).

Figure 7.5 shows the effects of lattice grid size *d* on three selected typical AE source parameters. Two time-domain parameters, peak amplitude and source rise time T_{rise}, are positively correlated with *d*, while source peak frequency dramatically decreases with the increase of *d*.

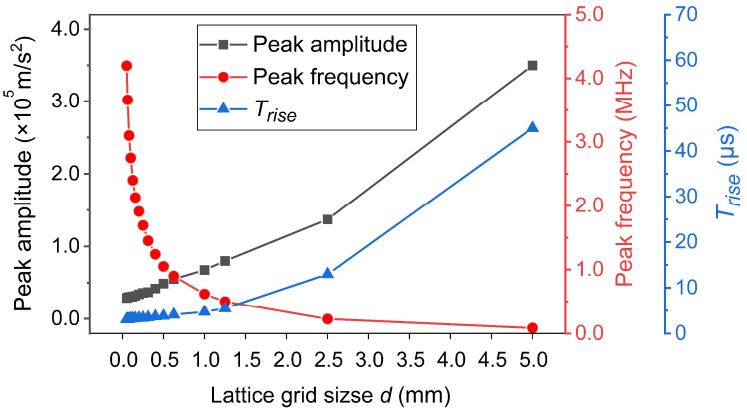

Figure 7.5 Effects of lattice grid size d on three AE source parameters in simulation case 5.

7.2.4 External loading rate

This sub-section investigates the influence of external loading rate on induced AE source signals (Case 6 in Table 7.1). The proposed lattice model adopts a rate-independent constitutive model (see Figure 3.2) and thus cannot realistically consider the dynamic amplification effect of concrete constitutive behavior in response to high-speed dynamic/impact loads (Gao et al. 2021). Therefore, small values of CMOD rate $\Delta\dot{u}$ in a range of $0.01\sim10\times10^{-6}$ m/s are selected for analyses, being restricted to quasi-static loading conditions.

Figure 7.6 shows the effects of CMOD rate $\Delta\dot{u}$ on three selected typical AE source parameters. Within the investigated parameter ranges, CMOD rate $\Delta\dot{u}$ is positively and negatively correlated with peak amplitude and source rise time T_{rise}, respectively, while the peak frequency is irrelevant to external load rate. This is because external loading conditions influence mainly the early-stage displacement jump of the fracture area that triggers subsequent vibrations, while the frequency/vibration characteristics of the fracture area are mainly determined by its inherent properties, as discussed in Section 5.7.

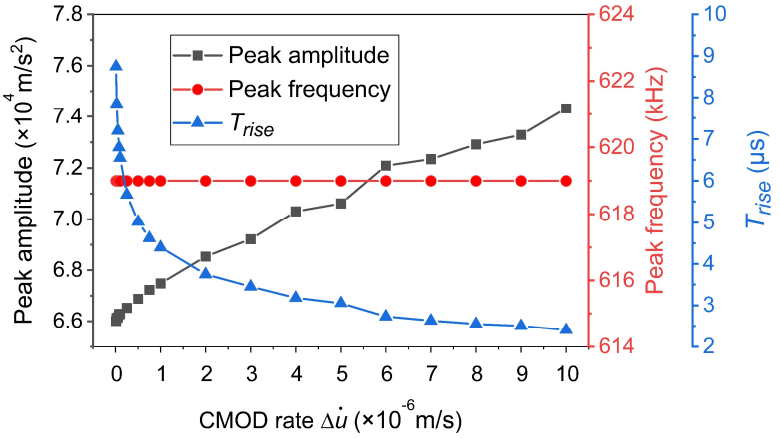

Figure 7.6 Effects of CMOD rate $\Delta\dot{u}$ on three AE source parameters in simulation case 6.

7.3 Development of a quantitative AE indicator for concrete tensile cracking behaviour

This section aims to develop a physically grounded AE indicator for quantifying the tensile cracking behaviour of concrete, building upon the findings of the preceding numerical parametric analysis. As discussed above, the three investigated AE source parameters are affected to varying degrees by different influencing factors. Therefore, it is necessary to compare the relative influence of each factor on the AE source parameters in order to identify the most deterministic one for developing a reliable AE-based indicator of concrete tensile cracking behaviour.

To achieve this, the variation in each source parameter resulting from changes in a given model input across the simulation cases (Cases 1~6 in Table 7.1) is normalized as follows:

$$\Delta\tilde{x} = \frac{|\Delta x|}{x_{\max}} = \frac{x_{\max} - x_{\min}}{x_{\max}} \tag{7.2}$$

where x represents the three AE source parameters under investigation. $|\Delta x|$ denotes the absolute difference between the maximum (denoted as $x_{\max}$) and minimum (denoted as $x_{\min}$) values of a source parameter across the input variations. $\Delta\tilde{x}$ serves as a normalized metric characterizing the degree of change in each parameter due to a specific model input.

Given that the range of each influencing factor has been selected to reflect a broad spectrum of concrete properties and working conditions, the normalized metric $\Delta\tilde{x}$ can be interpreted as a general index of the influence level of each factor on the AE source parameters associated with tensile cracking in concrete. The value of $\Delta\tilde{x}$ ranges from 0 to 1,

where a larger value indicates a greater influence of the varied input, and a value of zero signifies no correlation between the model input and the resulting AE source parameter.

Figure 7.7 illustrates the effects of various factors on the three selected AE source parameters. The two time-domain source parameters, namely the source peak amplitude and the source rise time T_{rise}, are influenced by multiple factors. Among these, the first tensile softening parameter a_1 and the lattice grid size (d) exert a more significant influence on these two parameters. It is important to note that a_1 is not a directly measurable material property, but rather a calibrated model parameter introduced by the assumed constitutive law (see Section 3.2). While it is physically interpreted as representing the fracture brittleness of concrete during the early softening stage, as illustrated in Figure 5.7, a_1 remains a model-derived parameter.

Interestingly, the peak frequency of the AE source is only influenced by concrete density (ρ), elastic modulus E and lattice grid size d, which aligns with the results obtained from the analytical modelling of a 1-DoF system in in Section 5.7 (see Equation (5.42)). In addition to ρ and E, the lattice grid size d also also holds clear physical significance. The breakage of a lattice element serves as a mechanical representation of a crack propagation step (see Chapter 6). As shown in Figure 3.1, two nodes connected by a broken lattice element represent a specific fracture volume ϕ_f (see Equation (3.3)) that actively generates AE. In the current numerical case, the critical element E0 links one edge node and one outer corner node (see Figure 6.1). Therefore, the fracture volume represented by the studied element E0 is calculated as $\phi_f = 1.25d^2w$.

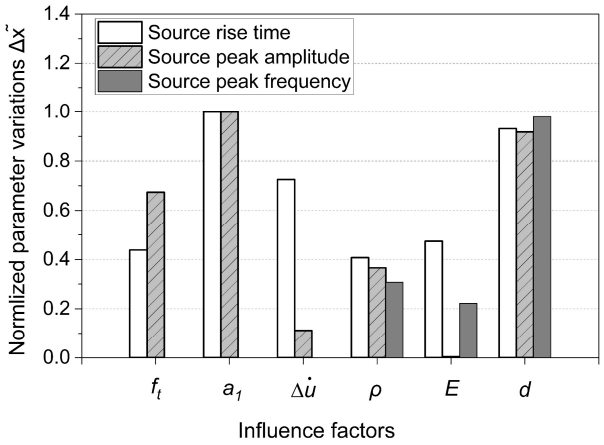

Figure 7.7 Normalized variations of three AE source parameters affected by different model inputs.

It is important to note that the fracture volume ϕ_f is different from the volume of fracture process zone (FPZ) ϕ_{FPZ} that is defined as the entire region of the fracture area experiencing inelastic strains (Bažant and Lin 1988). In the one-degree-of-freedom (1-DOF) case discussed in Chapter 5, ϕ_f equals to ϕ_{FPZ}, as the FPZ in one dimension involves only a single step of crack propagation. However, in the two-dimensional (2D) case examined in this chapter, which features a progressive crack propagation process, ϕ_f represents only a portion of the overall ϕ_{FPZ}. As illustrated in Figure 7.8, ϕ_f corresponds to the newly formed fracturing volume associated with a single crack propagation step during the early stage of tensile softening (ε_{cr}~$a_1\varepsilon_{cr}$) which actively generates AE signals (see Figure 6.3).

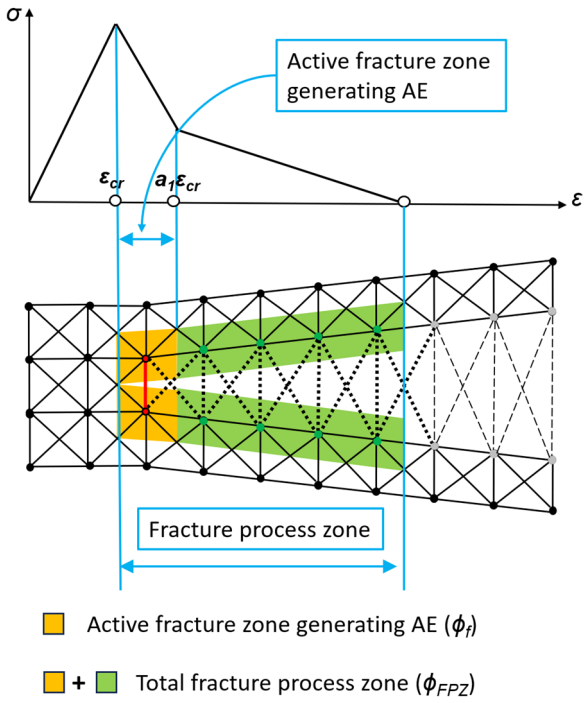

Figure 7.8 Illustration for the fracture zone of volume ϕ_f that actively generates AE.

Since the values of the two experimentally measurable properties, concrete density ρ and elastic modulus E, tend to be consistent within the same concrete structure, the source peak frequencies of different tensile cracking-induced AE sources generated in the same structure are primarily governed by the corresponding fracture volumes ϕ_f. This implies that the source peak frequencies of AE signals can serve as direct indicators of the internal tensile fracture volumes within a given concrete structure.

Based on this understanding, the objective of the following section is to establish a source peak frequency-based AE indicator for quantifying the fracture volume ϕ_f. ϕ_f is correlated with the AE source peak frequency (denoted as $f_p^{(s)}$), concrete density ρ and elastic modulus E in the following general form:

$$\phi_f = g\left(f_p^{(s)}, E, \rho\right) \tag{7.3}$$

Here, g represents a functional relationship. However, it is not feasible to derive a closed-form expression for Equation (7.3) that universally applies to various experimental scenarios with different values of E and ρ, due to the complex nature of AE source signals. These signals result from nonlinear vibrations of a multi-degree-of-freedom (multi-DoF) system (see Section 6.3).

Instead, the relationship can be empirically established through numerical lattice modelling. The numerical results of AE source peak frequency $f_p^{(s)}$ and corresponding fracture volume ϕ_f (calculated by Equation (3.3)) are plotted in Figure 7.9 based on the simulation case 5 (see Table 7.1). Drawing inspiration from the observation in the 1-DoF system (Chapter 5) that the dominant frequency of a fracturing region is inversely proportional to the square root of its volume (see Equation (5.43)), the numerical data are fitted using the following empirical relationship:

$$\phi_f = c_1\left(f_p^{(s)}\right)^{-2} + c_2 \tag{7.4}$$

where c_1 and c_2 are two fitting constants varying with concrete density ρ and elastic modulus E (see Equation (7.3)). In this equation, ϕ_f and $f_p^{(s)}$ are expressed in units of mm^3 and MHz, respectively. The resulting fitting function demonstrates strong agreement with the numerical data and can thus serve as a practical AE-based indicator for estimating concrete fracture volume.

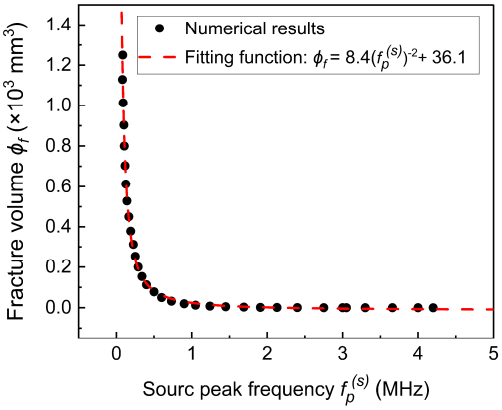

Figure 7.9 The proposed AE indicator based on simulation case 5 for the relationship between source peak frequency $f_p^{(s)}$ and fracture volume ϕ_f.

As indicated by Equation (7.3), the two fitting c_1 and c_2 of the proposed AE indicator (Equation (7.3)) are dependent on concrete density ρ and elastic modulus E. The values presented in Figure 7.9 are specifically fitted based on the material properties used in Case 5 (refer to Table 7.1).

To enable broader applicability and facilitate the practical use of the proposed AE indicator, we provide the values of c_1 and c_2 for various common concrete classes, as summarized in Table 7.2. This table is developed based on the same modelling framework as Case 5, with adjusted values of ρ and E reflecting different concrete classes in accordance with the fib Model Code 2010 (MC2010) (Walraven 2012).

Table 7.2 Fitting constants c_1 and c_2 of the the proposed AE indicator in Equation (7.4) for common concrete classes (C12~C90) (Walraven 2012).

Concrete classes	Material density ρ (kg/m^3)	Elastic modulus E (GPa)	c_1	c_2
C12	2500	27.1	7.8	16.7
C16		28.6	8.1	18.6
C20		30.0	8.5	20.2
C25		31.5	8.5	23.1
C30		32.8	8.7	25.0
C35		34.1	9.0	28.0
C40		35.2	9.1	28.4
C45		36.3	9.1	30.8
C50		37.3	9.2	30.3
C55		38.2	9.3	31.1
C60		39.1	9.4	31.4
C70		40.7	9.4	32.0
C80		42.2	9.5	32.5
C90		43.6	9.6	32.4

7.4 Practical applications of the proposed AE indicator

Although the AE indicator proposed above provides a theoretical basis for quantifying fracture volume, it cannot be directly applied in practical scenarios, as the source peak frequency itself is not directly measurable. In experimental settings, the recorded AE signal is significantly influenced by wave propagation effects and sensor response characteristics (see Section 4.4.3).

In the following, we explore potential applications of the proposed AE indicator within the context of practical AE monitoring, considering the limitations imposed by real-world measurement conditions.

7.4.1 Estimating fracture volume through AE measurements

The size of the fracture process zone (FPZ) is a critical factor influencing the fracturing behaviour of quasi-brittle materials and serves as a key parameter in several classical fracture models (Ba and Kazemi 1990; Cusatis and Schauffert 2009). However, accurately measuring the evolution of FPZ size during the fracture process remains a significant experimental challenge.

The AE indicator developed in Equation (7.4) establishes a quantitative relationship between the AE source peak frequency $f_p^{(s)}$ and the fracture volume ϕ_f that constitutes a portion of the FPZ (see Figure 7.9). This method enables the quantification of the fracture volume associated with each crack propagation increment that actively generates AE, thereby offering a means to evaluate the evolution of FPZ size throughout the crack growth process.

Since the source peak frequency $f_p^{(s)}$ is not directly measurable in real AE applications, an alternative approach is to rely on parameters derived from measured AE signals. In this context, the peak frequency of the measured AE signals, denoted as $f_p^{(m)}$, is selected as a measurable proxy for estimating the fracture volume ϕ_f. It is worth noting that other frequency-domain parameters closely related to source frequency characteristics (e.g., frequency centroid and partial powers (Unnþórsson 2013)) may also be employed to estimate ϕ_f, depending on the specifics of the application.

The measured peak frequency $f_p^{(m)}$ are further influenced by the signal attenuation in wave travel path (denoted as I_{wave}) and the sensor response (denoted as I_{sensor}) (Equation (7.5a)). By substituting Equation (7.5a) into the original indicator formulation in Equation (7.3), we can express the relationship between fracture volume ϕ_f and the measured AE peak frequency $f_p^{(m)}$ in Equation (7.5b).

$$f_p^{(m)} = g'(f_p^{(s)}, I_{wave}, I_{sensor}) \tag{7.5a}$$

$$\phi_f = g''(f_p^{(m)}, I_{wave}, I_{sensor}, E, \rho) \tag{7.5b}$$

where g' and g'' represent functional relationships incorporating the relevant influencing factors.

A closed-form solution to Equation (7.5b) cannot be derived as a universal AE criterion applicable across different experimental conditions involving varying values of E, ρ, S_{wave} and S_{sensor}. This limitation arises because experimentally measured AE signals result from the nonlinear vibrations of a multi-degree-of-freedom (multi-DoF) system (see Section 5.3) and are significantly influenced by the nonlinear characteristics of the sensor response (see Chapter 4).

As an alternative, case-specific numerical solutions to Equation (7.5b) can be developed using lattice modelling. In this approach, E and ρ are treated as model inputs, while I_{wave} and I_{sensor} are explicitly represented within the model framework. By numerically establishing the relationship between $f_p^{(m)}$ and ϕ_f, it becomes feasible to estimate ϕ_f from experimentally obtained $f_p^{(m)}$ values.

7.4.1.1 Demonstration cases

To demonstrate the proposed approach, two numerical case studies are conducted based on the simulation Case 5 in Table 7.1. Lattice modelling is used to simulate AE signals generated by the tensile failure of the critical element E0 at various lattice grid levels corresponding to different fracture volumes ϕ_f (see Figure 6.1). These signals are received by two virtual R15a sensors, S1 and S3, positioned at the closest and farthest distances from the source, respectively, in a three-point bending test of a notched concrete beam (see Section 4.3).

Wave propagation and associated attenuation effects are inherently captured within the lattice model through the implementation of Rayleigh damping (see Section 3.2). Additionally, the sensor response, accounting for the geometry and frequency-dependent sensitivity of the sensors, is incorporated following the modelling procedure described in Section 4.2.

Figure 7.10 shows the numerical correlations between fracture volume ϕ_f and the peak frequency of numerical AE signals $f_p^{(m)}$, as simulated by the two selected virtual AE sensors S1 and S3. It is observed that wave propagation and sensor response transform the broader and smoother distribution of the source peak frequency $f_p^{(s)}$ (up to 4 MHz in Figure 7.9) into significantly narrowed distributions of $f_p^{(m)}$, limited to below 500 kHz.

Moreover, the distribution of $f_p^{(m)}$ for both virtual sensors exhibit a non-smooth, three-phase evolution trend. Specifically, the slopes of the curves in Figures 7.10a and 7.10b both decrease sharply within the range of $100\ \text{kHz} < f_p^{(m)} < 200\ \text{kHz}$. Within this range, the frequency values cluster around 150 kHz, corresponding to the resonant frequency of the modelled R15a sensors (see Figure 4.2).

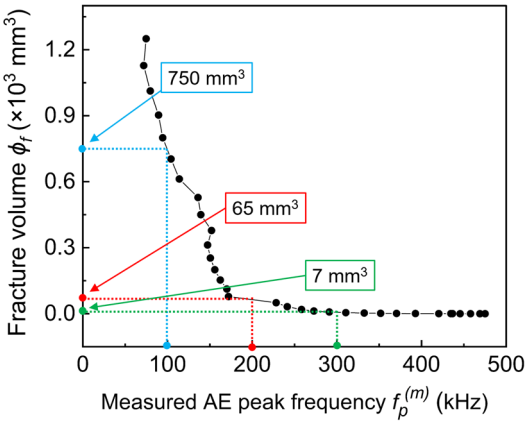

(a)

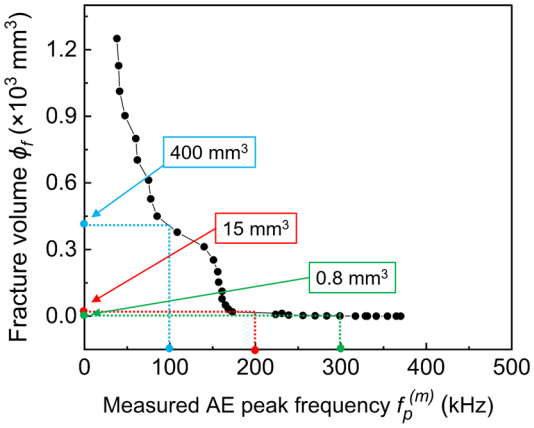

(b)

Figure 7.10 Relationships between the fracture volume ϕ_f and the peak frequency of numerical AE signals $f_p^{(m)}$ received by different sensors: (a) S1 and (b) S3.

Additionally, the relationship between ϕ_f and $f_p^{(m)}$ is strongly dependent on the wave travel distance. The values of ϕ_f corresponding to three critical values of $f_p^{(m)}$ (100, 200 and 300 kHz) measured by virtual sensors S1 and S3 are marked in Figure 7.8. It is evident that the same $f_p^{(m)}$ measured by the closer sensor (S1) corresponds to a larger fracture volume ϕ_f.

Nevertheless, the numerical AE peak frequency $f_p^{(m)}$ maintains a clear negative correlation with the fracture volume ϕ_f in Figure 7.10. This relationship provides a practical basis for estimating ϕ_f in experimental settings using the measured AE peak frequency

$f_p^{(m)}$, as the numerical values of $f_p^{(m)}$ in Figure 7.10 have been obtained by accounting for the entire acquisition process of experimental AE signals.

However, due to the uncertainties introduced by wave propagation effects and sensor response characteristics, it is not feasible to establish a precise mathematical function between $f_p^{(m)}$ and ϕ_f that would allow for accurate fracture volume prediction.

As an alternative, based on the numerical trends shown in Figure 7.10, it is possible to estimate approximate ranges of ϕ_f corresponding to different value intervals of $f_p^{(m)}$. Table 7.3 proposes AE peak frequency-based criteria for the two virtual sensors (S1 and S3) to estimate fracture volume ranges. The AE peak frequency range of 0~400 kHz, which covers the effective operating bandwidth of the modelled R15a sensors (see Figure 4.2), is divided into four equal subranges. For each subrange, the corresponding value range of ϕ_f is determined from the numerical data presented in Figure 7.10. It should be a more detailed frequency-based classification was not applied to achieve finer estimation of fracture volume, since high-frequency components (e.g., >200 kHz) attenuate rapidly and are seldom detected in experiments.

Table 7.3 Criteria established for estimating fracture volume based on the measured AE peak frequency, derived from the simulation results of two virtual R15a sensors (S1 and S3).

Measured AE Peak frequency $f_p^{(m)}$ (kHz)	Fracture volume ϕ_f (mm^3)	
	S1	S3
<100	>750	>400
100~200	65~750	15~400
200~300	7~65	0.8~15
>300	<7	<0.8

The AE criteria established in Table 7.3 are then applied to estimate the experimental fracture volumes based on the AE peak frequency values measured by AE sensors S1 and S3 during the three-point bending test, as described in Section 4.3. Figure 7.11 presents the estimated fracture volumes ϕ_f corresponding to the experimentally measured AE peak frequency $f_p^{(m)}$ values. It can be observed that the estimates derived from the experimental AE data for the two R15a sensors, located at different positions (see Section 4.3), are consistent. Approximately 80% of the fracturing areas that generated AE signals (highlighted by red braces) exhibit fracture volumes ϕ_f on the order of $10^1 \sim 10^2$ mm^3.

Assuming the experimental cracks in the three-point bending test are through-thickness type, similar to those modelled in the 2D lattice model, the experimental cracking areas

(denoted as S_f and calculated as $S_f = \phi_f / w$, where w is the specimen thickness) corresponding to each crack increment (each measured AE signal) are typically on the order of 10^{-1}~10^{0} mm^2.

However, it is important to acknowledge that, in the above demonstration case, the sensor-to-source distance varies during the crack propagation process in the experiment (see Figure 4.10), whereas the criteria presented in Table 7.3 are established based on a fixed source element E0 in the lattice modelling (see Figure 6.1). This discrepancy introduces extra errors in the estimation of experimental fracture volumes ϕ_f as presented above. For a more accurate estimation, future studies should incorporate the dynamic variation of sensor-to-source distance throughout the crack propagation process.

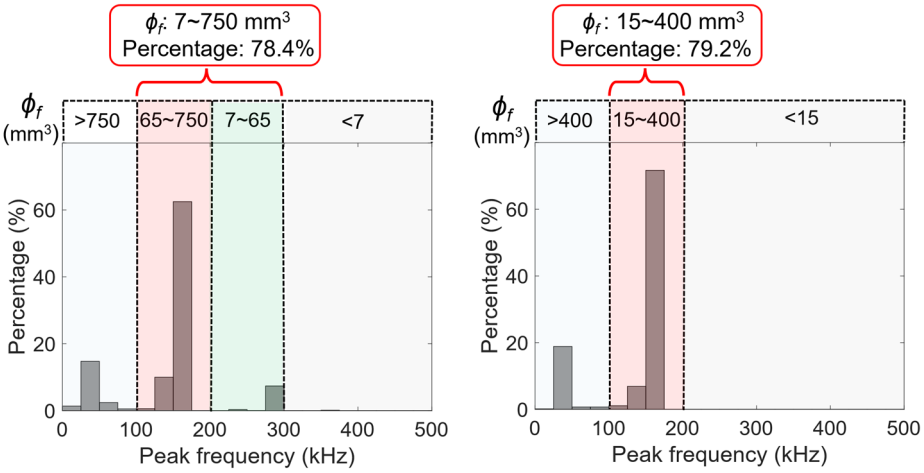

Figure 7.11 Experimental fracture volumes ϕ_f estimated by the AE criteria in Table 7.3 considering different AE sensor locations: (a) S1 and (b) S3.

7.4.1.2 Application guidance

The above procedure can alternatively be implemented using a range of numerical models and experimental methods to establish a criterion for estimating the active fracture volume ϕ_f based on measured AE peak frequency $f_p^{(m)}$ (or other relevant parameters of measured AE signals) (see Table 7.2). This approach is made feasible by the proposed AE indicator (Equation (7.4)), which eliminates the need for specialized, fracture-specific AE source modelling, such as that required in lattice-based simulations.

The step-by-step procedure for estimating fracture volume through AE measurements is summarized as follows:

- **Step 1**: Define source waveforms for various fracture volumes.

For each fracture volume ϕ_f, the corresponding source peak frequency $f_p^{(s)}$ can be determined using Equation (7.4). The corresponding source waveforms can then be approximated as Gaussian pulses (Bauer et al. 1984a). These pulses should have a broad frequency bandwidth approximately spanning the range (0, $2f_p^{(s)}$), centred at $f_p^{(s)}$, in order to closely replicate the spectral characteristics of AE sources generated by tensile fracture (see Figure 6.2).

- **Step 2**: Generate AE signals and extract relevant parameters.

The source waveforms defined in Step 1 can be used in numerical simulations or experimental setups to generate AE signals. From these, key signal parameters, such as peak frequency $f_p^{(m)}$ or other frequency-domain parameters of the resulting AE signals, can be obtained. In numerical modelling, the effects of wave propagation and the sensor response can be explicitly accounted for using the methods described in Sections 3.2 and 4.3, respectively. In experimental studies, these effects are inherently embedded in the measurements.

- **Step 3**: Establish correlations between measured AE parameters and fracture volume.

By developing a case-specific correlation between fracture volume ϕ_f and AE signal parameters such as $f_p^{(m)}$, it becomes possible to estimate ϕ_f from experimental data. This correlation serves as a practical criterion for quantifying fracture activity using AE measurements.

7.4.2 Sensor type selection and sensor layout optimization for monitoring targeted fracture scales

Proper sensor type selection and sensor layout design are essential components of effective AE monitoring. Traditionally, these are determined solely based on the attenuation characteristics of elastic waves propagating through the monitored medium (Cui et al. 2019). While it is ideal to also consider the AE source response to enhance the accuracy of sensor selection and layout design, conventional approaches are limited by the insufficient understanding of AE source characteristics.

This limitation can be addressed by leveraging the quantitative relationship between the AE source peak frequency $f_p^{(s)}$ and the corresponding fracture volume ϕ_f, as provided by the proposed AE indicator. For a targeted fracture volume range, the corresponding

AE source waveforms can be determined. By further analysing the attenuation characteristics of corresponding propagated waves, appropriate sensor types can be selected, and sensor layouts can be optimized to effectively monitor the desired fracture scales.

7.4.2.1 Demonstration case

To demonstrate the proposed approach, numerical case studies are performed using simulation Case 5 from Table 7.1. These studies employ lattice modelling to simulate AE signals generated by the tensile failure of the critical element E0 at different lattice grid resolutions, thereby representing varying fracture volumes ϕ_f (see Figure 6.1).

To enhance the observation of wave attenuation effects, the length of the numerical specimen is extended from 550 mm to 2500 mm, while all other boundary conditions and geometric and material properties remain unchanged. Attenuation of the AE waves is inherently captured by the lattice model through the implementation of Rayleigh damping (see Section 3.2). Moreover, as the focus is on the attenuation characteristics of generated AE waves, sensor response is not included in the simulation. Instead, the AE waveforms are represented by the *y*-direction accelerations of single nodes located on the bottom surface at various distances from the source in the notched beam specimen (refer to Section 4.3).

This numerical setup enables a detailed investigation of both time-domain and frequency-domain attenuation characteristics of AE waves generated by varying fracture volumes ϕ_f.

Figure 7.12 presents the time-domain attenuation behaviour of AE waves generated by different fracture volumes ϕ_f, illustrated by the variation in normalized peak amplitudes $\tilde{A}_p$ with wave propagation distance L_{wave}. Each peak amplitude is normalized by the maximum amplitude of its corresponding source wave. While larger ϕ_f values (linked to larger lattice grid sizes *d*) typically produce source waves with higher peak amplitudes (see Section 7.2.3), the source peak amplitude is also significantly affected by fracture brittleness, characterized by the first tensile softening parameter a_1 (see Section 7.2.2). Given the high heterogeneity of concrete at the microscale, a smaller but more brittle fracture volume can generate a higher source peak amplitude than a larger, more ductile one. Therefore, to ensure consistency in comparison, the source peak amplitudes at $L_{wave} = 0$ for all fracture volumes ϕ_f are all normalized to 1 (i.e., 0 dB in Figure 7.12).

It can be observed that the AE waves with higher frequencies, corresponding to smaller fracture volumes ϕ_f, attenuate more rapidly. This is because such waves involve more cycles of particle motion within the same travel time, leading to greater energy loss during

propagation (Bormann, Engdahl, and Kind 2012). Assuming a detection threshold (denoted as $\Delta\tilde{A}_p^{(cr)}$) of -50 dB relative to the source peak amplitude, as indicated by the blue dashed line in Figure 7.12, a shorter propagation distance is required for detecting higher-frequency AE waves generated by smaller fracture volumes ϕ_f.

Based on this understanding, we can determine the maximum allowable sensor-to-source distance, denoted as $L_{wave}^{(max)}$, to enable the detection of a minimum target fracture volume, denoted as $\phi_{f,min}$. As illustrated in Figure 7.12, for a given $\phi_{f,min}$, $L_{wave}^{(max)}$ can be determined as the wave travel distance at which the attenuation curve of the corresponding source wave (red solid line in Figure 7.12) intersects the detectable threshold (blue dashed line in Figure 7.12). This value, $L_{wave}^{(max)}$, serves as a critical constraint in the design of the sensor layout. Specifically, the maximum sensor-to-source distance in any sensor array must be less than $L_{wave}^{(max)}$ to ensure reliable detection of fracture volumes satisfying $\phi_f \geq \phi_{f,min}$.

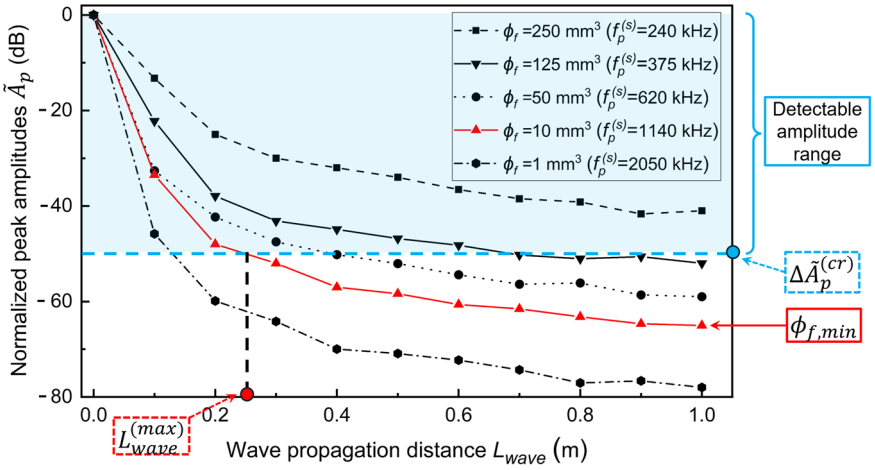

Figure 7.12 Time-domain attenuation characteristics of AE waves induced by various fracture volumes.

Figure 7.13 illustrates the frequency-domain attenuation characteristics of AE waves generated by various fracture volumes ϕ_f, shown as the variation in wave peak frequency (denoted as $f_p^{(w)}$) with wave propagation distance L_{wave}. A general decreasing trend in $f_p^{(w)}$ is observed with increasing ϕ_f and L_{wave}, despite some scatter. This trend provides a valuable basis for selecting appropriate sensor types to monitor a target fracture volume range ($\phi_{f,min}$, $\phi_{f,max}$).

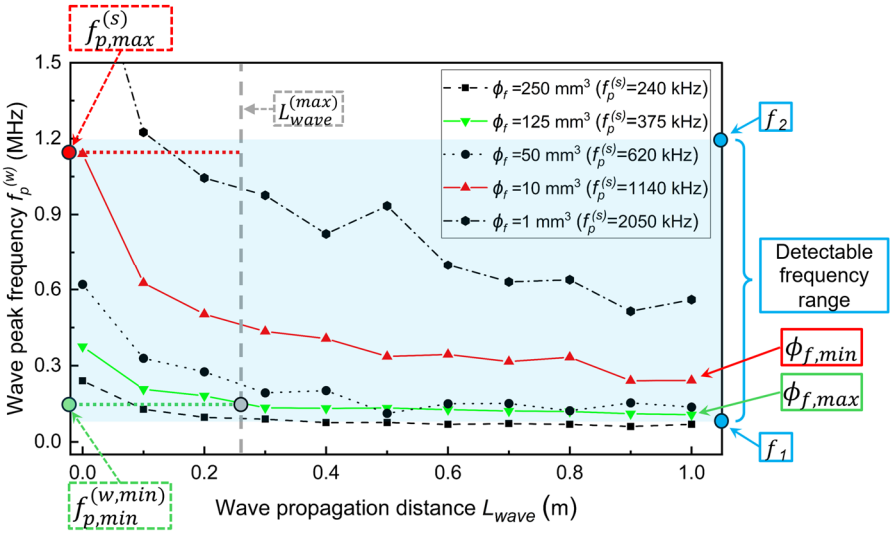

Figure 7.13 Frequency-domain attenuation of AE waves induced by various fracture volumes.

Within the previously determined maximum allowable sensor-to-source distance $L_{wave}^{(max)}$, two critical frequency values define the detectable frequency range for AE signals from the target fracture volume range ($\phi_{f,min}$, $\phi_{f,max}$):

- The minimum peak frequency of AE waves generated by the maximum fracture volume $\phi_{f,max}$ and propagating with the critical wave propagation distance $L_{wave}^{(max)}$, denoted as $f_{p,min}^{(w,min)}$, is marked by the green circle in Figure 7.13.
- The maximum peak frequency of AE waves generated by the minimum fracture volume $\phi_{f,min}$, corresponding to its source peak frequency (denoted as $f_{p,max}^{(s)}$) and can be directly calculated by Equation (7.4), is marked by the red circle in Figure 7.13.

These two values, $f_{p,min}^{(w,min)}$ and $f_{p,max}^{(s)}$, represent the lower and upper boundaries, respectively, of all possible AE wave peak frequencies generated within the target fracture volume range ($\phi_{f,min}$, $\phi_{f,max}$), considering the propagation limit $L_{wave}^{(max)}$.

To effectively monitor the target fracture volume range of ($\phi_{f,min}$, $\phi_{f,max}$) within the determined maximum allowable sensor-to-source distance $L_{wave}^{(max)}$, the selected sensor type should have a working frequency range (f_1, f_2) covering the frequency range of ($f_{p,min}^{(w,min)}$, $f_{p,max}^{(s)}$), as marked by the two blue circles in Figure 7.13. Moreover, in practical AE monitoring, the lower bound frequency f_1 should exceed 20 kHz to effectively

suppress ambient noise interference (Grosse and Ohtsu 2008a). These criteria are summarized in the following expressions:

$$20\,\text{kHz} \le f_1 \le f_{p,\min}^{(w,\min)} \tag{7.6a}$$

$$f_2 \ge f_{p,\max}^{(s)} \tag{7.6b}$$

7.4.2.2 Application guidance

The procedure described above can be alternatively implemented using alternative numerical models and experimental methods to determine the attenuation characteristics of AE source waves associated with specific fracture volumes, based on the AE indicator introduced in Equation (7.4). Once the attenuation characteristics of the source waves for target fracture volumes are established, sensor layouts and sensor types can be effectively optimized for monitoring the desired fracture volume range.

The design workflow to monitor a target fracture volume range ($\phi_{f,min}$, $\phi_{f,max}$) is summarized in the following steps:

- **Step 1**: Define source waveforms for boundary fracture volumes.

  Using the AE indicator established in Equation (7.4), we can determine the source peak frequency values $f_{p,max}^{(s)}$ and $f_{p,min}^{(s)}$ corresponding to the minimum and maximum target fracture volumes $\phi_{f,min}$ and $\phi_{f,max}$, respectively. Corresponding source waveforms can then be approximated as Gaussian pulses with broad frequency bandwidths $(0, 2f_{p,max/min}^{(s)})$ and centred at $f_{p,max/min}^{(s)}$. This design mimics the spectral characteristics of AE sources generated by tensile fracture (see Figure 6.2).

- **Step 2** Analyse attenuation characteristics of propagated waves.

  The source waves corresponding the minimum and maximum target fracture volumes $\phi_{f,min}$ and $\phi_{f,max}$ can be used as inputs for either numerical modelling or experimental measurements. In numerical models, wave propagation and attenuation can be explicitly captured following the method described in Section 3.2, while these effects are inherently captured in experimental data. By accounting for wave propagation and attenuation effects, the time-domain and frequency-domain attenuation characteristics of the propagated AE waves can be analysed.

- **Step 3**: Sensor layout design based on time-domain attenuation.

  Using the time-domain attenuation characteristics from Step 2, the maximum allowable sensor-to-source distance, $L_{wave}^{(max)}$, can be determined. This distance corresponds to a critical drop in the peak amplitude of AE waves generated by the minimum target fracture volume $\phi_{f,min}$ (e.g., 50 dB in the above demonstration case). This maximum distance serves as a key constraint in sensor placement design. (see Figure 7.12)

- **Step 4:** Sensor type selection based on frequency-domain attenuation.

  Based on the frequency-domain attenuation data for the maximum target fracture volume $\phi_{f,max}$ obtained in step 2, the minimum AE peak frequency value, $f_{p,min}^{(m,min)}$, can be identified from all AE signals that travel within the critical sensor-to-source distance $L_{wave}^{(max)}$. (see Figure 7.13)

  The selected sensor type should have a working frequency range (f_1, f_2) that covers the frequency range of ($f_{p,min}^{(w,min)}$, $f_{p,max}^{(s)}$) ($f_{p,max}^{(s)}$ is determined in step 1).

However, the correspondence between the fracture volumes ϕ_f responsible for AE generation, which is used as the design target in the above procedure, and the actual concrete fracturing processes remains unclear. According to the limited available theoretical and experimental work, ϕ_f, as a portion of the FPZ (see Figure 7.8), appears to be correlated with the structural sizes (Tarokh et al. 2017) and external loading conditions (Ghamgosar and Erarslan 2016) in quasi-brittle materials. Establishing a clearer understanding of the relationship between ϕ_f and concrete fracture processes in future studies would enable the proposed procedure to be effectively applied for selecting appropriate sensor types and optimizing sensor layouts across different structural scales and external loading types.

7.5 Discussions

This section explains the observed difference between current study and classical AE source theories for explaining the frequency characteristics of acoustic emission sources.

In this study, we found that the peak frequency of a tensile cracking-induced AE source is determined by the inherent properties of corresponding fracture area. This conflicts with the classical AE theories that are established based on the dislocation theory, where the frequency characteristics of modelled AE signals are alternatively determined by the source rise time that is defined as the duration of a displacement dislocation (see Section 2.3.2.3).

The source rise time and peak frequency of all numerical AE source signals obtained in the above simulation cases (Cases 0-6 in Table 7.1) are plotted in Figure 7.14. No clear correlation is found between these two parameters in lattice modelling.

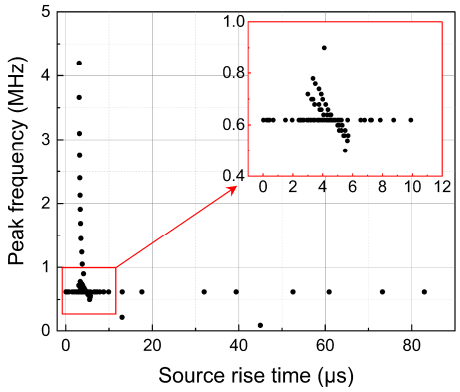

Figure 7.14 Correlation between values of source peak amplitudes and source rise time obtained in lattice simulations.

In the following, we discuss and explain such a discrepancy about the determinants of AE source frequency characteristics between this study and the classical dislocation theory-based AE theories.

In the classical continuum mechanics-based AE theories (e.g., the MT (Ohtsu 1995) and FEM based models (Sause and Richler 2015) as reviewed in Section 2.4.1), the frequency characteristics of resultant AE signals is fully determined by the assumed source rise time (Sause and Richler 2015). Specifically, the classical AE theories are formulated in the framework of the dislocation theory (Mura 2013), assuming that an AE signal is caused by a discontinuity/dislocation (namely a displacement jump) at local material regions as illustrated in Figure 7.15a (see also Section 2.3.2.3). The time history of a crack dislocation (called source-time function in AE field (Niwa, Ohtsu, and Shiomi 1982) or jump function in continuum mechanics (Yavari and Sarkani 2001)) are introduced through assumptions, since such a transient process cannot be accurately measured (the duration of a crack dislocation is in the magnitude less than 10^{-6} s (van Gemmeren, Graf, and Dual 2020)). Furthermore, according to the classical micromechanics (Kachanov 1980) that the dynamic process of a crack dislocation should start with a zero slope and smoothly approach to a constant displacement peak (see Figure 7.15a), the time history of a crack dislocation is usually assumed as symmetric in time domain within the classical AE theories.

Due to the time-domain symmetry of assumed displacement jump history, the velocity/acceleration of a crack dislocation, which is considered as representation of AE sources and

calculated as the derivative of the displacement jump with respect to time, are then in forms of symmetric pulse signals (see Figure 7.15a). Such a pulse signal causes an instantaneous impact wave/load on the local area and generates elastic waves in the whole system. The source rise time T_{rise} (defined as the duration of a displacement dislocation) is then the duration of resultant velocity/acceleration pulses (namely transient local impact load). As a pulse signal, the frequency is totally determined by its duration, namely the assumed source rise time T_{rise} (see also Equation (2.8)).

The displacement discontinuity and corresponding source signal induced by fracturing of source element E0 in lattice simulation case 0 (corresponding to Figure 6.3c and e) are illustrated in Figure 7.15b. Although the numerical displacement discontinuity in lattice modelling is in a similar shape with the time-domain symmetric displacement jump assumed in the classical AE theories, it is asymmetric involving two different dynamic phases, a displacement jump and subsequent vibration, as can be clearly seen in the acceleration signals in Figure 7.15b (see also Figure 6.3). The displacement jumps act only as a trigger for an AE signal and thus its duration (namely source rise time T_{rise}) is less relevant to the signal frequency. The signal frequency in lattice modelling is alternatively determined by the inherent properties of the fracturing zone in subsequent vibration stages (see also Section 5.7.3).

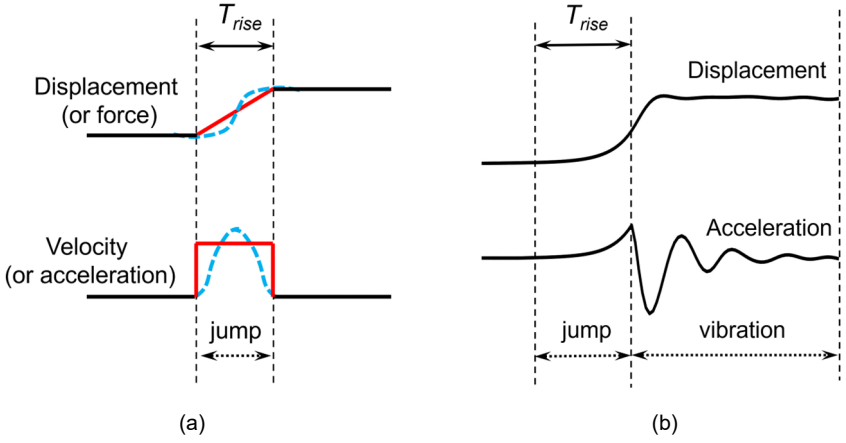

Figure 7.15 Explanation for the relationship between source rise time and source peak frequency in: (a) classical AE theories and (b) lattice modelling.

Since the AE source dynamic history in lattice modelling is rigorously derived through the nonlinear material behaviour and the principals of dynamics, the new insights from current study about the source frequency characteristics of AE signals are more reliable than the explanation provided by classical AE theories, for which the source response is

derived based on the fully assumed dynamic history of local displacement discontinuity with time-domain symmetry.

7.6 Summary

This chapter quantifies the AE sources induced by concrete tensile cracking in numerical models, excluding the uncertainties introduced by wave propagation and sensor effects in experimental measurements. A numerical sensitivity analysis is conducted to assess the influence of various factors on the typical parameters of AE sources generated by concrete tensile cracking, as identified in Chapter 5. This analysis utilizes the lattice model proposed in Chapter 3. Through a quantitative comparison of the influence of different parameters, it is found that time-domain AE source parameters are sensitive to all studied factors, whereas frequency-domain AE source parameters are primarily determined by the intrinsic properties of the corresponding fracture zone, including material density, elastic modulus, and fracture volume.

Building on the findings of the numerical parametric analysis, we propose a physically grounded AE indicator in the form of a quantitative relationship between the AE source peak frequency and the corresponding fracture volume that generates AE. Since the source peak frequency itself is not directly measurable, we further explore potential applications of the proposed AE indicator in the context of practical AE monitoring, accounting for the limitations of real-world measurement conditions. We present demonstration cases for the application of the proposed AE indicator, including the estimation of fracture volume through the measured AE peak frequency, by incorporating sensor response modelling methods as presented in Chapter 4. Additionally, the proposed AE indicator is explored as a design tool for selecting appropriate sensor types and optimizing sensor layout to monitor target fracture scales.

8. Understanding the evolution of acoustic emission parameters during concrete tensile cracking propagation

8.1 Introduction

Building upon the understanding of numerical acoustic emission (AE) signals generated by the tensile failure of individual lattice elements (i.e., individual cracking steps), as established in previous chapters, this final chapter shifts focus to the evolution of numerical AE signals resulting from the progressive failure of multiple elements (i.e., successive cracking steps) during tensile crack propagation in concrete.

As reviewed in Chapter 2, analysing the evolution of AE parameters during fracturing processes provides valuable insights into distinguishing various damage mechanisms in concrete structures and assessing their structural integrity. However, the physical mechanisms underlying the observed trends in experimental AE measurements remain inadequately understood. This limitation hampers both the rational interpretation of AE parameter evolution trends in experiments and the development of a robust AE-based methods for evaluating the integrity of concrete structures.

This chapter investigates the evolution of typical acoustic emission parameters during tensile crack propagation in concrete. Using the lattice model introduced in Chapters 3 and 4, the study examines individual contributions of AE source characteristics, wave propagation, and sensor response to the experimentally observed evolution patterns of AE parameters during tensile fracturing, with the goal of providing guidance for more rational interpretation of AE measurements in future experimental studies. Furthermore, by directly analysing the numerical AE source parameters at fracture zones and corresponding microscopic fracturing activities, this study seeks to elucidate the fracturing mechanisms that govern the evolution of AE parameters throughout the crack propagation process, with the goal of providing physical bases for the observed evolutionary trends in experimental AE measurements.

The chapter is organized as follows. Section 8.2 presents the setup and input parameters of the lattice models used in the analysis. Section 8.3 outlines the post-processing procedure for extracting numerical AE source signals during crack propagation. Section 8.4 interprets the observed evolution trends in typical AE parameters by distinguishing individual contributions of AE source characteristics, wave propagation, and sensor response in lattice modelling. Section 8.5 explores the underlying fracturing mechanisms responsible for AE parameter evolution through a combined analysis of AE source signals and the corresponding microscopic fracturing activity. Finally, Section 8.6 discusses the implications of the insights gained from lattice modelling of numerical AE sources for understanding physical AE sources in real-world scenarios.

8.2 Numerical model description

As reviewed in Chapter 2, numerous experimental studies have reported changes in acoustic emission (AE) parameters during progressive concrete fracturing and have proposed phenomenological models that associate these evolution trends with specific damage stages for evaluating structural integrity (Aggelis 2011; Rao and Lakshmi 2005; Zheng et al. 2022). However, these relationships are often case-specific, and the underlying mechanisms remain insufficiently understood, primarily due to the challenge of isolating the individual contributions of AE source characteristics, wave propagation, and sensor response in experimental settings.

The lattice modelling framework introduced in Chapters 3 and 4 enables the separate consideration of AE source behaviour, wave propagation effects, and sensor responses. This provides a powerful approach to investigating the physical mechanisms underlying the evolution of AE parameters during tensile cracking in concrete. Understanding these mechanisms not only establishes a physical basis for existing phenomenological models but also contributes to more reasonable interpretation of the evolution trends of experimental AE measurements during tensile crack propagation.

This chapter focuses on the evolution trends of representative AE parameters during tensile crack propagation, using the three-point bending simulation case described in Section 4.4. Differently from the original numerical model setup in Section 4.4, a smaller time step of 2×10^{-8} s is used in the explicit integration procedure to achieve a higher sampling rate of 50 MHz. This high temporal resolution is necessary because the analysis focuses on AE source signals recorded directly at the fracture zones, which exhibit significantly higher frequency content than signals recorded after wave propagation, as demonstrated in Chapter 6.

Furthermore, since the characteristics of AE signals generated by tensile cracking in concrete are strongly influenced by the fracture volume (i.e., the lattice grid size), as discussed in Chapter 7, three numerical simulations were conducted using different grid sizes, 0.5 mm, 1 mm, and 2.5 mm, to investigate their effects on AE signal evolution during crack propagation. For all numerical discretization levels, the dimensions of the notch in the specimen are kept consistent, 5 mm in width and 30 mm in depth, to align with the experimental setup described in Section 4.3. The total number of nodes (and corresponding elements) in the three lattice models is 330,861 (1,319,060), 83,232 (330,731), and 13,469 (52,989) for grid sizes of 0.5 mm, 1 mm, and 2.5 mm, respectively. The selection of these three grid sizes is based on two main considerations. First, computational efficiency imposes practical limitations; for instance, the simulation with a 0.5 mm grid size requires approximately 72 days to complete on a high-performance workstation. Second, the relationship between lattice grid size and the frequency resolution of simulated AE signals, as described by Equation (3.28), necessitates fine

discretization to accurately capture high-frequency components. Coarser grids are incapable of resolving higher-frequency AE content, for example, the largest grid size used (2.5 mm) results in a cut-off frequency of approximately 440 kHz.

The material properties of the notched beam specimen, as listed in Table 3.1, are employed in the numerical analyses. The tensile softening parameters a_1, a_2 and a_3 are calibrated to 5.5, 120, and 620, respectively, for 1 mm orthogonal lattice elements, following the procedure outlined in Figure 3.3. For other element sizes, including diagonal elements within the 1 mm grid model and all elements in the remaining grid configurations, the tensile softening parameters are regularized using Equation (7.1) to ensure consistent fracture energy across different discretization levels. The effects of fracture energy regularization on the simulation of both local AE source characteristics and global mechanical behaviour are discussed in detail in Appendixes J and K, respectively.

In the following sections, we focus on analysing the evolution trends of representative AE parameters during tensile crack propagation. Additional numerical results are presented in Appendix L, where comparisons between the spatial distributions of visible cracks, simulated AE sources, and localized AE events are made to clarify why experimentally observed AE events often appear scattered around the main visible crack.

8.3 Extraction procedure of AE source signals

To understand the fracturing mechanisms governing the evolution of AE parameters during the propagation of tensile cracks in concrete, it is essential to extract AE source signals directly from the fracture zone during the loading process in lattice simulations, in order to exclude the uncertainties of wave propagation and sensor response introduced in experiments. As discussed in Section 6.2, an AE source signal is defined here as the motion of a node directly connected to broken elements, excluding any effects from wave attenuation and sensor response.

Unlike the straightforward analysis of individual source signals generated by the breakage of single lattice elements in previous chapters, the extraction of all source signals throughout the entire loading process necessitates specialized post-processing techniques. The procedure for extracting numerical AE source signals is illustrated in Figure 8.1. During each time step of the simulation, the x-direction accelerations of all numerical nodes and the locations of broken elements are recorded. In this context, broken elements are identified as those with tensile strain values exceeding the cracking strain threshold ε_{cr}, since AE signals induced by tensile cracking primarily occur during the early tensile softening stage when the strain surpasses the material's elastic limit, as discussed in Section 6.3.1.

For each node, AE hits are isolated from continuous waveform streams, and the corresponding waveforms are extracted following the procedure outlined in Section 4.4.2.2. In this chapter, a lower threshold value of 0.15 m/s² (twice the peak amplitude of numerical noise) is employed to ensure the extraction of all numerical AE signals for analysis. The arrival time of each AE hit is determined using the Akaike information criterion (AIC) method (Liu et al. 2017). Subsequently, the extracted signals from different nodes are clustered into AE events based on their arrival time differences, according to the methodology described in Section 4.5.2.

The AE source signal for each identified event is defined as the signal with the earliest arrival time among all clustered waveforms. The waveforms of these identified source signals are saved with a pre-trigger time of 10 μs and a total duration of 150 μs, which encompasses the maximum observed length of AE source signals. These signals are then used to compute AE parameters for further analysis.

Additionally, the spatial locations and occurrence times of broken elements corresponding to the durations of the selected AE source signals are also identified for subsequent analyses.

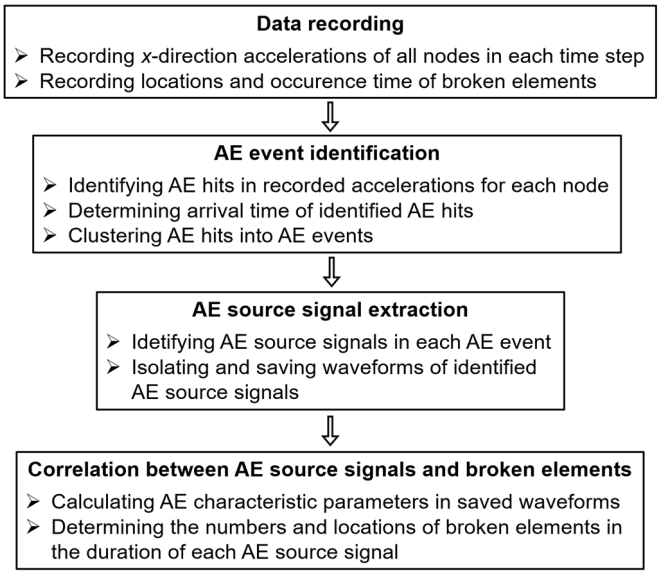

Figure. 8.1 Flowchart for the extraction procedure of AE source signals.

8.4 Interpretation for the evolution patterns of measured acoustic emission parameters

This section interprets the evolution patterns of experimental acoustic emission parameters measured during the tensile cracking propagation in the three-point bending test described in Section 4.3. The focus is on understanding the influence of each individual contributions from AE source characteristics, wave propagation, and sensor response on shaping the observed evolution of typical AE parameters during the loading process, aimed at providing guidance for more rational interpretation of AE measurements in future experimental studies.

To achieve this, we compare the evolution patterns of representative AE parameters obtained from both experimental measurements and lattice simulations during the tensile crack propagation process. The individual contributions of AE source characteristics, wave propagation, and sensor response are efficiently distinguished in the lattice modelling.

As demonstrated in Chapter 7, the AE peak frequency is closely related to the fracture scales of AE sources. It is therefore selected as one of the AE parameters analysed in this section. Additionally, peak amplitude and AE energy are two time-domain parameters commonly employed in experimental studies (Behnia, Chai, and Shiotani 2014), where their evolution trends are used to assess structural integrity. However, given that peak amplitude is influenced by multiple factors and has been found to be an unstable indicator of tensile cracking behaviour (see Section 7.3), this chapter focuses on AE energy as a more reliable parameter (this will be demonstrated in Section 8.6). Definitions of the selected AE parameters are provided in Appendix A.

8.4.1 AE peak frequency

This subsection interprets the observed evolution pattern of AE peak frequency during tensile cracking propagation in the three-point bending test described in Section 4.3. The analyses are based on the signals measured by AE sensor S1.

The peak frequency distributions of experimental and numerical AE signals received by AE sensor S1 during the tensile crack propagation is shown in Figure 8.2. Each red dot represents an AE hit. The numerical results are those accounting for sensor response following the modelling procedure in Section 4.2. Numerical and experimental peak frequency values both show zonal distributions in the loading processes.

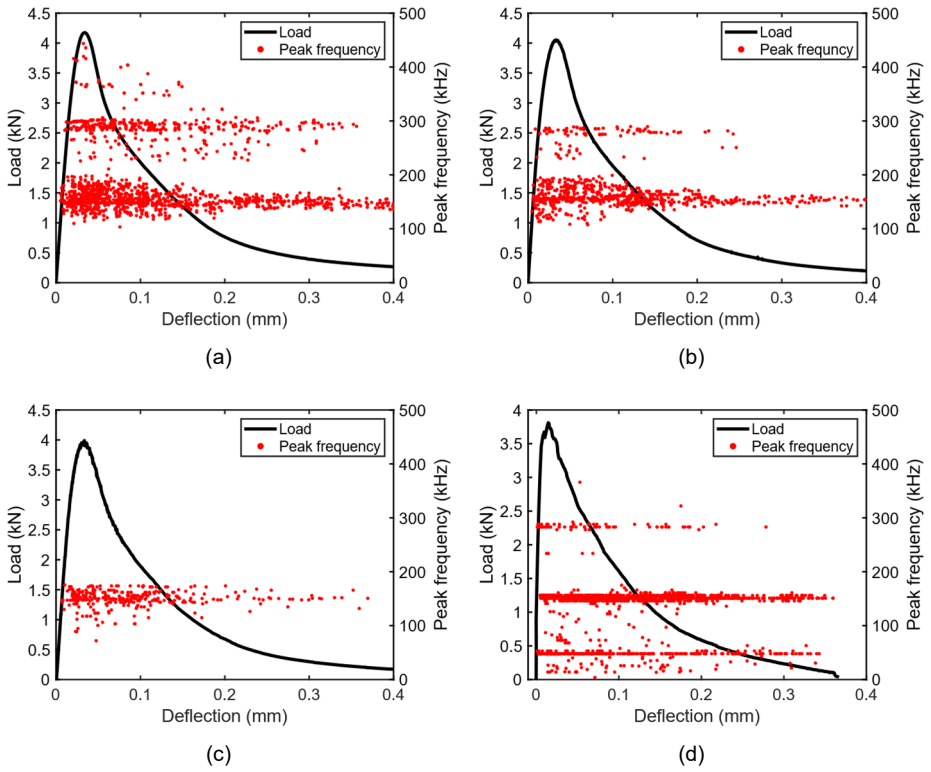

Figure. 8.2 Distribution of AE peak frequency recorded by AE sensor S1 in loading process: (a) numerical results with 0.5 mm grid size; (b) numerical results with 1 mm grid size; (c) numerical results with 2.5 mm grid size and (d) experimental results.

By isolating the individual contributions of AE source characteristics, wave propagation, and sensor response within the lattice modelling framework, the observed evolution patterns in the measured AE peak frequency can be explained in the following.

Effect of sensor response:

Figure 8.3 presents the raw numerical results obtained without incorporating the sensor response, represented by the acceleration at a single node located at the centre of the virtual sensor S1. The peak frequencies of these raw AE signals exhibit a much more scattered distribution throughout the loading process, spanning a broader frequency range.

A comparison between Figures 8.2 and 8.3 demonstrates that the experimentally observed zonal distributions of peak frequency primarily result from the frequency-response sensitivity of the sensors used. Most signal frequencies are concentrated around 150 kHz, which corresponds to the resonance frequency of the R15α sensors (MISTRAS 2011b). Additionally, a secondary distribution band of peak frequencies appears around 300 kHz in both the experimental data and the numerical simulations with 0.5 mm and 1 mm lattice

grid sizes. As shown in Figure 4.2, this aligns with a secondary peak in the frequency-response sensitivity curve of the R15α sensors.

Moreover, as discussed in Appendix D, the high-frequency components of AE signals are attenuated by the sensor's geometry due to the so-called "aperture effect" (Grosse et al. 2021). Consequently, higher-frequency components are more evident in the raw numerical AE signals (Figure 8.3), while the peak frequencies of numerical signals incorporating the sensor response remain below 500 kHz across all three discretization levels (Figure 8.2).

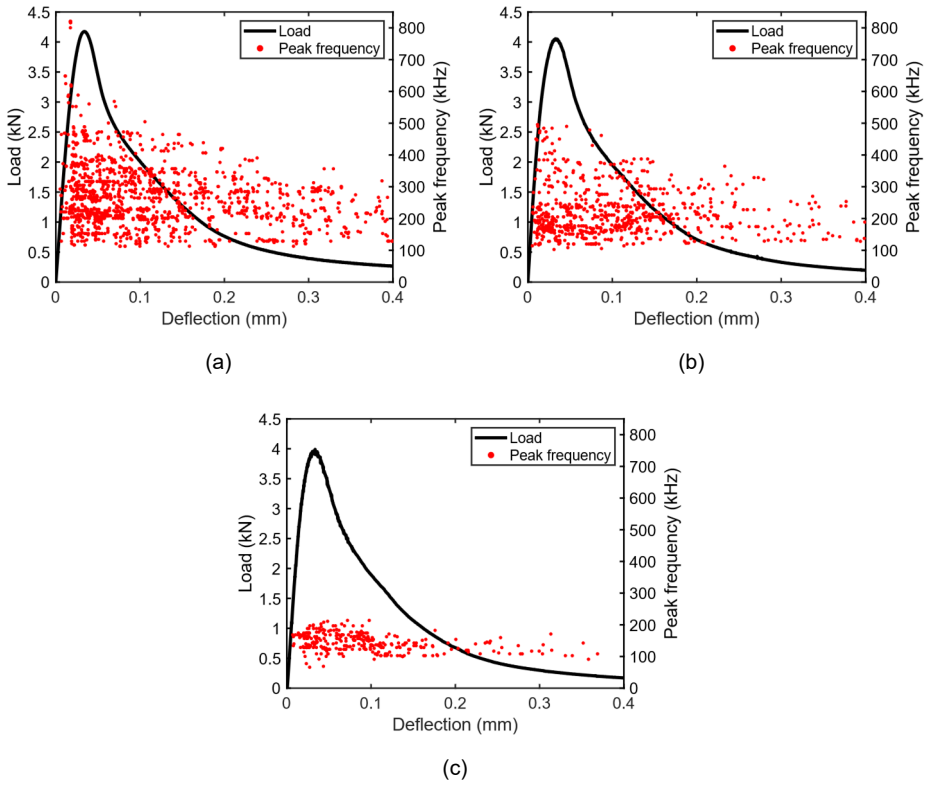

Figure 8.3 Distribution of AE peak frequency of a single node located in the centre of sensor S1 in loading process: (a) 0.5 mm grid size; (b) 1 mm grid size and (c) 2.5 mm grid size.

Effect of wave propagation:

For the measured AE signals recorded with sensors (Figure 8.2), the main distribution band around 150 kHz persists throughout the entire loading process. In contrast, signals within the secondary band around 300 kHz appear predominantly during the early loading stage, corresponding to a mid-span deflection range of 0–0.2 mm. A similar trend is

observed in the raw numerical signals without sensor response (Figure 8.3), where high-frequency components diminish in the later stages of loading.

This trend can be interpreted by examining the numerical AE source signals, which exclude both sensor response and wave attenuation effects. Figure 8.4 illustrates the evolution of peak frequency in the numerical AE source signals, showing that high-frequency components persist consistently throughout the entire loading process. Therefore, the observed reduction in high-frequency content in the measured signals is primarily attributed to wave attenuation.

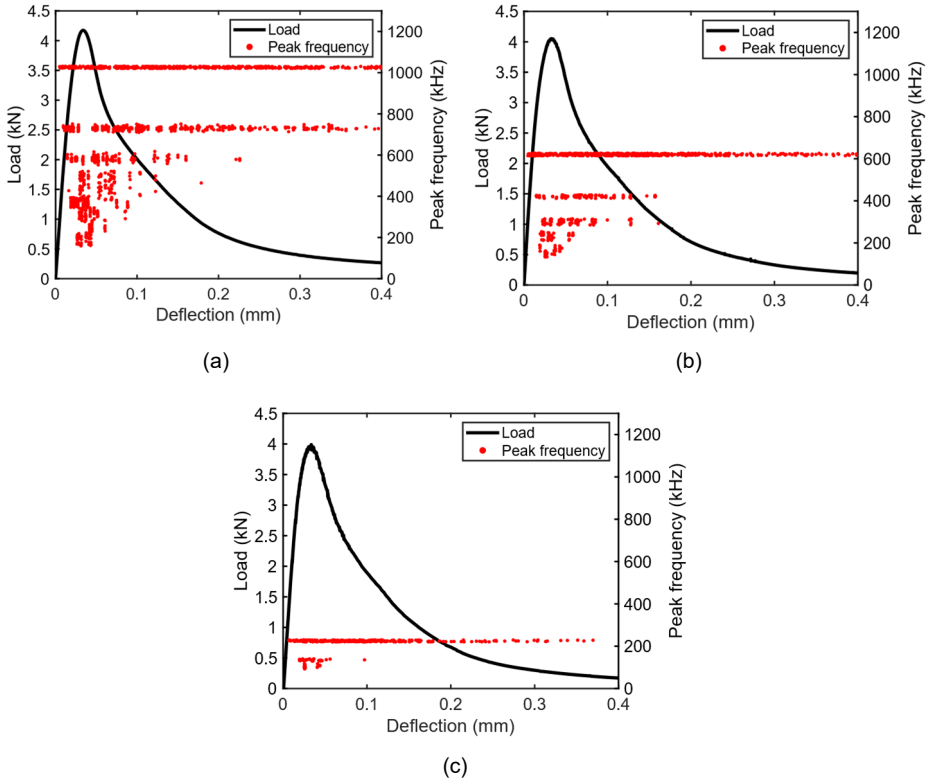

Figure. 8.4 Distribution of peak frequency of AE source signals: (a) 0.5 mm grid size; (b) 1 mm grid size and (c) 2.5 mm grid size.

As shown in Figure 4.10 (see also Figure L.1), the crack propagates in an upward direction during loading, increasing the source-to-sensor distance over time. As sensor S1 remains in a fixed location, this growing distance leads to progressively greater signal attenuation. Since high-frequency components attenuate more rapidly over the same propagation path (Wyllie, Gardner, and Gregory 1962), they are more likely to be fully attenuated in the later stages of loading.

Source characteristics:

The numerical source peak frequencies across different discretization levels exhibit a similar overall distribution pattern, as shown in Figure 8.4. Specifically, a longer distribution zone of high-frequency signals is accompanied by several shorter zones associated with lower peak frequencies throughout the loading process. Furthermore, the peak frequency distributions of numerical signals demonstrate a strong dependency on the mesh size. High-frequency signals exceeding 350 kHz are observed only in the 0.5 mm grid size simulations, while all signals generated at the 2.5 mm grid size level exhibit peak frequencies below 200 kHz. As discussed in Chapter 7, this mesh-size dependency of AE source signals physically represents the fracture scale. Further explanation of this trend in AE source peak frequency will be provided in Section 8.5.

This mesh-size dependency helps explain the discrepancy between the numerical and experimental AE signals observed in Figure 8.2. Specifically, the experimental data shows an additional distribution band of low peak frequencies around 50 kHz, which is absent in the simulations. As discussed in Section 4.6.1, these low-frequency signals may arise from either stick-slip friction between crack surfaces or from larger fracture scales that are not captured by the current lattice discretization. However, since the low-frequency signals are consistently observed throughout the entire loading process (Figure 8.2d), it is more reasonable to attribute them to large-scale fracture processes beyond the resolution of the three adopted lattice grid levels. This interpretation is supported by the fact that persistent shear deformation along crack surfaces, especially in the early linear portion of the load-deflection curve, is unlikely. Additionally, as demonstrated in Figure 7.5, large fracture scales corresponding to grid sizes of 5 mm or greater are capable of generating such low-frequency AE signals.

8.4.2 AE energy

This subsection interprets the observed evolution pattern of AE energy during the propagation of tensile cracking. The analysis is based on signals measured by AE sensor S1, as described in Section 4.3.

Figure 8.5 presents the energy distributions of AE signals received by sensor S1 throughout the loading process. To facilitate comparison between numerical and experimental results, the AE energy values are normalized by dividing each value by the corresponding maximum energy, accounting for potential differences in units. Both the numerical and experimental results exhibit a similar evolution trend: high-energy signals are predominantly concentrated around the peak load, while the occurrence of such high-energy events gradually diminishes during the post-peak stage.

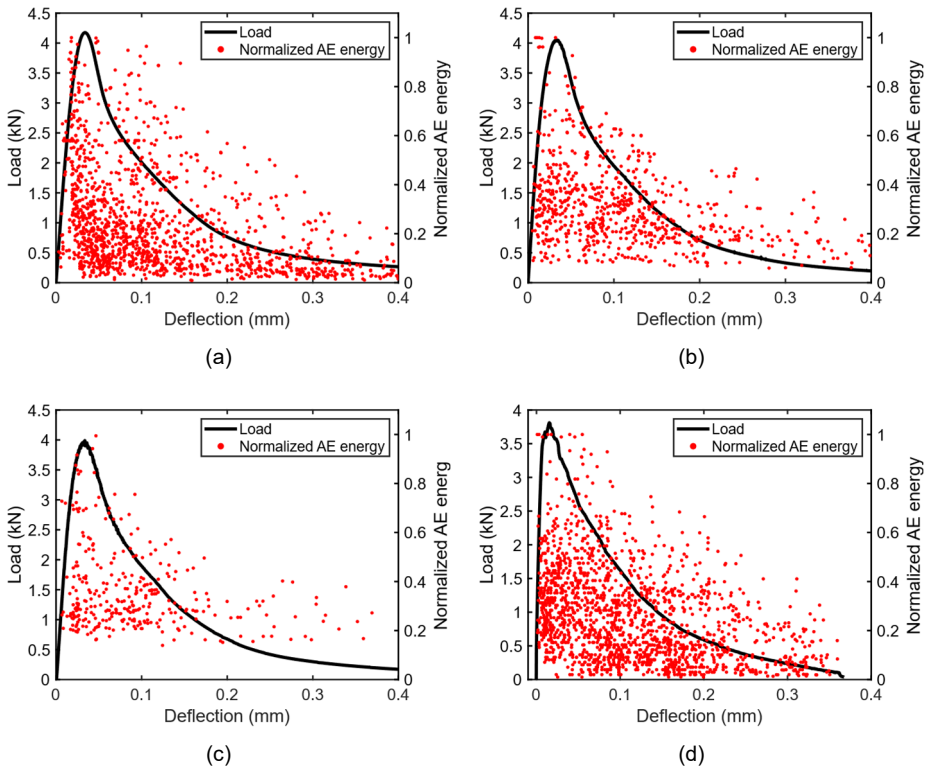

Figure. 8.5 Distribution of AE energy recorded by AE sensor S1 in loading process: (a) numerical results with 0.5 mm grid size; (b) numerical results with 1 mm grid size; (c) numerical results with 2.5 mm grid size and (d) experimental results.

By isolating the individual contributions of AE source characteristics, wave propagation, and sensor response within the lattice modelling framework, the observed evolution patterns in the measured AE energy can be explained in the following.

Effect of sensor response:

Figure 8.6 presents the raw numerical results obtained without incorporating the sensor response, represented by the acceleration at a single node located at the centre of the virtual sensor S1. Compared to its significant effect on AE peak frequency, the sensor response exhibits a much more limited influence on AE energy. The evolution of AE energy in the raw AE signals shows a similar trend to that observed in the processed numerical signals that account for sensor response (Figure 8.5), with high-energy signals predominantly concentrated around the peak load. The number of these high-energy signals gradually decreases throughout the loading process.

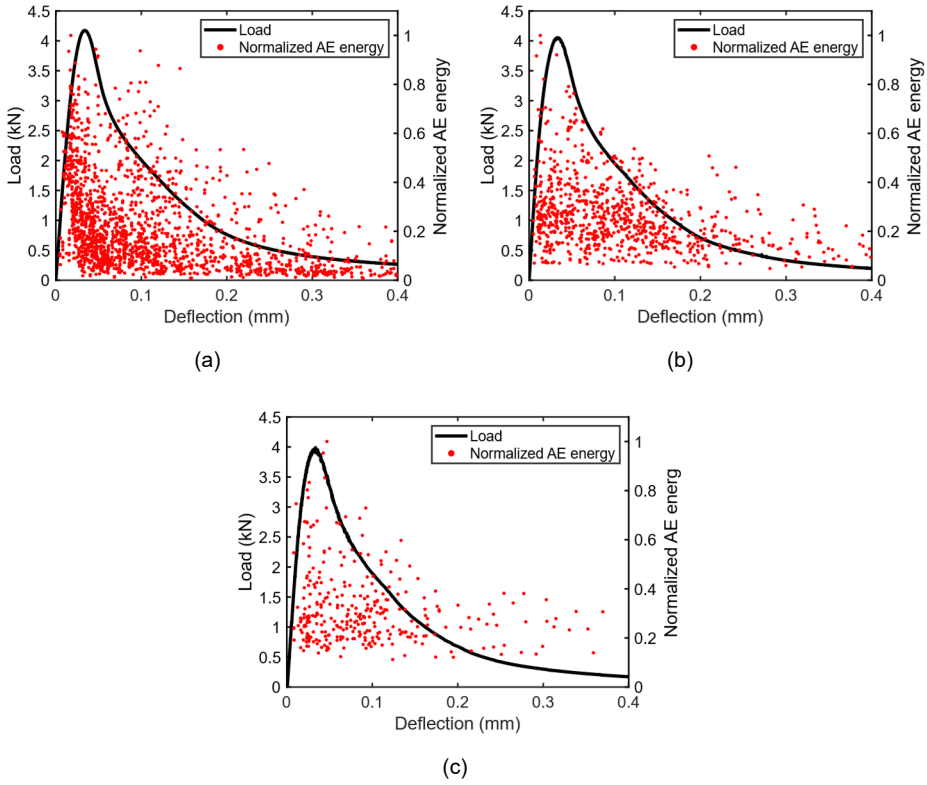

Figure 8.6 Distribution of numerical AE energy of a single node located in the centre of sensor S1 in loading process: (a) 0.5 mm grid size; (b) 1 mm grid size and (c) 2.5 mm grid size.

Effect of wave propagation:

Figure 8.7 shows the evolution patterns of normalized AE source energy during the loading process, showing that low-energy components persist consistently throughout the entire loading process. The high-energy signals at around peak load in experimental measurements are observed in AE source, while no decrease trend in signal energy is observed in later loading stages.

A comparison between Figures 8.6 and 8.7 clearly demonstrates that the experimentally observed decrease trend in signal energy in later loading stages are from wave attenuation due to the increased wave travel distances to the fixed sensor S1 during the crack propagation process. Moreover, the high-energy signals around peak load in experiments (Figure 8.5) are from the characteristics of AE sources themselves.

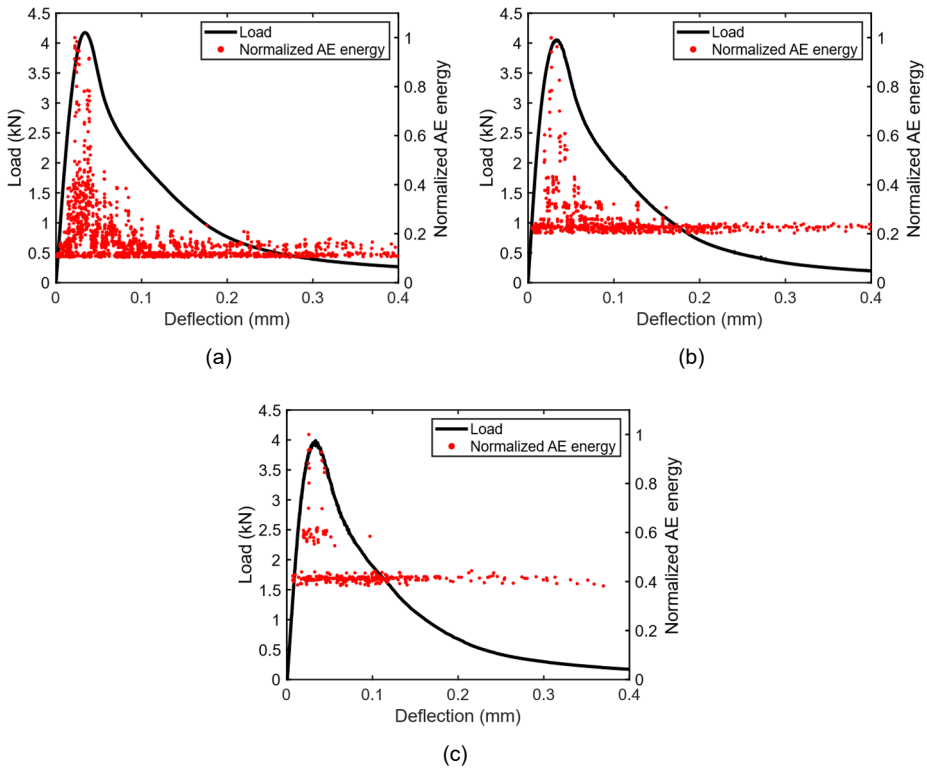

Figure. 8.7 Distribution of energy of AE source signals: (a) 0.5 mm grid size; (b) 1 mm grid size and (c) 2.5 mm grid size.

Source characteristics:

Three numerical cases under different numerical discretization levels show a similar AE energy distribution pattern: a main distribution zone of low energy source signals persistently exist in the whole loading process, while high-energy sources are reduced in numbers and mainly distributed at around the peak load (Figure 8.7). Moreover, the energy of numerical source signals also shows a mesh size dependency. The lower energy contents cannot be reproduced in the simulation cases with larger grid sizes. This will be physically explained in Section 8.5.

8.5 Fracturing mechanisms governing the evolution of acoustic emission source characteristics

After understanding the individual contributions of source characteristics, wave propagation, and sensor response to the evolutionary trends of typical AE parameters observed in the experiments in the previous section, this section presents a physical interpretation of the corresponding numerical AE source characteristics. The aim is to

establish a general physical foundation for understanding the observed trends in AE measurements across various experimental contexts.

As shown in Figures 8.4 and 8.7, the AE sources that exclude both sensor response and wave attenuation effects still exhibit distinct characteristics at different stages of tensile crack propagation for each uniform lattice grid discretization level. The source peak frequency and source energy display zonal distributions throughout the loading process.

Notably, high-energy and low-frequency sources are predominantly concentrated around the peak load. This observation is consistent with findings from many other experimental studies (Backers, Stanchits, and Dresen 2005; Dong, Xiangdong, and Libin 2014; Jiang et al. 2021; Zheng et al. 2023; Du et al. 2020), which reported that AE signals with high energy and low frequency tend to occur near the peak load or during other loading stages associated with rapid changes in global stiffness.

In the following analysis, we provide a physical explanation for these evolutionary trends in AE sources by examining the microscopic fracturing processes captured through the lattice modelling approach.

8.5.1 Correlation between microscopic fracturing activities and acoustic emission source characteristics

As illustrated in Chapters 5 and 6, a broken lattice element in the early tensile softening stage, ranging approximately from ε_{cr}~$a_1\varepsilon_{cr}$, physically represents a discrete microcrack propagation step that induces a local displacement jump responsible for generating acoustic emission (AE) phenomena (see Figures 5.7 and 6.3). Therefore, in this section, we investigate the evolutionary trend of broken elements as a physical analogue to AE-related microscopic fracturing activities. The procedure for determining the occurrence time and spatial location of broken elements is detailed in Section 8.3.

The evolution of broken element rates throughout the loading process is presented in Figure 8.8, alongside a comparison with AE event rates. In this analysis, the rate values are calculated as the number of AE events and broken elements per second. The numerical broken element rates follow a similar trend to the AE event rates, with both peaking around the peak load, corresponding to rapid changes in specimen stiffness globally during this critical phase. The spatial distributions of broken elements and AE events are provided in Appendix L.

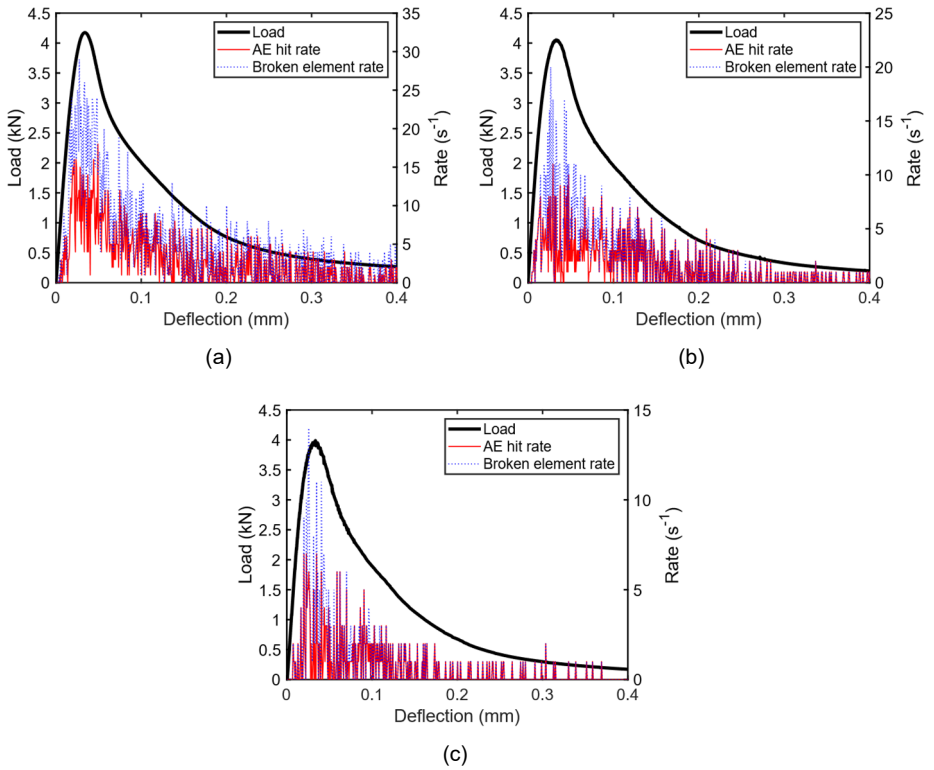

Figure. 8.8 Rates of AE hits and numerical broken elements in the loading process (unit: s^{-1}): (a) numerical results with 0.5 mm grid size; (b) numerical results with 1 mm grid size and (c) numerical results with 2.5 mm grid size.

As shown in Figure 8.8, the physical sources of acoustic emission, namely the broken elements, exhibit a higher rate than the corresponding AE hits, particularly around the peak load, where high-energy and low-frequency AE sources are observed (see Figures 8.4 and 8.7).

To further highlight the difference between the rates of numerical broken elements and AE events in lattice simulations, the evolution of their rate difference (defined as the broken element rate minus the AE event rate) throughout the loading process is presented in Figure 8.9.

Notably, the observed evolution trend of the rate difference between broken elements and AE rates closely aligns with the trends in source parameters. The loading stages exhibiting larger differences in rates in Figure 8.9 correspond to the occurrence of the distribution zones of lower-frequency and higher-energy AE sources, as shown in Figures 8.4 and 8.7. Given that a very low threshold was used to extract all AE hits (see Section 8.3), this discrepancy is not attributable to data processing errors. Rather, it likely reflects a

fundamental aspect of AE signal generation, offering a physical explanation for the observed variations in AE source characteristics during tensile crack propagation.

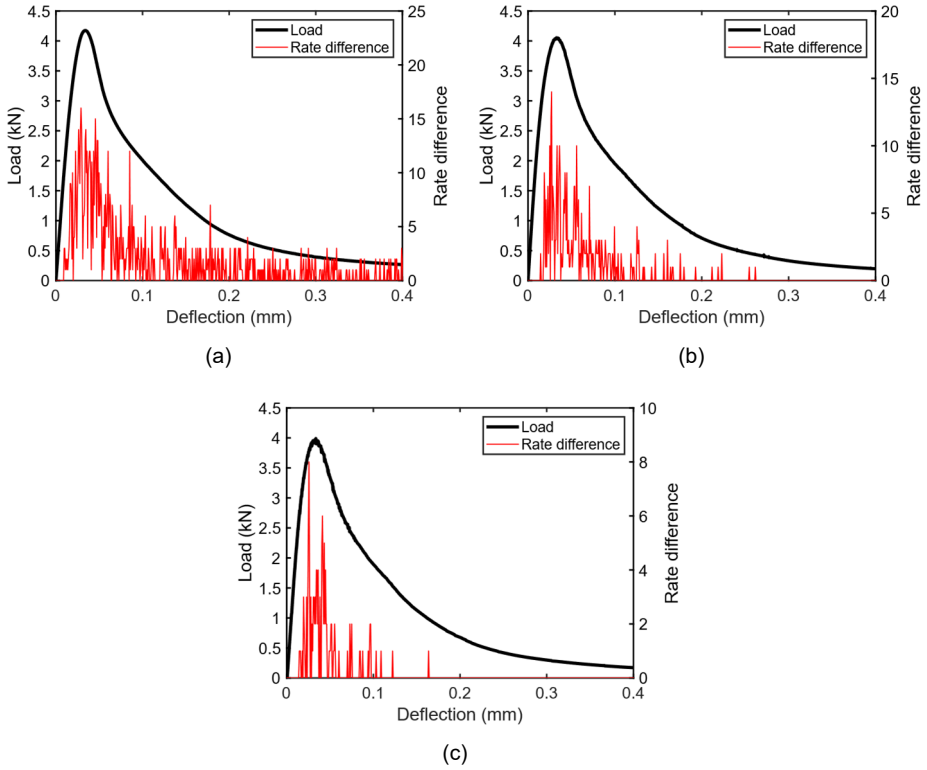

Figure. 8.9 Rate difference between broken elements and AE events in lattice simulations: (a) 0.5 mm grid size; (b) 1 mm grid size and (c) 2.5 mm grid size.

For each individual AE source signal, the observed rate difference between broken elements and AE events leads to variability in the number of broken elements occurring within the duration of the signal. To explore this relationship, a statistical analysis is conducted to correlate the AE source characteristics with the number of broken elements involved. The procedure for determining the number of broken elements associated with each AE source signal duration is described in Section 8.3.

Figure 8.10 presents statistical results, displayed as point plots with error bars, showing the correlation between typical AE source parameters and the number of broken elements involved, under three different lattice discretization levels. The two studied source parameters under three numerical discretization levels show a similar trend: the broken element numbers involved in the signal duration are positively and negatively related to normalized AE energy and peak frequencies, respectively, of corresponding source signals.

Notably, each error bar in Figure 8.10 corresponds to a distribution zone of specific AE source parameters shown in Figures 8.4 and 8.7. This suggests that the observed evolutionary trends in AE source characteristics are driven by variations in the number of broken elements occurring within the duration of individual source signals.

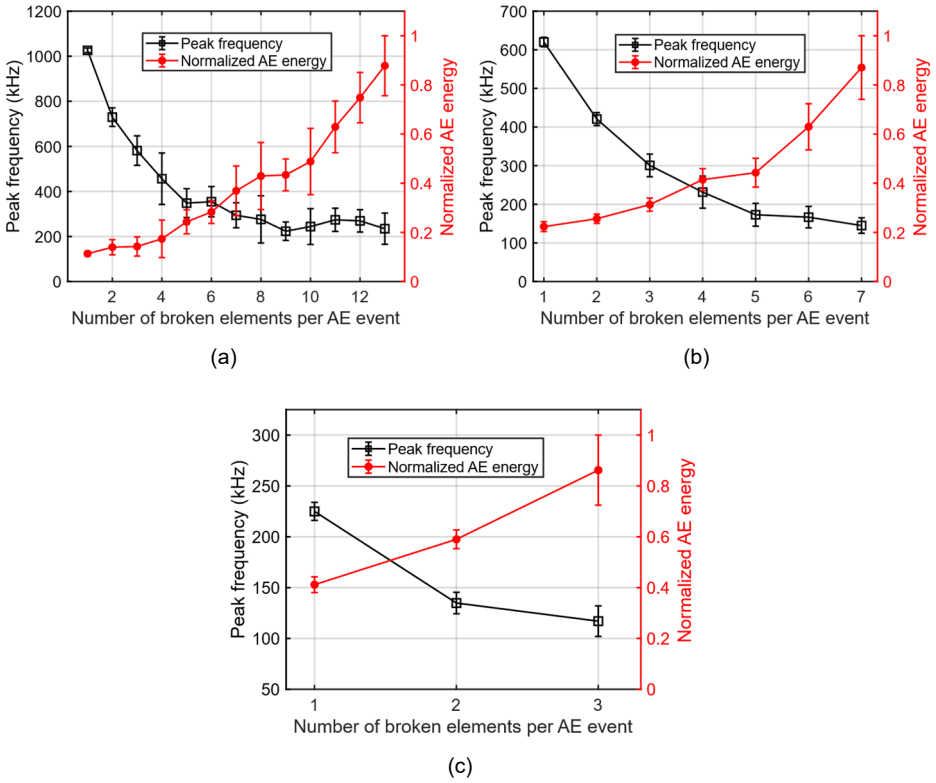

Figure. 8.10 Correlation between parameters of AE source signals and number of broken elements: (a) 0.5 mm grid size; (b) 1 mm grid size and (c) 2.5 mm grid size.

8.5.2 Physical mechanisms underlying the evolution of AE source characteristics

As discussed above, the observed evolutionary trends in AE source characteristics in Figures 8.4 and 8.7 are primarily governed by variations in the number of broken elements involved in the signal duration. Physically, the number of broken elements corresponds to the number of microcracks and thus the volume of active fracture zones responsible for generating AE signals (see Figures 5.7 and 7.3). Therefore, in the following analysis, the characteristics of AE sources, specifically the source peak frequency and source energy, are interpreted in relation to the physical significance of the number of broken elements participating in AE generation.

8.5.2.1 AE source peak frequency

Figure 8.11 presents typical AE source signals and the corresponding distribution patterns of broken elements occurring during their durations across three numerical discretization levels to understand the observed evolution trends of AE source peak frequency. For each lattice grid size, two representative source signals are selected, each associated with a different number of broken elements activated during the signal duration. The broken elements are highlighted in red. Since the broken elements physically corresponds to the volumes of the active fracture zone responsible for AE generation (as illustrated in Figure 6.3), the fracturing zones are marked in orange to facilitate the examination of their influence on the source peak frequency.

The three subfigures in the first column of Figure 8.11 illustrate typical AE source signals generated by a single broken element at different numerical discretization levels. Physically, these signals are generated by a single microcracking step within their durations. These source signals all exhibit the characteristics of Gaussian pulse signals (Bauer et al. 1984a), featuring short durations in the time domain and a single dominant peak in the frequency domain (see also Section 6.2). According to the negative correlation between fracture volumes and AE source frequency in Section 7.3, a larger fracturing area results in a lower central (peak) frequency of the sources.

The three subfigures in the second column of Figure 8.11 show typical AE source signals involving multiple broken elements within their durations at different numerical discretization levels. Physically, these signals are generated by a series of successive microcracks occurring within a short transient period, that is, within the duration of the source signals. These signals exhibit more complex characteristics compared to those induced by a single element breakage: they have longer durations and display multiple peaks in both the time and frequency domains. Despite this complexity, a comparison between these three source signals emphasizes the significant influence of the fracture zone size on the frequency characteristics of the generated source signals: a larger fracture zone consistently results in a lower peak frequency.

Moreover, at a same lattice grid level, the source signals induced by several broken elements and thus larger fracture zones consistently exhibit lower peak frequency values than those induced by one element breakage.

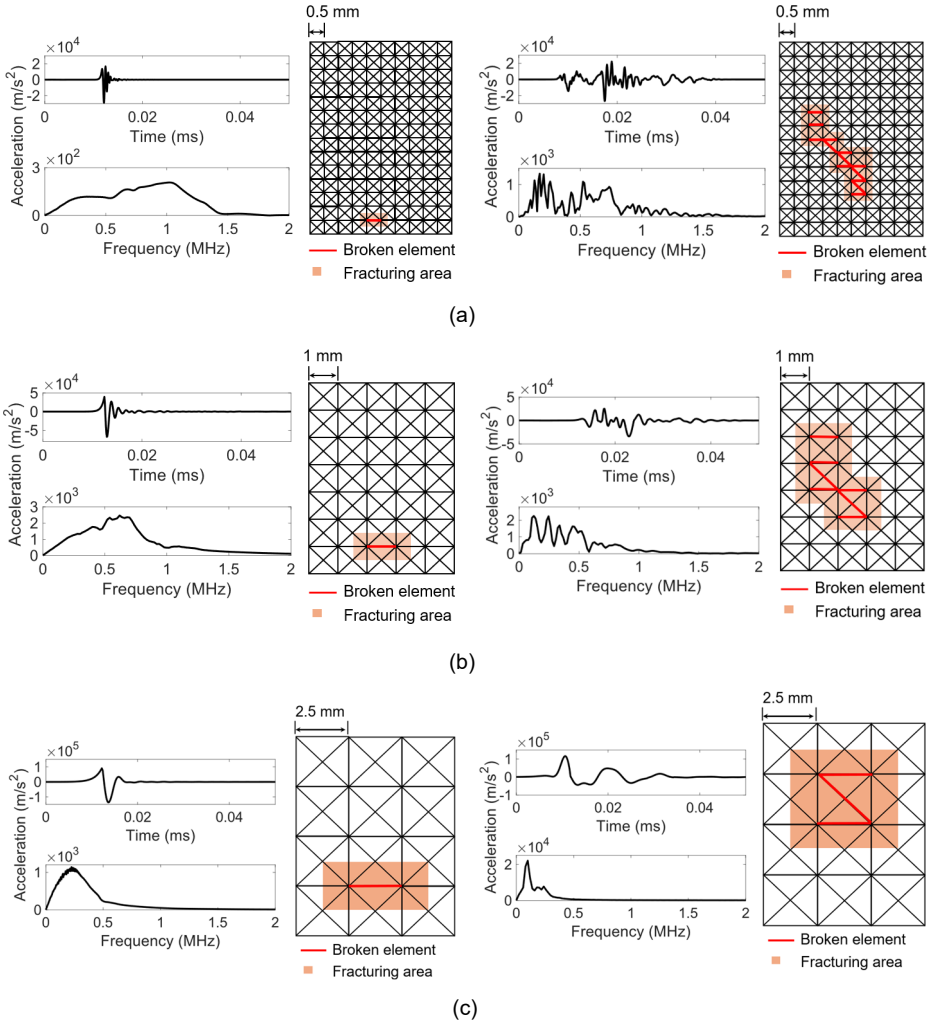

Figure. 8.11 Typical AE source signals and corresponding broken elements: (a) 0.5 mm grid size; (b) 1 mm grid size and (c) 2.5 mm grid size.

Since the source peak frequency is closely related to the volume of the corresponding fracture zone in both scenarios (one or more broken elements involved in one AE source) presented in Figure 8.11, we convert the statistical results of the number of broken elements in Figure 8.10 into the corresponding fracture volumes. The fracture volume associated with a source signal generated by one or multiple broken elements is denoted as $\phi_f^{(sum)}$, to distinguish it from the single-element fracture volume ϕ_f defined in Equation (3.3). The value of $\phi_f^{(sum)}$ is calculated as the sum of the volumes represented by all the nodes (lumped masses) involved in the fracture zone actively responsible for AE generation (see Figure 7.8), as follows:

$$\phi_f^{(sum)} = \sum_{i=1}^{q} \phi_{n,i} \tag{8.1}$$

where $\phi_{n,i}$ is the fracture volume represented by i-th node (see Equation (3.1b) for the expression of $\phi_{n,i}$) and q is the number of nodes (lumped masses) involved in the fracture zone.

The correlation between $\phi_f^{(sum)}$ and the source peak frequency ($f_p^{(s)}$) is illustrated in Figure 8.12, displayed as point plots with error bars, incorporating all numerical source signals under three different lattice grid levels. Since the simulation setup presented in this chapter is consistent with that in Chapter 7, the AE indicator proposed in Chapter 7 for quantifying the relationship between $f_p^{(s)}$ and the single-element fracture volume ϕ_f (see Equation (7.3)) is also plotted in Figure 8.12 to assess its applicability to AE sources induced by multiple successive microcracks (i.e., multiple broken elements). Despite some scatter, the proposed AE indicator demonstrates a good fit with the numerical data across all source signal scenarios and lattice discretization levels. This result reinforces the validity of the AE source peak frequency as a reliable indicator for characterizing concrete tensile fracturing behaviour. Such a correlation explains that the observed evolutionary trends of AE source peak frequency in Figure 8.4. The variations in source peak frequency are physically explained by the variations in the volumes of active fracture zones responsible for AE generation in different loading stages.

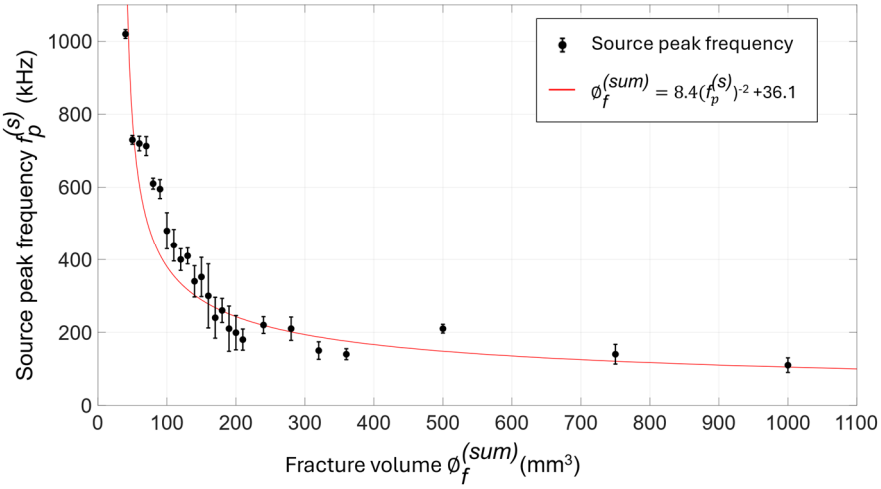

Figure. 8.12 Correlation between AE source peak frequency and corresponding active fracture volume for all numerical source signals under three different lattice grid levels.

8.5.2.2 AE source energy

As can be seen in Figure 8.11, the characteristics of AE energy is also closely related to the scale of the corresponding fracture zones.

For AE source signals generated by a single broken element, as illustrated in the three subfigures in the first column of Figure 8.11, a larger fracture volume results in both a longer signal duration and a higher amplitude. This is attributed to the longer rise time of the displacement jump, which develops in a continuous manner (see Chapters 5 and 6). The combined effect of increased duration and amplitude leads to a higher source energy.

For AE source signals generated by several broken elements, as illustrated in the three subfigures in the second column of Figure 8.11, the signals exhibit longer durations, but similar amplitudes compared to those induced by single-element breakage at the same grid level. The increased duration contributes to higher source energy.

Figure 8.13 illustrates the breakage sequence of lattice elements corresponding to a typical source signal induced by multiple broken elements obtained at the 1 mm lattice grid level to understand the characteristics of such source signals. The initiation times of element breakage, defined as the moments when the element strain exceeds the cracking strain ε_{cr} (see Section 8.3), are marked with red dots. To visualize the temporal progression of fracture, the evolution of the fracturing area responsible for the AE signal is presented as a series of broken element patterns corresponding to each red dot. It can be found that the involved broken elements are not all broken at the same time but in a progressive fracturing manner during the signal duration.

As illustrated in Chapters 5 and 6, a tensile cracking-induced AE signal originates from a local displacement jump caused by microcracks (i.e., broken elements). In the case of a single-element breakage (see subfigures in the first column of Figure 8.11), this displacement jump is rapidly attenuated due to material damping and wave geometric spreading loss (refer to Section 3.2.3). However, when multiple elements break in succession (as shown in the second column of Figure 8.11), each subsequent element breakage introduces new displacement jumps before the response from earlier ones is fully attenuated. This results in continuous dynamic disturbances within the system, leading to extended signal durations. Since signal energy is positively correlated with signal duration (as demonstrated in Appendix A), such events exhibit higher total source energy. Therefore, the observed evolutionary trends of AE source energy in Figure 8.7 are from the variations in fracture sequence of the total active fracture zones corresponding each source signal in different loading stages.

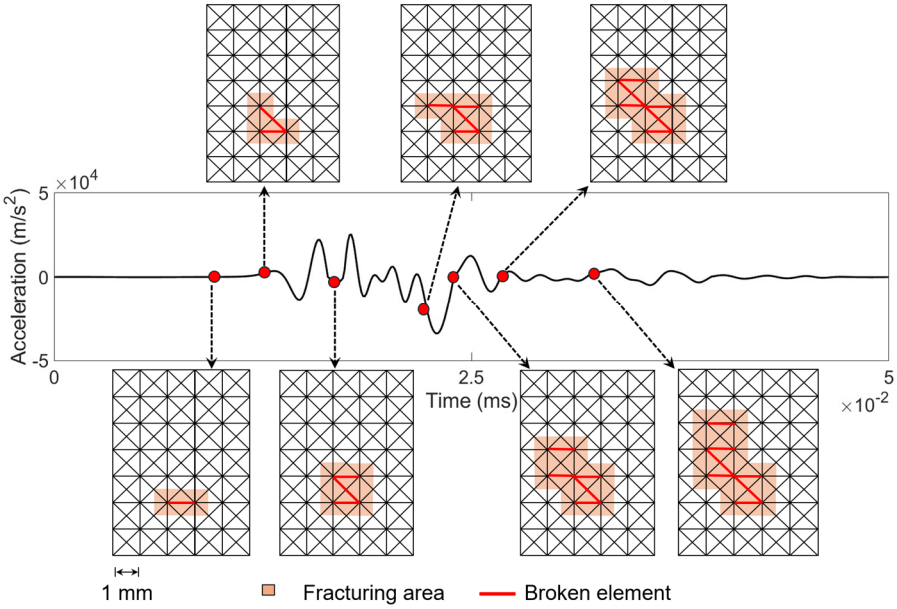

Figure. 8.13 Occurrence sequence of broken elements in a typical AE source signal.

Figure 8.14 presents the normalized energy and duration values of the experimental AE signals recorded by sensor S1 (see Section 4.3), with each dataset scaled by its maximum value. The results demonstrate a clear positive correlation between AE energy and signal duration, reinforcing the above conclusion that longer source durations are a key factor contributing to higher source energies. However, it should be mentioned that parts of experimental AE signals can be generated by the friction mechanisms (shear fracture), while all the numerical signals are induced by tensile cracking. In a future study, the friction-related AE mechanisms should be further investigated (see Appendix M for more details).

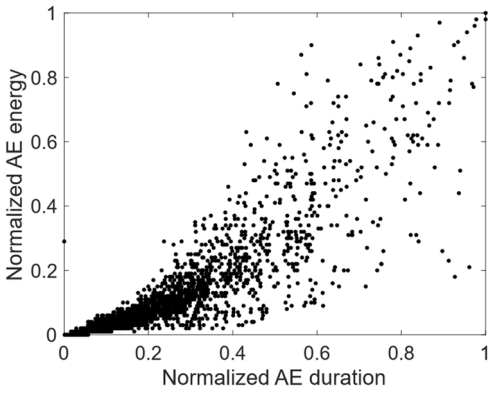

Figure. 8.14 Correlation between the energy and duration of experimental AE signals measured by sensor S1.

8.6 Discussion

This section explores how the above derived insights into numerical AE sources from lattice modelling can be applied to real-world scenarios. The preceding analyses revealed that AE source characteristics are significantly influenced by both the scale of the corresponding fracture zones and the sequence of fracturing events within those zones. These implications for physical AE sources can be categorized into two representative scenarios:

Scenario 1: numerical signals from single-element breakage.

Numerical sources resulting from single-element breakage at different lattice grid levels (see the first column of Figure 8.11) correspond to physical AE sources generated by continuous microcrack growth, wherein the fracture zone fails in a single, uninterrupted cracking step.

Scenario 2: numerical signals from multiple-element breakage.

Numerical sources produced by multiple-element breakages at the same lattice grid level (see the second column of Figure 8.11) represent physical AE sources arising from discontinuous microcrack growth. In this case, the fracture zone fails progressively over a short period, but the resulting AE signal is perceived as a single source.

These two scenarios cannot be simultaneously reproduced in a single lattice simulation due to the constraints imposed by the adopted uniform lattice grid, which limits the variability in fracture scale and sequence. However, in real materials such as concrete, which behaves as a strongly heterogeneous continuum, a range of fracture scales and diverse fracturing sequences can occur concurrently during crack propagation. In the

following, we discuss the shared characteristics and distinctions of numerical AE sources in these two scenarios and the implications for physical AE sources in experiments:

Shared numerical characteristics and experimental implications:

Because both scenarios can coexist in real materials, their combined characteristics offer a representative depiction of physical AE sources. In both cases, the frequency of the resulting AE sources shows a negative correlation with the fracture zone volume, as the frequency contents of AE sources are determined by the vibrational characteristics of corresponding fracture zones (see Section 7.5). This relationship can be quantified using the AE indicator proposed in Equation (7.3) (see Figure 8.12). Furthermore, larger fracture scales tend to produce longer source durations and, consequently, higher source energies (see Figure 8.11). However, a precise quantitative relationship between fracture scale and source energy cannot be established due to variability in the time intervals between successive microcrack events (see Figure 8.13). This suggests that source peak frequency is a more stable parameter than source energy for characterizing microscopic fracturing behaviour in concrete, a conclusion supported by the observation in Figure 8.10, where AE energy shows more scatter (i.e., longer error bars) than peak frequency.

These shared characteristics also help explain results reported in multiple experimental studies (Backers, Stanchits, and Dresen 2005; Dong, Xiangdong, and Libin 2014; Jiang et al. 2021; Zheng et al. 2023; Du et al. 2020). These studies observed that AE signals with high energy and low frequency typically occur near peak load or during loading stages marked by rapid reductions in global stiffness (see also the experiment results of the modelled three-point bending test in Figures 8.2 and 8.5). Such global stiffness changes indicate the fracturing of a large portion of the overall fracture zone, as the global stiffness of a specimen is governed by that of its constituent sub-volumes. This condition increases the likelihood of sub-zones of large scales failing within a short time frame, producing AE sources with lower frequencies and higher energies, regardless of whether the failure occurs continuously (Scenario 1) or discontinuously (Scenario 2).

Numerical distinctions and experimental implications:

Despite these shared characteristics, the two scenarios exhibit notable differences in source amplitude, which is primarily governed by the behaviour of displacement jumps caused by individual microcracks within a fracture zone (see also Chapter 5). As shown in Figure 8.11, a clear correlation exists between peak amplitude and fracture zone size when the fracture zone fails in a continuous manner (Scenario 1) (see also Chapter 7). However, this relationship does not hold for AE signals generated by multiple breakages at the same lattice grid level (Scenario 2), due to the discontinuous nature of the fracturing

process. This distinction suggests that AE energy is a more reliable time-domain parameter than amplitude for characterizing fracture scale, as it is less affected by the sequence of microcrack events.

8.7 Summary

This chapter provides a fundamental interpretation of the evolution trends of typical acoustic emission (AE) parameters observed during tensile crack propagation in the three-point bending test described in Section 4.3. By applying the lattice modelling framework developed in Chapters 3 and 4, we systematically disentangle the individual contributions of AE source characteristics, wave propagation effects, and sensor response to the observed evolution of AE parameters.

The analysis reveals that while the trends observed in experiments are significantly influenced by case-dependent factors such as wave attenuation and the sensor's frequency response, some features of the AE sources are retained in the measured parameters. We further explore the fracture mechanisms driving the evolution of AE source characteristics and examine their implications for interpreting physical AE sources in real-world scenarios.

It is found that AE source characteristics are primarily governed by the scale of the associated fracture zones and the sequence of microcrack growth within them, both of which evolve throughout the cracking process. AE source peak frequency shows a negative correlation with fracture zone volume, reflecting the fact that the frequency content of AE signals is shaped by the vibrational properties of the fracture zones. AE source energy, in contrast, increases with fracture zone size, as larger zones tend to produce longer-duration signals, whether from a single continuous microcrack or from successive, discontinuous microcracks.

Although the analyses are based on a specific experimental case, the findings offer broadly applicable insights that can guide more rational interpretation of AE data across different test configurations and materials. Key experimental phenomena are clarified as follows:

- **Spatial distribution of AE events**: The scattered locations of AE events around visible cracks are not solely due to localization errors but also reflect the broader widths of the active fracturing zones generating the AE signals (see Appendix L).
- **Zonal patterns of AE peak frequency**: The spatial clustering of peak frequency values is primarily a result of the frequency-response characteristics of the AE sensors. These patterns should not be used as criteria for identifying AE source types (see Section 8.4.1).

- **Fracture zone size and AE source parameters**: The size of the fracture zone is positively correlated with AE source energy and negatively correlated with AE source peak frequency (see Section 8.5.2).
- **High-energy, low-frequency AE near peak load**: AE signals with high energy and low peak frequency tend to occur near the peak load or during other loading stages marked by rapid changes in global stiffness, due to the involvement of larger fracture zones occurring in short period at these critical stages (see Section 8.5.3).
- **AE energy vs. peak amplitude**: AE energy is a more robust time-domain parameter than peak amplitude for characterizing fracture behaviour, as it is less sensitive to the sequence in which microcracks occur within a given fracture zone that induces an AE response (see Section 8.5.3).

9. Conclusions and Recommendations

9.1 Retrospective view

This study aims at deepening the understanding of the mechanisms behind acoustic emission (AE) generated during concrete fracture processes, with the goal of enhancing the reliability of AE techniques for monitoring concrete structures under loading. Since tensile cracking is the primary source of AE in concrete, the main objective of this dissertation is to model and quantify AE signals induced by tensile cracking in concrete.

To achieve this overarching goal, the research addresses several sub-goals:

- **Sub-goal 1**: Develop a modelling framework for AE wave propagation with attenuation in concrete (Chapter 3), as well as for sensor response (Chapter 4), thus enabling simulation of the complete waveforms of concrete tensile cracking-induced AE signals.
- **Sub-goal 2**: Achieve a fundamental understanding of how tensile cracking in concrete gives rise to AE phenomena (Chapters 5 and 6).
- **Sub-goal 3**: develop physics-grounded and quantitative AE indicators that influence AE parameters (Chapter 7).
- **Sub-goal 4**: Gain fundamental insights into the effects of successive tensile fracturing processes on AE parameters in concrete (Chapter 8).

The following sub-sections summarize the accomplishment of these sub-goals and highlight the key contributions of this dissertation.

9.1.1 A lattice modelling framework for the complete acoustic emission waveforms in concrete tensile fracturing processes

Chapter 3 presents a general modelling framework that simulate the propagation and attenuation of AE-induced elastic waves in concrete using a lattice modelling approach. This is achieved by incorporating two novel techniques: (1) a proportional-integral-derivative (PID) control algorithm, which suppresses spurious noise unrelated to fracture-induced responses within the explicit time integration procedure; (2) a Rayleigh damping-based theoretical approach, along with a corresponding calibration procedure, to model the attenuation of AE signals. Furthermore, a quantitative relationship is established between lattice mesh sizes and frequency resolution of simulated waves.

Chapter 4 implements the model to simulate the full AE waveforms by proposing additional techniques to explicitly account for AE sensor responses in computational modelling, including the physical geometry and frequency-response sensitivity of AE sensors.

The model is further experimentally validated through comparison with experimental results from a three-point bending test on a notched concrete beam.

9.1.2 Revelation of the source mechanisms of concrete tensile cracking-induced AE phenomena

Chapter 5 presents an analytical modelling approach to understand AE phenomena induced by concrete tensile cracking. A one-degree-of-freedom (1-DoF) dynamic system is used to represent a localized tensile cracking region in concrete. The analysis reveals that AE phenomena are caused by the sudden opening of crack tips during the early softening stage. Mathematically, this results in an exponential form of the dynamic response at the fracture zone, which physically manifests as a local displacement jump and further induces subsequent vibrations of the fracture region.

Chapter 6 builds on the foundation of analytical modelling by applying the lattice modelling framework (developed in Chapters 3 and 4) to a more realistic two-dimensional (2D) case. The simulations reveal that the dynamic response of a tensile cracking region consists of two distinct stages: an initial stage characterized by an exponential-shaped acceleration jump, followed by a second stage of attenuated vibrations. Together, these two stages generate a Gaussian-shaped acceleration pulse in the local fracture area, which is the source of the acoustic emission signal.

9.1.3 A physically grounded AE indicator for quantifying concrete tensile cracking behaviour

Chapter 7 utilizes the lattice modelling framework developed in Chapters 3 and 4 to quantify AE source parameters induced by concrete tensile cracking, these parameters are initially identified through the analytical modelling in Chapter 5. A comparative analysis of various influencing factors reveals that time-domain AE source parameters are sensitive to a wide range of input variables, while frequency-domain source parameters are predominantly governed by intrinsic properties of the fracture zone, such as material density, elastic modulus, and fracture volume.

Based on these findings, a quantitative relationship is established between the AE source peak frequency and the corresponding fracture volume. This relationship serves as a physically grounded AE indicator for characterizing concrete tensile cracking behaviour. Several case studies are conducted to demonstrate the practical applications of this indicator, including: (1) estimating the size of the fracture zone in concrete based on measured AE peak frequency, and (2) optimizing AE sensor layout and AE types to effectively monitor AE signals associated with specific fracture volume scales.

9.1.4 Physical explanations for the evolution trends of acoustic emission parameters during concrete tensile cracking propagation

Chapter 8 employed the lattice modelling framework developed in Chapters 3 and 4 to provide a fundamental interpretation the variation of typical AE parameters observed during successive tensile crack propagation in a three-point bending test. The analysis shows that, although measured AE signals are significantly influenced by wave attenuation and sensor frequency response, key features of the AE sources are still preserved in the experimental data. Specifically, AE source peak frequency is found to be negatively correlated with fracture zone volume, due to the vibrational properties of the source, while AE source energy increases with fracture zone size, reflecting the longer signal durations generated by larger or successively activated crack tips.

9.2 Conclusions

This section provides the key insights gained from the analytical and numerical modelling conducted in this dissertation, as outlined below:

- **Tensile cracking-induced AE originates from sudden propagation of crack tip**.

  The fundamental source of AE in concrete tensile cracking is the sudden propagation of crack tip, which results in rapid stiffness degradation within both the local fracture zone and the overall structure. This degradation simultaneously produces a transient displacement discontinuity at the microscale and a sharp drop in global load or stress at the macroscale (see Section 6.3). Such a transient displacement discontinuity follows by the vibrations of the fracture zone that generates acoustic emission (see Section 5.7).

- **The frequency characteristics of an AE signal at its source are determined by vibration characteristics of fracture zones**.

  Since the physical nature of tensile cracking-induced AE sources is the cracking-induced vibrations of local fracture zone, the frequency characteristics of tensile cracking-induced AE at the source should be interpreted from the point view of the vibration characteristics (namely volume, elasticity and density that determine the nature frequencies) of the fracture zone instead of the transient duration of cracking increment (i.e., the source rise time characterizing fracturing velocity) as in the classical AE theory (see Section 5.4 and Section 7.5).

- **There is no direct relation between fracture energy and AE phenomena**.

  AE activity does not directly reflect Mode-I fracture energy in concrete. AE signals are triggered by the sudden propagation of microcracks, representing only a small

fraction of the total energy dissipated during the tensile fracture process. (see Section 6.4.2)

- **Wider spatial distributions of AE sources than visible cracks are not only from localization errors**.

  The scattered spatial distribution of AE events around the main visible cracks observed in experiments is not solely due to localization errors. It also reflects the broader extent of the fracturing zones that actively generate AE signals. (see Section 4.5.2, Section 7.5.1 and Appendix L)

- **Measured AE parameters are significantly affected by sensor response**.

  The sensors largely altered the original AE waves, for which the influence from both the diameter of sensor surface and the frequency-response sensitivity. Sensor geometry can reduce time-domain amplitudes and attenuate high-frequency components of AE signals. Additionally, the frequency-response of AE sensors reshapes the wide-band frequency content of original waves into narrower-bands response of measured AE signals. (see Section 4.6.3 and appendix D)

  The zonal distribution patterns of AE peak frequencies during loading history are largely influenced by the frequency-response characteristics of the sensors used. As such, these patterns should not be used as definitive indicators for AE source type classification. (see Section 8.2)

- **Frequency-domain AE source parameters are more reliable than time-domain source parameters**.

  Frequency-domain AE source parameters (e.g., AE source peak frequency) are generally more reliable indicators of concrete fracture behaviour than time-domain source parameters, as AE source frequency is primarily influenced by inherent properties of fracture zone while the time-domain parameters are affected by many other factors, such as tensile strength, fracture brittleness and external loading conditions. (see Section 5.8, Section 7.3 and Section 7.5.2)

  Among other time-domain source parameters, AE source energy is more reliable than source peak amplitude for characterizing fracturing behaviour because it is less affected by the sequencing of successive fracture events. (see Section 8.5)

- **Rapid global stiffness degradation leads to lower-frequency and higher-energy signals.**

  AE signals with high energy and low peak frequency that occur near peak load or during phases of rapid global stiffness degradation that are attributable to larger fracture zones. (see Section 8.6.3)

9.3 Recommendations for the future work

This section highlights several research directions closely related to the work presented in this dissertation and proposes them as promising avenues for future investigation.

9.3.1 Improvement of the proposed lattice model

Chapters 3 and 4 introduced a lattice modelling framework capable of simulating the complete waveforms of AE signals generated by concrete tensile cracking. However, several limitations remain that should be addressed in future work:

- Directional dependence of elastic wave velocities:

  The current 2D truss-based square lattice network exhibits direction-dependent Poisson's ratios, resulting in unequal elastic wave velocities in different propagation directions. One can consider using advanced lattice configurations that mitigate these Poisson's ratio constraints, enabling more accurate simulation of elastic wave propagation (see Section 3.6.2).

- Interaction of waves with existing cracks:

  The current model does not adequately capture the effects of existing cracks to elastic wave propagation. This limitation can be addressed by assigning increased damping values to nodes connected by broken elements, thereby more realistically modelling wave-crack interactions (see Section 4.6.2).

- Effect of concrete heterogeneity on AE response:

  Concrete was treated as a homogeneous material at the mesoscale in this study, and the influence of material heterogeneity on AE response was not explored. This can be incorporated in future models by introducing randomly distributed material properties across elements or using randomly generated lattice meshes to represent heterogeneity within the lattice modelling framework (see Section 4.6.2).

- 2D simulations:

  This study is restricted to 2D modelling due to computational efficiency constraints, as AE simulation requires small time steps and fine lattice grids. Future work could explore 3D lattice modelling by implementing adaptive time-stepping techniques or by coupling lattice fracture elements with high-order elastic finite elements within a hybrid modelling approach (see Section 4.6.2).

- AE sensor response:

  AE sensors are not only responsive to waves arriving perpendicular to the PZT element but also to those arriving laterally or at intermediate angles. Such directional characteristics can influence signal amplitude and frequency content, particularly in

complex propagation fields. In a future study, such directional effects of AE sensors can be further investigated. Moreover, this study uses particle accelerations to numerically represent AE signals. Nevertheless, in classical AE theories (Grosse et al. 2021), an AE signal is usually represented by particle velocity. The numerical representation methods of AE signals should be further investigated in a future study.

9.3.2 Modelling friction-induced AE sources with lattice model

Tensile cracking at crack tips and friction along macrocrack surfaces are two major sources of acoustic emission (AE) during concrete fracturing processes under different modes (see Section 2.4). This dissertation focuses on modelling and understanding AE relating tensile cracking. However, the potential applicability of the proposed lattice modelling approach to friction-induced AE remains an open area for future investigation, with the goal of simulating AE signals generated by different concrete fracture modes under various external loading conditions.

Preliminary efforts towards simulating friction-induced AE signals are presented in Appendix M. These results demonstrate that implementing a dynamic stick-slip friction law, such as that proposed by Raous and Barbarin (Raous and Barbarin 1996), can successfully reproduce the long-rise times and low-frequency characteristics typical of friction-induced AE observed in experiments. However, coupling tensile cracking and stick-slip friction within the current lattice modelling framework has not yet been achieved mainly due to the following numerical challenges:

- Identification of friction pairs:

  Friction physically occurs only along surfaces that have already undergone tensile cracking in quasi-brittle materials. This could be implemented in the lattice modelling by adopting techniques from the extended finite element method (XFEM), which introduces additional degrees of freedom to identify tensile-cracked elements and nodes as potential crack surfaces (Xu, Hajibeygi, and Sluys 2024).

  Furthermore, friction along crack surfaces involves large deformations, and the contact areas where friction forces act can change dynamically during crack propagation. Defining friction pairs is essential to determine the appropriate application points/areas of frictional forces within the model. Useful numerical techniques for defining such friction pairs are discussed in the work by Karpenko and Akay (Karpenko and Akay 2001).

- Modelling and calibration of rate-dependent stick-slip friction laws:

  As demonstrated in Appendix M, AE signals related to friction are mainly generated by stick-slip mechanisms between cracking surfaces, which requires the numerical

implementation of the dynamic stick-slip friction laws between the identified friction pairs. A relevant implementation example can be found in the work by Hoving and Metrikine (Hoving and Metrikine 2017).

The implementation of the stick-slip friction laws also requires dedicated numerical algorithms for physically describing the contact conditions of potential friction pairs (e.g., the determinisation of critical crack open thresholds to allow the contact of crack surfaces and the avoidance of normal penetration of the contact surfaces through the penalty method (Stefancu, Melenciuc, and Budescu 2011)).

Additionally, since this type of friction laws involves multiple parameters (see Appendix M), corresponding experimental methods for parameter identification or model calibration are essential for improving predictive accuracy.

9.3.3 Determination of microscopic material constitutive parameters through AE measurements

Most existing discrete element methods (DEM) and microscopic fracture models rely on nonlinear material parameters that are not directly measurable through conventional experimental techniques. However, as demonstrated in Chapters 5, 6, and Appendix M, AE signals reflect the dynamic response of a system to local nonlinear effects caused by fracture and contact interactions. This indicates that AE measurements, which are inherently linked to these localized nonlinear behaviours, hold potential as an indirect method for identifying parameters in microscopic nonlinear constitutive laws.

Chapter 5 presents a closed-form solution for determining the critical tensile strain range associated with microcracking behaviour responsible for generating AE. Additionally, Chapter 7 establishes a quantitative relationship between AE source peak frequency and the corresponding fracture volume. Building on these insights, future research should focus on exploring the correlations between various AE (source) parameters and microscopic fracturing or contact properties. Such investigations could be instrumental in identifying key material parameters that are otherwise inaccessible, thereby advancing the development and calibration of microscopic constitutive models.

9.3.4 More accurate AE measuring for better experimental AE source characterization

Chapter 7 establishes a quantitative relationship between AE source peak frequency and the corresponding fracture volume. However, the practical application of such an AE indicator is significantly constrained by the influence of sensor response on the measured AE signals. To achieve more reliable characterization of AE sources, it is essential to minimize the effect of sensor response in experimental settings.

Since this influence arises primarily from the sensor's surface diameter and its frequency-response sensitivity, using wide-band sensors with smaller diameters offers a promising solution. Sensors such as the 9203 (Mistras 2018) and S9208 (Mistras 2022)) are particularly suitable for this purpose, as they are designed to reduce the distortion of AE signal characteristics and better preserve the true frequency content of the source. Moreover, the laser doppler vibrometer (Tue, Theiler, and Tung 2014) can be an alternative vibration (wave) measuring technique that can fully remove the sensor response.

Moreover, proper selection of sensor type and sensor layout design are essential components of effective AE monitoring. Traditionally, these are determined solely based on the attenuation characteristics of elastic waves propagating through the monitored medium (Cui et al. 2019). While it is ideal to also consider the AE source response to enhance the accuracy of sensor selection and layout design, conventional approaches are limited by the insufficient understanding of AE source characteristics. Chapter 7 provides a procedure to optimized sensor layouts and sensor types for monitoring the desired fracture volume range. This procedure can be implemented in future experimental studies.

Furthermore, it is important to note that the quantitative relationship established in Chapter 7 between the AE source peak frequency and the corresponding fracture volume applies exclusively to tensile cracking. However, in real concrete fracturing processes, AE signals may also arise from frictional mechanisms. For friction-induced AE signals, further research is required (see Section 9.3.2) to validate the relationship between fracture volume (i.e., the slip zone defined in Appendix M) and signal frequency characteristics. Until the underlying mechanisms of friction-induced AE are better understood, a practical interim solution is to classify AE source types (tensile versus frictional) using an established classification criterion (Zhang et al. 2022). By isolating the frictional signals, the proposed indicator in Chapter 7 (as well as other conclusions of this dissertation) can then be more reliably applied for AE source characterization.

Notation

Roman upper case

A	Wave amplitude
A^*	Effective wave amplitude
$\bar{A}$	Average wave amplitude
$\tilde{A}$	Normalized wave amplitude
A_p	Wave peak amplitude
$\tilde{A}_p$	Normalized wave peak amplitude
A_{sensor}	Wave amplitude with "sensor effect"
C_i, C_i', C_i'', C_i'''	i-th constant coefficient (i =1, 2)
D	Sensor diameter
E	Young's modulus
F	Nodal force
F_0	Driving force
F_e	Element force
F_{ei}	Force of i-th element (i =1, 2)
F_{fr}	Friction force
F_{frs}	Maximum static friction force
F_{frd}	Dynamic friction force
G_f	Fracture energy
H_i	i-order polynomial function
I_{sensor}	Sensor frequency-response sensitivity function
I_{wave}	Effects of wave propagation and attenuation
K^*	Effective system stiffness
$K_{structure}$	Structural stiffness
K_{FPZ}	Stiffness of the fracture process zone
L	Structural length
L_{wave}	Wave propagation distance
P_0	Force boundary condition
$\dot{P}$	External loading rate
Q_i	i-order polynomial function
S	Area
S^*	Lattice element cross-sectional area
S_f	Size of a fracture area
T	Wave period
T_{rise}	Source rise time
V	Wave velocity
V_P	Pressure wave velocity
V_R	Rayleigh wave velocity
V_S	Shear wave velocity
W	Strain energy
W^*	Effective strain energy
$\boldsymbol{C}$	Damping matrix
$\boldsymbol{F}$	Internal nodal force vector
$\boldsymbol{K}$	Stiffness matrix

$\boldsymbol{M}$	Mass matrix
$\boldsymbol{P}$	External force vector

Roman lower case

a_i	i-th tensile softening factor (i =1, 2, 3)
b_i	i-th force reduction factor (i =1, 2)
c	Damping
c_0	Critical damping
c_i	i-th constant coefficient (i =1, 2)
d	Lattice grid level
d_0	A critical lattice grid level used for constitutive law calibration
e	PID tracking error
f	Wave frequency
f_c	Compressive strength
$f_{c,cube}$	Cube compressive strength
f_{max}	Cut-off frequency
f_{Ny}	Nyquist frequency
f_{sp}	Sampling frequency
f_t	Tensile strength
$f_p^{(s)}$	AE source peak frequency
$f_p^{(w)}$	Peak frequency of AE waves
$f_p^{(m)}$	Measured AE peak frequency
g, g', g''	A function
h_p	Proportional PID parameter
h_i	Integral PID parameter
h_d	Derivative PID parameter
k	Stiffness
l	Lattice element size
m	Mass
m_n	Mass of a lattice node (lumped mass)
n	A number
p	A constant coefficient
q	A constant coefficient
r	Distance to source
s	Sensor area presented by a node
t	Time
t_1	Loading time corresponds to cracking strain
t_2	Loading time corresponds to first tensile softening limit
t_3	End time of the source vibration
t_{max}	Total processing time
u	Nodal displacement
u'	Nodal displacement of a symmetric node
u_0	A critical displacement value
u_x	x-direction displacement
u_y	y-direction displacement

u^0	A particular solution of displacement
$\dot{u}$	Nodal velocity
$\dot{u}_0$	External loading rate prescribed by a constant velocity
$\dot{u}_{frd}$	Friction velocity corresponds to the maximum static friction force
$\dot{u}_{frs}$	Friction velocity at the onset of slip
$\ddot{u}$	Nodal acceleration
v_0	Applied boundary velocity
w	Specimen thickness
x	Coordinate
y	Coordinate
z	Coordinate
$\boldsymbol{u}$	Displacement vector
$\dot{\boldsymbol{u}}$	Velocity vector
$\ddot{\boldsymbol{u}}$	Acceleration vector

Greek upper case

$\Delta\tilde{A}_p^{(cr)}$	A detection threshold of wave amplitude
Δd_{max}	Maximum sensor spacing distance
Δr	Relative distance
Δt	Time step (interval)
Δt_{max}	Maximum arrival time difference of signals in an AE event
$\Delta \dot{u}$	Crack mouth opening displacement (CMOD) rate
Δx	Variation of AE source parameters
$\Delta\tilde{x}$	Normalized variation of AE source parameters
Ω^+, Ω^-	Two sub-domains divided by a fracture

Greek lower case

α	Mass-proportional damping coefficient
β	Stiffness-proportional damping coefficient
β_0	A critical value of β
γ	Attenuation from material damping
$\tilde{\gamma}$	Normalized attenuation of material damping
$\gamma_{\text{logarithmic}}$	Logarithmic decrement
δ	A constant coefficient
ε	Strain
ε_{cr}	Cracking strain
ε_e	Element strain
ε_i	Strain of *i*-th element (*i* =1, 2, ...)
ε_x	*x*-direction strain
ε_y	*y*-direction strain
$\dot{\varepsilon}$	Strain rate
ζ	A constant coefficient
η	Material damping factor
η_0	Wave geometric spreading loss variable

η_R	Material damping factor of Rayleigh wave
θ	The angle between strain-axis and force-axis directions of the non-linear force-strain constitutive curve of lattice element
θ_{cr}	A critical value of θ
θ_i	The angle between strain-axis and force-axis directions in the (i+1)-th tensile softening stage (i =0, 1, ...)
λ	Wavelength
λ_P	Pressure wavelength
λ_{P_Ny}	Nyquist pressure wavelength
μ	Function root
μ_i	i-th function root (i =1 and 2)
μ_0	Repeated function root
υ	Poisson's ratio
ξ	Damping ratio
ρ	Material density
σ	Normal stress
τ	Shear stress
φ	Wave phase angle
ϕ	Volume
ϕ_f	Fracture volume represented by a broken lattice element
$\phi_f^{(sum)}$	Sum of the volumes represented by all the nodes (lumped masses) Involved in the fracture zone actively responsible for AE generation
ϕ_{FPZ}	Volume of the fracture process zone
ϕ_n	Material volume represented by a lattice node (lumped mass)
χ	Imaginary unit
ω	Wave angular frequency
ω_0	A critical wave angular frequency value
ϑ	A positive constant characterizing the change degree of friction force in the stick-slip transition process

Subscripts and superscripts

*	Effective quantity
0	Quantity related to critical or initial values
P	Quantity related to pressure waves
R	Quantity related to Rayleigh waves
S	Quantity related to shear waves
c	Quantity related to compressive strength
e	Quantity related to element
f	Quantity related to fracture
i	Integer index
j	Integer index
k	Integer index
m	Quantity related to measured AE signals
n	Quantity related to node
p	Quantity related to peak values

t	Quantity related to tensile strength or time
s/source	Quantity related to acoustic emission source
w/wave	Quantity related to AE waves
x	Quantity related to *x*-direction
y	Quantity related to *y*-direction
FPZ	Quantity related to fracture process zone
Ny	Quantity related to Nyquist criteria
cr	Quantity related to cracking strain or a critical value
cube	Quantity related to cube specimen
fr	Quantity related to friction
frd	Quantity related to dynamic friction
frs	Quantity related to static friction
jump	Quantity related to displacement jump
logarithmic	Logarithmic quantity
max	Quantity related to maximum values/ upper bound
min	Quantity related to minimum values/ lower bound
numerical	Numerical values
rise	Quantity related to source rise time
sensor	Quantity related to acoustic emission sensor effect
structure	Quantity related to the whole structure
sum	Quantity related to the sum of broken element
targeted	Targeted values
theoretical	Theoretical values
vibrate	Quantity related to vibrations

Abbreviations

AE	Acoustic emission
AIC	Akaike information criterion
DEM	Discrete element method
DPC	Dry-point-contact transducer
FEM	Finite element method
P-wave	Pressure wave
R-wave	Rayleigh wave
S-wave	Shear wave
Si	*i*-th sensor (*i* =0, 1, ..., 7)
E0	Fracture source element
LVDT	Linear variable differential transducer
PLB	Pencil-leak break test
PDT	Peak definition time
HDT	Hit definition time
HLT	Hit lockout time
DIC	Digital image correlation
PDE	Partial differential equation
DoF	Degree-of-freedom
FPZ	Fracture process zone
ODE	Ordinary differential equation

MC2010	Fib Model Code 2010
CMOD	Crack mouth opening displacement

Appendix A. Definition of typical AE parameters

As many AE parameters are mentioned and analyzed in this dissertation, the definition of typical AE parameters used in this thesis is briefly described in this Appendix. AE parameters can be mainly distinguished into three categories, including hit definition parameters, characteristic parameters and hit-based waveform recording parameters.

The hit definition parameters are used to extract burst AE signals (AE hits) from a measured continuous waveform flow. Threshold, peak definition time (PDT), hit definition time (HDT) and hit lockout time (HLT) are four hit definition parameters. As illustrated in Figure B1.1a, the threshold specifies the starting time of an AE hit. The PDT is the period that allows to determine the peak amplitude of an AE hit. The HDT is the maximum allowed period between threshold crossing in an AE hit: the hit has ended if no threshold crossing occurs during the HDT. The HLT is the minimum period for detecting a new hit after the end of previous hits, to avoid falsely detecting the reflected or delayed waves as independent AE hits.

After identifying an AE hit, its characteristic parameters can be calculated. Typical time-domain characteristic parameters are illustrated in Figure A.1a. Duration is the period between the first and last threshold crossing. Rise time is the period between the first threshold crossing and the peak amplitude. AE count is the number of signal oscillations crossing the threshold. The ratio between count and duration is defined as average frequency. As illustrated in Figure A.1b, peak frequency and frequency centroid are two main frequency-domain characteristic parameters. The peak frequency is a frequency value corresponding to the maximum energy spectrum point. The frequency centroid is a frequency value that divides the frequency spectrum into two equal areas.

AE waveforms can be recorded in an AE acquisition system in two ways: either recording the complete continuous waveform flow or recording discrete waveforms based on AE hits. The second method is commonly used due to less need of storage space. Pre-trigger time and waveform recording length are two main parameters to recover AE waveforms from identified hits, as shown in Figure A.1b. The pre-trigger time is the period before the first threshold-level crossing. The waveform recording length is the total recording period for a waveform. It should be mentioned that the parameters mentioned herein are only parts of AE parameters. The definition of complete AE parameters can be found in the book (Unnþórsson 2013).

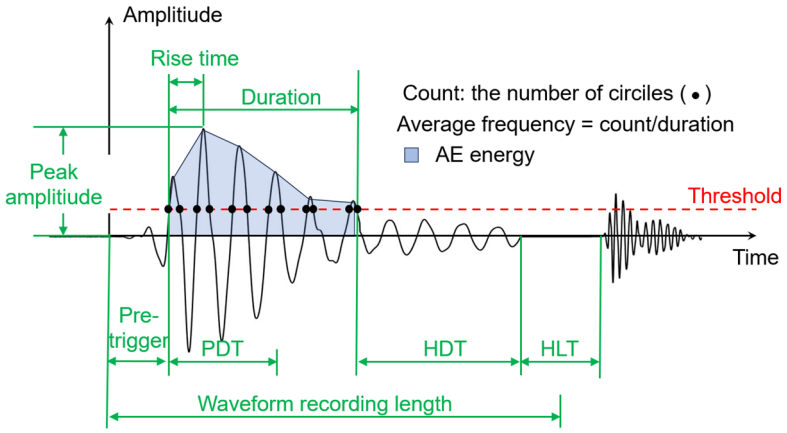

(a)

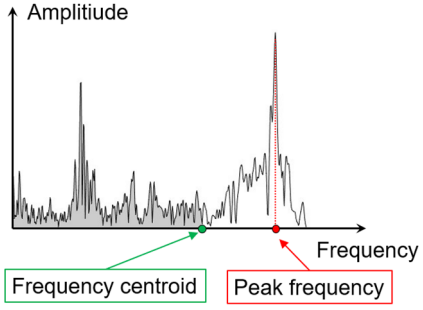

(b)

Figure A.1 Illustration for definition of typical AE parameters: (a) time domain; (b) frequency domain.

Appendix B. Derivative process of effective cross-sectional area of truss elements in adopted 2D square lattice network

The effective cross-sectional area of a lattice element in the adopted two-dimensional truss-based lattice model, $S^*(d)$, is a function of the lattice grid size d and is expressed as:

$$S^*(d) = \frac{3}{2(1+\sqrt{2})} dw \tag{B.1}$$

where w is the specimen thickness. The close-form derivative process of Equation (A.1) is given in the following. Consider a 2D isotropic continuum subjected to equally uniformed biaxial strain fields as:

$$\varepsilon_x = \varepsilon_y = \varepsilon \tag{B.2}$$

where ε_x and ε_y are strains in x and y directions, respectively. ε is a strain value. According to the Hook's law, the strains are further expressed as (Gurtin 1982):

$$\varepsilon_x = \varepsilon_y = \varepsilon = \sigma(\frac{1-\nu}{E}) \tag{B.3}$$

where σ represents stress. ν and E are the Poisson's ratio and Young's modulus, respectively. The elastic strain energy stored in the considered continuum, denoted as W, is then derived as:

$$W = \frac{1}{2}\int(\sigma_x\varepsilon_x + \sigma_y\varepsilon_y)\mathrm{d}\phi = \int\sigma\varepsilon\mathrm{d}\phi = \sigma\varepsilon wS = \varepsilon^2(\frac{E}{1-\nu})wS \tag{B.4}$$

where σ_x and σ_y are stresses in x and y directions, respectively. ϕ and S represents the volume and area of the considered 2D continuum, with $\phi = wS$.

We then use the 2D square truss lattice network to discretize the considered 2D continuum (see Figure 3.1). Assuming all elements (orthogonal and diagonal elements with different lengths) involved in each lattice grid size level d have same effective cross-sectional area $S^*(d)$, the total strain energy stored in the equivalent lattice representation, denoted as W^*, is then calculated as:

$$W^* = \frac{1}{2}\sum_{i=1}^{n}\frac{\left(F_i^e\right)^2 l_i}{ES^*(d)} = \frac{ES^*(d)\varepsilon^2}{2}\sum_{i=1}^{n} l_i \tag{B.5}$$

where F_i^e and l_i are the axial force and length of i-th lattice element.

The total strain energy stored in the considered 2D continuum must equal that in the corresponding discrete lattice elements as:

$$W = \varepsilon^2(\frac{E}{1-\nu})wS = W^* = \frac{ES^*(d)\varepsilon^2}{2}\sum_{i=1}^{n} l_i \tag{B.6}$$

The effective cross-sectional area $S^*(d)$ is then derived as:

$$S^*(d) = \frac{2wS}{(1-\nu)\sum_{i=1}^{n} l_i} \tag{B.7}$$

Selecting a basic unit area of area $S = d^2$ in the adopted 2D square truss lattice network (see Figure 3.1) for analyses, a total of eight elements of half element length (namely $n = 4$) are involved in the basic unit area consisted of two orthogonal elements of length $l = d$ and two diagonal elements of length $l = \sqrt{2}d$. Equation (B.7) is further expressed as:

$$S^*(d) = \frac{2wd^2}{(1-\nu)\sum_{i=1}^{8} l_i} = \frac{2wd^2}{(1-\nu)(2d+2\sqrt{2}d)} = \frac{1}{(1+\sqrt{2})(1-\nu)}wd \tag{A.8}$$

According to the work of Hrennikoff (Hrennikoff 1941), the average value of inherent Poisson's ratio of the adopted square truss-based lattice model equal to 1/3. By substituting $\nu = 1/3$ into Equation (B.8), we derive the expression of $S^*(d)$ as given in Equation (B.1).

Appendix C. Influence of sensor geometry on simulated AE signals

This Appendix conducts a quantitative parametric analysis on the influence of sensor geometry on simulated AE signals in lattice modelling and provides corresponding physical interpretation. Herein, the investigated sensor geometry parameter is the diameter of covering area (area of the bottom surface) of sensors, as we cannot modelling a real 3D sensor in the proposed 2D lattice model.

In chapter 4, we have considered the influence of the physical geometry of sensors in the presented simulation case. Nevertheless, the analyses account only for one geometry of a specific sensor type, namely R15α AE sensors with a circular surface of 19 mm diameter. In this appendix, we analyze the relationship between the diameter of surface D (see Figure 4.4) and typical parameters of simulated AE signals in lattice modelling. We adopt the same numerical case described in chapter 4 (see Section 4.3.1 for detailed numerical setup) for analyses. The first numerical AE signal in the loading process of the three-point bending test is considered. The analyses are based on a combination of nodes with a central coordinate of (250 mm, 0) (namely S1 in Figure 4.2). The weighted average accelerations in y direction calculated by Equation. (4.1) is used to account for the effect of sensor geometry.

The influence of sensor surface diameter D on peak amplitudes and peak frequency of simulated AE signals is shown in Figure C.1, where the values of peak amplitudes and peak frequency are normalized by dividing the maximum values. It can be observed that the peak amplitudes and peak frequency both decrease with increasing sensor diameters.

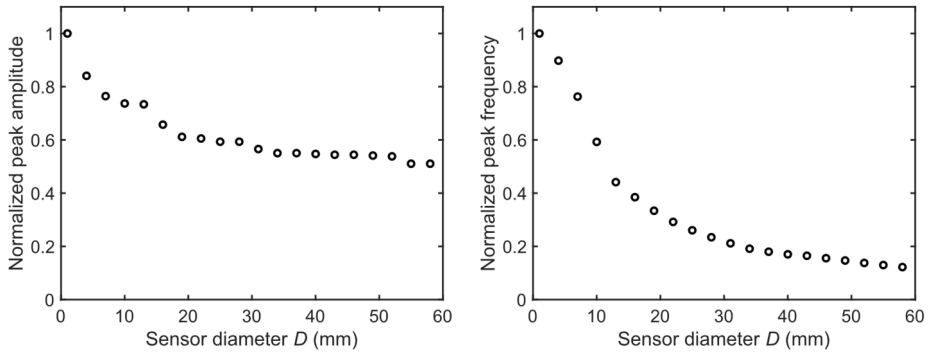

Figure C.1 Influence of sensor surface diameter D on typical parameters of simulated AE parameters: (a) peak amplitudes and (b) peak frequency.

A physical interpretation for above trends is given in Figure C.2. The sensor surface interferes with the waveform shape in both time and frequency domains, as the output of AE sensor comes from the average disturbance over the entire sensor surface, which is called “aperture” effect (Grosse et al. 2021). In the time domain, the high-amplitude components are suppressed because of being averaged over sensor surface (Figure C.2a). In the frequency domain, for the wave components with wavelength λ less than sensor diameter D, many cycles of the wave (multiple wavelengths) are simultaneously acting on the sensor surface, and their contribution is averaged (Figure C.2b). Such high-frequency components are then filtered by the sensors, as their wavelengths are stretched.

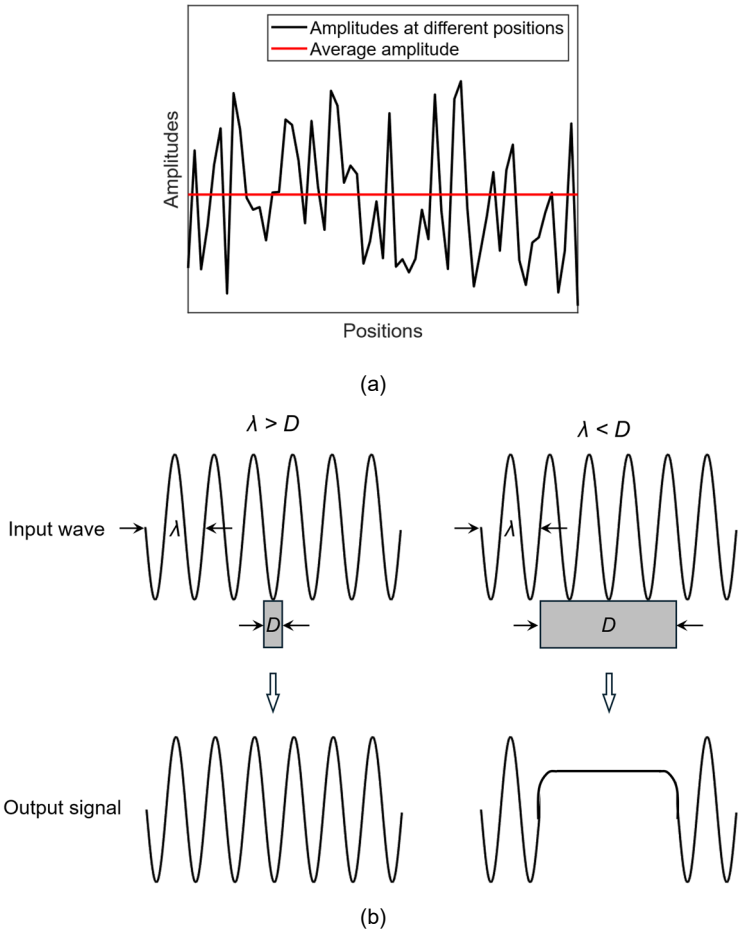

Figure C.2 Physical interpretation for the effect of sensor geometry: (a) amplitude and (b) frequency.

Appendix D. Additional results for numerical AE waveforms without “sensor effect”

This appendix belongs to Chapter 4. we only show numerical results with complete “sensor effect” that are calculated by Equation (4.2) considering both the geometry and frequency-response sensitivity of AE sensors in main text of Section 4.5. Corresponding numerical results in intermediate steps are presented in this appendix. All numerical results presented in this appendix are obtained in the numerical case described in Section 4.4. Throughout this appendix, figures marked with “single node” are *y*-direction accelerations of a single node located in the centre of virtual sensors, while those marked with “sensor geometry” are weighted average accelerations in *y* direction of all nodes included in covering surface of virtual sensors (Equation (4.1)) considering only the effect of sensor geometry.

Figure D.1 provides numerical results in intermediate steps for typical waveforms received by virtual sensor S1 at three different loading stages, corresponding to three typical waveforms presented in Figure 4.14.

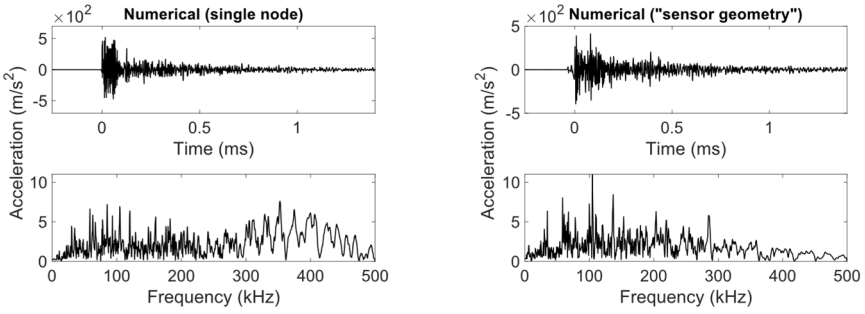

(a)

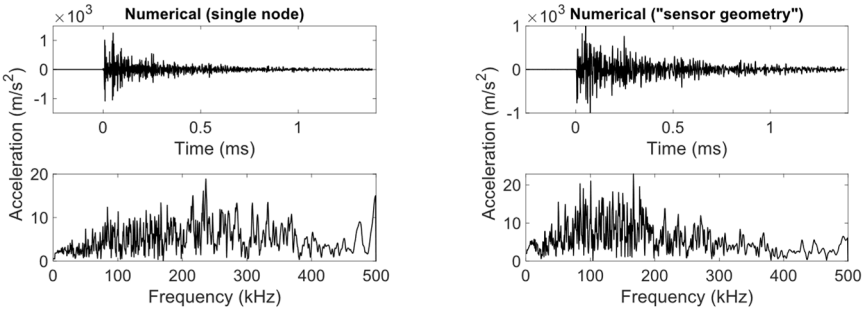

(b)

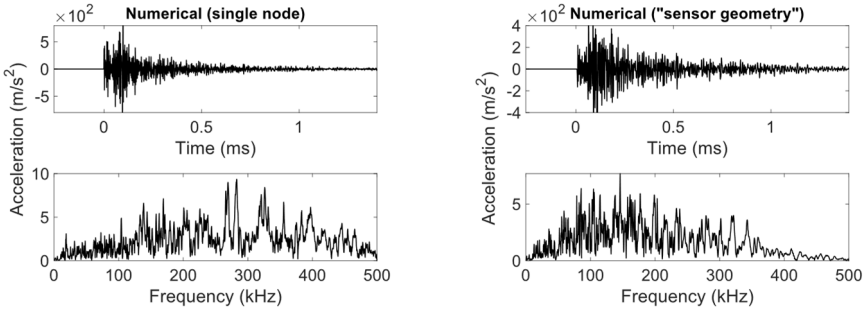

(c)

Figure D.1 Typical numerical AE waveforms received by virtual sensor S1 without complete “sensor effect” at (a) 50% pre-peak load; (b) peak load; (c) 50% post-peak load.

Figure D.2 provides numerical results in intermediate steps for statistical distributions of typical AE parameters received by virtual sensor S1, corresponding to the results given in Figure 4.15.

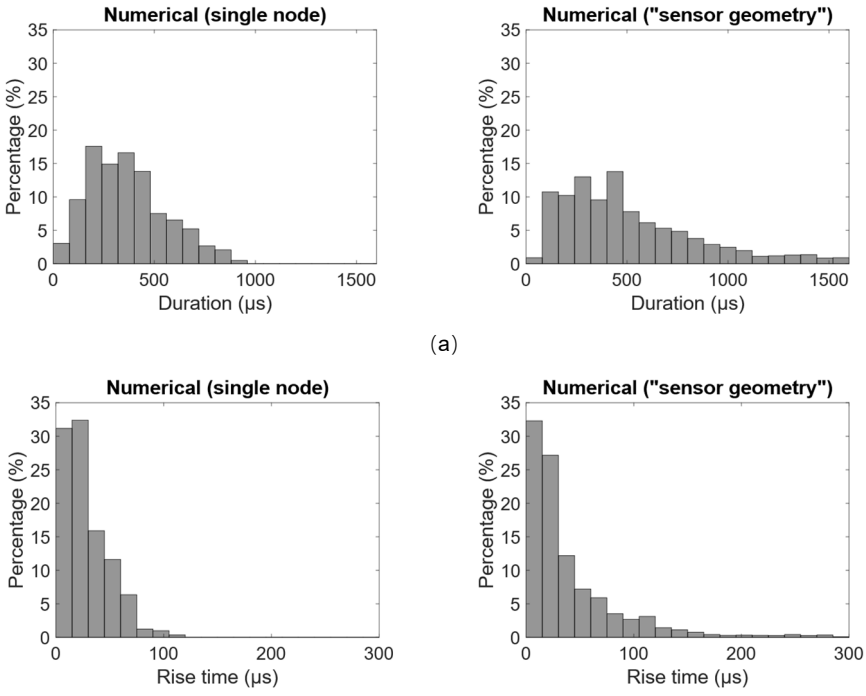

(a)

(b)

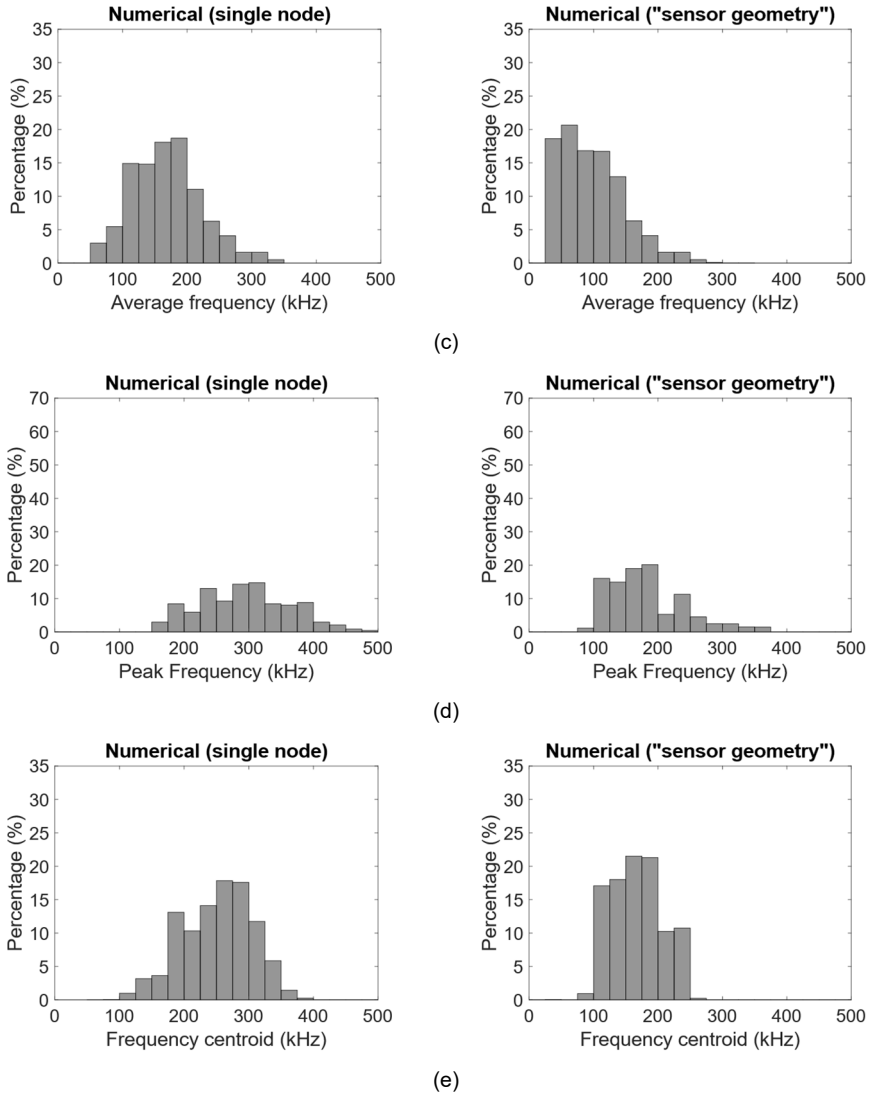

Figure D.2 Statistical distributions of numerical AE parameters received by virtual sensor S1 without complete “sensor effect”: (a) duration; (b) rise time; (c) average frequency (d) peak frequency; (e) frequency centroid.

Figure D.3 provides numerical results in intermediate steps for typical waveforms received by different sensor locations, corresponding to the results given in Figure 4.16.

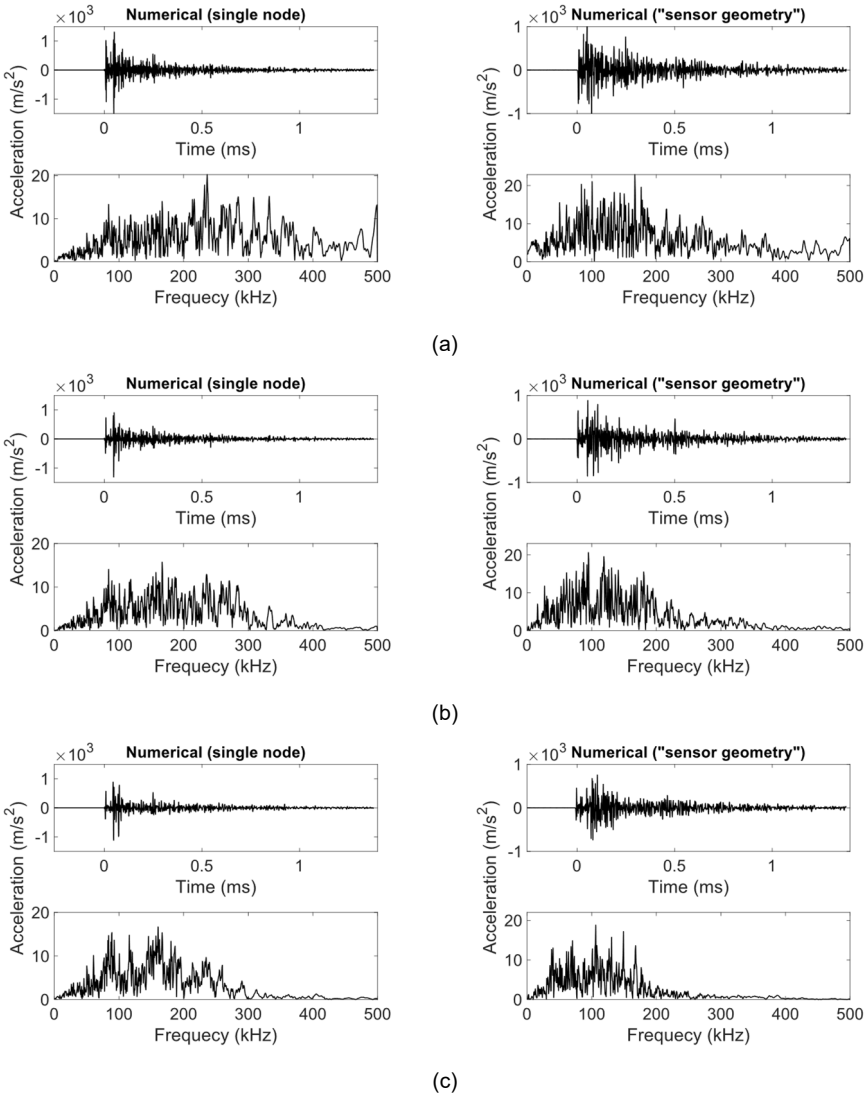

Figure D.3 Numerical waveforms of a typical AE event without complete “sensor effect” received at different sensor locations: (a) sensor S1; (b) sensor S1; (c) sensor S3.

Figure D.4 provides numerical results in intermediate steps for statistical distributions of peak amplitude drop of numerical signals received by virtual sensors S2 and S3, corresponding to the results given in Figure 4.17.

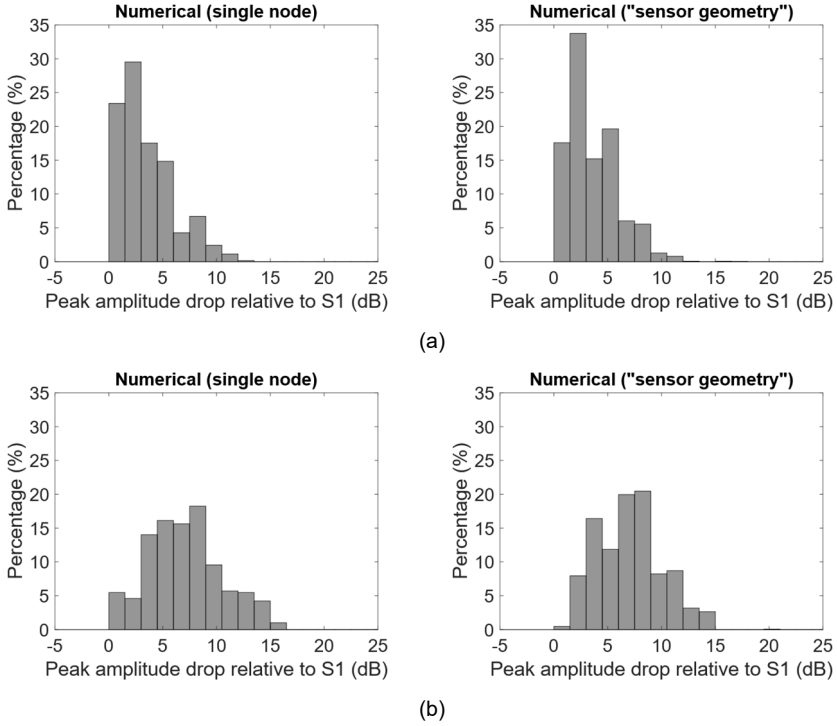

Figure D.4 Statistical distribution of peak amplitudes of AE signals received at different sensor locations relative to sensor S1: (a) S2 and (b) S3.

Figure D.5 provides numerical results in intermediate steps for statistical distributions of rise time of numerical signals received by virtual sensors S1, S2 and S3, corresponding to the results given in Figure 4.18.

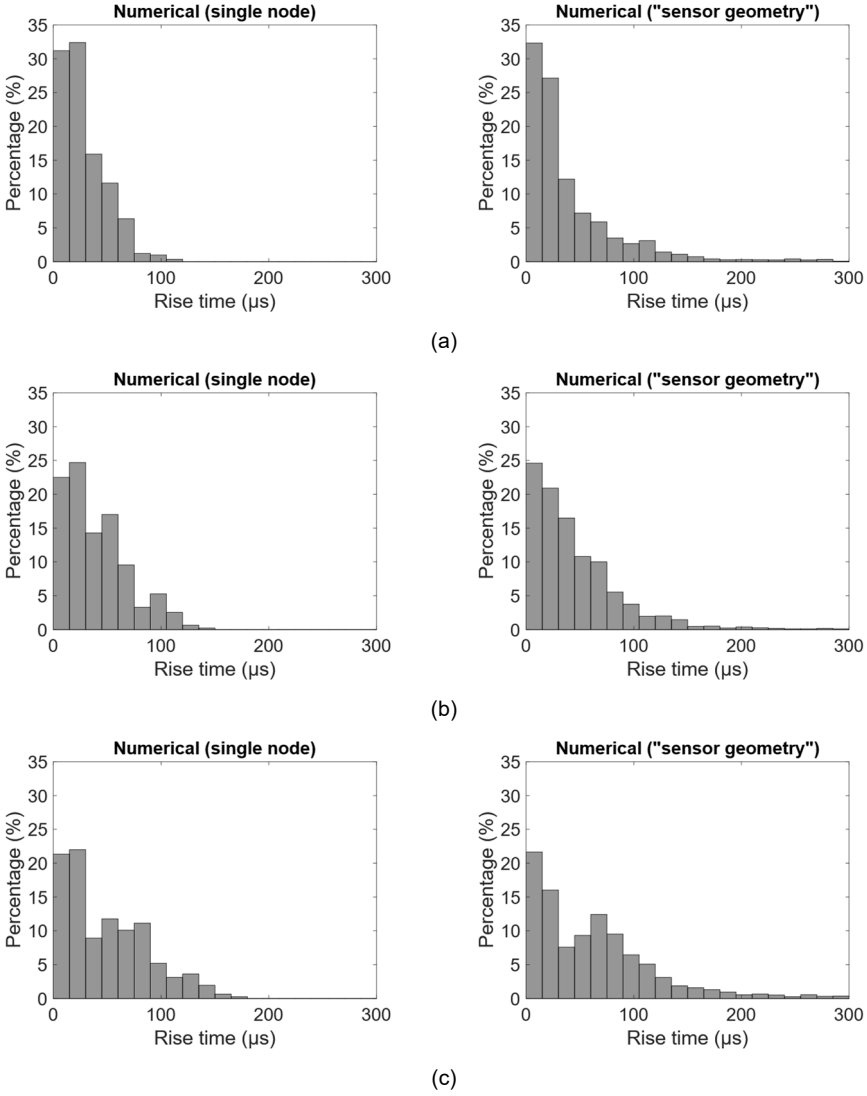

Figure D.5 Statistical distribution of rise time of AE signals received at different sensor locations: (a) S1; (b) S2; (c) S3.

Figure D.6 provides numerical results in intermediate steps for statistical distributions of peak frequency of numerical signals received by virtual sensors S1, S2 and S3, corresponding to the results given in Figure 4.19.

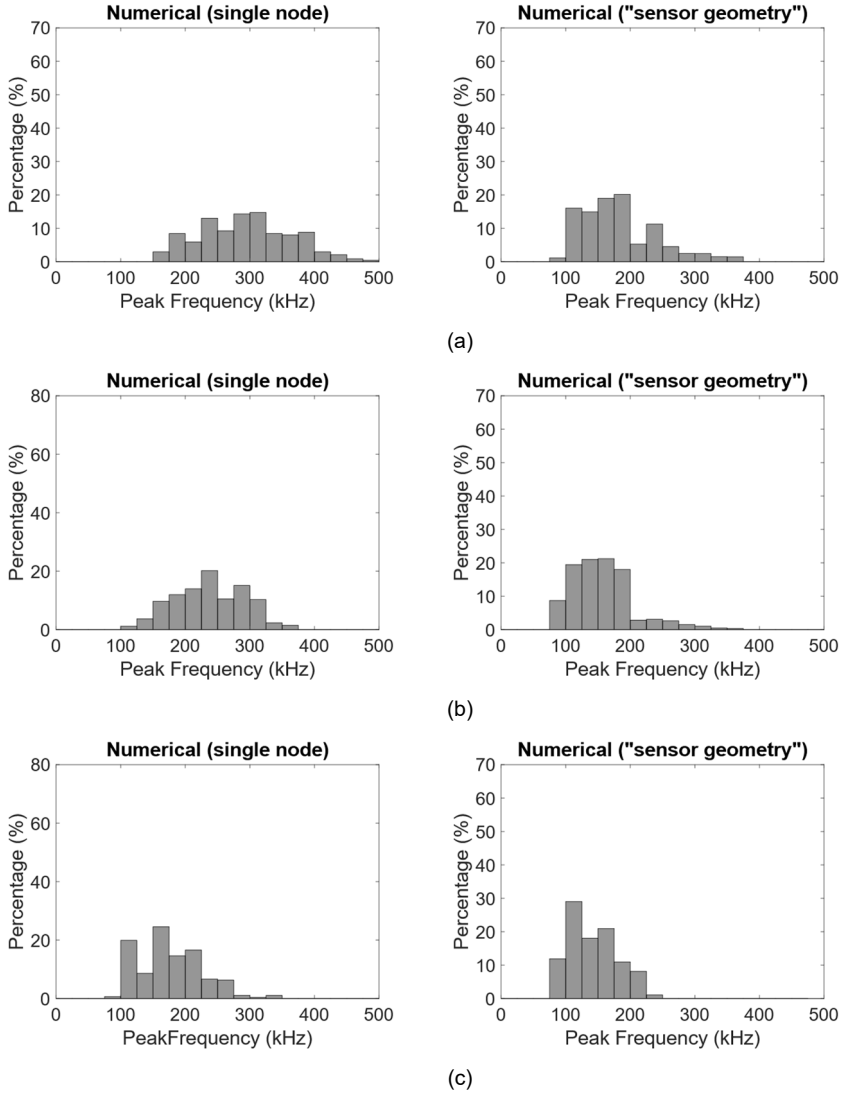

Figure D.6 Statistical distribution of peak frequency of signals received by different AE sensors: (a) S1; (b) S2; (c) S3

Appendix E. Solution forms to a general second-order linear differential equation with constant coefficients

This appendix provides standard solution procedures to general second-order linear differential equations with constant coefficients.

Consider the standard form of a second-order linear differential equation with constant coefficients:

$$\ddot{u}(t) + p\dot{u}(t) + qu(t) = g(t) \tag{E.1}$$

where $u(t)$, $\dot{u}(t)$ and $\ddot{u}(t)$ are the function to be solved, its first- and second-order derivative with respect to a variable t, respectively. p and q are two constants. $g(t)$ is a continuous function of t.

The characteristic equation of Equation (E.1) is given as:

$$\mu^2 + p\mu + q = 0 \tag{E.2}$$

where μ is the eigen root of Equation (E.1).

The solution forms to Equation (E.1), namely $u(t)$, depends on the solution types of Equation (E.2):

- In the case that eigenequation Equation (E.2) has two different real eigen roots μ_1 and μ_2, the solution to Equation (E.1) is expressed as:

$$u(t) = C_1 e^{\mu_1 t} + C_2 e^{\mu_2 t} + u^0(t) \tag{E.3a}$$

- In the case that eigenequation Eq. (E2) has one real repeated eigen root $\mu_1 = \mu_2 = \mu_0$, the solution to Eq. (E1) is expressed as:

$$u(t) = (C_1 + C_2 t) e^{\mu_0 t} + u^0(t) \tag{E.3b}$$

- In the case that eigenequation Eq. (E2) has two complex eigen roots in terms of conjugates $\mu_1 = \zeta + \chi\delta$ and $\mu_2 = \zeta - \chi\delta$ (where $\chi = \sqrt{-1}$ denotes the imaginary unit), the solution to Eq. (E1) is expressed as:

$$u(t) = e^{\zeta t}(C_1 \cos \delta t + C_2 \sin \delta t) + u^0(t) \tag{E.3c}$$

In Equation (E.3), C_1 and C_2 are two constants to be determined by initial conditions. $u^0(t)$ is a particular solution of Equation (E.1) and depends on the form of $g(t)$ (the right-side term in Equation (E.1)). In this study, $g(t)$ is a *i*-order polynomial of variable

t, denoted $g(t) = H_i(t)$ (i is the order of $H_i(t)$). When $\mu_1 \neq 0$ and $\mu_2 \neq 0$ as the case of this study, $u^0(t)$ is expressed as:

$$u^0(t) = Q_i(t) \tag{E.4}$$

where $Q_i(t)$ is a polynomial of variable t with the same order of $H_i(t)$. The coefficients in $Q_i(t)$ are obtained by substituting it back into Equation (E.1) and solved by the method of undetermined coefficients. A more detailed description about the solution to second order linear differential equation can be found in the book of Sibuya (Sibuya 1975).

Appendix F. Proof that Equation (5.17) is an increasing function of loading time

This appendix provides the procedure to prove that Equation (5.17) is an increasing function of time *t*.

Equation (5.17a) has the first order derivative with respect to time *t* as:

$$\dot{u}(t) = C_0^{'}\sqrt{-\frac{K^*(\theta_0)ES^*}{m}}\left\{e^{(t-t_1)\sqrt{-\frac{K^*(\theta_0)ES^*}{m}}} + e^{-(t-t_1)\sqrt{-\frac{K^*(\theta_0)ES^*}{m}}}\right\} + \frac{v_0}{K^*(\theta_0)L} \tag{F.1}$$

Because all sub-terms of the first term in right side of Equation (F.1) are positive, we can derive the following relationship considering the basic inequality:

$$\begin{aligned} & C_0^{'}\sqrt{-\frac{K^*(\theta_0)ES^*}{m}}\left\{e^{(t-t_1)\sqrt{-\frac{K^*(\theta_0)ES^*}{m}}} + e^{-(t-t_1)\sqrt{-\frac{K^*(\theta_0)ES^*}{m}}}\right\} \\ & \geq 2C_0^{'}\sqrt{-\frac{K^*(\theta_0)ES^*}{m}}\sqrt{\left\{e^{(t-t_1)\sqrt{-\frac{K^*(\theta_0)ES^*}{m}}}\right\}\left\{e^{-(t-t_1)\sqrt{-\frac{K^*(\theta_0)ES^*}{m}}}\right\}} \\ & = 2C_0^{'}\sqrt{-\frac{K^*(\theta_0)ES^*}{m}} \\ & = -\frac{2v_0}{(2L+l)K^*(\theta_0)}\left(1+\frac{1}{\tan\theta_0 ES^*}\right) \end{aligned} \tag{F.2}$$

Substituting Equation (F.2) into Equation (F.1), the following relationship is derived:

$$\dot{u}(t) \geq -\frac{2v_0}{(2L+l)K^*(\theta_0)}\left(1+\frac{1}{\tan\theta_0 ES^*}\right) + \frac{v_0}{K^*(\theta_0)L} = \frac{v_0 l}{2L+l} > 0 \tag{F.3}$$

Because $\dot{u}(t)$ is positive, $u(t)$ is an increasing function of time *t*.

Appendix G. Derivation process for the approximated expression of t_2

Equation (5.20) has no explicitly analytical solution and thus an approximate solution to t_2 is given by Equation (5.21). The approximate process of Equation (5.21) is given in this appendix.

By substituting Equation (5.7d) into Equation (5.20), Equation (5.20) can be expressed into another form as:

$$u(t_2)=\frac{l}{2}a_1\varepsilon_{cr}=C_0^{'}e^{(t_2-t_1)\sqrt{\left[\frac{2(1-b_1)}{l(a_1-1)}-\frac{1}{L}\right]\frac{ES^*}{m}}}-C_0^{'}e^{-(t_2-t_1)\sqrt{\left[\frac{2(1-b_1)}{l(a_1-1)}-\frac{1}{L}\right]\frac{ES^*}{m}}}-\frac{v_0 l(a_1-1)(t_2-t_1)}{2L(1-b_1)-l(a_1-1)}+\frac{l}{2}\varepsilon_{cr} \tag{G.1}$$

Equation (G.1) is a function of independent variable (t_2-t_1), with $t_2-t_1>0$. Equation (G.1) cannot be analytically solved; one or two of the first three terms in the right side of Equation (G.1) that involves the variable (t_2-t_1) must be ignored to derive an explicit expression of t_2. A comparison between the first three terms in the right side of Equation (G.1), in terms of absolute value ratios, is as follows:

$$\left|\frac{C_0^{'}e^{(t_2-t_1)\sqrt{\left[\frac{2(1-b_1)}{l(a_1-1)}-\frac{1}{L}\right]\frac{ES^*}{m}}}}{-C_0^{'}e^{-(t_2-t_1)\sqrt{\left[\frac{2(1-b_1)}{l(a_1-1)}-\frac{1}{L}\right]\frac{ES^*}{m}}}}\right|=e^{2(t_2-t_1)\sqrt{\left[\frac{2(1-b_1)}{l(a_1-1)}-\frac{1}{L}\right]\frac{ES^*}{m}}}>1 \tag{G.2a}$$

$$\left|\frac{C_0^{'}e^{(t_2-t_1)\sqrt{\left[\frac{2(1-b_1)}{l(a_1-1)}-\frac{1}{L}\right]\frac{ES^*}{m}}}}{-\frac{v_0 l(a_1-1)}{2L(1-b_1)-l(a_1-1)}(t_2-t_1)}\right|=\frac{(a_1-b_1)L}{(2L+l)(a_1-1)}\frac{e^{(t_2-t_1)\sqrt{\left[\frac{2(1-b_1)}{l(a_1-1)}-\frac{1}{L}\right]\frac{ES^*}{m}}}}{(t_2-t_1)\sqrt{\left[\frac{2(1-b_1)}{l(a_1-1)}-\frac{1}{L}\right]\frac{ES^*}{m}}}>0 \tag{G.2b}$$

where $|*|$ is the absolute value symbol. Mathematically, we can only prove that Equation (G.2a) and Equation (G.2b) are larger than 1 and 0, respectively. Their exact values depend on the involved coefficients.

Physically, concrete density (ρ), Young's modulus (E), and the length (l) and cross-section area (S^*) of the FPZ are on the magnitude orders of 10^3 kg/m^3, 10^{10} Pa, 10^{-3} m and 10^{-6} m^2, respectively. Moreover, since the fracture scale is relatively small with respect to structural scale especially in the case of acoustic emission-related micro-cracking processes, we assume that the scale of the FPZ is assumed to be much smaller than the structure, namely $L\gg l$. Further assuming that $(1-b_1)$ and (a_1-1) are in the same

magnitude (see Figure 5.3), the values of the terms $\sqrt{\left[\frac{2(1-b_1)}{l(a_1-1)}-\frac{1}{L}\right]\frac{ES^*}{m}}$ and $\frac{(a_1-b_1)L}{(2L+l)(a_1-1)}$ in Equation (G.2) are then on the magnitude orders of around 10^7 rad/s and 10^0, respectively. Moreover, according to the work of Ohtsu (Ohtsu 1995), the rise time of AE source signals, t_2-t_1, is on the order of around 10^{-6} s (see also in the lattice simulation results in Section 6.2). The values of (G.2a) and Equation (G.2b) are then on the orders of around e^{10} and $\frac{e^{10}}{10}$, respectively. Therefore, we can derive the following relationships in the case of concrete fracture:

$$\left|C_0' e^{(t_2-t_1)\sqrt{\left[\frac{2(1-b_1)}{l(a_1-1)}-\frac{1}{L}\right]\frac{ES^*}{m}}}\right| \gg \left|-C_0' e^{-(t_2-t_1)\sqrt{\left[\frac{2(1-b_1)}{l(a_1-1)}-\frac{1}{L}\right]\frac{ES^*}{m}}}\right| \tag{G.3a}$$

$$\left|C_0' e^{(t_2-t_1)\sqrt{\left[\frac{2(1-b_1)}{l(a_1-1)}-\frac{1}{L}\right]\frac{ES^*}{m}}}\right| \gg \left|-\frac{v_0 l(a_1-1)}{2L(1-b_1)-l(a_1-1)}(t_2-t_1)\right| \tag{G.3b}$$

Equation (G.3) means that the absolute values of the other two terms in the right side of Equation (G.1) that involves the variable (t_2-t_1) are negligible compared to the first term. Therefore, we ignore the last two terms in the right side of Equation (G.1) that involves the variable (t_2-t_1) and Equation (G.1) is then approximated as:

$$\frac{(a_1-b_1)v_0 lL\left(\left[\frac{2(1-b_1)}{l(a_1-1)}-\frac{1}{L}\right]\frac{ES^*}{m}\right)^{-1/2}}{(2L+l)\left[2L(1-b_1)-l(a_1-1)\right]} e^{(t_2-t_1)\sqrt{\left[\frac{2(1-b_1)}{l(a_1-1)}-\frac{1}{L}\right]\frac{ES^*}{m}}} \approx \frac{l}{2}(a_1-1)\varepsilon_{cr} \tag{G.4}$$

By solving Eq. (G.4), an approximated expression of t_2 is given as:

$$t_2 \approx t_1 + \frac{\ln\left\{\frac{\varepsilon_{cr}(a_1-1)(2L+l)\left[2L(1-b_1)-l(a_1-1)\right]}{2(a_1-b_1)v_0 L}\sqrt{\left[\frac{2(1-b_1)}{l(a_1-1)}-\frac{1}{L}\right]\frac{ES^*}{m}}\right\}}{\sqrt{\left[\frac{2(1-b_1)}{l(a_1-1)}-\frac{1}{L}\right]\frac{ES^*}{m}}} \tag{G.5}$$

Finally, by substituting Equation (5.7d) into Equation (G.5), the expression of t_2 is expressed as:

$$t_2 \approx t_1 + \frac{\ln\left\{-\frac{\varepsilon_{cr}\left(a_1-1\right)\left(2L+l\right)K^*(\theta_0)}{2v_0}\left(1+\frac{1}{\tan\theta_0 ES^*}\right)\sqrt{-\frac{X(\theta_0)ES^*}{m}}\right\}}{\sqrt{-\frac{X(\theta_0)ES^*}{m}}} \tag{G.6}$$

Appendix H. Derivation process for the approximate expressions of the velocity and acceleration of the FPZ at the end of displacement jump stage

This appendix provides the detailed derivation processes for the approximate expressions of $\dot{u}(t_2)$ and $\ddot{u}(t_2)$. Taking the first- and the second-order derivative of Equation (5.17) with respect to time t and further substituting $t = t_2$ and Equation (5.7d) into Equation (5.17), we derive the following expression for $\dot{u}(t_2)$ and $\ddot{u}(t_2)$:

$$\dot{u}(t_2) = -\frac{v_0 l(a_1-1)}{2L(1-b_1)-l(a_1-1)} + \frac{(a_1-b_1)v_0 lL}{(2L+l)\left[2L(1-b_1)-l(a_1-1)\right]}\left\{e^{(t_2-t_1)\sqrt{\left[\frac{2(1-b_1)}{l(a_1-1)}-\frac{1}{L}\right]\frac{ES^*}{m}}} + e^{-(t_2-t_1)\sqrt{\left[\frac{2(1-b_1)}{l(a_1-1)}-\frac{1}{L}\right]\frac{ES^*}{m}}}\right\} \tag{H.1a}$$

$$\ddot{u}(t_2) = \frac{(a_1-b_1)v_0 lL\sqrt{\left[\frac{2(1-b_1)}{l(a_1-1)}-\frac{1}{L}\right]\frac{ES^*}{m}}}{(2L+l)\left[2L(1-b_1)-l(a_1-1)\right]}\left\{e^{(t_2-t_1)\sqrt{\left[\frac{2(1-b_1)}{l(a_1-1)}-\frac{1}{L}\right]\frac{ES^*}{m}}} - e^{-(t_2-t_1)\sqrt{\left[\frac{2(1-b_1)}{l(a_1-1)}-\frac{1}{L}\right]\frac{ES^*}{m}}}\right\} \tag{H.1b}$$

According to Equation (G.2), we ignore the terms with far less absolute values in the right side of Eq. (H1), which is then approximated to:

$$\dot{u}(t_2) \approx \frac{(a_1-b_1)v_0 lL}{(2L+l)\left[2L(1-b_1)-l(a_1-1)\right]}\left\{e^{(t_2-t_1)\sqrt{\left[\frac{2(1-b_1)}{l(a_1-1)}-\frac{1}{L}\right]\frac{ES^*}{m}}}\right\} \tag{H.2a}$$

$$\ddot{u}(t_2) \approx \frac{(a_1-b_1)v_0 lL\sqrt{\left[\frac{2(1-b_1)}{l(a_1-1)}-\frac{1}{L}\right]\frac{ES^*}{m}}}{(2L+l)\left[2L(1-b_1)-l(a_1-1)\right]}\left\{e^{(t_2-t_1)\sqrt{\left[\frac{2(1-b_1)}{l(a_1-1)}-\frac{1}{L}\right]\frac{ES^*}{m}}}\right\} \tag{H.2a}$$

By substituting the expression of t_2 in Equation (5.21) into Equation (H.2), $\dot{u}(t_2)$ and $\ddot{u}(t_2)$ are further expressed as:

$$\dot{u}(t_2) \approx \frac{(a_1-1)l\varepsilon_{cr}}{2}\sqrt{\left[\frac{2(1-b_1)}{l(a_1-1)}-\frac{1}{L}\right]\frac{ES^*}{m}} \tag{H.3a}$$

$$\ddot{u}\left(t_2\right) \approx \frac{(a_1-1)l\varepsilon_{cr}}{2}\left[\frac{2\left(1-b_1\right)}{l(a_1-1)}-\frac{1}{L}\right]\frac{ES^*}{m} \tag{H.3b}$$

Appendix I. Influence of fracture scale and fracture early-stage ductility coefficient on source rise time

This appendix provides the procedure to prove that the source rise time T_{rise} is positively correlated with both fracture scale l and fracture early-stage ductility coefficient a_1.

Since the fracture scale is relatively small with respect to structural scale especially in the case of acoustic emission-related micro-cracking processes, the scale of the FPZ is assumed to be much smaller than that of the structure, namely $L \gg l$. Under this assumption ($L \gg l$), the expression of T_{rise} in Equation (5.39) is further simplified as:

$$T_{rise} = t_2 - t_1 \approx l\sqrt{\frac{(a_1-1)\rho}{2(1-b_1)E}}\ln\left[\frac{2f_t(1-b_1)\sqrt{\frac{2(1-b_1)}{E\rho(a_1-1)}}}{\left(1+\frac{1-b_1}{a_1-1}\right)\dot{\varepsilon}l}\right] \tag{I.1}$$

The partial derivative of Equation (I.1) with respect to l is then expressed as:

$$\frac{\partial T_{rise}}{\partial l} = \sqrt{\frac{(a_1-1)\rho}{2(1-b_1)E}}\left\{\ln\left[\frac{2f_t(1-b_1)\sqrt{\frac{2(1-b_1)}{E\rho(a_1-1)}}}{\left(1+\frac{1-b_1}{a_1-1}\right)\dot{\varepsilon}l}\right]-1\right\} \tag{I.2}$$

Because $b_1 < 1 < a_1$ (see Equation (5.2a) and Equation (5.2b)), the first term in right side of Equation (I. 2) is positive; therefore, the value of $\frac{\partial T_{rise}}{\partial l}$ depends on values of parameters involved in the second term in right side of Equation (I.2) (the term in curly bracket).

Physically, concrete elastic modulus E, tensile strength f_t and length of the FPZ l are on the magnitude orders of around $10^9\ Pa$, $10^6\ Pa$ and $10^{-3}\ m$, respectively. The second term in the right side of Equation (I. 2) is then positive in the case that the strain rate $\dot{\varepsilon}$ is on the magnitude order less than $10^3\ s^{-1}$. For typical concrete working conditions without considering high-speed impact loads, the value of strain rate $\dot{\varepsilon}$ is far less than $10^3\ s^{-1}$ (Cusatis 2011). In such case, $\frac{\partial T_{rise}}{\partial l}$ is positive and thus T_{rise} is an increasing function of l.

The partial derivative of T_{rise} with respect to a_1 is derived as:

$$\frac{\partial T_{rise}}{\partial a_1}=\frac{l}{2}\sqrt{\frac{\rho}{2(1-b_1)(a_1-1)E}}\left\{\ln\left[\frac{2f_t(1-b_1)\sqrt{\frac{2(1-b_1)}{E\rho(a_1-1)}}}{\left(1+\frac{1-b_1}{a_1-1}\right)\dot{\varepsilon}l}\right]+\frac{1-b_1}{a_1-b_1}-\frac{a_1-1}{a_1-b_1}\right\} \tag{I.3}$$

Because $b_1 < 1 < a_1$ (see Equation (5.2a) and Equation (5.2b)), we can derive the following inequation:

$$\frac{a_1-1}{a_1-b_1}<\frac{a_1-b_1}{a_1-b_1}=1 \tag{I.4}$$

By substituting Equation (I.4) into Equation (I.3), we can derive the following relationship:

$$\frac{\partial T_{rise}}{\partial a_1}=\frac{l}{2}\sqrt{\frac{\rho}{2(1-b_1)(a_1-1)E}}\left\{\ln\left[\frac{2f_t(1-b_1)\sqrt{\frac{2(1-b_1)}{E\rho(a_1-1)}}}{\left(1+\frac{1-b_1}{a_1-1}\right)\dot{\varepsilon}l}\right]+\frac{1-b_1}{a_1-b_1}-\frac{a_1-1}{a_1-b_1}\right\} \tag{I.5a}$$

$$>\frac{l}{2}\sqrt{\frac{\rho}{2(1-b_1)(a_1-1)E}}\left\{\ln\left[\frac{2f_t(1-b_1)\sqrt{\frac{2(1-b_1)}{E\rho(a_1-1)}}}{\left(1+\frac{1-b_1}{a_1-1}\right)\dot{\varepsilon}l}\right]+\frac{1-b_1}{a_1-b_1}-1\right\} \tag{I.5b}$$

$$>\frac{l}{2}\sqrt{\frac{\rho}{2(1-b_1)(a_1-1)E}}\left\{\ln\left[\frac{2f_t(1-b_1)\sqrt{\frac{2(1-b_1)}{E\rho(a_1-1)}}}{\left(1+\frac{1-b_1}{a_1-1}\right)\dot{\varepsilon}l}\right]-1\right\} \tag{I.5c}$$

The first term in the right side of Equation (I.5c) is always positive because $b_1 < 1 < a_1$ (see Equation (5.2)). According to the above analyses for $\frac{\partial T_{rise}}{\partial l}$ (Equation (I.2)), the second term in the right side of Equation (I.5c) (the term in curly bracket) is positive for typical concrete working conditions without considering high-speed impact loads (when $\dot{\varepsilon}$ is on the magnitude order less than $10^3\ s^{-1}$). In such case, $\frac{\partial T_{rise}}{\partial a_1}$ is positive and thus T_{rise} is an increasing function of a_1.

Appendix J. Effect of fracture energy regularization on AE source signal

This appendix demonstrates the effect of implemented fracture energy regularization technique (Equation (7.1)) on AE source signals induced by concrete tensile fracturing.

In the three-point bending simulation case performed in Section 7.2, the length of lattice elements ($l = d$ for orthogonal elements or $l = \sqrt{2}d$ for diagonal elements) and the mass values of nodes (fracture volumes) are both changed when adopting different grid levels d for spatial discretization (namely case 5 in Table 7.1). A different simulation case is then performed in this appendix to distinguish these two parameters and to illustrate the effect of the implemented fracture energy regularization technique for AE simulation.

The adopted numerical model and boundary conditions are shown in Figure J.1. The material properties, time step and numerical damping values are kept same with that used in previous sections (Case 0 in Table 7.1), while an additional element is created at the top surface as fracturing source element (marked as red in Figure J.1). The length of source element is denoted as $l_{(source)}$. A y-direction displacement in terms of prescribed velocity ($\mathrm{d}u_y(t)/\mathrm{d}t = 1 \times 10^{-3}$ mm/s) is applied on the upper node to induce the fracturing of source element. The y-direction accelerations of the lower node of source element, marked in green and denoted as S0 in Figure J.1, are considered as the AE source signals. The analyses are performed by varying the size of fracturing source element $l_{(source)}$, while the grid size d of remaining domain is kept constant as 1 mm. In such case, the masses of all nodes are kept constant when varying $l_{(source)}$ values.

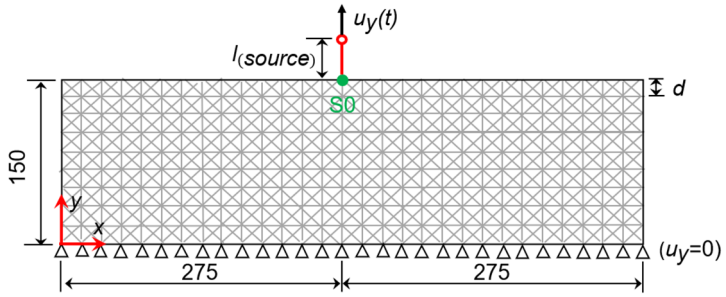

Figure J.1. Numerical model and boundary conditions to illustrate the influence of elements sizes on simulated source signal (unit: mm).

Several simulations are performed either adopting a same force-strain constitutive relationship (without fracture energy regularization) for different $l_{(source)}$ values or regularized force-strain constitutive relationships by Equation (7.1) (with fracture energy regularization). Typical AE source signals with and without fracture energy regularization are shown in Figure J.1a and b, respectively, adopting varied source element sizes

($l_{(source)} = 1$ or 5 mm).

The simulated signals are largely different in amplitudes for different $l_{(source)}$ values in the case without fracture energy regularization (Figure J.1a), while those with fracture energy regularization are similar (Figure J.1b). This demonstrates that the implemented fracture energy regularization eliminates the mesh size dependence of simulated fracture source signals; the difference in AE source signals involved in different grid levels d is caused only by the difference in node masses (fracture volumes) with a clear physical meaning.

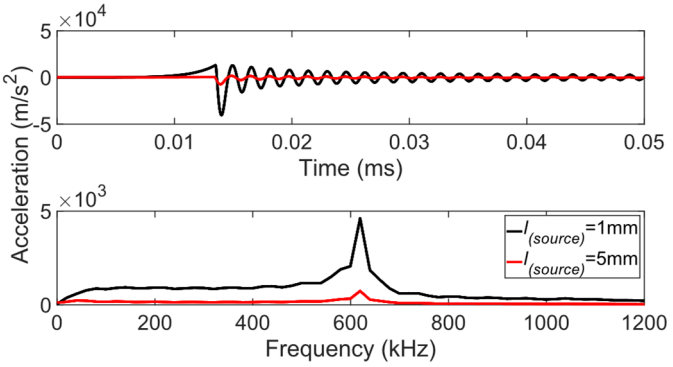

(a)

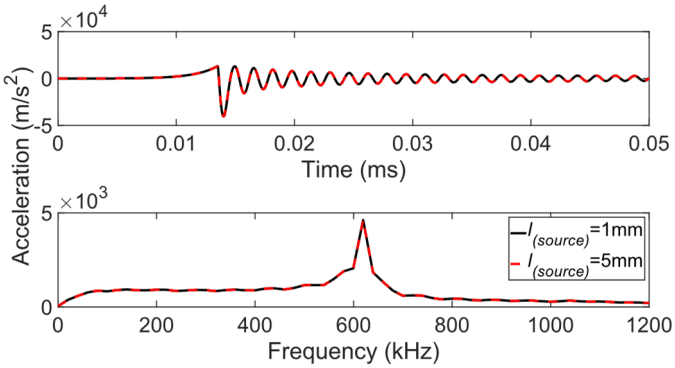

(b)

Figure J.2. Fracture-induced AE source signals received by virtual sensor S0 in the simulation case presented in Figure J.1 with varied source element sizes $l_{(source)}$: (a) without fracture energy regularization and (b) with fracture energy regularization.

Appendix K. Lattice mesh size dependency in global mechanical behaviour

This appendix investigates the dependency of global mechanical behaviour on lattice mesh size, as examined through three simulation cases of the three-point bending test using lattice grid sizes of 0.5 mm, 1.0 mm, and 2.5 mm, as presented in Chapter 8. The corresponding model parameters and simulation setups are detailed in Section 8.2.

Figure K.1 presents a comparison of the numerical load–deflection curves obtained for the different lattice grid sizes with the experimental results from the three-point bending test described in Section 4.3. Overall, the simulated results show good agreement with the experimental data. The most notable discrepancies occur around the peak load, where the experimental curve displays a lower peak value and exhibits greater instability (i.e., more fluctuations). These differences can be primarily attributed to imperfections in the experimental loading conditions.

While the numerical load–deflection curves vary only slightly across the three mesh sizes, some dependency on the lattice discretization remains. Although the nonlinear segments of the constitutive force–strain relationships have been regularized using the fracture energy approach (see Section 7.2) to mitigate mesh size effects, this dependence cannot be completely eliminated. This residual dependency arises from variations in the stiffness values of the lattice elements at different discretization levels, denoted as $ES^*(d)$, which are computed based on strain energy balance considerations (see Appendix B).

Furthermore, since the proposed model employs a dynamic solver, the global mechanical response is influenced by inertial forces related to mass. As discussed in Section 3.2 (see Equation (3.3)), varying levels of numerical discretization inherently correspond to different fracture volumes and hence different effective masses which in turn affect the mechanical response.

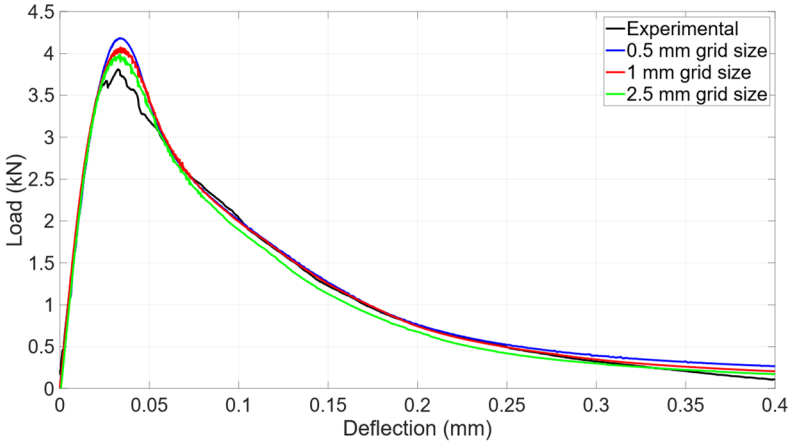

Figure. K.1 Load-deflection curves for different lattice grid sizes.

Appendix L. Comparison in spatial distributions of visible cracks, AE sources and AE event localization results

This appendix aims to elucidate why the acoustic emission (AE) events observed in experiments are largely scattered around the major visible crack, by comparing the spatial distributions of visible cracks, AE sources, and AE event localization results in lattice modelling. This analysis is conducted using three simulation cases of the three-point bending test with lattice grid sizes of 0.5 mm, 1.0 mm, and 2.5 mm, as presented in Chapter 8.

Figure L.1 presents the numerical cracking patterns obtained using lattice grid sizes of 0.5 mm and 2.5 mm. The corresponding experimental results, along with those from the simulation case using a 1.0 mm lattice grid size, are provided in Figure 4.10. These patterns are represented by the strain fields in the x-direction at four distinct loading stages: 50% of the pre-peak load, peak load, 50% of the post-peak load, and 10% of the post-peak load.

The localized strain patterns serve as a physical analogue for visible cracks. Across all loading stages, the fracture morphology and strain magnitudes are comparable between the different mesh sizes. However, a notable discrepancy is observed in the widths of the cracking patterns. This mesh size dependency in the numerical cracking width arises from strain localization. Since strain localizes within discrete elements that vary with mesh resolution, coarser grids (i.e., larger lattice elements) result in broader bands of localized strain, which manifest as wider visible cracks.

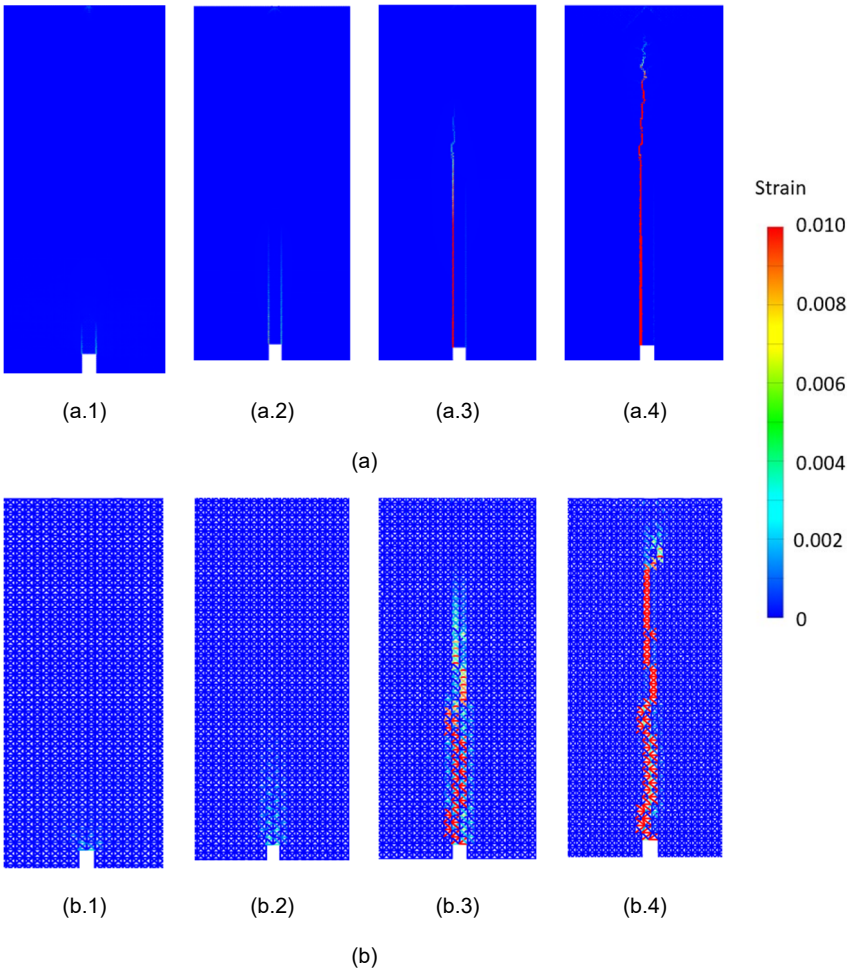

Figure.L.1 Numerical results of *x*-direction strain fields at different loading stages obtained by using different lattice grid sizes: (a) 0.5 mm lattice grid size and (b) 2.5 mm lattice grid size, with (a.1) (b.1) at 50% pre-peak load, (a.2) (b.2) at peak load, (a.3) (b.3) at 50% post-peak load, (a.4) (b.4) at 10% post-peak load.

Figure L.2 illustrates the distribution patterns of accumulated broken elements obtained using lattice grid sizes of 0.5 mm and 2.5 mm at 10% of the post-peak load. The corresponding numerical results for the 1.0 mm lattice grid size are presented in Figure 4.9b.

The broken element patterns serve as a physical analogue for AE sources. The simulation results across different mesh resolutions reveal a generally consistent distribution pattern of broken elements: the majority are concentrated within a height range of approximately 0.03 to 0.08 m. At greater heights, the bands of broken elements become narrower and more irregular, often appearing in curved configurations, due to unstable crack propagation associated with large deformations during the later stages of loading (see Section

4.5.1 for further discussion on large deformation effects in lattice modeling). Despite these similarities, a clear mesh size dependency is observed in the width of the broken element distribution bands. Specifically, the simulation with the 2.5 mm grid size exhibits a broader distribution compared to those with finer meshes.

Furthermore, a comparison between Figures L.1 and L.2 reveals that the bands of AE sources (represented by broken element patterns in Figure L.2) are generally wider than the corresponding visible cracks (represented by localized strain patterns in Figure L.1), particularly in the lower region within the 0.03–0.08 m height range. As discussed in Chapter 7, the broken elements that serve as sources of AE signals represent segments of the fracture process zone (FPZ), which physically extends around the visible cracks during crack propagation.

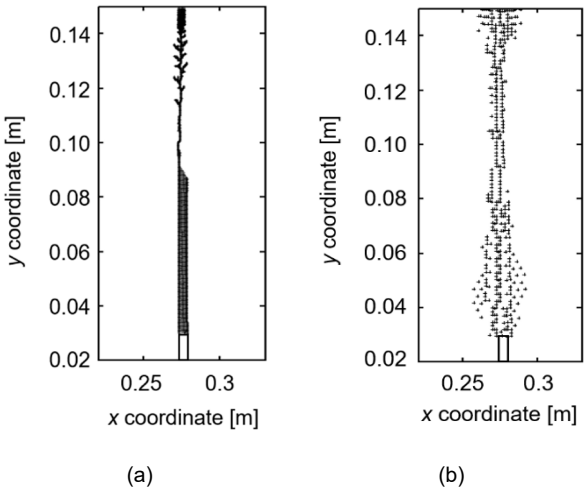

Figure. L.2 Distribution of accumulated numerical broken elements at 10% post-peak load: (a) 0.5 mm and (b) 2.5 mm grid sizes.

Figure L.3 presents the numerical AE event localization results obtained for lattice grid sizes of 0.5 mm and 2.5 mm. The AE localization methodology is detailed in Section 4.5.2. The corresponding experimental results and simulation outcomes for the 1.0 mm lattice grid size are shown in Figure 4.13.

The spatial distributions of the numerical AE events in Figure L.3 closely resemble those of the corresponding AE sources (i.e., broken elements) shown in Figure L.2. For example, the simulation using a 2.5 mm grid size exhibits a more dispersed pattern of AE events, which corresponds to the broader distribution of its AE sources.

However, it is also evident that the AE event distributions in Figure L.3 are more scattered than the broken element patterns in Figure L.2. This discrepancy arises from two main

aspects. First, errors in the picking of signal arrival times in the numerical AE signals can introduce spatial inaccuracies. The sensor geometry and frequency response characteristics used in the numerical simulations significantly influence the AE waveforms (see Section 4.5.3), thereby increasing uncertainty in arrival time detection. Second, localization errors are also introduced by directional variations in wave velocity, which are a result of the anisotropic behaviour of the 2D square truss-based lattice network, particularly due to the directional dependency of Poisson's ratio, as discussed in Section 3.3.

A comparative analysis of the spatial distributions of visible cracks (localized strain fields) in Figure L.1, AE sources (broken elements) in Figure L.2, and AE events in Figure L.3 provides insight into why AE events observed in the three-point bending tests (see Section 4.5) tend to be widely scattered around the main visible crack. This observation, consistent with experimental findings reported by (Maji and Shah 1988; Muralidhara et al. 2010; Ohno 2015; Zietlow and Labuz 1998), suggests that the spatial spread of AE events is not solely attributable to localization errors. Rather, it also reflects the broader extent of the fracture process zone, which actively generates AE signals during crack propagation.

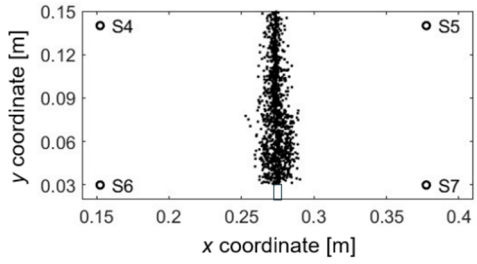

(a)

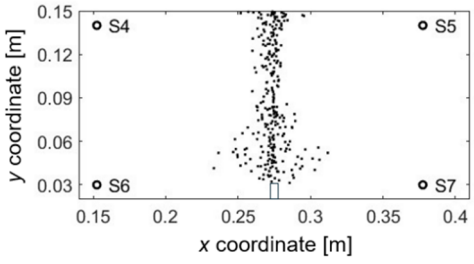

(b)

Figure L.3 Localization results of accumulated AE events at 10% post-peak load (unit: m): (a) numerical results with 0.5 mm grid size and (b) numerical results with 2.5 mm grid size.

Appendix M. Preliminary modelling results of friction-induced acoustic emission signals in concrete fracture processes

This appendix provides preliminary modelling results of friction-induced acoustic emission signals in concrete fracture processes, including an analytical explanation for the relationship between the stick-slip friction and AE phenomena and the results of a trial simulation of a stick-sliding friction-induced AE waveform through lattice modelling.

- A simple analytical analysis on stick-sliding friction & AE phenomena

Consider a pair of cracking surfaces where the upper surface of mass m slides along the fixed lower surface under a constant driving force (Figure M.1a).

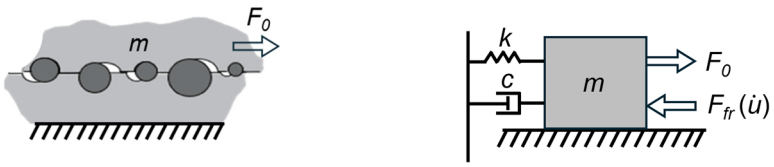

Figure M.1 Illustration for (a) a pair of sliding cracking surfaces and (b) corresponding simplified 1-DoF dynamic system.

We then simplify the upper sliding surface into a one-degree-of-freedom (1-DoF) dynamic system (Figure M.1b). The dynamic force equilibrium of the 1-DoF system is expressed as:

$$m\ddot{u}(t) + c\dot{u}(t) + ku(t) = F_0 - F_{fr}(\dot{u}) \tag{M.1}$$

where $u(t)$, $\dot{u}(t)$ and $\ddot{u}(t)$ are the displacement, velocity and acceleration of the sliding mass m, respectively. m, k and c are the mass, stiffness and damping of the system, respectively. F_0 and $F_{fr}(\dot{u})$ are the constant external driving force and the velocity (strain rate)-dependent friction force along cracking surfaces, respectively.

We then adopt a simplified bilinear stick-slip friction law (Raous and Barbarin 1996) to describe the velocity-dependent stick-slip friction force, as shown Figure M.2, where F_{frs} and F_{frd} are the maximum static friction force and the dynamic friction force corresponding to two critical velocities $\dot{u}_{frd}$ and $\dot{u}_{frs}$ of the sliding mass, respectively. Readers are referred to the classical work of (Haessig Jr and Friedland 1991) for more details of stick-slip theory (see also Section 2.3.2.2.2).

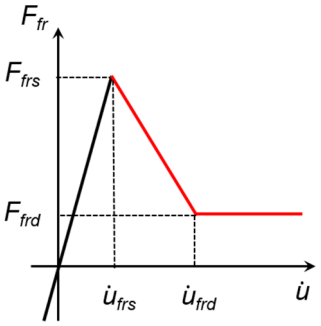

Figure M.2. A simplified bilinear stick-sliding friction law (adapted from (Raous and Barbarin 1996)).

Herein, we only consider the nonlinear part of the stick-slip friction force $F_{fr}(\dot{u})$ (the red part in Figure M.2 when the velocity of the sliding mass m larger than $\dot{u}_{frs}$), since the AE signals does not occur in the static states of friction surface as discussed in Section 2.3.2.2.2 (see also the classical work (McLaskey et al. 2012; Sirorattanakul et al. 2025)). The stick-slip friction force $F_{fr}(\dot{u})$ in the nonlinear range can be mathematically expressed as:

$$\begin{cases} F_{fr}(\dot{u}) = F_{frs} - \vartheta\dot{u}(t) & \text{if } \dot{u}_{frs} \le \dot{u}(t) < \dot{u}_{frd} \quad \text{(M.2a)} \\ F_{fr}(\dot{u}) = F_{frd} & \text{if } \dot{u}(t) \ge \dot{u}_{frd} \quad \text{(M.2b)} \end{cases}$$

$$\text{with } \vartheta = \frac{F_{frs} - F_{frd}}{\dot{u}_{frd} - \dot{u}_{frs}} \quad \text{(M.2c)}$$

where ϑ is a positive constant characterizing the change degree of friction force in the stick-slip transition process (the absolute value of the slop of the stick-sliding friction curve in the velocity range $\dot{u}_{frs} \le \dot{u}(t) < \dot{u}_{frd}$ in Figure M.2).

By substituting Equation (M.2) into Equation (M.1), the dynamic force equilibrium of the considered one-DoF system in the velocity range of $\dot{u}(t) \ge \dot{u}_{frd}$ can be further expressed as:

$$\begin{cases} m\ddot{u}(t) + (c - \vartheta)\dot{u}(t) + ku(t) = F_0 - F_{frs} & \text{if } \dot{u}_{frs} \le \dot{u}(t) < \dot{u}_{frd} \quad \text{(M.3a)} \\ m\ddot{u}(t) + c\dot{u}(t) + ku(t) = F_0 - F_{frd} & \text{if } \dot{u}(t) \ge \dot{u}_{frd} \quad \text{(M.3b)} \end{cases}$$

Considering the sharp drop of friction force and thus a large value of ϑ in the in the stick-slip transition process $\dot{u}_{frs} \le \dot{u}(t) < \dot{u}_{frd}$ (Liu et al. 2022) and the small value of damping c in case of the underdamping problem of wave propagation (Gaul 1999) (see also

Section 3.2.3), we further assume the following conditions for the coefficients involved in Equation (M.3):

$$c - \vartheta < 0 \tag{M.4a}$$

$$(c - \vartheta)^2 - 4km < 0 \tag{M.4b}$$

$$c^2 - 4km < 0 \tag{M.4c}$$

According to the assumed conditions in Equation (M.4), Equation (M.3) is solved as follows (see Appendix E for the solution procedures to general second-order linear differential equations with constant coefficients):

$$\begin{cases} u(t) = e^{\frac{\vartheta - c}{2m}t}\left[C_1''' \cos\left(\frac{\sqrt{4mk - (\vartheta - c)^2}}{2m}t\right) + C_2''' \sin\left(\frac{\sqrt{4mk - (\vartheta - c)^2}}{2m}t\right)\right] + \frac{F_0 - F_{frs}}{k} & \text{if } \dot{u}_{frs} \le \dot{u}(t) < \dot{u}_{frd} \\ u(t) = e^{-\frac{c}{2m}t}\left[C_1'''' \cos\left(\frac{\sqrt{4mk - c^2}}{2m}t\right) + C_2'''' \sin\left(\frac{\sqrt{4mk - c^2}}{2m}t\right)\right] + \frac{F_0 - F_{frd}}{k} & \text{if } \dot{u}(t) \ge \dot{u}_{frd} \end{cases} \tag{M.5a, M.5b}$$

where C_1''', C_2''', $C_1''''$and C_2'''' are four constants to be determined by initial conditions.

According to Equation (M.5) and the slick-slip friction theory (Haessig Jr and Friedland 1991) (see also Section 2.3.2.2.2), the dynamic response of the sliding mass m involves two different phases, as follows:

- In stick-sliding transition process ($\dot{u}_{frs} \le \dot{u}(t) < \dot{u}_{frd}$): the force equilibrium of the sliding mass in this stage is characterized by a negative value of effective (system) damping (namely $c - \vartheta < 0$ in Equation (M.3a)). Such a negative value of effective damping leads to a mathematical solution form of a trigonometric function multiplied with an exponential function of a positive exponential coefficient for the dynamic response (see Equation (M.5a)), which physically manifests as unstable amplified vibrations of the sliding mass (cracking surfaces) with an increased vibrating trend of wave amplitudes.
- In steady sliding process ($\dot{u}(t) \ge \dot{u}_{frd}$): the force equilibrium of the sliding mass in this stage is characterized by a positive damping value ($c > 0$ in Equation (M.3b)). Such a positive damping value leads to a mathematical solution form of a

trigonometric function multiplied with an exponential function of a positive exponential coefficient for the dynamic response (see Equation (M.5b)), which physically manifest as absorbed vibrations of the sliding mass and thus attenuated wave amplitudes.

Considering the temporal displacement continuity, the dynamic response of the sliding mass (cracking surfaces) is manifested as a continuous pulse signal with a first phase of increased amplitudes in stick-slip transition process ($\dot{u}_{frs} \leq \dot{u}(t) < \dot{u}_{frd}$) and a second phase of decreased (attenuated) amplitudes in later steady sliding process ($\dot{u}(t) \geq \dot{u}_{frd}$) (see also Figure M.4).

- A trial simulation of stick-sliding friction-induced AE with lattice model

As illustrated above, adopting a nonlinear velocity-dependent slick-slip friction law (namely a rate-dependent shear constitutive law) is possible to explicitly model the friction-induced AE signals in concrete fracturing processes. However, we have not yet achieved the implementation of such a velocity-dependent friction constitutive law in the proposed lattice modelling framework (see Section 9.3.2 for more discussion on this). Therefore, herein, we perform a trial simulation in the lattice model with the velocity-dependent slick-slip friction force being applied indirectly, to demonstrate the feasibility of the nonlinear velocity-dependent slick-slip friction law for numerical simulation of the friction-induced AE signals along cracking surfaces.

The boundary conditions of the numerical model are shown in Figure M.3a. We adopt a basic lattice unit for analysis, consisted of four nodes (numbered as node 1~4 in Figure M.3a) and six truss elements. The lattice grid size is selected as 1 mm (namely d =1 mm in Figure L.3a). The material properties of truss elements and two Rayleigh damping coefficients are kept same with those used in previous chapters (see Section 4.2). Two bottom nodes (nodes 3 and 4) are fixed, and the right upper node (node 2) is prescribed by a x-direction constant velocity of 1×10^{-6} m/s (namely $\dot{u}_0 = 1\times10^{-6}$ m/s in Figure M.3a) to induce the shear deformation of the basic lattice unit. The PID control algorithm is implemented with the x-direction constant velocity of node 2 as the control variable. The PID parameters are kept same with those used in previous chapters (see Section 4.3.1).

An additional x-direction negative damping force is applied to nodes 1 and 2 in terms of the friction-related damping coefficient $\vartheta(t)$ (see Equation (M.2)). The expression of $\vartheta(t)$ is given in Equation (M.6) with a value of $\vartheta = 2c$ being applied from 0.1 ms to 0.3 ms of simulation time to achieve a negative effective damping value (namely $c - \vartheta = -c$) in this duration (see Equation (L.3a)).

The physical meanings of the above-described boundary conditions are illustrated in Figure M.3b. The applied boundary conditions are used to mimic the stick-sliding friction

process of two lays of particles that sliding along each other. The applied $\vartheta(t)$ (Equation (M.6)) is to mimic the velocity-dependent drop of friction force $f(\dot{u})$ during the stick-sliding friction transition process (see Equation (M.2) for the relationship between $\vartheta(t)$ and $f(\dot{u})$). The x-direction accelerations of node 1 is used to mimic an AE waveform induced by the stick-slip friction along cracking surfaces.

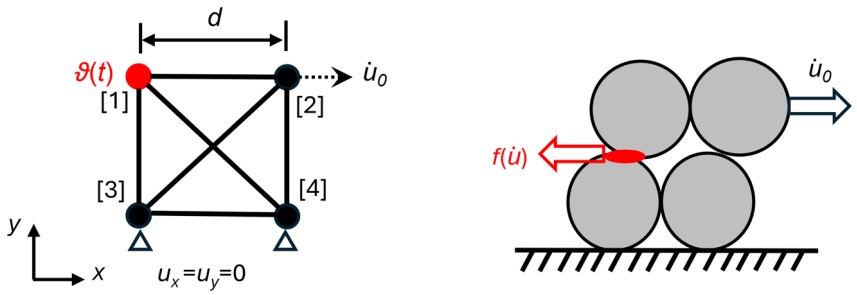

(a) (b)

Figure M.3. Indirect simulation of slick-slip friction-induced AE with lattice model: (a) the numerical model and boundary conditions (unit: mm) and (b) corresponding physical meanings.

$$\begin{cases} \vartheta(t) = 0 & \text{if } 0 \le t < 0.1 \text{ ms} \quad \text{(M.6a)} \\ \vartheta(t) = 2c & \text{if } 0.1 \le t < 0.3 \text{ ms} \quad \text{(M.6b)} \\ \vartheta(t) = 0 & \text{if } t \ge 0.3 \text{ ms} \quad \text{(M.6c)} \end{cases}$$

The simulated AE waveform in terms of x-direction accelerations of node 1 is shown in Figure M.4. The numerical AE signal is in line with analytical results predicted by Equation (M.5), showing a first phase of increased amplitudes during stick-slip friction transition process and then a second phase of gradually attenuated amplitudes.

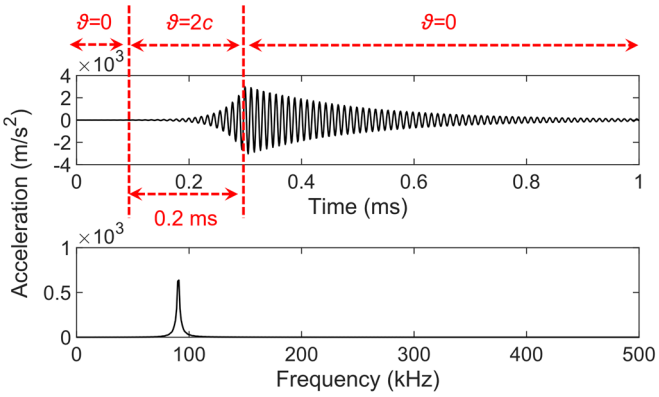

Figure M.4. *X*-direction accelerations of node 1.

As the AE signal shown in Figure M.4 is the dynamic response of a sliding node, it can be seen as an AE source signal. Such a friction-induced AE source signal shows fundamental difference in waveforms with respect to the tensile cracking-induced AE source signals shown in Chapter 6 (see Figure 6.2). The difference in waveforms between these two types of AE sources are compared and explained as follows:

- In time domain, a tensile-induced AE source waveform shows a sharply exponential increasing trend in amplitudes (in terms of an exponential function) in early tensile softening stages; the increased amplitudes are then gradually attenuated in later tensile softening stages due to material damping and geometric spreading loss (see Section 3.2.3). Such an exponential increase of amplitude in early tensile softening stages is mathematically triggered by a negative value of effective stiffness of the system (the negative coefficient of the displacement term in Equation (5.28a), namely $K^*(\theta_i) < 0$) and physically due to the sharp strain (displacement)-dependent tensile stress (force) drop in the FPZ (see Section 5.2.4.1.2).

  The friction-induced AE source waveform shows a viscous behaviour with a slower vibrating increasing trend in amplitudes (mathematically in terms of a trigonometric function multiplied with an exponential function) during stick-slip transition process; the increased amplitudes are then gradually attenuated in later steady sliding processes, also due to material damping and geometric spreading loss. Such a slow vibrating increase of amplitude in stick-slip transition process is mathematically triggered by a negative value of effective damping of the system (the negative coefficient of the velocity term in Equation (M.3a), namely $c - \vartheta < 0$) and physically due to the strain rate (velocity)-dependent friction force (stress) drop in the slip zone (defined as the areas with sliding velocities/displacements exceeding a threshold value (Daemen 1983)) during stick-slip transition process.

- For frequency, similarly to a tensile cracking-induced AE source signal with the source frequency inversely correlated to the active fracture volume as part of the FPZ at crack tip (see Section 7.3), the source frequency of a stick-slip friction-induced AE source signal is inversely correlated with the size of the sliding mass (see Equation (M.5)).

  The sliding mass in the considered single DoF system is defined as a slip zone (Sibson 2003) in a structural level, as illustrated in Figure M.5. Since the size of slip zone is positively related to the length of contacted cracking surfaces (see the classical work (Wang, Vuik, and Hajibeygi 2022; Phan et al. 2003) for the correlation between the slip zone size and the contacted cracking length in stick-slip friction processes), the slip zone along the existing cracking surfaces should have a much larger scale than the fracture area as portions of the FPZ (see Figure L.5); therefore, the frequency of a friction-induced AE source signal would be much lower than that of a tensile cracking-induced one.

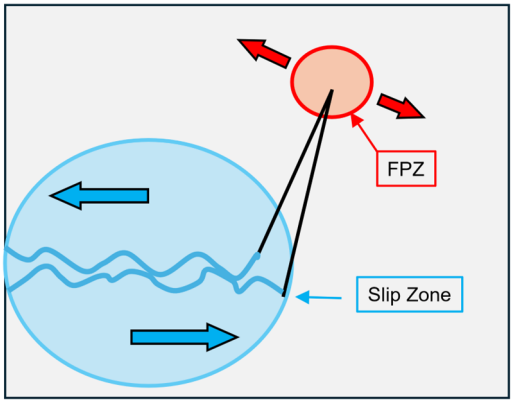

Figure M.5. Illustration for a slip zone along cracking surfaces (adapted from (Xu, Hajibeygi, and Sluys 2024)).

The above reasons may partially explain the experimental observations for the different waveforms of the two AE source types involved in concrete fracturing processes that the friction-induced AE signals have longer rise time and lower frequency than the tensile cracking-induced ones, as illustrated in Figure M.6 (Zhang et al. 2022).

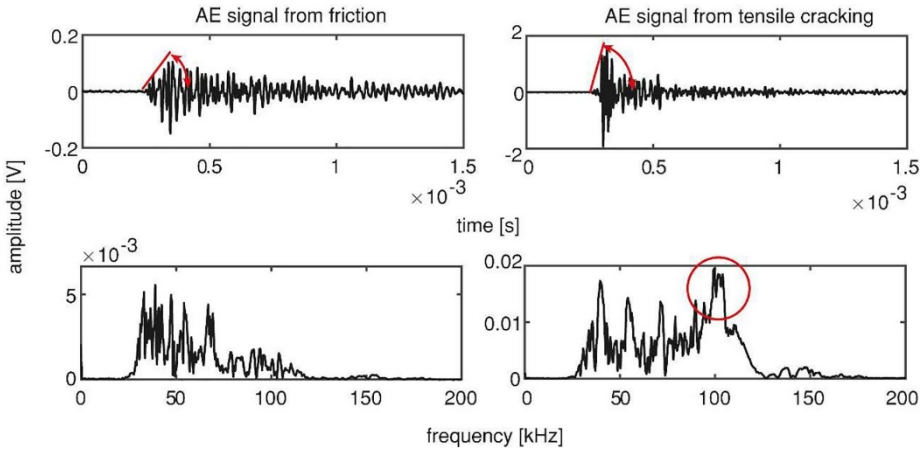

Figure M.6. Examples of AE waveforms from tensile cracking and friction recorded in a concrete failure test (adapted from (Zhang et al. 2022)).

Nevertheless, it should be mentioned the numerical waveform of friction-induced AE presented in this appendix is simulated in a rough and indirect way. In a future study, the velocity (strain rate)-dependent stick-sliding contact law should be strictly and directly implemented in a numerical model, to quantify the source mechanisms of AE phenomena induced by the friction along concrete cracking surfaces, to fundamentally understand why they are different with the tensile cracking-induced ones, and to further develop more reliable classification criterion for distinguishing these two AE source types. Readers are referred to Section 9.3.2 for more discussion on the recommendations for modelling of friction-induced AE phenomena in concrete fracture processes.

Reference

Abe, Steffen, James H Dieterich, Peter Mora, and David Place. 2002. 'Simulation of the influence of rate-and state-dependent friction on the macroscopic behavior of complex fault zones with the lattice solid model', *Pure and applied geophysics*, 159: 1967-83.

Abercrombie, Rachel E. 2021. 'Resolution and uncertainties in estimates of earthquake stress drop and energy release', *Philosophical Transactions of the Royal Society A*, 379: 20200131.

Abouhussien, Ahmed A, and Assem AA Hassan. 2020. 'Classification of damage in self-consolidating rubberized concrete using acoustic emission intensity analysis', *Ultrasonics*, 100: 105999.

Achenbach, Jan. 2012. *Wave propagation in elastic solids* (Elsevier).

ACS. 2023a. "Ultrasonic transducer S1803." In. ACS-Solutions GmbH Science Park 2 66123 Saarbrücken, Germany.

———. 2023b. "Ultrasonic transducer S1820." In. ACS-Solutions GmbH Science Park 2 66123 Saarbrücken, Germany.

Aggelis, Dimitrios G. 2011. 'Classification of cracking mode in concrete by acoustic emission parameters', *Mechanics Research Communications*, 38: 153-57.

Ai, Li, Bin Zhang, and Paul Ziehl. 2023. 'A transfer learning approach for acoustic emission zonal localization on steel plate-like structure using numerical simulation and unsupervised domain adaptation', *Mechanical Systems and Signal Processing*, 192: 110216.

Ajitesh, YVS. 1956. 'Condition assessment of existing structures using NDT techniques', Doctoral dissertation, Gitam University.

Aki, Keiiti. 1980. 'Quantitative seismology', *Theory and method*: 304-08.

Anderson, Ted L, and Ted L Anderson. 2005. *Fracture mechanics: fundamentals and applications* (CRC press).

André, Damien, Ivan Iordanoff, Jean-luc Charles, and Jérôme Néauport. 2012. 'Discrete element method to simulate continuous material by using the cohesive beam model', *Computer Methods in Applied Mechanics and Engineering*, 213: 113-25.

Ayatollahi, MR, M Rashidi Moghaddam, and Filippo Berto. 2015. 'A generalized strain energy density criterion for mixed mode fracture analysis in brittle and quasi-brittle materials', *Theoretical and Applied Fracture Mechanics*, 79: 70-76.

Ayatollahi, MR, and B Saboori. 2015. 'Maximum tangential strain energy density criterion for general mixed mode I/II/III brittle fracture', *International Journal of Damage Mechanics*, 24: 263-78.

Aydin, B. B., K. Tuncay, and B. Binici. 2019. 'Simulation of Reinforced Concrete Member Response Using Lattice Model', *Journal of Structural Engineering*, 145: 04019091.

Aydin, Beyazit B, Baris Binici, and Kagan Tuncay. 2021. 'Lattice simulation of concrete compressive behaviour as indirect tension failure', *Magazine of Concrete Research*, 73: 394-409.

Aydin, Beyazit B, Kagan Tuncay, and Baris Binici. 2018. 'Overlapping lattice modeling for concrete fracture simulations using sequentially linear analysis', *Structural Concrete*, 19: 568-81.

Aydin, Beyazit B., Baris Binici, Max A. N. Hendriks, and Kagan Tuncay. 2022. 'Lattice modeling and testing of aerated autoclaved concrete infilled frames', *Engineering Structures*, 251: 113467.

Ba, and MT Kazemi. 1990. 'Determination of fracture energy, process zone longth and brittleness number from size effect, with application to rock and conerete', *International Journal of Fracture*, 44: 111-31.

Backers, T, S Stanchits, and Georg Dresen. 2005. 'Tensile fracture propagation and acoustic emission activity in sandstone: The effect of loading rate', *International Journal of Rock Mechanics and Mining Sciences*, 42: 1094-101.

Ballandras, Sylvain, Raphael Lardat, Mikael Wilm, Th Pastureaud, Alexandre Reinhardt, N Champavert, William Steichen, William Daniau, Vincent Laude, and Raphaël Armati. 2009. 'A mixed finite element/boundary element approach to simulate complex guided elastic wave periodic transducers', *Journal of applied physics*, 105.

Ballatore, Enrico, Alberto Carpinteri, Gerardo Ferrara, and Giorgio Melchiorri. 1990. 'Mixed mode fracture energy of concrete', *Engineering Fracture Mechanics*, 35: 145-57.

Baltay, Annemarie, Satoshi Ide, German Prieto, and Gregory Beroza. 2011. 'Variability in earthquake stress drop and apparent stress', *Geophysical Research Letters*, 38.

Barai, Pallab, and Partha P Mukherjee. 2014. 'Mechano-electrochemical model for acoustic emission characterization in intercalation electrodes', *Journal of the Electrochemical Society*, 161: F3123.

Baranov, Victor M, Evgeny M Kudryavtsev, and Gennadii A Sarychev. 1997. 'Modelling of the parameters of acoustic emission under sliding friction of solids', *Wear*, 202: 125-33.

Barat, Vera, Denis Terentyev, Vladimir Bardakov, and Sergey Elizarov. 2019. 'Analytical modeling of acoustic emission signals in thin-walled objects', *Applied Sciences*, 10: 279.

Baudet, Vincent, Michaël Beuve, Fabrice Jaillet, Behzad Shariat, and Florence Zara. 2007. 'New mass-spring system integrating elasticity parameters in 2D'.

Bauer, C., R. Freeman, T. Frenkiel, J. Keeler, and A. J. Shaka. 1984a. 'Gaussian Pulses', *Journal of Magnetic Resonance*, 58: 442-57.

Bauer, Christopher, Ray Freeman, Tom Frenkiel, James Keeler, and AJ Shaka. 1984b. 'Gaussian pulses', *Journal of Magnetic Resonance (1969)*, 58: 442-57.

Bažant, Zdeněk P, and Luigi Cedolin. 1980. 'Fracture mechanics of reinforced concrete', *Journal of the Engineering Mechanics Division*, 106: 1287-306.

Bažant, Zdeněk P, and Feng-Bao Lin. 1988. 'Nonlocal smeared cracking model for concrete fracture', *Journal of Structural Engineering*, 114: 2493-510.

Bažant, Zdeněk P, and Byung H Oh. 1983. 'Crack band theory for fracture of concrete', *Matériaux et construction*, 16: 155-77.

Bazant, ZP. 2009. "Speech of acceptance of timoshenko medal: Reminiscences and reflections of a mechanician by luck." In *ASME International Mechanical Engineering Congress*.

Behnia, Arash, Hwa Kian Chai, and Tomoki Shiotani. 2014. 'Advanced structural health monitoring of concrete structures with the aid of acoustic emission', *Construction and Building Materials*, 65: 282-302.

Bengisu, MT, and Adnan Akay. 1999. 'Stick–slip oscillations: Dynamics of friction and surface roughness', *The Journal of the Acoustical Society of America*, 105: 194-205.

Berman, Alan D, William A Ducker, and Jacob N Israelachvili. 1996. 'Origin and characterization of different stick− slip friction mechanisms', *Langmuir*, 12: 4559-63.

Besel, Michael, and Eric Breitbarth. 2016. 'Advanced analysis of crack tip plastic zone under cyclic loading', *International Journal of Fatigue*, 93: 92-108.

Bićanić, Nenad. 2004. 'Discrete element methods', *Encyclopedia of computational mechanics*.

Birck, Gabriel, Ignacio Iturrioz, Giuseppe Lacidogna, and Alberto Carpinteri. 2016. 'Damage process in heterogeneous materials analyzed by a lattice model simulation', *Engineering Failure Analysis*, 70: 157-76.

Bocca, Pietro, and Alberto Carpinteri. 1990. 'Snap-back fracture instability in rock specimens: experimental detection through a negative impulse', *Engineering Fracture Mechanics*, 35: 241-50.

Bormann, Peter, Bob Engdahl, and Rainer Kind. 2012. 'Seismic wave propagation and earth models.' in, *New manual of seismological observatory practice 2 (NMSOP2)* (Deutsches GeoForschungsZentrum GFZ).

Bosia, Federico, Nicola Pugno, Giuseppe Lacidogna, and Alberto Carpinteri. 2008. 'Mesoscopic modeling of Acoustic Emission through an energetic approach', *International journal of solids and structures*, 45: 5856-66.

Brun, E, and RMG Boucher. 1956. 'Research on the Acoustic Air‐Jet Generator', *The Journal of the Acoustical Society of America*, 28: 802-03.

Bruna, R, and JD Riera. 1988. 'Towards the simultaneous generation of the three components of the seismic acceleration on rock surface', *Nuclear engineering and design*, 110: 153-63.

Bu, Fengchang, Lei Xue, Mengyang Zhai, Xiaolin Huang, Jinyu Dong, Ning Liang, and Chao Xu. 2022. 'Evaluation of the characterization of acoustic emission of brittle rocks from the experiment to numerical simulation', *Scientific Reports*, 12: 498.

Buttà, Paolo, Guido Cavallaro, and Carlo Marchioro. 2015. *Mathematical models of viscous friction* (Springer).

Caleap, Mihai, Christophe Aristégui, and Yves C Angel. 2009. 'Effect of crack opening and orientation on dispersion and attenuation of antiplane coherent wave', *Geophysical Journal International*, 177: 1151-65.

Cao, Anye, Yaoqi Liu, Fan Chen, Qi Hao, Xu Yang, Changbin Wang, and Xianxi Bai. 2022. 'Focal mechanism and source parameters analysis of mining-induced earthquakes based on relative moment tensor inversion',

International Journal of Environmental Research and Public Health, 19: 7352.

Carpinteri, Alberto. 1982. 'Application of fracture mechanics to concrete structures', *Journal of the Structural Division*, 108: 833-48.

———. 1989. 'Softening and snap‐back instability in cohesive solids', *International Journal for Numerical Methods in Engineering*, 28: 1521-37.

Carpinteri, Alberto, and Federico Accornero. 2018. 'Multiple snap-back instabilities in progressive microcracking coalescence', *Engineering Fracture Mechanics*, 187: 272-81.

Carpinteri, Alberto, Mauro Corrado, and Giuseppe Lacidogna. 2013. 'Heterogeneous materials in compression: Correlations between absorbed, released and acoustic emission energies', *Engineering Failure Analysis*, 33: 236-50.

Carpinteri, Alberto, Giuseppe Lacidogna, Mauro Corrado, and Emanuela Di Battista. 2016. 'Cracking and crackling in concrete-like materials: A dynamic energy balance', *Engineering Fracture Mechanics*, 155: 130-44.

Carpinteri, Alberto, Giuseppe Lacidogna, and Simone Puzzi. 2009. 'From criticality to final collapse: Evolution of the “b-value” from 1.5 to 1.0', *Chaos, Solitons & Fractals*, 41: 843-53.

Carpinteri, Alberto, Silvio Valente, G Ferrara, and G Melchiorrl. 1993. 'Is mode II fracture energy a real material property?', *Computers & Structures*, 48: 397-413.

Carroll, Jay D, Wael Abuzaid, John Lambros, and Huseyin Sehitoglu. 2013. 'High resolution digital image correlation measurements of strain accumulation in fatigue crack growth', *International Journal of Fatigue*, 57: 140-50.

Caughey, TK. 1960. 'Classical normal modes in damped linear dynamic systems'.

Caulk, Robert A. 2020. 'Modeling acoustic emissions in heterogeneous rocks during tensile fracture with the Discrete Element Method', *Open Geomechanics*, 2: 1-19.

Chang, S-H, and C-I Lee. 2004. 'Estimation of cracking and damage mechanisms in rock under triaxial compression by moment tensor analysis of acoustic emission', *International Journal of Rock Mechanics and Mining Sciences*, 41: 1069-86.

Chang, Ze, Hongzhi Zhang, Erik Schlangen, and Branko Šavija. 2020. 'Lattice fracture model for concrete fracture revisited: Calibration and validation', *Applied Sciences*, 10: 4822.

Chen, E., C. K. Y. Leung, S. W. Tang, and C. Lu. 2018. 'Displacement discontinuity method for cohesive crack propagation', *Engineering Fracture Mechanics*, 190: 319-30.

Chen, HH, and RKL Su. 2013. 'Tension softening curves of plain concrete', *Construction and Building Materials*, 44: 440-51.

Cheng, Lu, Haohui Xin, Roger M Groves, and Milan Veljkovic. 2021. 'Acoustic emission source location using Lamb wave propagation simulation and artificial neural network for I-shaped steel girder', *Construction and Building Materials*, 273: 121706.

Cheung, Yau Kai, and Aandrew YT Leung. 1992. *Finite element methods in dynamics* (Springer Science & Business Media).

Chisari, Corrado, Claudio Guarnaccia, and Gianvittorio Rizzano. 2020. 'Numerical simulation of acoustic emission activity in reinforced concrete structures by means of finite element modelling at the macroscale', *Structural Health Monitoring*, 19: 537-51.

Chowdhury, Indrajit, and Shambhu P Dasgupta. 2003. 'Computation of Rayleigh damping coefficients for large systems', *The Electronic Journal of Geotechnical Engineering*, 8: 1-11.

Chung, Jintai, and Jang Moo Lee. 1994. 'A new family of explicit time integration methods for linear and non‐linear structural dynamics', *International Journal for Numerical Methods in Engineering*, 37: 3961-76.

Ciamarra, M Pica, Eugenio Lippiello, Lucilla de Arcangelis, and Cataldo Godano. 2011. 'Statistics of slipping event sizes in granular seismic fault models', *Europhysics Letters*, 95: 54002.

Cocco, Massimo, Elisa Tinti, and Antonella Cirella. 2016. 'On the scale dependence of earthquake stress drop', *Journal of Seismology*, 20: 1151-70.

Coetzee, Corné J. 2016. 'Calibration of the discrete element method and the effect of particle shape', *Powder technology*, 297: 50-70.

Colombo, Ing S, IG Main, and MC Forde. 2003. 'Assessing damage of reinforced concrete beam using “b-value” analysis of acoustic emission signals', *Journal of materials in civil engineering*, 15: 280-86.

Cottica, Pricila, Leandro Friedrich, Ederli Marangon, and Ignacio Iturrioz. 2020. "Application of peridynamics in the simulation of acoustic emission in quasi-brittle materials." In *XLI Ibero-Latin American Congress on Computational Methods in Engineering*.

Cuadra, J, PA Vanniamparambil, D Servansky, I Bartoli, and A Kontsos. 2015. 'Acoustic emission source modeling using a data-driven approach', *Journal of Sound and Vibration*, 341: 222-36.

Cuadra, Jefferson A. 2015. 'A Computational Modeling Approach of Fracture-Induced Acoustic Emission', Drexel University.

Cui, Xiwang, Yong Yan, Yonghui Hu, and Miao Guo. 2019. 'Performance comparison of acoustic emission sensor arrays in different topologies for the localization of gas leakage on a flat-surface structure', *Sensors and Actuators A: Physical*, 300: 111659.

Cull, SJ. 1999. 'On the modelling of Coulomb friction', *Journal of Physics A: Mathematical and General*, 32: 2103.

Cusatis, G. 2011. 'Strain-rate effects on concrete behavior', *International Journal of Impact Engineering*, 38: 162-70.

Cusatis, G., and E. A. Schauffert. 2009. 'Cohesive crack analysis of size effect', *Engineering Fracture Mechanics*, 76: 2163-73.

Cusatis, Gianluca, Zdeněk P Bažant, and Luigi Cedolin. 2003. 'Confinement-shear lattice model for concrete damage in tension and compression: I. Theory', *Journal of engineering mechanics*, 129: 1439-48.

Daemen, JJK. 1983. "Slip zones for discontinuities parallel to circular tunnels or shafts." In *International Journal of Rock Mechanics and Mining Sciences & Geomechanics Abstracts*, 135-48. Elsevier.

Dahm, Torsten. 1996. 'Relative moment tensor inversion based on ray theory: theory and synthetic tests', *Geophysical Journal International*, 124: 245-57.

Dahm, Torsten, and F Krüger. 1999. 'Higher-degree moment tensor inversion using far-field broad-band recordings: theory and evaluation of the method with application to the 1994 Bolivia deep earthquake', *Geophysical Journal International*, 137: 35-50.

Datta, Dibakar. 2013. 'Introduction to extended finite element (XFEM) method', *arXiv preprint arXiv:1308.5208*.

Desoer, C. A., and Y. T. Wang. 1980. 'On the Generalized Nyquist Stability-Criterion', *Ieee Transactions on Automatic Control*, 25: 187-96.

Dhatt, Gouri, Emmanuel Lefrançois, and Gilbert Touzot. 2012. *Finite element method* (John Wiley & Sons).

Di Benedetti, M, and Antonio Nanni. 2014. 'Acoustic emission intensity analysis for in situ evaluation of reinforced concrete slabs', *Journal of materials in civil engineering*, 26: 6-13.

Dieterich, James H. 1978. 'Time-dependent friction and the mechanics of stick-slip', *Pure and applied geophysics*, 116: 790-806.

Dong, Duan, Zhang Xiangdong, and Liu Libin. 2014. 'Research on relationship between parameters correlation of acoustic emission and rock failure', *Sensors & Transducers*, 183: 147.

Dong, Longjun, Yihan Zhang, Shuijin Bi, Ju Ma, Yihao Yan, and Heng Cao. 2023. 'Uncertainty investigation for the classification of rock micro-fracture types using acoustic emission parameters', *International Journal of Rock Mechanics and Mining Sciences*, 162: 105292.

Dormy, Emmanuel, and Albert Tarantola. 1995. 'Numerical simulation of elastic wave propagation using a finite volume method', *Journal of Geophysical Research: Solid Earth*, 100: 2123-33.

Du, Kun, Xuefeng Li, Ming Tao, and Shaofeng Wang. 2020. 'Experimental study on acoustic emission (AE) characteristics and crack classification during rock fracture in several basic lab tests', *International Journal of Rock Mechanics and Mining Sciences*, 133: 104411.

Duffy, Dean G. 2015. *Green's functions with applications* (Chapman and Hall/CRC).

Eitzen, DG, and HNG Wadley. 1984. 'Acoustic emission: establishing the fundamentals', *Journal of research of the National Bureau of Standards*, 89: 75.

Elices, M, C Rocco, and C Roselló. 2009. 'Cohesive crack modelling of a simple concrete: Experimental and numerical results', *Engineering Fracture Mechanics*, 76: 1398-410.

Enoki, M, T Kishi, and S Kohara. 1986. 'Determination of micro-cracking moment tensor of quasi-cleavage facet by AE source characterization', *Progress in Acoustic Emission III, JSNDI*: 763-70.

Erdogan, F. 1983. 'Stress intensity factors'.

Eringen, AC, and ES Suhubi. 1975. 'Elastodynamics. Volume 2- Linear theory(Book)', *New York, Academic Press, Inc., 1975. 671 p.*

Fan, Yibo, Fengshou Gu, and Andrew Ball. 2010. 'Modelling acoustic emissions generated by sliding friction', *Wear*, 268: 811-15.

Farhidzadeh, Alireza, Salvatore Salamone, Bismarck Luna, and Andrew Whittaker. 2013. 'Acoustic emission monitoring of a reinforced concrete shear wall by b-value–based outlier analysis', *Structural Health Monitoring*, 12: 3-13.

Fei, Fan, and Jinhyun Choo. 2020. 'A phase-field method for modeling cracks with frictional contact', *International Journal for Numerical Methods in Engineering*, 121: 740-62.

Ferdowsi, B, M Griffa, RA Guyer, PA Johnson, C Marone, and J Carmeliet. 2013. 'Microslips as precursors of large slip events in the stick-slip dynamics of sheared granular layers: A discrete element model analysis', *Geophysical Research Letters*, 40: 4194-98.

Ferrer, C, F Salas, M Pascual, and J Orozco. 2010. 'Discrete acoustic emission waves during stick–slip friction between steel samples', *Tribology International*, 43: 1-6.

FOWLER, TIMOTHYJ, JAMESA BLESSING, and PETERJ CONLISK. 1989. "New directions in testing." In *AECM-3: International Symposium on Acoustic Emission from Composite Materials, 3 rd, Paris, France*, 16-27.

Friedel, Jacques. 2013. *Dislocations: international series of monographs on solid state physics* (Elsevier).

Friedrich, Leandro Ferreira, Boris Nahuel Rojo Tanzi, Angélica Bordin Colpo, Mario Sobczyk, Giuseppe Lacidogna, Gianni Niccolini, and Ignacio Iturrioz. 2022. 'Analysis of acoustic emission activity during progressive failure in heterogeneous materials: experimental and numerical investigation', *Applied Sciences*, 12: 3918.

Fries, Thomas-Peter, and Ted Belytschko. 2010. 'The extended/generalized finite element method: an overview of the method and its applications', *International Journal for Numerical Methods in Engineering*, 84: 253-304.

Galvanetto, Ugo, SR Bishop, and L Briseghella. 1995. 'Mechanical stick-slip vibrations', *International Journal of Bifurcation and Chaos*, 5: 637-51.

Gao, Chao, Doris Kuhlmann-Wilsdorf, and David D Makel. 1993. 'Fundamentals of stick-slip', *Wear*, 162: 1139-49.

Gao, Ke, Robert Guyer, Esteban Rougier, Christopher X Ren, and Paul A Johnson. 2019. 'From stress chains to acoustic emission', *Physical review letters*, 123: 048003.

Gao, Xiangling, Laijun Zhou, Xiaodan Ren, and Jie Li. 2021. 'Rate effect on the stress–strain behavior of concrete under uniaxial tensile stress', *Structural Concrete*, 22: E815-E30.

Gaul, L. 1999. 'The influence of damping on waves and vibrations', *Mechanical Systems and Signal Processing*, 13: 1-30.

Gaydeck, PA, FM Burdekin, W Damaj, DG John, and PA Payne. 1992. 'Digital deconvolution analysis of ultrasonic signals influenced by the presence of longitudinally aligned steel cables in pre-stressed concrete', *Measurement Science and Technology*, 3: 909.

Gdoutos, Emmanuel E. 2020. *Fracture mechanics: an introduction* (Springer Nature).

Gerstle, Walter Herbert. 2015. *Introduction to practical peridynamics: computational solid mechanics without stress and strain* (World Scientific Publishing Company).

Ghamgosar, M, and N Erarslan. 2016. 'Experimental and numerical studies on development of fracture process zone (FPZ) in rocks under cyclic and static loadings', *Rock Mechanics and Rock Engineering*, 49: 893-908.

Gharehbaghi, Vahid Reza, Ehsan Noroozinejad Farsangi, Mohammad Noori, Tony Y Yang, Shaofan Li, Andy Nguyen, Christian Málaga-Chuquitaype, Paolo Gardoni, and Seyedali Mirjalili. 2022. 'A critical review on structural health monitoring: Definitions, methods, and perspectives', *Archives of Computational Methods in Engineering*, 29: 2209-35.

Gholizadeh, Samira, Z Leman, and BTHT Baharudin. 2015. 'A review of the application of acoustic emission technique in engineering', *Struct. Eng. Mech*, 54: 1075-95.

Ghosh, Subha, Nirjhar Dhang, and Arghya Deb. 2020. 'Influence of aggregate geometry and material fabric on tensile cracking in concrete', *Engineering Fracture Mechanics*, 239: 107321.

Givoli, Dan. 1991. 'Non-reflecting boundary conditions', *Journal of computational physics*, 94: 1-29.

GOM. 2016. "Digital Image Correlation and Strain Computation Basics." In.: GOM Braunschweig, Germany.

Grabec, Igor, and Jože Petrišič. 1986. 'The application of a semielastic lattice model to the description of acoustic emission', *Engineering Fracture Mechanics*, 23: 621-29.

Graff, Karl F. 2012. *Wave motion in elastic solids* (Courier Corporation).

Graham, Caroline C, Sergei Stanchits, Ian G Main, and Georg Dresen. 2010. 'Comparison of polarity and moment tensor inversion methods for source analysis of acoustic emission data', *International Journal of Rock Mechanics and Mining Sciences*, 47: 161-69.

Gresil, Matthieu, and Victor Giurgiutiu. 2015. 'Prediction of attenuated guided waves propagation in carbon fiber composites using Rayleigh damping model', *Journal of Intelligent Material Systems and Structures*, 26: 2151-69.

Griffith, Alan Arnold. 1921. 'VI. The phenomena of rupture and flow in solids', *Philosophical transactions of the royal society of london. Series A, containing papers of a mathematical or physical character*, 221: 163-98.

Griffiths, DV, and Graham GW Mustoe. 2001. 'Modelling of elastic continua using a grillage of structural elements based on discrete element concepts', *International Journal for Numerical Methods in Engineering*, 50: 1759-75.

Grosse, C, H Reinhardt, and Torsten Dahm. 1997. 'Localization and classification of fracture types in concrete with quantitative acoustic emission measurement techniques', *Ndt & E International*, 30: 223-30.

Grosse, Christian U, and Masayasu Ohtsu. 2008a. *Acoustic emission testing* (Springer Science & Business Media).

Grosse, Christian U, Masayasu Ohtsu, Dimitrios G Aggelis, and Tomoki Shiotani. 2021. *Acoustic emission testing: Basics for research–applications in engineering* (Springer Nature).

Grosse, CU, and M Ohtsu. 2008b. 'Acoustic Emission Testing–Basics for Research–Applications in Civil Engineering Springer Verlag', *Berlin Heidelberg*.

Gurtin, Morton E. 1982. *An introduction to continuum mechanics* (Academic press).

Gutenberg, Beno, and Charles Richter. 1954. *Seismicity of the earth and associated phenomena* (Princeton University Press).

Haessig Jr, David A, and Bernard Friedland. 1991. 'On the modeling and simulation of friction'.

Haldorsen, Jakob BU. 2020. "Spatial aliasing." In *SEG International Exposition and Annual Meeting*. OnePetro.

Hamam, Zeina, Nathalie Godin, Claudio Fusco, Aurélien Doitrand, and Thomas Monnier. 2021. 'Acoustic emission signal due to fiber break and fiber matrix debonding in model composite: A computational study', *Applied Sciences*, 11: 8406.

Hamam, Zeina, Nathalie Godin, Claudio Fusco, and Thomas Monnier. 2019. 'Modelling of acoustic emission signals due to fiber break in a model composite carbon/epoxy: Experimental validation and parametric study', *Applied Sciences*, 9: 5124.

Hamstad, Marvin A. 2007a. 'Acoustic emission signals generated by monopole (pencil lead break) versus dipole sources: finite element modeling and experiments', *J. Acoust. Emiss*, 25: 92-106.

———. 2007b. 'Acoustic emission signals generated by monopole (pencil lead break) versus dipole sources: finite element modeling and experiments', *J. Acoust. Emiss*, 25: 92-106.

Hamstad, Marvin A, Agnes O'Gallagher, and John M Gary. 1999. 'Modeling of buried monopole and dipole sources of acoustic emission with a finite element technique'.

Han, Q. H., G. Yang, and J. Xu. 2018. 'Experimental study on the relationship between acoustic emission energy and fracture energy of crumb rubber concrete', *Structural Control & Health Monitoring*, 25: e2240.

Hao, Qiushi, Yi Shen, Yan Wang, and Xin Zhang. 2019. 'A fractal model of acoustic emission signals in sliding friction', *Tribology Letters*, 67: 1-10.

Hariri-Ardebili, Mohammad Amin, Leandro Sanchez, and Roozbeh Rezakhani. 2020. 'Aging of Concrete Structures and Infrastructures: Causes, Consequences, and Cures (C-3)', *Advances in Materials Science and Engineering*, 2020: 9370591.

Harris, John G. 2001. *Linear elastic waves* (Cambridge University Press).

HART, ROGER D. 1993. 'An introduction to distinct element modeling for rock engineering.' in, *Analysis and Design Methods* (Elsevier).

Haskett, Matthew, Deric John Oehlers, MS Mohamed Ali, and Surjit Kumar Sharma. 2011. 'Evaluating the shear-friction resistance across sliding planes in concrete', *Engineering Structures*, 33: 1357-64.

Hassan, Farrukh, Ahmad Kamil Bin Mahmood, Norashikin Yahya, Abdul Saboor, Muhammad Zahid Abbas, Zia Khan, and Mohamed Rimsan. 2021. 'State-of-the-art review on the acoustic emission source localization techniques', *IEEE Access*, 9: 101246-66.

Hazzard, James F, and R Paul Young. 2002. 'Moment tensors and micromechanical models', *Tectonophysics*, 356: 181-97.

Hazzard, JF, and RP Young. 2000. 'Simulating acoustic emissions in bonded-particle models of rock', *International Journal of Rock Mechanics and Mining Sciences*, 37: 867-72.

Higson, GRt. 1964. 'Recent advances in strain gauges', *Journal of Scientific Instruments*, 41: 405.

Hora, Petr, and Olga Červená. 2010. 'Acoustic emission source modeling', *Applied and Computational Mechanics*, 4.

Horabik, Józef, and Marek Molenda. 2016. 'Parameters and contact models for DEM simulations of agricultural granular materials: A review', *Biosystems engineering*, 147: 206-25.

Hoving, Jeroen, and Andrei Metrikine. 2017. "Wave reflection at the interface between a nonlinear discrete lattice and a matching linear system." In *24th International Congress on Sound and Vibration: London Calling, 2017*.

Howell, Deborah, Olivier de Weck, and David W Miller. 2008. "Spatial Nyquist fidelity method for structural models of opto-mechanical systems." In *Modeling, Systems Engineering, and Project Management for Astronomy III*, 416-27. SPIE.

Hrennikoff, Alexander. 1941. 'Solution of problems of elasticity by the framework method'.

Hughes, Thomas JR. 2003. *The finite element method: linear static and dynamic finite element analysis* (Courier Corporation).

Humar, Jagmohan. 2012. *Dynamics of structures* (CRC press).

Hussain, MA, SL Pu, and J Underwood. 1973. "Strain energy release rate for a crack under combined mode I and mode II." In *1973 National Symposium on Fracture Mechanics, Part II*, 1-27. ASTM International.

Hussin, Siti Farah, Gauri Birasamy, and Zunainah Hamid. 2016. 'Design of butterworth band-pass filter', *Politeknik & Kolej Komuniti Journal of Engineering and Technology*, 1.

Ince, Nuri Firat, Chu-Shu Kao, Mostafa Kaveh, A Tewfik, and Joseph F Labuz. 2010. 'A machine learning approach for locating acoustic emission', *EURASIP Journal on Advances in Signal Processing*, 2010: 1-14.

Irwin, George R. 1957. 'Analysis of stresses and strains near the end of a crack traversing a plate'.

ISO. 2019. "Non-Destructive Testing—Acoustic Emission Testing—Test Method for Classification of Active Cracks in Concrete Structures." In. Geneva, Switzerland: ISO.

Iturrioz, I, G Lacidogna, and A Carpinteri. 2013. 'Experimental analysis and truss-like discrete element model simulation of concrete specimens under uniaxial compression', *Engineering Fracture Mechanics*, 110: 81-98.

———. 2014. 'Acoustic emission detection in concrete specimens: Experimental analysis and lattice model simulations', *International Journal of Damage Mechanics*, 23: 327-58.

Iturrioz, Ignacio, and Jorge D Riera. 2021. 'Assessment of the Lattice Discrete Element Method in the simulation of wave propagation in

inhomogeneous linearly elastic geologic materials', *Soil Dynamics and Earthquake Engineering*, 151: 106952.

Javili, Ali, Rico Morasata, Erkan Oterkus, and Selda Oterkus. 2019. 'Peridynamics review', *Mathematics and Mechanics of Solids*, 24: 3714-39.

Ji, Shunying, and Shaocheng Di. 2013. 'Discrete element modeling of acoustic emission in rock fracture', *Theoretical and Applied Mechanics Letters*, 3: 021009.

Jiang, Ruochen, Feng Dai, Yi Liu, Ang Li, and Peng Feng. 2021. 'Frequency characteristics of acoustic emissions induced by crack propagation in rock tensile fracture', *Rock Mechanics and Rock Engineering*, 54: 2053-65.

Johnson, John A. 1987. 'Numerical calculations of acoustic emission', *Journal of nondestructive evaluation*, 6: 159-66.

Johnson, Paul A, Behrooz Ferdowsi, Bryan M Kaproth, MARCO Scuderi, Michele Griffa, Jan Carmeliet, Robert A Guyer, P-Y Le Bas, Daniel T Trugman, and Chris Marone. 2013. 'Acoustic emission and microslip precursors to stick-slip failure in sheared granular material', *Geophysical Research Letters*, 40: 5627-31.

Kachanov, Mark. 1980. 'Continuum model of medium with cracks', *Journal of the Engineering Mechanics Division*, 106: 1039-51.

Kanamori, Hiroo, and Clarence R Allen. 1986. 'Earthquake repeat time and average stress drop', *Earthquake source mechanics*, 37: 227-35.

Kao, C-S, FCS Carvalho, and Joseph F Labuz. 2011. 'Micromechanisms of fracture from acoustic emission', *International Journal of Rock Mechanics and Mining Sciences*, 48: 666-73.

Karihaloo, Bhushan Lal, PF Shao, and QZ Xiao. 2003. 'Lattice modelling of the failure of particle composites', *Engineering Fracture Mechanics*, 70: 2385-406.

Karpenko, Yu A, and Adnan Akay. 2001. 'A numerical model of friction between rough surfaces', *Tribology International*, 34: 531-45.

Kerlins, Victor. 1987. 'Modes of fracture'.

Khalaf, Mohammed A, Cheah Chee Ban, and Mahyuddin Ramli. 2019. 'The constituents, properties and application of heavyweight concrete: A review', *Construction and Building Materials*, 215: 73-89.

Khoei, Amir R. 2015. *Extended finite element method: theory and applications* (John Wiley & Sons).

Kim, Kwang Yul, and Wolfgang Sachse. 1986. 'Characteristics of an acoustic emission source from a thermal crack in glass', *International journal of fracture*, 31: 211-31.

Komatitsch, Dimitri, and Jeroen Tromp. 1999. 'Introduction to the spectral element method for three-dimensional seismic wave propagation', *Geophysical Journal International*, 139: 806-22.

Komijani, M, and R Gracie. 2017. 'An enriched finite element model for wave propagation in fractured media', *Finite Elements in Analysis and Design*, 125: 14-23.

Komijani, M, R Gracie, and Y Yuan. 2020. 'Simulation of fracture propagation induced acoustic emission in porous media', *Engineering Fracture Mechanics*, 229: 106950.

Komijani, Mohammad. 2018. 'Simulation of Hydraulic Stimulation: Acoustic Wave Emission in Fractured Porous Media Using Local and Global Partition-of-Unity Finite Element'.

Komijani, Mohammad, and Robert Gracie. 2019. 'Enriched mixed finite element models for dynamic analysis of continuous and fractured porous media', *Computer Methods in Applied Mechanics and Engineering*, 343: 74-99.

Komijani, Mohammad, Peter Wriggers, and Taha Goudarzi. 2023. 'An enriched mixed finite element model for the simulation of microseismic and acoustic emissions in fractured porous media with multi‐phase flow and thermal coupling', *International journal for numerical and analytical methods in geomechanics*, 47: 2968-3004.

Kosteski, Luis, Ignacio Iturrioz, Ruben Galiano Batista, and Adrián P Cisilino. 2011. 'The truss‐like discrete element method in fracture and damage mechanics', *Engineering Computations*, 28: 765-87.

Kukudzhanov, Vladimir N. 2012. *Numerical continuum mechanics* (Walter de Gruyter).

Kundu, Tribikram. 2014. 'Acoustic source localization', *Ultrasonics*, 54: 25-38.

Kurz, Jochen H, Florian Finck, Christian U Grosse, and Hans-Wolf Reinhardt. 2006. 'Stress drop and stress redistribution in concrete quantified over time by the b-value analysis', *Structural Health Monitoring*, 5: 69-81.

Lacidogna, Giuseppe, Federico Accornero, and Alberto Carpinteri. 2019. 'Influence of snap-back instabilities on Acoustic Emission damage monitoring', *Engineering Fracture Mechanics*, 210: 3-12.

Lai, Ning-An, and Ziheng Tu. 2020. 'Strauss exponent for semilinear wave equations with scattering space dependent damping', *Journal of Mathematical Analysis and Applications*, 489: 124189.

Lambri, OA. 2000. 'A review on the problem of measuring non-linear damping and the obtainment of intrinsic damping', *Materials Instabilities*: 249-80.

Landa, M, J Cerv, A Machová, and Z Rosecky. 2003. 'Acoustic emission sources by atomistic simulations', *Journal of acoustic emission*, 20: 25-38.

Landis, E. N., and L. Baillon. 2002. 'Experiments to relate acoustic emission energy to fracture energy of concrete', *Journal of Engineering Mechanics-Asce*, 128: 698-702.

Lantsoght, Eva Olivia Leontien, Cor van der Veen, Joost Walraven, and Ane de Boer. 2013. 'Recommendations for the shear assessment of reinforced concrete slab bridges from experiments', *Structural Engineering International*, 23: 418-26.

Li, Ping, Xiaodan Ren, and Jie Li. 2024. 'Damage assessment of concrete via acoustic emission and mesoscopic damage constitutive model', *Engineering Fracture Mechanics*, 303: 110133.

Li, Shijin, and Alister Smith. 2022. 'Relationship between acoustic emission and energy dissipation: a DEM study of soil–structure interaction', *Acta Geotechnica*: 1-20.

———. 2023a. 'Acoustic emission and energy dissipation in soils during triaxial shearing', *Computers and Geotechnics*, 162: 105639.
———. 2023b. 'Relationship between acoustic emission and energy dissipation: a DEM study of soil–structure interaction', *Acta Geotechnica*, 18: 2971-90.
Li, Zhaofeng, YH Wang, CH Ma, and Chit Man Benjamin Mok. 2017. 'Experimental characterization and 3D DEM simulation of bond breakages in artificially cemented sands with different bond strengths when subjected to triaxial shearing', *Acta Geotechnica*, 12: 987-1002.
Lilliu, G, and Jan GM van Mier. 2003. '3D lattice type fracture model for concrete', *Engineering Fracture Mechanics*, 70: 927-41.
Lisjak, A, Q Liu, Q Zhao, OK Mahabadi, and G Grasselli. 2013a. 'Numerical simulation of acoustic emission in brittle rocks by two-dimensional finite-discrete element analysis', *Geophysical Journal International*, 195: 423-43.
Lisjak, A., Q. Liu, Q. Zhao, O. K. Mahabadi, and G. Grasselli. 2013b. 'Numerical simulation of acoustic emission in brittle rocks by two-dimensional finite-discrete element analysis', *Geophysical Journal International*, 195: 423-43.
Liu, M. Z., J. X. Yang, Y. P. Cao, W. A. Fu, and Y. L. Cao. 2017. 'A new method for arrival time determination of impact signal based on HHT and AIC', *Mechanical Systems and Signal Processing*, 86: 177-87.
Liu, Zhiwei, and Paul H Ziehl. 2009. 'Evaluation of reinforced concrete beam specimens with acoustic emission and cyclic load test methods', *ACI Structural Journal*, 106: 288.
Liu, Zi-ming, Yao Jiang, Dao-jie Wang, and Yan-ju Fu. 2022. 'Four types of acoustic emission characteristics during granular stick-slip evolution', *Journal of Mountain Science*, 19: 276-88.
Lu, MMGR, and GR McDowell. 2007. 'The importance of modelling ballast particle shape in the discrete element method', *Granular matter*, 9: 69-80.
Ma, Xiaochuan, Qingsong Feng, Linya Liu, Jinhui Xu, Pengfei Zhang, and Huapeng Chen. 2022. 'A non-local method in peridynamic theory for simulating elastic wave propagation in solids', *Applied Mathematical Modelling*, 103: 360-75.
Madariaga, R. 1977. 'High-Frequency Radiation from Crack (Stress Drop) Models of Earthquake Faulting', *Geophysical Journal of the Royal Astronomical Society*, 51: 625-51.
Madariaga, Raul. 1979. 'On the relation between seismic moment and stress drop in the presence of stress and strength heterogeneity', *Journal of Geophysical Research: Solid Earth*, 84: 2243-50.
Main, Ian G, Philip G Meredith, and Colin Jones. 1989. 'A reinterpretation of the precursory seismic b-value anomaly from fracture mechanics', *Geophysical Journal International*, 96: 131-38.
Maji, A, and Surendra P Shah. 1988. 'Process zone and acoustic-emission measurements in concrete', *Experimental mechanics*, 28: 27-33.

Malekpour, Sheida, John A Gubner, and William A Sethares. 2018. 'Measures of generalized magnitude-squared coherence: Differences and similarities', *Journal of the Franklin Institute*, 355: 2932-50.

Manbachi, Amir, and Richard SC Cobbold. 2011. 'Development and application of piezoelectric materials for ultrasound generation and detection', *Ultrasound*, 19: 187-96.

Marasanov, VV, and AA Sharko. 2017. "Discrete models characteristics of the acoustic emission signal origin forerunners." In *2017 IEEE First Ukraine Conference on Electrical and Computer Engineering (UKRCON)*, 680-83. IEEE.

Marfurt, Kurt J. 1984. 'Accuracy of finite-difference and finite-element modeling of the scalar and elastic wave equations', *Geophysics*, 49: 533-49.

Matthews, James R. 1983. *Acoustic emission* (CRC Press).

McCormick, Nick, and Jerry Lord. 2010. 'Digital image correlation', *Materials today*, 13: 52-54.

McLaskey, Gregory C, and Steven D Glaser. 2012. 'Acoustic emission sensor calibration for absolute source measurements', *Journal of nondestructive evaluation*, 31: 157-68.

McLaskey, Gregory C, and Brian D Kilgore. 2013. 'Foreshocks during the nucleation of stick‐slip instability', *Journal of Geophysical Research: Solid Earth*, 118: 2982-97.

McLaskey, Gregory C, Amanda M Thomas, Steven D Glaser, and Robert M Nadeau. 2012. 'Fault healing promotes high-frequency earthquakes in laboratory experiments and on natural faults', *Nature*, 491: 101-04.

McLaskey, Gregory Christofer. 2011. 'Stress wave source characterization: Impact, fracture, and sliding friction', UC Berkeley.

Meirovitch, Leonard. 2010. *Methods of analytical dynamics* (Courier Corporation).

Minozzi, Manuela, Guido Caldarelli, Luciano Pietronero, and Stefano Zapperi. 2003. 'Dynamic fracture model for acoustic emission', *The European Physical Journal B-Condensed Matter and Complex Systems*, 36: 203-07.

Mirbagheri, Ya, H Nahvi, Jamshid Parvizian, and Alexander Düster. 2015. 'Reducing spurious oscillations in discontinuous wave propagation simulation using high-order finite elements', *Computers & Mathematics with Applications*, 70: 1640-58.

Mirgal, Paresh, Ram Kumar Singh, and Sauvik Banerjee. 2023. 'Acoustic and fracture energy correlation in mode I fracture with concrete damage plasticity model and three-point bend experiment', *Journal of materials in civil engineering*, 35: 04023002.

MISTRAS. 2011a. "MICRO-II – COMPACT PCI AE CHASSIS." In. Princeton Jctction, NJ 08550, USA, Products & System Division.

———. 2011b. "R15α Sensor." In. Princeton Jctction, NJ 08550, USA, Products & System Division.

———. 2018. '9203-ASL Sensor **Product Data Sheet**'. http://www.physicalacoustics.com/content/literature/sensors/Model_9203-ASL.pdf.

———. 2022. 'S9208 Sensor Product Data Sheet'. http://www.physicalacoustics.com/content/literature/sensors/Model_S9208.pdf.
———. 2023. '32-Channel Micro-II AE System Product Data Sheet'.
Monette, L, and MP Anderson. 1994. 'Elastic and fracture properties of the two-dimensional triangular and square lattices', *Modelling and Simulation in Materials Science and Engineering*, 2: 53.
Mora, Peter, and David Place. 1993. 'A lattice solid model for the nonlinear dynamics of earthquakes', *International Journal of Modern Physics C*, 4: 1059-74.
Morelli, Andrea, and Adam M Dziewonski. 1993. 'Body wave traveltimes and a spherically symmetric P-and S-wave velocity model', *Geophysical Journal International*, 112: 178-94.
Morgan, Stephen Philip. 2015. 'An experimental and numerical study on the fracturing processes in Opalinus shale', Massachusetts Institute of Technology, Department of Civil and Environmental ….
Munjiza, Antonio A. 2004. *The combined finite-discrete element method* (John Wiley & Sons).
Mura, Toshio. 2013. *Micromechanics of defects in solids* (Springer Science & Business Media).
Muralidhara, S, BK Raghu Prasad, Bhushan Lal Karihaloo, and RK Singh. 2011. 'Size-independent fracture energy in plain concrete beams using tri-linear model', *Construction and Building Materials*, 25: 3051-58.
Muralidhara, Sundareshan, BK Raghu Prasad, Hamid Eskandari, and Bhushan Lal Karihaloo. 2010. 'Fracture process zone size and true fracture energy of concrete using acoustic emission', *Construction and Building Materials*, 24: 479-86.
Nagy, Edwin, Eric N Landis, and William G Davids. 2010. 'Acoustic emission measurements and lattice simulations of microfracture events in spruce'.
Nazarchuk, Zinoviy, Valentyn Skalskyi, and Oleh Serhiyenko. 2017. 'Acoustic emission', *Foundations of Engineering Mechanics*.
Newman, John, and Phil Owens. 2003. 'Properties of lightweight concrete', *Advanced concrete technology*, 3: 1-29.
Nhung, Nguyen Thi Cam, Huu Quyet Nguyen, Dang Thi Huyen, Duc Binh Nguyen, and Minh Tran Quang. 2023. 'Development and application of linear variable differential transformer (LVDT) sensors for the structural health monitoring of an urban railway bridge in Vietnam', *Engineering, Technology & Applied Science Research*, 13: 11622-27.
Nickell, Robert E. 1976. 'Nonlinear dynamics by mode superposition', *Computer Methods in Applied Mechanics and Engineering*, 7: 107-29.
Nikolić, Mijo, Emir Karavelić, Adnan Ibrahimbegovic, and Predrag Miščević. 2018. 'Lattice element models and their peculiarities', *Archives of Computational Methods in Engineering*, 25: 753-84.
Niwa, Yoshiji, Masayasu Ohtsu, and Hiroyuki Shiomi. 1982. 'Waveform analysis of acoustic emission in concrete', *Memoirs of the Faculty of Engineering, Kyoto University*, 43: 319-30.

Noorsuhada, MN. 2016. 'An overview on fatigue damage assessment of reinforced concrete structures with the aid of acoustic emission technique', *Construction and Building Materials*, 112: 424-39.

O'Rourke, Michael F, and David E Gallagher. 1996. 'Pulse wave analysis', *Journal of hypertension. Supplement: official journal of the International Society of Hypertension*, 14: S147-57.

OHNAKA, Mitiyasu. 1973. 'Experimental studies of stick-slip and their application to the earthquake source mechanism', *Journal of Physics of the Earth*, 21: 285-303.

Ohno, Kentaro. 2015. 'Identification of the fracture process zone in concrete materials by acoustic emission.' in, *Acoustic Emission and Related Non-Destructive Evaluation Techniques in the Fracture Mechanics of Concrete* (Elsevier).

Ohno, Kentaro, and Masayasu Ohtsu. 2010. 'Crack classification in concrete based on acoustic emission', *Construction and Building Materials*, 24: 2339-46.

Ohtsu, M. 1989. 'Source kinematics of acoustic emission based on a moment tensor', *NDT international*, 22: 14-20.

———. 1995. 'Acoustic emission theory for moment tensor analysis', *Research in Nondestructive Evaluation*, 6: 169-84.

OHTSU, Masayasu. 1988. 'Source inversion of acoustic emission waveform', *Doboku Gakkai Ronbunshu*, 1988: 71-79.

———. 1991. 'Simplified moment tensor analysis and unified decomposition of acoustic emission source: application to in situ hydrofracturing test', *Journal of Geophysical Research: Solid Earth*, 96: 6211-21.

———. 1996. 'The history and development of acoustic emission in concrete engineering', *Magazine of concrete research*, 48: 321-30.

Ohtsu, Masayasu, Toshiro Isoda, and Yuichi Tomoda. 2007. 'Acoustic emission techniques standardized for concrete structures', *Journal of acoustic emission*, 25: 21-32.

Ohtsu, Masayasu, Y Kaminaga, and Muzo C Munwam. 1999. 'Experimental and numerical crack analysis of mixed-mode failure in concrete by acoustic emission and boundary element method', *Construction and Building Materials*, 13: 57-64.

Ohtsu, Masayasu, and Kanji Ono. 1986. 'The generalized theory and source representations of acoustic emission', *Journal of acoustic emission*, 5: 124-33.

Ohtsu, Masayasu, Shigenori Yuyama, and Takuichi Imanaka. 1987. 'Theoretical treatment of acoustic emission sources in microfracturing due to disbonding', *The Journal of the Acoustical Society of America*, 82: 506-12.

Ono, Kanji. 2011. 'ACOUSTIC EMISSION IN MATERIALS RESEARCH-A REVIEW', *Journal of acoustic emission*, 29.

Ostoja-Starzewski, M, PY Sheng, and K Alzebdeh. 1996. 'Spring network models in elasticity and fracture of composites and polycrystals', *Computational Materials Science*, 7: 82-93.

Ostoja-Starzewski, Martin. 2002. 'Lattice models in micromechanics', *Appl. Mech. Rev.*, 55: 35-60.

PAC. 2005. "DiSP with AEwin User's Manual Rev. 3." In. Princeton, New Jersey, USA: Physical Acoustic Corporation.

Pal, P. 2019. 'Dynamic Poisson's Ratio and Modulus of Elasticity of Pozzolana Portland Cement Concrete', *International Journal of Engineering and Technology Innovation*, 9: 131-44.

Pan, Bing. 2011. 'Recent progress in digital image correlation', *Experimental mechanics*, 51: 1223-35.

Pan, Tanbo, Yonglai Zheng, Yubao Zhou, Wenbin Luo, Xubing Xu, Chenyu Hou, and Yujue Zhou. 2023. 'Damage pattern recognition for corroded beams strengthened by CFRP anchorage system based on acoustic emission techniques', *Construction and Building Materials*, 406: 133474.

Pan, Z. C., R. J. Ma, D. L. Wang, and A. R. Chen. 2018. 'A review of lattice type model in fracture mechanics: theory, applications, and perspectives', *Engineering Fracture Mechanics*, 190: 382-409.

Parisi, Andrea, and Guido Caldarelli. 2000. 'Self-affine properties of fractures in brittle materials', *Physica A: Statistical Mechanics and its Applications*, 280: 161-65.

Park, Kyoungsoo, Glaucio H Paulino, and Jeffery Roesler. 2010. 'Cohesive fracture model for functionally graded fiber reinforced concrete', *Cement and concrete research*, 40: 956-65.

Park, Kyoungsoo, Glaucio H Paulino, and Jeffery R Roesler. 2008. 'Determination of the kink point in the bilinear softening model for concrete', *Engineering Fracture Mechanics*, 75: 3806-18.

Peterson, PE. 1980. 'Fracture energy of concrete: Method of determination', *Cement and Concrete research*, 10: 79-89.

Phan, A-V, JAL Napier, LJ Gray, and T19833291062 Kaplan. 2003. 'Symmetric-Galerkin BEM simulation of fracture with frictional contact', *International Journal for Numerical Methods in Engineering*, 57: 835-51.

Philippidis, T. P., and D. G. Aggelis. 2005. 'Experimental study of wave dispersion and attenuation in concrete', *Ultrasonics*, 43: 584-95.

Place, David, and Peter Mora. 1999. 'The lattice solid model to simulate the physics of rocks and earthquakes: Incorporation of friction', *Journal of Computational Physics*, 150: 332-72.

Pollock, Adrian A. 1986. 'Classical wave theory in practical AE testing', *Progress in acoustic emission III-JAP society of non-destructive testing*: 708-21.

———. 2018. 'Acoustic emission inspection.' in, *Nondestructive evaluation of materials* (ASM international).

Polycarpou, AA, and A Soom. 1995. 'Application of a two-dimensional model of continuous sliding friction to stick-slip', *Wear*, 181: 32-41.

Potyondy, David O, and PA Cundall. 2004. 'A bonded-particle model for rock', *International Journal of Rock Mechanics and Mining Sciences*, 41: 1329-64.

Prassianakis, IN, and NI Prassianakis. 2004. 'Ultrasonic testing of non-metallic materials: concrete and marble', *Theoretical and Applied Fracture Mechanics*, 42: 191-98.

Prosser, W. H., M. A. Hamstad, J. Gary, and A. O'Gallagher. 1999. 'Finite element and plate theory modeling of acoustic emission waveforms', *Journal of nondestructive evaluation*, 18: 83-90.

Pundit. 2021. "Pundit 200: Concrete properties analysis using ultrasound pulse velocity." In. Screening Eagle Technologies AG, Ringstrasse 2, 8603 Schwerzenbach - Zurich.

Qin, Yan, Chun Liu, Xiaoyu Zhang, Xingang Wang, Bin Shi, Yue Wang, and Shang Deng. 2021. 'A three-dimensional discrete element model of triaxial tests based on a new flexible membrane boundary', *Scientific Reports*, 11: 4753.

Raley, Sean M. 2019. 'Application of Elastodynamic Finite Integration Technique (EFIT) to three-dimensional wave propagation and scattering in arbitrary geometries'.

Ramadas, C, Krishnan Balasubramaniam, Avinash Hood, Makarand Joshi, and CV Krishnamurthy. 2011. 'Modelling of attenuation of Lamb waves using Rayleigh damping: Numerical and experimental studies', *Composite Structures*, 93: 2020-25.

Rao, MVMS, and KJ Prasanna Lakshmi. 2005. 'Analysis of b-value and improved b-value of acoustic emissions accompanying rock fracture', *Current science*: 1577-82.

Raous, M, and S Barbarin. 1996. 'Stress waves in a sliding contact Part 2: modelling.' in, *Tribology Series* (Elsevier).

Reinhardt, Hans W, Hans AW Cornelissen, and Dirk A Hordijk. 1986. 'Tensile tests and failure analysis of concrete', *Journal of Structural Engineering*, 112: 2462-77.

Ritchie, Robert O. 2011. 'The conflicts between strength and toughness', *Nature materials*, 10: 817-22.

Rodrigues, Rodolfo S, Gabriel Birck, and Ignacio Iturrioz. 2016. 'Damage index proposals applied to quasi-brittle materials simulated using the lattice discrete element method', *International Journal of Damage Mechanics*, 25: 1017-39.

Rozman, MG, M Urbakh, and J Klafter. 1997. 'Stick-slip dynamics as a probe of frictional forces', *Europhysics Letters*, 39: 183.

Sagar, R Vidya, and BK Raghu Prasad. 2012. 'A review of recent developments in parametric based acoustic emission techniques applied to concrete structures', *Nondestructive Testing and Evaluation*, 27: 47-68.

Sause, Markus GR, and Siegfried R Horn. 2010. 'Influence of specimen geometry on acoustic emission signals in fiber reinforced composites: FEM-simulations and experiments'.

Sause, Markus GR, and Stefan Richler. 2015. 'Finite element modelling of cracks as acoustic emission sources', *Journal of nondestructive evaluation*, 34: 1-13.

Schapery, Richard A. 1984. 'Correspondence principles and a generalized J integral for large deformation and fracture analysis of viscoelastic media', *International journal of fracture*, 25: 195-223.

Schlangen, Erik, and Edward J Garboczi. 1997. 'Fracture simulations of concrete using lattice models: computational aspects', *Engineering Fracture Mechanics*, 57: 319-32.

Schmicker, D, S Duczek, S Liefold, and Ulrich Gabbert. 2014. 'Wave propagation analysis using high-order finite element methods: spurious oscillations excited by internal element eigenfrequencies', *Technische Mechanik-European Journal of Engineering Mechanics*, 34: 51-71.

Scholz, Christopher H. 2019. *The mechanics of earthquakes and faulting* (Cambridge university press).

Schubert, Frank, and Barbara Schechinger. 2002. 'Numerical modeling of acoustic emission sources and wave propagation in concrete', *Journal of Nondestructive Testing(Germany)*, 7: 1-8.

Schubert, Konstantin J, and Axel S Herrmann. 2011. 'On attenuation and measurement of Lamb waves in viscoelastic composites', *Composite Structures*, 94: 177-85.

Scruby, C. B. 1987a. 'An Introduction to Acoustic-Emission', *Journal of Physics E-Scientific Instruments*, 20: 947-53.

Scruby, Christopher B. 1987b. 'An introduction to acoustic emission', *Journal of Physics E: Scientific Instruments*, 20: 946.

Seco, Fernando, and Antonio R Jiménez. 2012. 'Modelling the generation and propagation of ultrasonic signals in cylindrical waveguides', *Ultrasonic waves*, 28.

Sedlak, Petr, Yuichiro Hirose, and Manabu Enoki. 2013. 'Acoustic emission localization in thin multi-layer plates using first-arrival determination', *Mechanical Systems and Signal Processing*, 36: 636-49.

Sedlak, Petr, Yuichiro Hirose, Sabrina A Khan, Manabu Enoki, and Josef Sikula. 2009. 'New automatic localization technique of acoustic emission signals in thin metal plates', *Ultrasonics*, 49: 254-62.

Semblat, J. F., L. Lenti, and A. Gandomzadeh. 2011. 'A simple multi-directional absorbing layer method to simulate elastic wave propagation in unbounded domains', *International Journal for Numerical Methods in Engineering*, 85: 1543-63.

Serón, FJ, FJ Sanz, M Kindelan, and JI Badal. 1990. 'Finite-element method for elastic wave propagation', *Communications in applied numerical methods*, 6: 359-68.

Shah, Surendra P, Stuart E Swartz, and Chengsheng Ouyang. 1995. *Fracture mechanics of concrete: applications of fracture mechanics to concrete, rock and other quasi-brittle materials* (John Wiley & Sons).

Shahidan, Shahiron, Norazura Muhamad Bunnori, Noorshuhada Md Nor, and Siti Ramziah Basri. 2011. "Damage severity evaluation on reinforced concrete beam by means of acoustic emission signal and intensity analysis." In *2011 IEEE Symposium on Industrial Electronics and Applications*, 337-41. IEEE.

Shigeishi, Mitsuhiro, and Masayasu Ohtsu. 2001. 'Acoustic emission moment tensor analysis: development for crack identification in concrete materials', *Construction and Building Materials*, 15: 311-19.

Shiotani, T. 1994. 'Evaluation of progressive failure using AE sources and improved b-value on slope model tests', *Progress in Acoustic Emission VII, JSNDI*: 529-34.

———. 2001. 'Application of the AE improved b-value to quantiative evaluation of fracture process in concrete-materials', *Journal of acoustic emission*, 19: 118-33.

Shiotani, Tomoki. 2006. 'Evaluation of long-term stability for rock slope by means of acoustic emission technique', *Ndt & E International*, 39: 217-28.

Shiotani, Tomoki, Masayasu Ohtsu, and Kenji Ikeda. 2001. 'Detection and evaluation of AE waves due to rock deformation', *Construction and Building Materials*, 15: 235-46.

Sibson, Richard H. 2003. 'Thickness of the seismic slip zone', *Bulletin of the Seismological Society of America*, 93: 1169-78.

Sibuya, Yasutaka. 1975. *Global theory of a second order linear ordinary differential equation with a polynomial coefficient* (Elsevier).

Sirorattanakul, Krittanon, Stacy Larochelle, Vito Rubino, Nadia Lapusta, and Ares J Rosakis. 2025. 'Sliding and healing of frictional interfaces that appear stationary', *Nature*: 1-7.

Song, Gangbing, Haichang Gu, and Yi-Lung Mo. 2008. 'Smart aggregates: multi-functional sensors for concrete structures—a tutorial and a review', *Smart Materials and Structures*, 17: 033001.

Spencer, Anthony James Merrill. 2004. *Continuum mechanics* (Courier Corporation).

Stefancu, Andrei-Ionut, Silviu-Cristian Melenciuc, and Mihai Budescu. 2011. 'Penalty based algorithms for frictional contact problems', *Buletinul Institutului Politehnic din Iasi. Sectia Constructii, Arhitectura*, 57: 119.

Steketee, JA. 1958. 'On Volterra's dislocations in a semi-infinite elastic medium', *Canadian Journal of Physics*, 36: 192-205.

Stone, DEW, and PF Dingwall. 1977. 'Acoustic emission parameters and their interpretation', *NDT international*, 10: 51-62.

Strouboulis, Theofanis, Kevin Copps, and Ivo Babuška. 2001. 'The generalized finite element method', *Computer Methods in Applied Mechanics and Engineering*, 190: 4081-193.

Suiker, A. S. J., A. V. Metrikine, and R. de Borst. 2001a. 'Comparison of wave propagation characteristics of the Cosserat continuum model and corresponding discrete lattice models', *International Journal of Solids and Structures*, 38: 1563-83.

Suiker, ASJ, AV Metrikine, and R De Borst. 2001b. 'Comparison of wave propagation characteristics of the Cosserat continuum model and corresponding discrete lattice models', *International journal of solids and structures*, 38: 1563-83.

Sun, Chin-Teh, and Zhihe Jin. 2011. *Fracture mechanics* (Academic press).

Tarokh, Ali, Roman Y Makhnenko, Ali Fakhimi, and Joseph F Labuz. 2017. 'Scaling of the fracture process zone in rock', *International journal of fracture*, 204: 191-204.

Tavarez, Federico A, and Michael E Plesha. 2007. 'Discrete element method for modelling solid and particulate materials', *International Journal for Numerical Methods in Engineering*, 70: 379-404.

Thirumalaiselvi, A, and Saptarshi Sasmal. 2019. 'Acoustic emission monitoring and classification of signals in cement composites during early-age hydration', *Construction and Building Materials*, 196: 411-27.

Tian, Z., L. S. Huo, W. H. Gao, H. N. Li, and G. B. Song. 2017a. 'Modeling of the attenuation of stress waves in concrete based on the Rayleigh damping model using time-reversal and PZT transducers', *Smart materials and structures*, 26: 105030.

Tian, Zhen, Linsheng Huo, Weihang Gao, Hongnan Li, and Gangbing Song. 2017b. 'Modeling of the attenuation of stress waves in concrete based on the Rayleigh damping model using time-reversal and PZT transducers', *Smart Materials and Structures*, 26: 105030.

Torkan, Masoud, Alireza Baghbanan, Siavash Norouzi, Hamid Amrollahi, and Hamid Hashemolhosseini. 2019. 'Evaluating modes I, II, and mixed mode I-II fracture toughnesses of crystalline rocks using discrete element method', *Particulate Science and Technology*, 37: 1-9.

Trochidis, A, and B Polyzos. 1995. 'Acoustic emission during plastic deformation of crystals: A lattice‐dynamics approach', *Journal of applied physics*, 78: 170-75.

Troyer, Steve, Kurt Griffis, and Ray Shackelford. 2005. 'Structural Truss Elements and Forces', *Tech Directions*, 65: 13.

Tue, Nguyen Viet, Werner Theiler, and Nguyen Duc Tung. 2014. 'Schubverhalten von Biegebauteilen ohne Querkraftbewehrung', *Beton - und Stahlbetonbau*, 109: 666-77.

Udd, Eric. 1995. 'An overview of fiber‐optic sensors', *review of scientific instruments*, 66: 4015-30.

Unnþórsson, Rúnar. 2013. 'Hit detection and determination in AE bursts', *Acoustic emission-research and applications*: 1-20.

van Gemmeren, Valentin, Timothy Graf, and Jurg Dual. 2020. 'Modeling the acoustic emissions generated during dynamic fracture under bending', *International journal of solids and structures*, 203: 84-91.

Van Mier, Jan GM. 2017. *Fracture processes of concrete* (CRC press).

Van Mier, JGM. 1991. 'Mode I fracture of concrete: discontinuous crack growth and crack interface grain bridging', *Cement and concrete research*, 21: 1-15.

W. Goebel, TH, Danijel Schorlemmer, TW Becker, G Dresen, and CG Sammis. 2013. 'Acoustic emissions document stress changes over many seismic cycles in stick‐slip experiments', *Geophysical Research Letters*, 40: 2049-54.

Wadley, HNG, CB Scruby, and JE Sinclair. 1980. 'Acoustic emission source characterization', *The Journal of the Acoustical Society of America*, 68: S103-S04.

Walraven, Joost C. 1981. 'Fundamental analysis of aggregate interlock', *Journal of the Structural Division*, 107: 2245-70.

———. 2012. *Model Code 2010-Final Draft: Volume 1* (fib Fédération internationale du béton).

Wang, Chaoyi, Derek Elsworth, and Yi Fang. 2017. 'Influence of weakening minerals on ensemble strength and slip stability of faults', *Journal of Geophysical Research: Solid Earth*, 122: 7090-110.

Wang, Chun-lai. 2014. 'Identification of early-warning key point for rockmass instability using acoustic emission/microseismic activity monitoring', *International Journal of Rock Mechanics and Mining Sciences*, 71: 171-75.

Wang, Jian, and A Brooks Harris. 1989. 'Central-force models which exhibit a splay-rigid phase', *Physical Review B*, 40: 7256.

Wang, Lili. 2011. *Foundations of stress waves* (Elsevier).

Wang, Luyu, Cornelis Vuik, and Hadi Hajibeygi. 2022. 'A stabilized mixed-FE scheme for frictional contact and shear failure analyses in deformable fractured media', *Engineering Fracture Mechanics*, 267: 108427.

Wang, Zhiheng, Yong Li, Weibing Cai, Weishen Zhu, Weiqiu Kong, Feng Dai, Chen Wang, and Kai Wang. 2021. 'Crack propagation process and acoustic emission characteristics of rock-like specimens with double parallel flaws under uniaxial compression', *Theoretical and Applied Fracture Mechanics*, 114: 102983.

Weaver, R. L., and W. Sachse. 1995. 'Diffusion of Ultrasound in a Glass Bead Slurry', *Journal of the Acoustical Society of America*, 97: 2094-102.

Wu, Yu, Dongdong Ma, Xunjian Hu, Yang Hao, Chunhui Liu, and Haiyang Zhou. 2023. 'Numerical simulation on fracture and acoustic emission behavior of sandstone with partial filling flaw in semi-circular three-point bending tests', *Theoretical and Applied Fracture Mechanics*, 125: 103841.

Wu, Zhijun, Penglin Zhang, Lifeng Fan, and Quansheng Liu. 2019. 'Numerical study of the effect of confining pressure on the rock breakage efficiency and fragment size distribution of a TBM cutter using a coupled FEM-DEM method', *Tunnelling and Underground Space Technology*, 88: 260-75.

Wyllie, MRJ, GHF Gardner, and AR Gregory. 1962. 'Studies of elastic wave attenuation in porous media', *Geophysics*, 27: 569-89.

Xia, Chang, Yongtao Wu, Guangjun Cui, Jin Liao, Zhen Liu, and Cuiying Zhou. 2023. 'A Coupled Tensor–DEM–FEM Model for the Whole Process of Internal Fine-Scale Damage to Surface Damage in Red-Bed Soft Rocks in the Coastal Area of South China', *Journal of Marine Science and Engineering*, 11: 1542.

Xie, Chao, Linjuan Yuan, Min Zhao, and Yinghui Jia. 2020. 'Study on failure mechanism of porous concrete based on acoustic emission and discrete element method', *Construction and Building Materials*, 235: 117409.

Xu, F, H Hajibeygi, and Lambertus J Sluys. 2024. 'Multiscale Extended Finite Element Method for the Simulation of Fractured Geological Formations'.

Xuan, Ling-kuan, Guo-yong Jin, Jing-feng Gong, Wen-ping Zhang, and Ping-jian Ming. 2014. 'Time domain finite volume method for three-dimensional structural–acoustic coupling analysis', *Applied acoustics*, 76: 138-49.

Yang, Yanjun, Giovanni Cascante, and Maria Anna Polak. 2011. 'New method for the evaluation of material damping using the wavelet transform',

Journal of geotechnical and geoenvironmental engineering, 137: 798-808.

Yao, Zhigang, Yong Fang, Rui Zhang, Song Pu, Guangming Zhao, Tao Yu, and Chunchi Ma. 2023. 'The mechanism of stick–slip as a rockburst source in jointed rockmass: an experimental study', *Rock Mechanics and Rock Engineering*, 56: 3573-93.

Yavari, Arash, and Shahram Sarkani. 2001. 'On applications of generalized functions to the analysis of Euler–Bernoulli beam–columns with jump discontinuities', *International Journal of Mechanical Sciences*, 43: 1543-62.

Ying, SP. 1973. 'Characteristics and mechanisms of acoustic emission from solids under applied stress', *Critical Reviews in Solid State and Material Sciences*, 4: 85-123.

Zelenyak, Andreea-Manuela, Marvin A Hamstad, and Markus GR Sause. 2015. 'Modeling of acoustic emission signal propagation in waveguides', *Sensors*, 15: 11805-22.

Zelenyak, Andreea Manuela, Marvin A Hamstad, and Markus GR Sause. 2014. 'Finite element modeling of acoustic emission signal propagation with various shaped waveguides'.

Zerwer, A, Giovanni Cascante, and J Hutchinson. 2002. 'Parameter estimation in finite element simulations of Rayleigh waves', *Journal of Geotechnical and Geoenvironmental Engineering*, 128: 250-61.

Zhang, F. 2022. 'Acoustic emission-based indicators of shear failure of reinforced concrete structures without shear reinforcement'.

Zhang, Fengqiao, Lotfollah Pahlavan, and Yuguang Yang. 2020. 'Evaluation of acoustic emission source localization accuracy in concrete structures', *Structural Health Monitoring*, 19: 2063-74.

Zhang, Fengqiao, Yuguang Yang, Sonja AAM Fennis, and Max AN Hendriks. 2022. 'Developing a new acoustic emission source classification criterion for concrete structures based on signal parameters', *Construction and Building Materials*, 318: 126163.

Zhang, Han, and Zhenyuan Lin. 2023. 'Analytical solution of acoustic emission in soft material with cracks by using reciprocity theorem', *Engineering Fracture Mechanics*, 277: 108996.

Zhang, Qi, and Xiao-Ping Zhang. 2017. 'A numerical study on cracking processes in limestone by the b-value analysis of acoustic emissions', *Computers and Geotechnics*, 92: 1-10.

Zhang, Rui, Xiaofeng Yan, and Li Guo. 2022. 'Deep learning-based classification of damage-induced acoustic emission signals in UHPC', *Construction and Building Materials*, 356: 129285.

Zhang, Wohua, and Yuanqiang Cai. 2010. *Continuum damage mechanics and numerical applications* (Springer Science & Business Media).

Zhao, Liang, Le Kang, and Shuang Yao. 2018. 'Research and application of acoustic emission signal processing technology', *IEEE Access*, 7: 984-93.

Zhao, Q, A Lisjak, G Grasselli, and Q Liu. 'Numerical simulation of acoustic emission in rocks using FEM/DEM'.

Zhao, Qi. 2013. 'Numerical Studies of Frictional Sliding Behavior and Influences of Confining Pressure on Accoustic Activities in Compression Tests Using FEM/DEM'.

Zhao, Tongyang, Wanpeng Huang, Donghai Jiang, Huanyu Li, Yaxin Liu, Le Sui, and Keke Hou. 2024. 'Experimental study on creep disturbance mechanics and acoustic emission characteristics of coal under different stress control', *Construction and Building Materials*, 448: 138236.

Zheng, Kun, Chaolin Wang, Yu Zhao, Jing Bi, and Haifeng Liu. 2023. 'Theoretical and experimental exploration on the combined mode I+ III fracture toughness of shale using the edge-notched disk bending method with acoustic emission monitoring', *Theoretical and Applied Fracture Mechanics*, 125: 103870.

Zheng, Yonglai, Yuan Wen, Tanbo Pan, Yongcheng Liu, Yujue Zhou, Ruizhi Li, and Yubao Zhou. 2022. 'Fractal characteristics and damage evaluation of corroded beams under four-point bending tests based on acoustic emission techniques', *Measurement*, 202: 111792.

Zheng, Yonglai, Yujue Zhou, Yubao Zhou, Tanbo Pan, Limin Sun, and Don Liu. 2020. 'Localized corrosion induced damage monitoring of large-scale RC piles using acoustic emission technique in the marine environment', *Construction and Building Materials*, 243: 118270.

Zhou, Yubao, Beyazit Bestami Aydin, Fengqiao Zhang, Max AN Hendriks, and Yuguang Yang. 2024. 'A lattice modelling framework for fracture-induced acoustic emission wave propagation in concrete', *Engineering Fracture Mechanics*, 312: 110589.

Zhu, Changyun, Guoliang Qin, and Jiazhong Zhang. 2011. 'Implicit Chebyshev spectral element method for acoustics wave equations', *Finite Elements in Analysis and Design*, 47: 184-94.

Zhu, Zhiwen, Zihan Jiang, Federico Accornero, and Alberto Carpinteri. 2024. 'Correlation between seismic activity and acoustic emission on the basis of in situ monitoring', *Natural Hazards and Earth System Sciences*, 24: 4133-43.

Ziegler, John G, and Nathaniel B Nichols. 1942. 'Optimum settings for automatic controllers', *Transactions of the American society of mechanical engineers*, 64: 759-65.

Zietlow, William Kurtis, and JF Labuz. 1998. 'Measurement of the intrinsic process zone in rock using acoustic emission', *International Journal of Rock Mechanics and Mining Sciences*, 35: 291-99.

Acknowledgment

Five years have passed since the day I first arrived at Delft University of Technology. This journey feels like a dream—one so vivid and extraordinary that, upon waking, I find my PhD years have quietly come to an end. I often wish I could remain in that dream forever, for it has been filled with unforgettable moments of joy, sorrow, and growth. I am deeply grateful to everyone who has appeared along the way; it is you who have made this dream so remarkable.

First and foremost, I must express my heartful gratitude to my dear friend and "Academic Daddy", Beyazit Bestami Aydin. Without you, I could not have completed my PhD thesis, which is entirely based on your lattice model. Our journey has only just begun, and I look forward to a lifelong collaboration and creating even more impactful research together. Let us continue to challenge the classical and make a difference in the world.

I would like to sincerely thank my daily supervisor, Dr. Yuguang Yang. You gave me the opportunity to transition into a research field that truly fascinates me. You have invested an extraordinary amount of time and energy in me: meeting with me every week, patiently revising my manuscripts countless times, and even personally guiding each of my experiments—something that most supervisors would rarely do. Your meticulous guidance not only enabled me to complete my PhD within four years but also taught me how to conduct genuine scientific research. From you, I have learned many qualities and principles of great scientists. You taught me how to think critically, reason rigorously, and write systematically. More generally, from daily interactions to academic presentations, you have shown me how to think and communicate logically and effectively. I am deeply grateful for everything you have done to make my PhD journey so meaningful. I hope I can become a true scientist like you in future!

I am deeply grateful to my promotor, Prof. Max Hendriks, for your insightful and prompt feedback, patience, and unwavering support. I may be the PhD student who has had the most frequent meetings with you, from monthly meetings to semi-monthly meetings during certain periods. Thank you for the time and effort you have devoted to me. One of the most valuable lessons you have imparted is the importance of critical thinking and questioning the literature. Beyond academics, your execution capability is something I aspire to emulate in my future career; you consistently respond promptly to every request, demonstrating a quality that truly paves the way to success.

I have been fortunate to receive support from many professors, to whom I am deeply grateful. I would like to extend my sincere appreciation to Rita Esposito, Bert Sluys, Erik Schlangen, and Andrei Metrikine at TU Delft; Tsukasa Shiotani at Kyoto University; Dimitris Aggelis at Vrije Universiteit Brussel; and Christian Grosse at TU Munich, for their invaluable guidance and generous assistance.

I am deeply grateful to all my colleagues at Concrete Structures Section. I would like to extend special thanks to Hao Cheng, Yitao Huang, Jiandong Lu, Gabriela Zarate Garnica, Shozab Mustafa, Zhenxu Qian, Emilia Andrade Borges, Pengwei Guo and Chuanrui Guo, whose steadfast and collaborative spirit have been a constant source of motivation and strength.

I would definitely like to thank my intimate friends at TU Delft Jinbao Xie, Minfei Liang, Hanting Ye, Xiaoyu Liu, Zhaochong Cai, Weikang Feng, Chen Liu and many others. While I cannot list everyone here, please know your companions have meant a lot to me.

In addition, I would like to thank those who have once harboured hostility or even caused me harm. Your presence has constantly reminded me to strengthen myself, ultimately earning the basic respect from you.

I would like to thank my parents. Just like Luo Zhongli's painting *Father*, as traditional Chinese parents, I can feel that I have been the centre of your lives. Thank you for your wholehearted love and unconditional support! I hope that your retirement years will be lived fully for yourselves. （我要感谢我的父母。就像罗中立的油画《父亲》所呈现的那样，作为传统的中国父母，我能感受到自己仿佛一直是你们生命的全部意义。感谢你们给予我的全心全意的爱与无条件的支持！希望你们的退休生活能够真正为自己而活。）

Last but by no means least, I want to thank my fiancée. I love you, Xinling Yue. Meeting you has been the greatest fortune of my life, and choosing you remains the most important decision I have ever made. Thank you for your companionship, which has brought me joy every single day over the past five years. I have experienced an unusual PhD journey with several struggling periods, and without your support during the most critical moments, I would not have been able to overcome the struggles along the way.

About the author

Yubao ZHOU (zhouyubao16@gmail.com)

Born on October 15, 1993, in Kunming, Yunnan, China.

He received his B.S. degree in Channels and Coastal Engineering and his M.S. degree in Hydraulic Engineering from Tongji University, China, in 2016 and 2020, respectively. In 2017, he worked as a construction engineer at Shanghai Construction Group, China.

He commenced his research at Delft University of Technology on 15 November 2020 in the Faculty of Civil Engineering and Geosciences. During his first year, he was affiliated with the Section of Applied Mechanics, where he worked on multiscale modelling of masonry under the supervision of Dr. Rita Esposito and Prof. Bert Sluys. Since 1 December 2021, Yubao has been pursuing his Ph.D. within the Section of Concrete Structures under the supervision of Dr. Yuguang Yang and Prof. M.A.N. Hendriks.

His Ph.D. research focuses on developing advanced numerical methods to elucidate the physical mechanisms underlying acoustic emission (AE) phenomena induced by quasi-brittle fracture. The overarching aim is to enable more reliable applications of AE techniques in the structural health monitoring of concrete structures.

His current research interests include quasi-brittle fracture, stress waves, and nonlinear dynamic processes such as earthquakes and faulting.

ISBN 978-94-6518-207-0

TU Delft